

Dissertation zur Erlangung des Doktorgrades
de Fakultät für Chemie und Pharmazie
der Ludwig-Maximilians-Universität München

Single Molecule Traffic in Mesoporous Materials

AND

New Photostable Water-Soluble Terrylenediimide Derivatives

Christophe Jung
from
Haguenau

2007

Erklärung

Diese Dissertation wurde im Sinne von § 13 Abs. 3 bzw. 4 der Promotionsordnung vom 29. Januar 1998 von Prof. Dr. C. Bräuchle betreut.

Ehrenwörtliche Versicherung

Diese Dissertation wurde selbständig, ohne unerlaubte Hilfe erarbeitet.

München, den 14. September 2007

Dissertation eingereicht am 14.09.2007

1. Gutachter: Prof. Dr. C. Bräuchle

2. Gutachter: Prof. Dr. T. Bein

Mündliche Prüfung am 16.10.2007

Contents

1	Introduction	5
2	Theoretical background and methods	9
2.1	Fluorescence microscopy	9
2.1.1	Fluorescence	9
2.1.2	Single molecule spectroscopy (SMS)	12
2.1.3	Apparatus and methods	17
2.2	Diffusion theory and trajectory analysis	33
2.2.1	Diffusion theory: microscopic approach	33
2.2.2	Analysis of trajectories	35
3	Translational, orientational and spectral dynamics of single dye molecules in highly oriented mesoporous materials	37
3.1	Introduction to mesoporous materials	37
3.2	Diffusion and orientation of single TDI molecules in different mesophases of Brij-56-templated mesoporous films	42
3.2.1	Sample systems	42
3.2.2	Diffusion behavior of single TDI molecules in pure hexagonal and lamellar phases	43
3.2.3	Diffusion of single TDI molecules in the phase mixture - Phase switching	49

3.2.4	Mean squared displacement analysis	51
3.2.5	Conclusion	53
3.3	Translational, orientational and spectral dynamics of single TDI molecules in CTAB-templated mesoporous films	54
3.3.1	The M41S CTAB-templated mesoporous system	54
3.3.2	Simultaneous measurement of orientational and translational dy- namics	54
3.3.3	Simultaneous measurement of orientational and spectral dynamics	58
3.3.4	Conclusion	73
3.4	Preparation and single molecule investigation of highly structured do- mains in CTAB-templated mesoporous films	74
3.4.1	Growth of the highly structured domains	74
3.4.2	Translational and orientational dynamics of single TDI molecules diffusing in the highly structured domains	85
3.4.3	Conclusion	100
3.5	Experimental section	101
4	New photostable water-soluble terrylenediimide derivatives for appli- cations in single molecule studies and membrane labelling	105
4.1	Introduction: novel fluorophores for biological labelling	105
4.2	WS-TDI as a powerful dye for applications in single molecule studies and membrane labelling	108
4.2.1	Absorption and emission spectra	109
4.2.2	Single molecule studies	112
4.2.3	Protein labelling	115
4.2.4	WS-TDI as a membrane marker	117
4.3	Two other WS-TDI derivatives: WS-TDI dodecyl and WS-TDI pyridoxy	121

4.3.1	New derivatives for a larger panel of applications	121
4.3.2	Photophysical parameters	121
4.3.3	Fluorescence spectra in presence in cells	126
4.3.4	Membrane labelling in living cells	127
4.4	Localization of the three WS-TDI derivatives in the early and late endo- cytic pathway of living cells	132
4.5	Conclusion	137
4.6	Experimental section	138
5	Summary	141
5.1	Single molecule traffic in mesoporous materials	141
5.2	Photostable water-soluble terrylenediimide derivatives for applications in single molecule studies and membrane labelling	144
6	Appendix	147
6.1	Orientation of TDI molecules encapsulated in ordered mesoporous chan- nels in anodic alumina membrane hosts	147
6.2	List of abbreviations	150
6.3	Published work and contributions to conferences and meetings	151
6.3.1	Publications	151
6.3.2	Contributions to conferences and meetings	152

Chapter 1

Introduction

Until 20 years ago chemistry was dealing with molecules in the sense of moles. In 1952 E. Schrödinger stated: "...we never experiment with just one electron or atom or molecule. In thought experiments we sometimes assume we do..." Hence, chemists were thinking in terms of ensembles of molecules, nearly forgetting that each molecule is an individual entity. Only slowly scientists started dreaming about resolving molecules individually. This was supported by the development of more and more sensitive detectors culminating in high- performance detectors able to detect the fluorescence signal of single emitters. In 1989 and 1990 the absorption and fluorescence excitation spectra of single molecules were measured for the first time by the groups of Mörner¹ and Orrit,² respectively. Those revealed that spectra of single molecules, which were until then considered as a stable property of a given dye molecule, could exhibit unsuspected strong dynamics such as intensity fluctuations or large spectral jumps. Since then a variety of single molecule spectroscopy (SMS) methods have been developed to observe not only the fluorescence spectra of individual emitters, but a whole range of properties like the orientation of their dipole moment,³⁻⁹ their photostability (i.e. their resistance against photo-destruction),¹⁰⁻¹⁴ or their translational diffusion.¹⁵⁻²¹ These techniques paved the way for a new type of investigation, where not only the mean value of a specific molecular property can be obtained, but the distribution of values for this property with large variations from molecule to molecule.

The advantage of SMS studies compared to standard ensemble techniques is crucial in fields ranging from fundamental investigations up to industrial applications. A single molecule incorporated as a guest into polymeric or porous solids, will act as a reporter revealing a wealth of details about the host structure and the dynamics involved.²²⁻²⁸ A prominent example are mesoporous materials which constitute a rapidly growing field of host systems. Their scientific and technological relevance is based on the presence

of pores of controllable dimensions at the nanometer lengthscale.^{29,30} The presence of voids enable these materials to discriminate between molecules and allow interactions with only a subfraction of them. Research efforts in this field have been driven by emerging technological applications such as nanocatalysis,^{31–33} gas separation,³⁴ chemical sensing,³⁵ photonics,^{36,37} or novel drug delivery systems.^{38,39} The current challenges include the design of mesostructures for optimized applications as well as the fundamental understanding of host-guest interactions.

Standard characterization methods, such as NMR, IR, UV/Vis spectroscopy, electron microscopy and X-ray diffractometry characterize the host structure and host-guest interactions at the ensemble level.^{40–42} However, the nanometer-scale behavior of the molecules is both spatially and temporally heterogeneous, and a complete characterization of the host-guest system is not possible with these methods. Information about such heterogeneities is indeed lost in the ensemble averaging process. Hence SMS techniques are the methods of choice to directly observe details of the molecular behavior because they work on a molecule-by-molecule basis. The position of a single molecule, the orientation of its dipole moment as well as the position, intensity and width of the fluorescence spectrum, or photophysical parameters such as brightness and photostability provide valuable information about the host, which are difficult or even impossible to obtain with standard methods.

The first part of this thesis is devoted to the detailed investigation via SMS of the translational, orientational and spectral dynamics of single terrylenediimide (TDI) dye molecules incorporated in various mesoporous films (synthesized by Barbara Platschek in Prof. Bein's group, Munich). Diffusion in mesoporous materials differs from free diffusion e.g. in a liquid in the sense that the molecules have to move through channels of molecular dimension. As a consequence strong interactions between the diffusing molecules and the material framework occur, and the molecular motion of the dye molecules is thus determined by the exact size and shape of the channel. It will be shown how the observed spatial and temporal heterogeneities of single molecule dynamics provide deep insight into the host-guest interactions, i.e. if and how properties of molecules are influenced by the nanoscale heterogeneities of the porous material.

The second part of this thesis focuses on biological investigations since not only industrial technologies but also biology benefit from single molecules techniques. A fluorophore can be attached to a biological system to report about biological functions. In the past few years, an increasingly wide variety of biological molecules such as proteins, lipids, DNA, etc. labelled with fluorophores, have been individually detected after labelling with fluorophores, allowing investigations as diverse as membrane dynamics,^{43–46} complex assembly, disassembly or mobilization,⁴⁷ and all types of DNA translocations.^{48–50} The

findings of these studies unraveled mechanisms which remained so far enigmatic due to experimental limitations.

A critical parameter for the investigation of such biological processes is the ability to visualize labels and events with high spatial and temporal resolution. Maximum accuracy can be achieved using fluorophores emitting a high number of photons per molecule. However, most of the available water-soluble dye molecules suffer from low resistance towards photodegradation, thereby dramatically limiting the number of emitted photons. Hence, efforts are focused on developing new fluorophores as brighter and more photostable markers. The task in the second part of this thesis is to characterize three novel high-performing water-soluble terrylenediimide derivatives synthesized by Fabian Nolde in the Professor Müllen's Group (MPI, Mainz),⁵¹ to show valuable applications of these dyes in single molecules investigations, and to demonstrate their utilization as brilliant membrane markers in biological studies.

Synopsis

The thesis comprises one introductory chapter, three chapters containing a large variety of experiments as described below, further completed by a summary, a biography, and appendices.

Chapter 2 covers the theoretical background and describes the experimental setups. It begins with the principles of fluorescence microscopy and introduces SMS showing the versatility and explaining some of the numerous abilities of this method. This is followed by a description of the different experimental methods used in this thesis to visualize fluorescent dye molecules in different systems. The last part of the chapter focuses on the theory of diffusion, a central topic throughout the experiments.

Chapter 3 presents the investigation of translational, orientational and spectral dynamics of single terrylenediimide (TDI) dye molecules diffusing as guests in the pores of various mesoporous host films. After introducing mesoporous materials and their synthesis procedures, the results of single molecules tracking experiments in different mesoporous mesophases obtained with poly(oxyethylene)cetylother-copolymer (Brij-56) as structure directing agent (template) are discussed. Focus is given on the comparison of the orientation and mobility of the guest molecules. The two following parts of the chapter deal with mesoporous thin films prepared with cetyltrimethylammonium-bromid (CTAB) surfactant as template. The results of simultaneous measurements of translational/orientational as well as spectral/orientational dynamics of diffusing single

molecules are discussed, giving novel insight into host-guest interactions in mesoporous materials. Finally it is shown how large, highly structured domains of parallel pores could for the first time be prepared within CTAB-templated mesoporous films, and how single TDI molecules diffuse in the very linear pores of these domains.

Chapter 4 emphasizes the characterization and potential biological applications of three new water-soluble TDI dye molecules: WS-TDI, WS-TDI dodecyl and WS-TDI pyridoxy. After depicting the reasons for engineering new water-soluble fluorophores, the results of the investigation of WS-TDI are presented. These investigations demonstrate the suitability of WS-TDI for SMS studies, and emphasize its improved characteristic properties for biological studies compared to currently available dyes, notably due to their much higher photostability. The second part of the chapter presents the results of the investigation of WS-TDI dodecyl and WS-TDI pyridoxy, and focuses on their advantages compared to WS-TDI. Finally, a study of the dye-uptake process in living cells is presented, showing a potential utilization of the three new fluorophores for the investigation of biological systems.

Chapter 2

Theoretical background and methods

2.1 Fluorescence microscopy

This chapter is subdivided into two Sections: the first introduces the basics of fluorescence microscopy. It starts with the theoretical background about the phenomenon of fluorescence, then introduces single molecule spectroscopy. This is followed by a description of the optical microscopy equipments used, and the principles of single particle tracking (SPT) are explained. The last Section gives a short introduction to the theory of diffusion, since the phenomenon of diffusion is omnipresent in this work.

2.1.1 Fluorescence

2.1.1.1 The phenomenon

Fluorescence is the re-emission of light by a molecule that has absorbed photons. The processes that occur between the absorption and emission of light are illustrated by the Jablonski diagram in Figure 2.1. At room temperature a dye molecule occupies the ground state S_0 . After absorption of a photon the fluorophore is excited to a vibrational level of the first excited electronic state S_1 (in about 10^{-15} s), and then rapidly (typically within 10^{-12} s or less) relaxes to the lowest vibrational level of S_1 . The molecule remains in this electronic state for about $10^{-9} - 10^{-8}$ s, after which a radiative transition occurs to a higher excited vibrational level of S_0 , which then quickly (10^{-12} s) reaches thermal equilibrium.

As visible in the Jablonski scheme the energy of emission is less than that of absorption. Thus, the fluorescence is red-shifted with respect to the absorbed light. The difference between the wavelengths maxima of excitation and emission, known as the Stokes shift, is the critical property that makes fluorescence so powerful for microscopy.

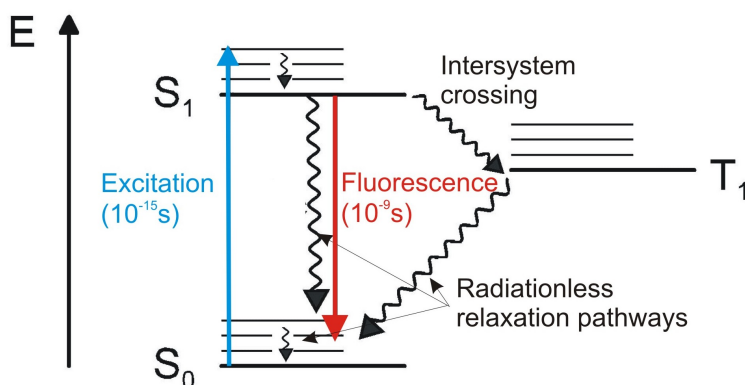


Figure 2.1: Jablonski diagram as a schematic representation of the electronic energy-level diagram. S_0 is the ground singlet state; S_1 is the first excited singlet; T_1 , lowest triplet state. For each electronic state, several vibrational levels are shown. The molecule is excited by absorption of light from S_0 to S_1 . The intersystem crossing and the radiationless relaxation pathways are shown as curved arrows.

So far, we considered only the two-level system of the ground (S_0) and first excited singlet states (S_1). These states maintain each electron in a pair of opposite spins. Organic molecules have also triplet states, the lowest triplet state is called T_1 . In this state an electron, excited on a higher orbital, has undergone a subsequent reversal in spin so that formerly paired electrons are then parallel (spin-flip). This conversion is called intersystem crossing. The population and decay rates of the triplet state are slow, because these transitions involve spin flips, an improbable process allowed only by weak spin-orbit coupling. This additional state will have some consequences on the fluorescence emission of single molecules, as will be discussed below.

2.1.1.2 Absorption and fluorescence emission spectra

Typical absorption and fluorescence spectra of an organic molecule are shown in Figure 2.2 for a terrylendiimide (TDI) derivative in chloroform. The peaks and the valleys in the respective spectra reflect the energy levels in the molecules Jablonski diagram shown in Figure 2.1, and as it is for most fluorophores the emission is the mirror image of the $S_0 \rightarrow S_1$ absorption.

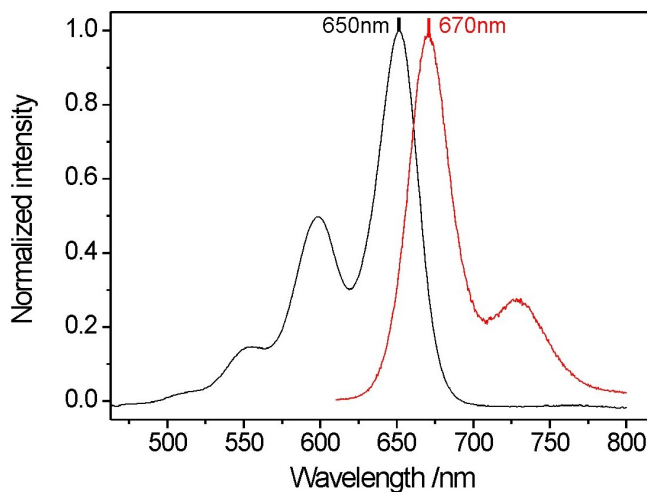


Figure 2.2: Absorption (black) and emission (red) spectra of a terrylendiimide (TDI) derivative (structure shown in Figure 4.1) in chloroform (excitation at 620 nm). The spectra are normalized. The Stokes shift is 20 nm for this fluorophore.

The probability that a fluorophore will absorb a photon is called its molar extinction coefficient, ϵ_λ , in units of $\text{M}^{-1}\text{cm}^{-1}$. This parameter can be experimentally determined at a specific wavelength using the Beer-Lambert Law:

$$\epsilon_\lambda = \frac{A}{c \cdot l} \quad (2.1)$$

where A is the absorbance, which can be directly taken from the absorption spectrum, c is the concentration of the fluorophore, and l the length of the sample.

2.1.1.3 Quantum yields and fluorescence lifetimes

A key parameter controlling the strength of fluorescence is the probability for photon emission per absorption event, i.e. the fluorescence quantum yield φ_f which is given by:

$$\varphi_f = \frac{k_{rad}}{k_{rad} + k_{nonrad}} \quad (2.2)$$

where k_{rad} is the radiative emission rate i.e. fluorescent rate and k_{nonrad} the sum of all nonradiative rates such as internal conversion or intersystem crossing. For bright fluorescence emission this parameter should be high, i.e. as close to unity as possible. The best fluorophores are generally those with relatively rigid structures so that the primary path for deactivation of the excited state is via the emission of a fluorescent photon.

The lifetime of the excited state is defined by the average time the molecule spends in the excited state prior to returning to the ground state. The fluorescence lifetime is a characteristic parameter of a fluorophore, whose values are typically $10^{-9} - 10^{-10}$ s.

2.1.2 Single molecule spectroscopy (SMS)

2.1.2.1 SMS studies *versus* high concentration studies

Single molecule Spectroscopy is essentially a technique that detects the absorption or the fluorescence of single fluorophores that are present at extremely low concentration in a certain medium (e.g. liquid solutions, polymers, molecular sieves, cells etc.). The transition in concentration from ensemble experiment to single molecule detection is illustrated in Figure 2.3. It shows three confocal images of a dilution series of water-soluble terrylenediimide (WS-TDI) dye molecules embedded in polymer films. The concentration used in Figure 2.3a corresponds to the limit between ensemble and single molecule concentration since the presence of individual molecules is already visible, but they cannot be clearly distinguished. In Figure 2.3b the fluorophore concentration is tenfold lower, and here the dye molecules appear with their typical diffraction limited spots. The spots are clearly separated for the highest dilution (Figure 2.3c), and photoblinking and photobleaching can be observed during the confocal scan of the spots marked with yellow circles. Photoblinking and photobleaching events are typical signatures of single molecules, as will be shown below.

By using SMS the experimenter avoids disturbing a sample by adding huge amounts of dye. This prevents, for example, the formation of dye aggregates, changes in the host crystal habitus, or the influence on biological processes when the dyes are used as labels. The most important feature of SMS, however, lies in the elimination of the so-called ensemble averaging. When analyzing a sample by conventional spectroscopy, millions of molecules are present in the sample and thus are observed simultaneously. Any property inferred from such a sample will be an overall average value for this specific property of the sample. This obscures the heterogeneities which each molecule experiences from its immediate surroundings. When going to the level of SMS studies these heterogeneities can be resolved and each single dye molecule conveys information from its environment. For instance, the spectra of two different molecules of the same type of fluorophore in the same sample can be different, exhibiting shifted emission maxima, or different vibrational couplings. In this way, the differences which depend on the molecule's immediate surroundings become apparent.

Figure 2.4 displays an exemplary sequence of fluorescence spectra of a single TDI molecule

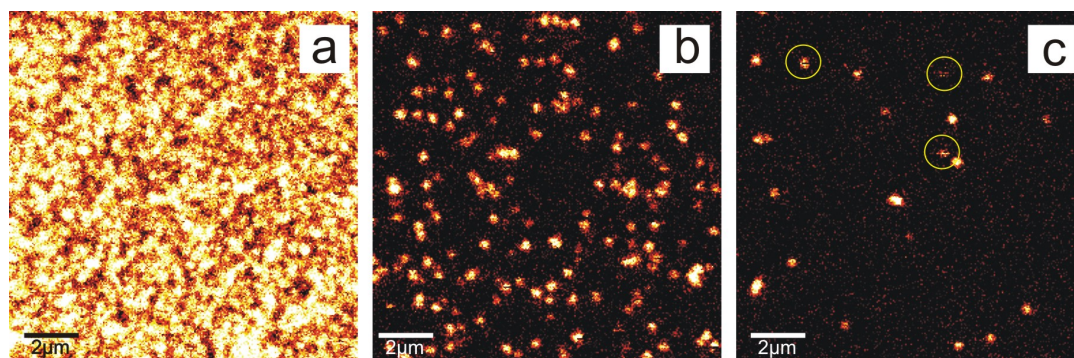


Figure 2.3: From ensemble to single molecules. Confocal images showing a dilution series of a water-soluble terrylendiimide dye molecules (WS-TDI, structure shown in Figure 4.1) embedded in thin polyvinyl-alcohol (PVA) polymer films. The concentrations of WS-TDI in the polymer solutions before spin-coating were (a) $\sim 10^{-7}$ mol/L, this concentration corresponds to the limit between ensemble and single molecule concentrations since some individual molecules are already visible. (b) $\sim 10^{-8}$ mol/L, and (c) $\sim 10^{-9}$ mol/L, these concentrations are suitable for SMS studies since the fluorescent spots corresponding to single molecules are spatially separated. The molecules corresponding to the spots marked with yellow circle exhibit photoblinking or photobleaching events during their confocal scanning time.

moving in the channels of a mesoporous material. In the first four fluorescence spectra the emission maximum is nearly constant, fluctuating only slightly around a mean value of about 678 nm. Then, an abrupt, large spectral jump of about 16 nm occurs, after which the emission maximum remains nearly constant (at around 662 nm) in the six following spectra. Such spectral dynamics are a consequence of the changes of the underlying electronic energy levels in the molecule, which depend very sensitively on the interaction with the surrounding host. Hence, the analysis of the dynamic behavior of the fluorescence spectrum has the potential to reveal dynamic molecular processes (like environmental changes) otherwise obscured in a bulk measurement due to ensemble averaging. Moreover, by recording the same property of many different individual molecules one gains access not only to a mean value for that property, but also to its distribution.

Early experiments, for example, showed that the spectral diffusion of molecular absorptions acted as indicator of low-temperature lattice dynamics.^{52,53} More recently, spectral diffusion and switching processes with jumps between two or more spectral states were investigated for single molecules at room temperature.^{54,55}

2.1.2.2 Single molecule photo-physics

The observation of fluorescence light from a single molecule differs from that of a large ensemble of molecules because the fluorescence becomes a digital shape with "yes" or

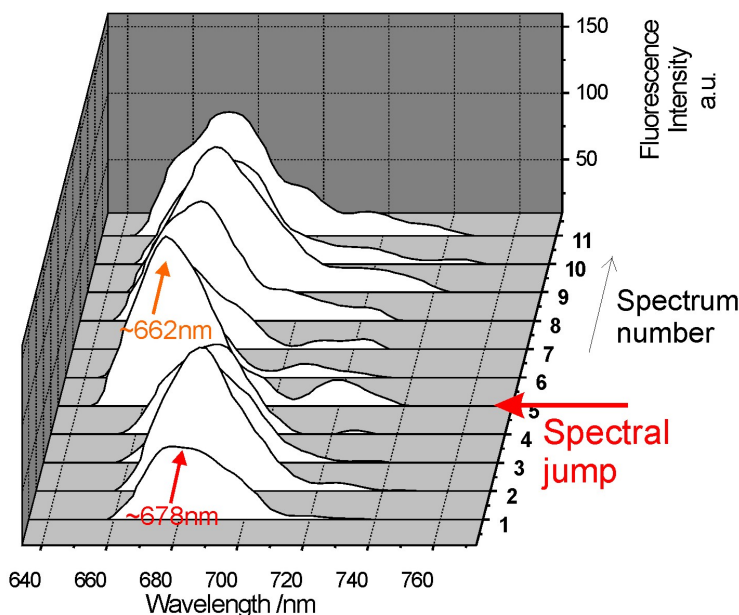


Figure 2.4: A spectral jump underwent by a single molecule. Sequence of fluorescence emission spectra of a single TDI molecule diffusing in a mesoporous material (Integration time is about 300 ms per spectrum). The wavelength of the fluorescence emission maximum is relatively stable during the first four spectra, fluctuating only slightly around 678 nm. Suddenly, a spectral jump of about 16 nm occurs between spectra 4 and 5. In the next 7 spectra the fluorescence emission is blue shifted with an emission maximum at around 662 nm.

”no” processes. As an example, in the intersystem crossing the individual molecule undergoes transitions from singlet state to triplet state and vice versa. However, the system can only be in one state at a given time. Hence, emission of fluorescent light is not continuous. Four phenomena limit the emission rate of fluorescence light: the anti-bunching, the bunching, the photoblinking and the photobleaching. They have different physical origins and usually occur at well-separated orders of timescales.

Anti-bunching Just after the absorption of a photon, the molecule is excited into an upper state and stays there for a while (in the order of 1 ns) before it relaxes back to the ground state by emitting a photon. During this period the molecule is prevented to undergo another excitation transition. This behavior gives rise to a phenomenon known as anti-bunching, which leads to the optical saturation of the transition for high laser powers. Before saturation, when the laser power is increased, more and more photons are emitted per second. When saturation occurs, further increases in laser power generate only more background rather than more signal. Thus, anti-bunching limits the maximum emission rate of a molecule.

Triplet bunching On a longer timescale the passage of the molecule in the triplet state T_1 leads to bunching of fluorescent photons. The "packets" of photons emitted between triplet events are like bunches of photons, hence the name "Triplet bunching". The molecule starts emitting at a high rate, and then it crosses over to the triplet where it is dark during the triplet lifetime, commonly in the order of microseconds to milliseconds.

Photoblinking Another process occurs when the fluorescence emission reaches another reversible dark state for a period of time in the order in the order of milliseconds to seconds. This phenomenon, called photoblinking, is frequently encountered experimentally, and is a typical signature of a single molecule. Figure 2.5 displays the fluorescence emission of a single molecule plotted *versus* time, the so-called fluorescence intensity time trajectory. The fluorescence signal is not continuous, but interrupted by three time intervals (indicated by orange arrows) where it reaches temporarily the background level. These OFF times correspond to photoblinking events.

Photobleaching Photobleaching is a special case which arises when a dark state is reached irreversibly. A photobleaching event can be observed in Figure 2.5 where the fluorescence intensity reaches irreversibly the background level at $t = 9$ s. The molecule is not able to emit light anymore. This phenomenon, not well understood yet,^{11,12,56} results from photo-degradation reactions, where the absorption characteristics of the products formed are different from those of the original molecule. On the molecular level, photobleaching is not observed as a process but as a singular irreversible event. It limits the observation time of the molecule and, therefore, the collected information.

Number of total emitted photons (TEP) and survival time (ST) before photobleaching

Typically, a molecule will photobleach irreversibly after a certain amount of photo-cycles. The latter is related via the fluorescence quantum yield to the number of total emitted photons (TEP) before photobleaching and gives, in average, how many photons can be extracted from a molecule before it dies. This number is a characteristic for a fluorescent dye molecule (commonly, the TEP is in the order of $10^4 - 10^8$), and can be determined experimentally as the integral over time of the fluorescence intensity time trajectory of a single molecule (gray area in Figure 2.5).

Another important parameter characterizing the photostability is the survival time (ST), which is the total time of fluorescence emission of the single molecule before the photobleaching step (indicated by a green arrow in Figure 2.5; in this example $ST = 9.7$ s).

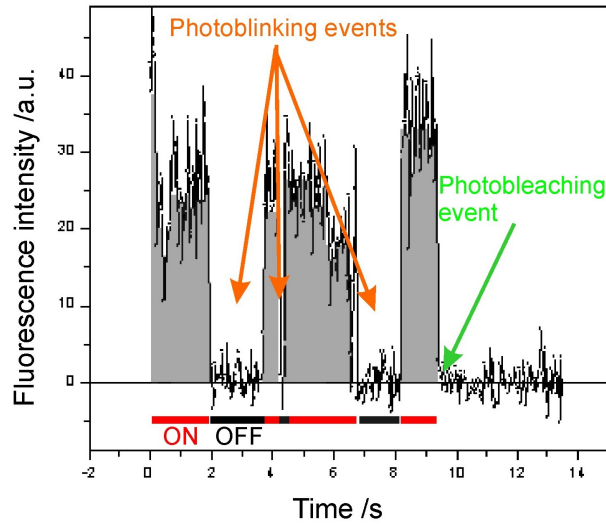


Figure 2.5: Fluorescence intensity time trajectory of a single molecule. Three photoblinking events occur (indicated by orange arrows) as well as the photobleaching step at the end of the life of the molecule (indicated by a red arrow).

Method of analysis of the photostability parameters

The analysis is based on calculating the probability distributions of the number of total emitted photons before photobleaching and of the survival times. Molski⁵⁷ developed a formalism to calculate the TEP and ST, and showed that the distributions of a photostability parameter x are well approximated by either mono- or multi-exponential distributions $S(x)$, which are defined by characteristic decay parameters.

$$S(x) = \sum_{i=0}^n A_i \exp\left(-\frac{x}{x_i}\right) \quad (2.3)$$

where x_i are the decay parameters and A_i the amplitudes of the individual components.

The number of exponential components can be determined by the decrease in the reduced χ^2 of the fit function. A minimum twofold decrease in the reduced χ^2 of the fit was required to justify an additional exponential decay in the model function.⁵⁸

For comparison of the photobleaching behavior between different dyes, an average TEP or ST can be defined as:

$$\langle x \rangle = \sum_{i=0}^n A_i \cdot x_i \quad (2.4)$$

2.1.3 Apparatus and methods

This Section presents the principles of the confocal and the wide-field microscopes, the two main setups used in this work, which is followed by the description of the methods used for orientational imaging as well as spectroscopy of individual molecules. The last part of this Section explains the technics used for fluorescence correlation spectroscopy (FCS) and life-time measurements.

2.1.3.1 Light microscopy

Numerical aperture The numerical aperture (NA) of an objective lens is a measure of the angular size of the focusing cone of light and is defined as follows:

$$NA = n \cdot \sin \theta \quad (2.5)$$

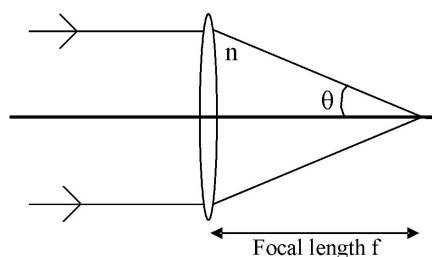


Figure 2.6: Definition of the numerical aperture (NA), where θ is the half-angle of the cone and n is the index of refraction of the medium containing the cone.

The NA represents the maximum cone width that can be collected with the focus. The higher the NA and the lower the focal length are, the more light is collected.

Lateral and axial resolution The limit of resolution is defined by the smallest separation between two point objects that still allows them to be distinguished. This is referred to as lateral resolution in optical microscopy, distinguishing it from axial resolution, which is measured along the optical axis. Due to diffraction the image of a point source of light is not a point, but a spot called Airy disk. Figure 2.7a displays the circularly symmetric profile of a single diffraction pattern for a point source (upper panel), and a plot of the intensity of light as a function of the radius (lower panel).

The Airy disk radius r_{Airy} is defined as the distance from its center to the first minimum, and can be calculated from:

$$r_{Airy} = 0.61 \cdot \frac{\lambda}{NA} \quad (2.6)$$

where λ represents the wavelength of light and NA the numerical aperture of the objective lens.

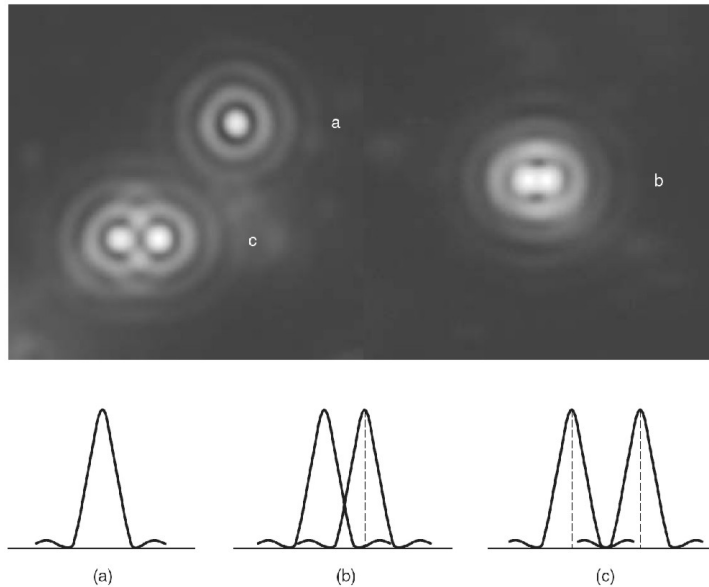


Figure 2.7: Rayleigh criterion for spatial resolution. (a) Profile of a single diffraction pattern (upper panel) and its intensity distributions as a function of separation distance (lower panel): the bright Airy disk and 1st- and 2nd-order diffraction rings are visible. (b) The same for two disks separated by a distance r_{Airy} such that the maximum of a disk overlaps the first minimum of the other disk: the points are just barely resolved. (c) The same for two disks at a separation distance of $2 \cdot r_{Airy}$: the points are clearly resolved. (Adapted from Murphy et al.⁵⁹)

According to Rayleigh's criterion, two point objects are just resolved when the center of one Airy disk falls on the first minimum of the other Airy disk. Hence, the lateral resolution of an objective lens is equal to r_{Airy} . Figures 2.7 (b) and (c) show two Airy disks and their intensity distributions in situations where the center-to-center distances between the zeroth order maxima are respectively $\sim r_{Airy}$, and $\sim 2 \cdot r_{Airy}$. Whereas in (b) two disks are just barely resolved, they can clearly be distinguished in (c).

We can also define the axial resolution by applying Rayleigh's criterion along the optic axis (this direction is generally referred to as the z-direction, while the plane perpendicular to the optical axis is the x-y plane).

Depth of field The axial range, through which an objective can be focused without any appreciable change in image sharpness, is referred to as the objective depth of field.

$$Z = n \times \frac{\lambda}{NA^2} \quad (2.7)$$

This value varies a lot from low to high numerical aperture objectives, usually decreasing with increasing numerical aperture. The unwanted light that expands the apparent depth of field is exactly what confocal imaging eliminates, as will be seen below.

2.1.3.2 Wide-field imaging microscopy and single particle tracking

2.1.3.2.1 Wide-field microscopy With this method, as the name implies, a laser is used to illuminate a large sample area of several micrometers in diameter (see Figure 2.8). The beam is expanded and focused onto the back-focal plane of the objective. Hence, the sample is illuminated uniformly by a parallel beam. Fluorescence light is collected by the same objective, and passes a dichroic mirror. The latter reflects light of wavelength smaller than a given value, and transmits long wavelengths emitted from the fluorescent dye. A set of fluorescence filters are used to eliminate the remaining excitation light and fluorescence light is then focused on a two-dimensional CCD detector.

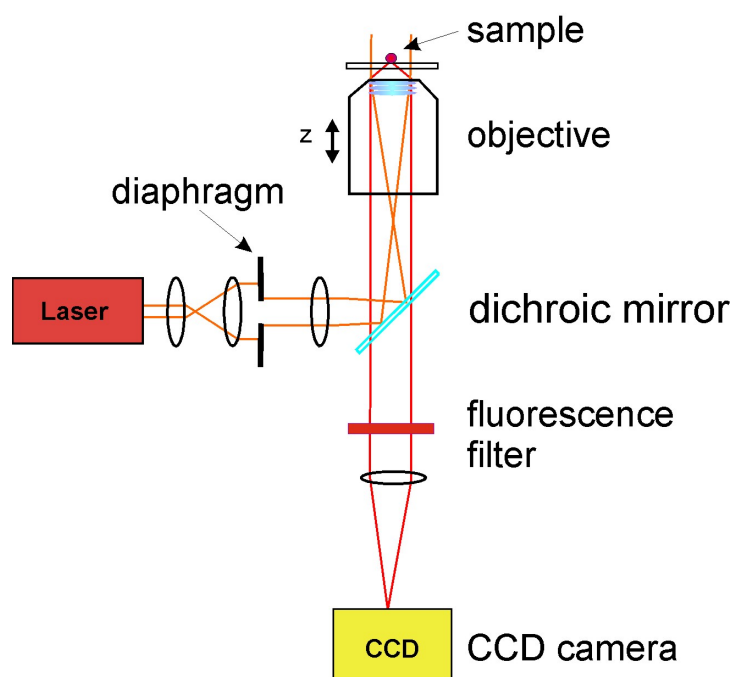


Figure 2.8: Optical system of a wide-field imaging setup.

The main advantage of this method is to acquire rapidly (usually in the range of 10 - 1000 ms) series of fluorescence images of hundreds of particles simultaneously. For example, the diffusion of single molecules in the channels of a mesoporous material can be observed in real time. The lateral and axial resolutions of a wide-field microscope are about 300 nm and 3 μm , respectively.

Laser sources All laser sources can be used in wide-field microscopy. These range from the UV wavelengths to the infrared. Frequent excitation sources are the helium-neon laser that emits at 633 nm or the argon-krypton mixed gas laser that gives useful spectral lines for excitation at 488 nm, 530 nm, 568 nm and 647 nm. These wavelengths cover many of the commonly used fluorophores.

Objective lens Two important parameters of an objective are the numerical aperture of the lens and the magnification. The axial resolution increases as the light gathered by the microscope objective given by its numerical aperture, increases. Therefore immersion objectives which have relatively high numerical aperture (1.0 - 1.2 for water-immersion, and 1.3 - 1.5 for oil-immersion objectives) are generally used.

Filters Several types of filters are used in wide-field microscopy. Optical density (OD) filters to attenuate the laser power, long pass filters to limit the wavelengths detected, band-pass and notch filters to select or reject a single line. Notch and long-pass filters are generally selected on the optimal compromise between blocking as much as possible the reflected laser light and permitting detection of fluorophores close to their emission maximum.

Specifications of the experimental setup It is based on a Eclipse TE200 (Nikon) epifluorescence microscope with a high numerical aperture oil immersion objective (Nikon Plan Apo 100 \times / 1.40 N.A. Oil). The molecules are excited at 633 nm with a He-Ne gas laser (Coherent, 75mW max. at 633 nm), and their fluorescence is detected with a back-illuminated EM-CCD camera in frame transfer mode (Andor iXon DV897, 512 px \times 512 px). Incident laser light is blocked by a dichroic mirror (640 nm cut-off, AHF) and a bandpass filter (730/140, AHF). Additional lenses ($f = 150$ nm, $f = 200$ nm, Achromat, Thorlabs) in the detection pathway give an overall magnification such that one pixel on the camera chip corresponds to 122 nm on the sample.

2.1.3.2.2 Single particle tracking (SPT) The wide-field microscope described above is used in this work to produce sequence of images showing the diffusion of individual particles. The tracking of these particles, i.e. following their position as a function of time, is a first important step for the evaluation of their diffusional behavior.

The resolution of a visible light microscope is commonly taken to be about $\lambda/2 \approx 300$ nm, with any object smaller than this dimension appearing as a diffraction-limited spot. Even though the details within a spot are not solvable, the center of the spot can nevertheless be determined to a precision in the order of a few nanometers by fitting the single particle fluorescence patterns obtained with a two-dimensional Gaussian function:

$$I_0 = A_0 \cdot \exp -\frac{(x - x_0)^2}{2\sigma^2} \cdot \exp -\frac{(y - y_0)^2}{2\sigma^2} \quad (2.8)$$

where A_0 is the amplitude and σ the width at half-maximum of the Gaussian curve, and x_0 and y_0 the coordinates of the position of the individual molecule.

The precision is only limited by the signal-to-noise ratio given a sufficient number of photons in the spot.^{60,61} The two important categories of noise are the shot noise of the photons in the spot and the background noise created by out-of-focus fluorescence. The typical positioning accuracy obtained with the setup described above is in the order of ± 10 nm. However, in some cases as achieved in this thesis, it could be improved to ± 2 nm.

A special case arises when transition dipole moments of single molecules are chiefly or fully oriented in the z direction of the optical axis of the setup. As the μ_z component of the transition dipole moment $\vec{\mu}$ is less accessible, these molecules will absorb less. While an ideal imaging system collects light from extremely high angles with respect to the optical axis and minimizes spherical aberration, any deviation from the idealized design condition aberrates the collected image, creating angle-dependent fluorescence images. Under such non-ideal conditions, light collected from high angle is out of focus relative to light emitted directly into the objective, thereby yielding an image containing angle-dependent information about the molecule orientation. Such non-idealities have been incorporated in fluorescence imaging techniques to directly visualize the true 3-D orientations of individual molecules.^{5,62,63}

When the transition dipole moment of the molecule remains fully z oriented during its motion, the single molecule appear in the wide-field fluorescence images with a "doughnut" pattern which can be well approximated and fitted with the product of a Gaussian function with a sine squared (Equation 2.9)

$$I_1 = I_0 \cdot \sin^2 \left(\frac{\pi \sqrt{(x - x_1)^2 + (y - y_1)^2}}{2r} \right) \quad (2.9)$$

where I_0 is defined in Equation 2.8, x_1 and y_1 the coordinates of the position of the individual molecule, and r the radius of the doughnut.

2.1.3.3 Laser scanning confocal microscopy (LSCM)

In the middle of the eighties two biologists at Cambridge University, Brad Amos and John White, built the first prototype of a confocal microscope. The aim was to develop a new technique, which permits to minimize the influence of the out of focus light in fluorescence microscopy. They looked at the technique called confocal imaging that was first proposed by Nipkow (1884) and pioneered by a post-doctorant at Harvard named Minsky who made the first stage scanning confocal microscope in 1957. This microscope could not be used commercially, because the technology needed to produce useful images was not available at the time. In 1986-87, a confocal microscope with the capabilities of producing very useful images was built by combining the technologies of the laser, the computer, and microelectronics. Confocal microscopes are particularly attractive because of their enhanced lateral and axial resolution, their three-dimensional imaging possibility, and the capability to address and observe the behavior of single molecules.

The scheme of a confocal microscope is shown in Figure 2.9. It is relatively similar to the scheme of the wide-field microscope i.e. excitation and fluorescence light passes through the same objective and the central part of the microscope is the dichroic mirror. "Confocal" is defined as "having the same focus", which means that the image has the same focus than the illumination in the sample. The focus is a diffraction limited volume. This so-called confocal volume has roughly the shape of an ellipsoid whose dimensions depend on the wavelength, the numerical aperture of the objective, and on the refractive index of the medium between the objective and the object. For example a typical size for the confocal volume is of roughly 300 nm in the focal plane and 900 nm along the optical axis for a 633 nm laser-line. This is the first difference compared to the wide-field microscope where a large area of the sample is illuminated. The second important difference is the presence of a confocal aperture (pinhole) placed in front of the photo-detector. Fluorescent light emitted from points on the sample that are outside the focal plane where the laser beam was focused will mainly be obstructed by the pinhole. In this way, out-of-focus light (both above and below the focal plane) is greatly reduced. Thus, a confocal microscope has a about three fold better axial resolution than a wide-field microscope ($\sim 1 \mu\text{m}$ for a confocal microscope).

Nevertheless, an important limitation in confocal microscopy compared to wide-field microscopy is that there is never a complete image of the sample. Only one point of the sample is observed. Therefore, a 2-D image is generated by scanning the sample at the focal plane. As two mirrors process the laser scan across the sample, the fluorescence signal is converted into a pixel-based image. In practice, the observation of one 512×512 pixel image requires a time from 1 to 64 seconds, depending on the integration time required. However, a 3-D reconstruction of a sample can be generated by stacking

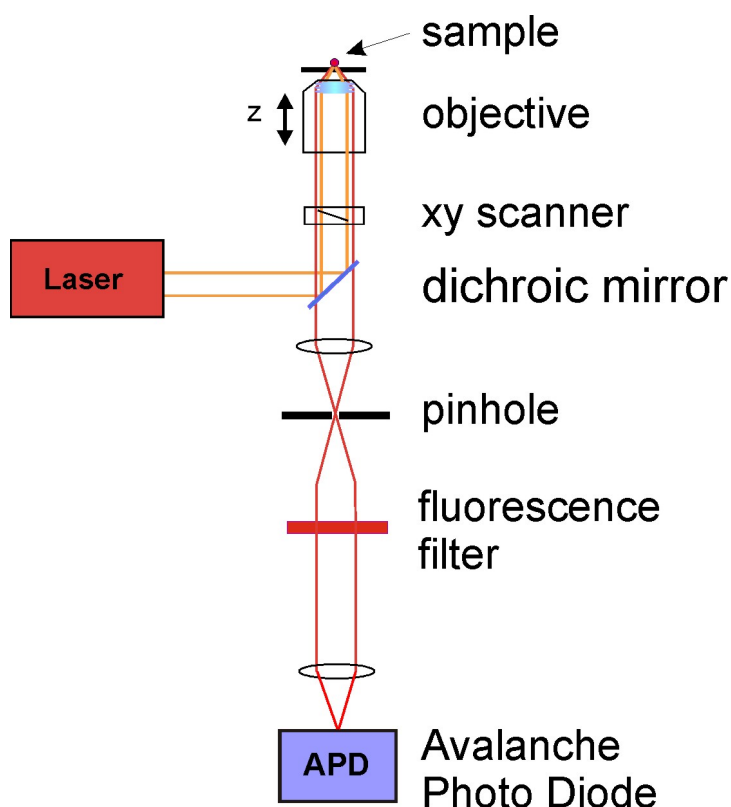


Figure 2.9: Optical system of a confocal microscope. A microscope objective is used to focus a laser beam onto the sample. The fluorescent light is collected by the same objective and focused onto the detector, an avalanche photodiode, via a dichroic mirror. The fluorescence emission is selected by a filter, which also blocks the excitation laser line. The pinhole is arranged in a plane conjugate to the focal plane of the objective. Light coming from planes above or below the focal plane is out of focus when it hits the pinhole. Most of it cannot pass the pinhole and therefore doesn't contribute to the formation of the image.

2-D optical Sections collected in series, which constitutes another important advantage of confocal microscopy in comparison to wide-field microscopy.

Two kind of detectors are generally used in confocal microscopy: a photomultiplier for classical bulk experiments, or an avalanche photodiode (APD) which is much more sensitive and can be used for single molecule detection.

Specifications of the experimental setup The experimental setup is based on a commercial ZEISS LSM 410 confocal laser scanning microscope. The fluorophores are excited with a HeNe (NEC) laser with $\lambda = 633$ nm. An oil immersion microscope objective (1.4 NA Zeiss 63x, oil immersion objectives) used for illumination and collection of fluorescence light. The red-shifted fluorescence light is separated from the excitation light with a combination of a dichroic (Q640LP, AHF Analysentechnik), notch (633 nm

notch, Kaiser) and longpass (HQ720/150, AHF Analysentechnik) filters. The fluorescence signal is then focused onto the detector, an avalanche photodiode, APD (EG&G SPCM-AQ 141).

2.1.3.4 Orientational imaging of single molecules

The orientation of the transition dipole moment can be utilized on a single molecule scale to probe spatial and mechanistic heterogeneities in both materials and biological systems. Orientational changes allow probing directly molecular motions within the system under study. Moreover, they are more readily interpretable than changes in photo-physical behavior such as fluorescence intensity or photobleaching rate. Hence, in addition to being able to pinpoint the location of a single emitter, knowing the orientation of a single molecule's transition dipole moment is desirable.

The projection of the transition dipole moment onto the focal plane can be determined by polarization-modulated excitation, as was demonstrated first at low temperature⁶⁴ and then by near-⁶⁵ and far-field^{66,67} microscopy at room temperature. All the polarization-modulated excitation methods for the determination of the transition dipole moment are based on the same principle: most molecules feature a linear transition dipole moment $\vec{\mu}$ in which case the transition rate is proportional to $|\vec{\mu} \cdot \vec{E}|^2$, whereby \vec{E} defines the electric field of the exciting light in the focus. The detection signal is plotted as a function of the angle between $\vec{\mu}$ and \vec{E} in Figure 2.10. The fluorescence signal obeys a cosine-squared function: it is maximal when the two vectors are parallel, and minimal when they are perpendicular. The idea behind polarization-modulated excitation measurements is that since the detected fluorescence intensity depends on the mutual orientation of the two vectors, controlling the orientation of the field \vec{E} can give access to the orientation of the molecule's transition dipole moment.

The in-plan orientation of the transition dipole moment of the single molecules are measured by implementing polarization optics in the confocal setup described above (see Figure 2.11). The polarization plane of the excitation light is modulated by rotating continuously (at ~ 3 Hz) with a servo-motor a $\lambda/2$ retardation plate, which is placed in the excitation beam directly at the entrance of the objective barrel. The polarization plane of the excitation light is monitored by a detector in transmission placed behind a polarizing filter. The setting of the polarization filter defines the frame of reference for the orientation. The modulation of the fluorescence signal in dependence of the polarization of the excitation light is recorded by an APD. These polarization dependent data can subsequently be analyzed by home-built Labview programs, as will be explained in details bellow.

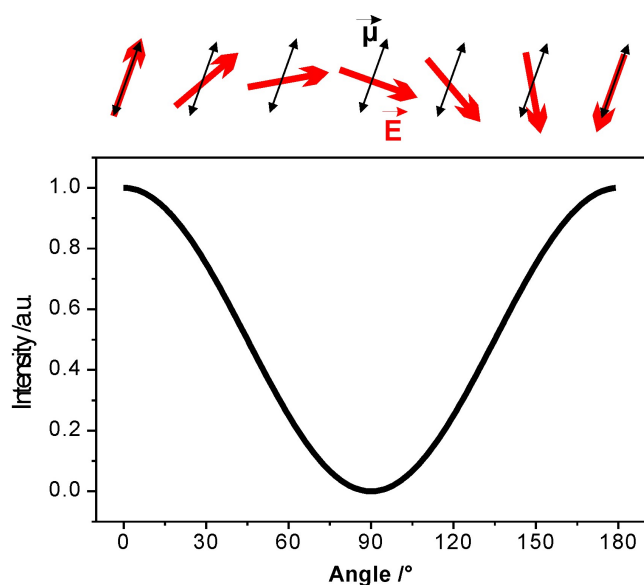


Figure 2.10: Simulated cosine-squared dependency of the detected fluorescence signal with the angle between the transition dipole moment of the molecule μ and the excitation electric field E .

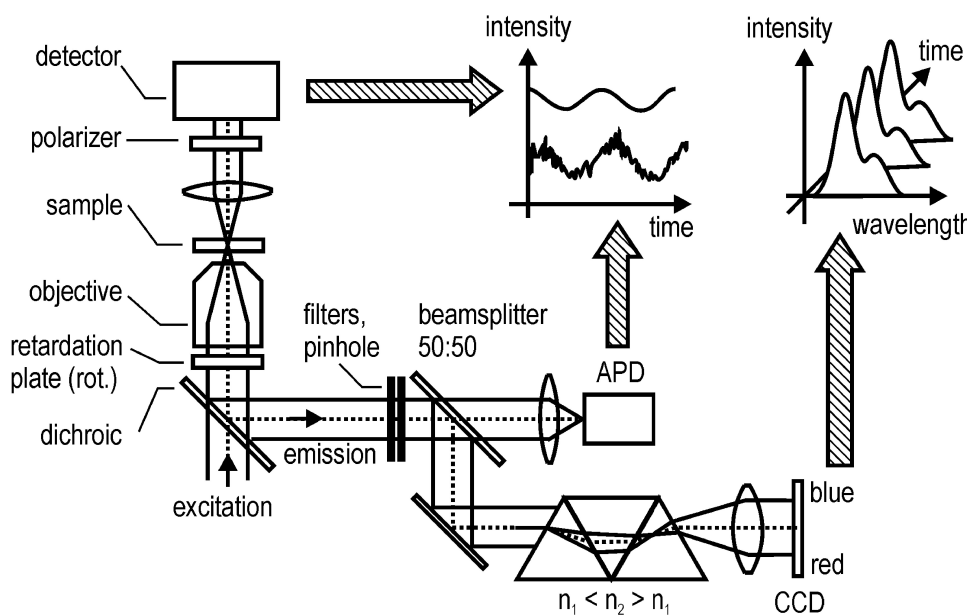


Figure 2.11: Experimental setup for the simultaneous measurement of the orientation and series of spectra of single molecules based on a confocal microscope.

Confocal images are acquired by scanning the excitation laser across the sample and simultaneously rotating the excitation polarization in the line-scan direction. Such a confocal image is shown in Figure 2.12a (left panel) for single TDI molecules diffusing in a mesoporous thin film. The molecules appear with a characteristic fluorescence-intensity striped profile. The orientations of their transition dipole moment is indicated

by yellow stripes. The polarization modulation is monitored by recording simultaneously the transmitted excitation light intensity behind the sample and after a polarization filter (right panel in Figure 2.12a).

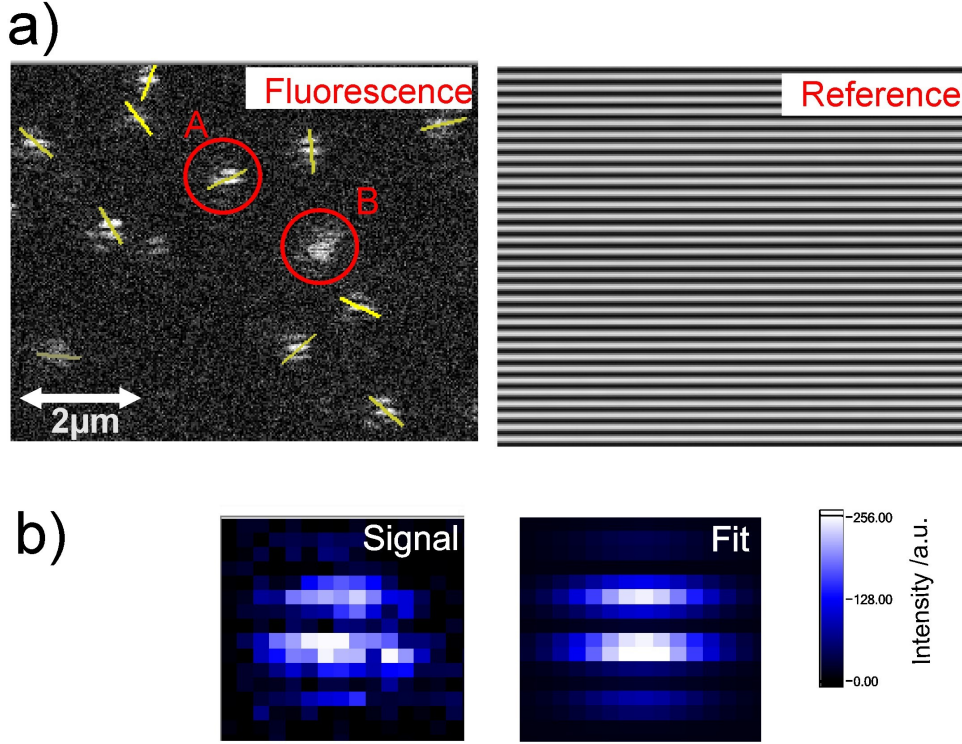


Figure 2.12: Methods for determination of the orientation of the molecules transition dipole moment. (a) Polarization dependent fluorescence image (left) and the corresponding transmitted excitation light (right) of individual TDI molecules diffusing in a CTAB-templated mesoporous film. The orientations of the transition dipole moments of molecules is overlaid as yellow bars. Many molecules appear with a characteristic stripped pattern, like molecule A marked with a red circle. Other molecules, like molecule B, reorient during the scanning time (typically 0.8 s). For these molecules it is not possible to determine an orientation. (b) Typical polarization dependent fluorescence pattern of a single molecule (left), with its fit (right) according to equation 2.10.

The molecule's position and two dimensional orientation in the focal plane are determined by fitting a cosine-squared modulated two-dimensional Gaussian function to the data according to Equation 2.10.

$$I = A_0 \exp -\frac{(x - x_0)^2}{2\sigma^2} \cdot \exp -\frac{(y - y_0)^2}{2\sigma^2} \cos^2(\omega t - \Phi_0) \quad (2.10)$$

where A_0 and σ are the amplitude and the width at half-maximum of the cosine-squared modulated Gaussian curve, x_0 and y_0 the coordinates of the position of the individual molecule, ω the angular speed of the $\lambda/2$ plate, and Φ_0 the phase of the signal.

Figure 2.12b shows images of the experimental fluorescence-intensity profile of a single molecule (left panel), and its fit according to Equation 2.10 (right panel).

The transmission signal is used as reference to obtain the absolute angle of the transition dipole moment. It passes through a polarizer and is recorded simultaneously to the fluorescence signal. The sum of the pixels values of the horizontal lines from a region of interest centered on x_0 and y_0 are plotted *versus* time, and was fitted with Equation 2.11.

$$I = A_1 \cos^2(\omega t - \Phi_1) \quad (2.11)$$

where A_1 is the amplitude of cosine-squared function, ω the angular speed of the $\lambda/2$ plate, and Φ_1 the phase of the signal.

The absolute orientation of the transition dipole moment is:

$$\Phi = \Phi_1 - \Phi_0 \quad (2.12)$$

where the reference for the zero of the angle is given by the direction of the main axis of the polarizer.

The orientation of a single molecule and its position are determined with a precision of typically $\pm 5^\circ$ and ± 60 nm respectively (standard deviation).

2.1.3.5 Simultaneous measurement of spectra and orientation of single molecules

Another interesting aspect of the confocal setup described previously is the possibility to monitor simultaneously the full emission spectrum and the in-plane angle of individual molecules. This is achieved by implementing a prism-CCD spectrometer in the detection pathway which allows the acquisition of sequences of spectra with a temporal resolution down to 30 ms. Compared to grating spectrometers the prism used in this setup has a superior transmission efficiency ($\sim 80\%$) allowing the acquisition of well-resolved spectra in a comparatively short time interval. A 50:50 beamsplitter placed after the pinhole splits the fluorescence emission signal into two parts which allows the detection of the fluorescence intensity and the acquisition of spectra simultaneously. More details of this setup can be found in the doctoral thesis of C. Seebacher⁶⁸ and C. Hellriegel.⁶⁹

The procedure to acquire a set of data for an individual molecule i.e. the polarization dependent intensity traces and sequences of spectra is the following: In a first step an image of the sample containing a fluorophore at single molecule concentration is acquired corresponding to an area of approximately $25 \times 25 \mu\text{m}$. The confocal volume of the microscope can then be centered on a spot corresponding to the diffraction limited pattern of an individual emitter. One can then record the polarization dependent fluorescence intensity trace, as well as a sequence of fluorescence spectra of the single molecule.

The first detector, the APD, records the modulated fluorescence intensity as the polarization plane of the excitation light is constantly being rotated. These data are evaluated against the polarization of the incident light and yield the in-plane orientation angle of the fluorescence signal. The second detector, a prism-CCD spectrometer (Princeton Instruments, EEV 1300/100-EMB-chip), records the emission spectra. Data acquisition is synchronized with the rotation of the $\lambda/2$ plate so that one spectrum is acquired for each 180° revolution of the excitation polarization (yielding an integration time of ~ 300 ms).

Orientation determination: The polarization dependent data obtained consists of two modulated signals that follow a cosine-square law. An example is shown in Figure 2.13a for a TDI molecule immobilized in a polymer film. The first signal (red line), acquired from the transmitted laser light, defines the orientation of the excitation polarization and is used as a reference. The second signal (black line), the single molecule fluorescence intensity, is modulated depending on the alignment of the fluorophore's transition dipole moment with respect to the excitation polarization. For the analysis the data is divided into segments of approximately 300 ms (corresponding to one 180° revolution of the polarization plane). These segments are subsequently analyzed using the following equations:

$$I_T(t) = A_T \cdot \cos^2(\omega \cdot t + \varphi_T) + c_T \quad (2.13)$$

$$I_F(t) = A_F \cdot \cos^2(\omega \cdot t + \varphi_F) + c_F \quad (2.14)$$

Here I_T is the transmission intensity and I_F the fluorescence intensity, $A_{T,F}$ the amplitude of the modulations, ω the rotation frequency, $\varphi_{T,F}$ the phases and $c_{T,F}$ the offsets e.g. which are caused by unspecific background. Note that these two equations share the frequency ω as a common parameter. The in-plane orientation of the molecule with respect to the reference in this segment is then:

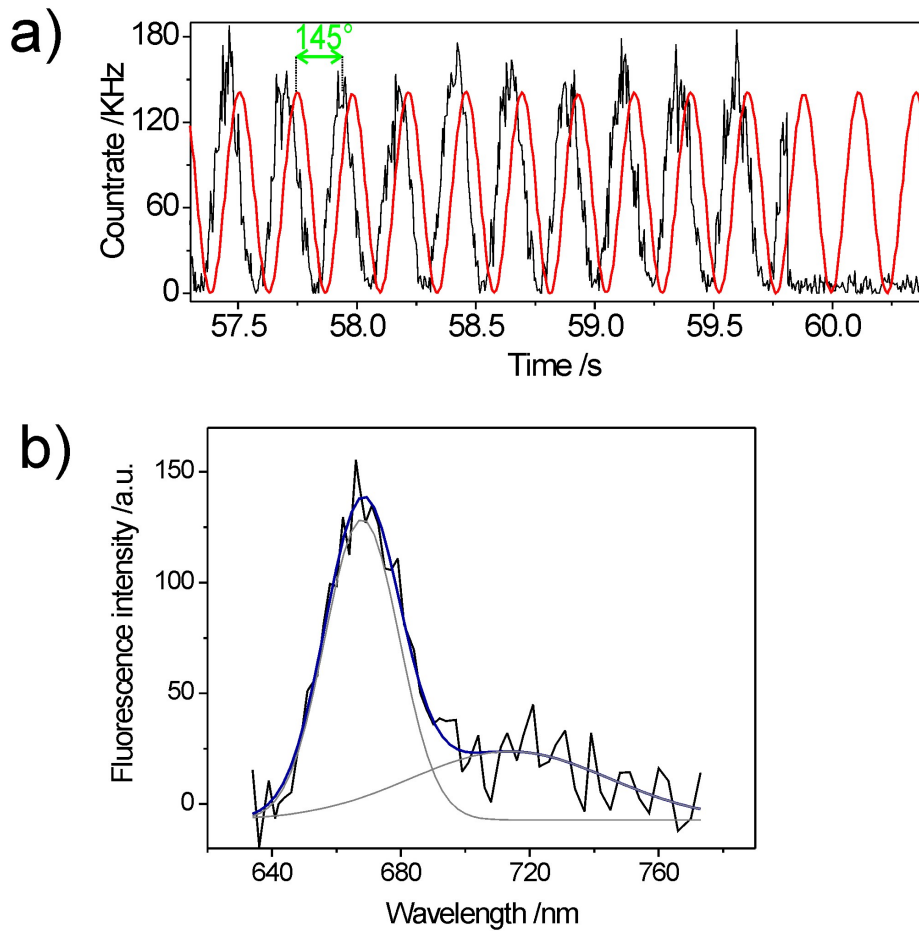


Figure 2.13: Simultaneous measurement of spectrum and orientation of single molecules. (a) Polarization-dependent fluorescence intensity trace (black) and transmitted excitation light (red) curves for an individual TDI molecule. These curves are described by cosine-squared function, and the difference of their respective phases gives the absolute angle of the dipole moment of the molecule, which is in this case 145° (green). (b) Emission spectrum (black) for the same molecule (integration time: ~ 300 ms). The blue curve is the fit of Equation 2.16 to the data.

$$\Phi = \varphi_T - \varphi_F \quad (2.15)$$

The operation is repeated by shifting the segment by one, two, three, etc. data-points. In this way it is possible to obtain the molecule's orientation Φ as a function of time. In the following it will be referred to $\Phi(t)$ as the angular trajectory. The error in Φ , given by the standard deviation from the fitting procedure, varies with the quality of the data e.g. signal-to-noise and is typically in the range between 2° and 5° . As an example, in the polarization-modulated trajectory shown in Figure 2.13a the orientation of the molecule's transition dipole moment is constant along the trajectory and has a value of $145^\circ \pm 3^\circ$.

Analysis of spectral dynamics: Sequences of single molecules spectra are acquired simultaneously with the modulated intensity traces. Figure 2.13b (black line) shows such a fluorescence spectrum extracted from the sequence of spectra corresponding to the intensity-time trajectory displayed Figure 2.13a. All spectra are calibrated in order to compensate for the non-linear dispersion curve of the prism and wavelength dependencies of the setup used. Additional unspecific fluorescence from the sample is recorded for every sequence of spectra after photobleaching of the observed molecule and subtracted from the data. The spectra of organic dye molecules show one pronounced main band followed by a broad vibronic shoulder, and can be fitted using a double Gaussian model:

$$I(\lambda) = A_m \cdot \exp - \frac{(\lambda - \lambda_m)^2}{2w_m^2} + A_s \cdot \exp - \frac{(\lambda - \lambda_s)^2}{2w_s^2} \quad (2.16)$$

In this equation $A_{m,s}$ are the amplitudes and $\lambda_{m,s}$ the central wavelengths of the main band and the side peak respectively. Parameters $w_{m,s}$ are the waist of the respective Gaussian. The fit with equation 2.16 of the fluorescence spectrum shown in Figure 2.13b is displayed in blue.

The result of the fitting procedure is a sequence of spectral fit-parameters, i.e. central wavelengths, amplitudes and widths, which describe the respective spectrum. The main parameter usually used is the central wavelength of the main band λ_m and its variations with time. The experimental error for the estimation of the central wavelength varies with the signal-to-noise ratio and lies typically between 0.5 and 2 nm (standard deviation of Gaussian fit).

2.1.3.6 Fluorescence correlation spectroscopy (FCS)

Fluorescence correlation spectroscopy (FCS) is a fluorescence technique which uses dye molecules, generally dissolved in a liquid, whose concentration is at the limit between ensemble and single molecule concentration. The method is based on observation of several molecules diffusing into and out the detection volume of a confocal microscope (see Figure 2.14a). As a dye molecule diffuses through the confocal volume, the detected fluorescence signal fluctuates. By autocorrelating this time-dependent fluorescence signal, for example, the average diffusion coefficient of the dye molecules and their concentration can be obtained.

The autocorrelation function, G_D , is calculated from the FCS measurements and fit with the three-dimensional Gaussian model for freely diffusing particles in solution.^{70,71}

$$G_D(\tau) = \frac{\gamma}{\langle N \rangle} \cdot \left(\frac{1}{1 + \tau/\tau_D} \right) \left(\frac{1}{1 + (\omega_r/\omega_z)^2 \tau/\tau_D} \right)^{\frac{1}{2}} \quad (2.17)$$

where γ is the geometrical correction factor (equal to $2^{-1.5}$), N is the average number of molecules in the detection volume, τ the correlation time, ω_i the radius of the laser focus in lateral (r) and axial (z) direction, respectively, to the distance where the intensity has decayed by a factor of $1/e^2$, and τ_D is the average diffusion time of a particle through the detection volume. $\tau_D = \frac{\omega_r^2}{4D}$, where D is the diffusion coefficient of the fluorescence particle.

Figure 2.14b shows a representative FCS autocorrelation curve of water-soluble perylindimide (WS-PDI) dye molecules diffusing freely in water. Its fit according to Equation 2.17 is displayed in red, and gives an average diffusion time through the detection volume of 0.85 s corresponding to a diffusion coefficient of $40 \mu\text{m}^2/\text{s}$.

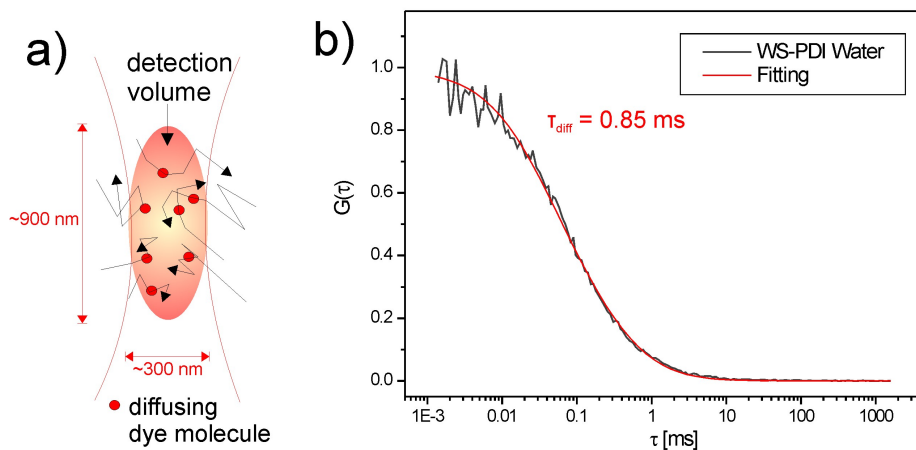


Figure 2.14: Autocorrelation curve of WS-PDI (Structure shown in Figure 4.1d) in water. The red curve is the fit of Equation 2.17 to the data, and gives an average diffusion time of $\tau = 0.85$ s. This leads to a diffusion coefficient of $40 \mu\text{m}^2/\text{s}$.

Experimental setup

FCS is performed using a homebuilt confocal setup. Details of the setup can be found in Müller et al.⁷² Briefly, the system is built around an inverted microscope (Axiovert200, Zeiss, Göttingen, Germany). The laser (LDH-P-C-635 and Sepia PDL808, PicoQuant, Berlin, Germany) is guided through a single-mode polarization-maintaining fiber (PMJ-3AF3AF-633-4/125-3-5-1, OZ Optics, Carp, Ontario, Canada) before entering the microscope and focused on the sample by a water immersion objective (C-Apochromat,

63x1.2, Zeiss, Göttingen, Germany). The fluorescence is collected by the same objective and separated by a dichroic mirror (DC532/633xr, AHF Analysentechnik, Tübingen, Germany). After passing an emission filter (HQ700/75, AHF Analysentechnik), the fluorescence is focused on a pinhole (50 μm , Owis, Staufen, Deutschland) and finally on an avalanche photodiode (SPCM-AQR-14, EG&G Optoelectronics, Vaudreuil, Quebec, Canada). The data are recorded by a digital real-time correlator (ALV GmbH, Langen, Germany) or time-correlated single-photon counting card (TimeHarp 200, PicoQuant, Berlin, Germany). The volume of the setup was calibrated using freely-diffusing Cy5 as a reference sample and assuming a diffusion coefficient of 250 $\mu\text{m}^2/\text{s}$.⁷³ The correlation functions were fit using Origin 6.0 (OriginLab Corporation, Northampton, MA, USA).

2.2 Diffusion theory and trajectory analysis

Classically, diffusion is the movement of particles from an area with high concentration to an area with low concentration, following Fick's law of macroscopic diffusion theory. In the following, the treatment of the diffusion theory will be restricted to a microscopic description since SMS allows the resolution of the diffusion of individual particles on a microscopic scale. In this work the diffusion of labelled biological particles like vesicles in living cell or of single dye molecules in mesoporous materials are studied in details. In the growing field of mesoporous materials, for example, the understanding of the transport mechanism in these systems can help the design and improvement of new applications.

2.2.1 Diffusion theory: microscopic approach

Diffusion of a moving particle can be described by the temporal behavior of the mean square displacement (MSD) $\langle r^2(\Delta t) \rangle$ in dependence of the time Δt . For normal Brownian diffusion the motion is a random walk and the MSD is directly proportional to time:⁷⁴

$$\langle r^2(\Delta t) \rangle = MSD(\Delta t) = 2kD\Delta t \quad (2.18)$$

where $r(\Delta t)$ is the displacement of the particle position within a time interval Δt of length δt , D the diffusion coefficient, and k the number of dimensions of the walk of the particle ($k=1, 2$ or 3). In two dimensions, for example, an interpretation for the diffusion coefficient is that D is a measure for the mean area that the particle explores per unit of time Δt during its walk.

The presence of noise in the position measurements of a particle is inherent to all SPT measurements. The position of the particle can be determined with a precision of typically ± 10 nm as seen before, which can usually not be neglected compared to step sizes of the walk. This noise leading to an error in the particle position can be taken into account in the analytical formula of the MSD. Assuming a mean error of the particle position σ , the MSD yields:

$$\langle r^2 \rangle = MSD(\Delta t) = 2kD\Delta t + k\sigma^2 \quad (2.19)$$

The linear plot of MSD vs time interval δt gives D as the slope and $k\sigma^2$ as the intercept.

A major advantage of SPT is the ability to resolve modes of motion of individual molecules, and a major result obtained by this technique is that motion is often not limited to pure Brownian diffusion. Several other modes of motion can be observed: anomalous diffusion, diffusion with flow, and corralled motion.

Assuming that the noise in the position measurements can be neglected, the analytical forms of the curves of MSD *versus* time for these different modes of motion are:⁴³

Anomalous diffusion

$$\langle r^2(\Delta t) \rangle = 2kD\Delta t^\alpha \quad (2.20)$$

Diffusion with flow

$$\langle r^2(\Delta t) \rangle = 2kD\Delta t + (Vt)^2 \quad (2.21)$$

Corralled motion

$$\langle r^2(\Delta t) \rangle = \langle r_c^2 \rangle [1 - A_1 \exp(\frac{-4A_2}{\langle r_c^2 \rangle} D\Delta t)] \quad (2.22)$$

where $\alpha < 1$ in Equation 2.20. In Equation 2.21 V is velocity and in 2.22 $\langle r_c^2 \rangle$ is the corral size, and A_1 and A_2 are constants determined by the corral geometry. The MSDs vs Δt plots of these different modes of motion are depicted in Figure 2.15.

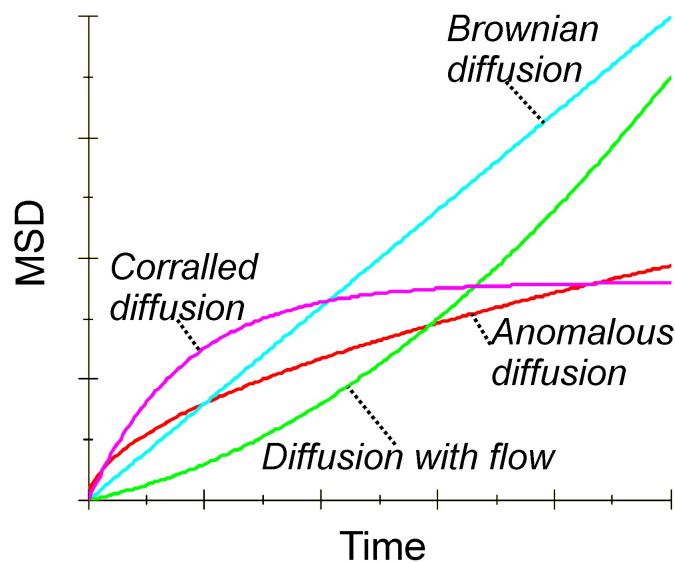


Figure 2.15: The mean square displacement $\langle r^2 \rangle$ as a function of time t for pure diffusion (blue line), anomalous diffusion (red line), diffusion with flow (green line), and corralled motion (violet line).

Anomalous diffusion, for example, has been observed in cell membranes.^{75,76} The investigation of this diffusion can be of paramount importance in membrane dynamics, both because anomalous diffusion is a probe of membrane microstructure and because it has a major influence on reaction kinetics within the membrane. Diffusion with flow was also observed in living cells. As an example a recent study report on the active transport by microtubules of nanosized gene carriers to the perinuclear region.⁷⁷

Such deviations from Brownian motion result usually from the presence of heterogeneities within the medium in which the particles of interest diffuse. In practice, the distribution of the step length is relatively broad, covering a large range of length- and time-scales. An example is the presence of trapping sites in the matrix where the particle remains immobile for a certain duration, and then starts diffusing in a random walk. Beside this extreme case of two well separated diffusion modes, other systems contain a distribution of heterogeneities which result in a very complicated mixture of different modes of diffusion. In these systems, a classical analysis based on the average MSD according to Equation 2.18 is not sufficient because the local heterogeneities are averaged out over the whole trajectories. It will be demonstrated in the following that the channel system of a mesoporous material, for instance, constitutes a complex system for the diffusion of dye molecules due to the presence of heterogeneities within the silica matrix.

2.2.2 Analysis of trajectories

The analysis of the trajectories obtained by the tracking procedure are a crucial step in the investigation of molecular diffusion because they can provide information about the presence of heterogeneities for example, influencing the single molecules' motion. A first method is based on the analysis of the MSD vs time. The latter can be determined directly by calculating the mean of the square displacements $r^2(\Delta t)$ for a certain time interval Δt over the whole trajectory. Another method consists in analyzing probability distributions. It allows for a more precise analysis since one avoids loss of information due to averaging. Hence, sub-populations of diffusing particles can be distinguished.

For each trajectory, a set of values for the square displacement, $r^2(\Delta t)$ between two observations separated by the time lag Δt are computed using a home-built Lab-view program.

$$r(\Delta t) = (\vec{r}(t + \Delta t) - \vec{r}(t))^2 \quad (2.23)$$

where $\vec{r}(t)$ is the position of the particle at time t .

The MSD for every time lag can be obtained by analyzing the distribution of the squared displacements u (with $u = r^2$), which is given in 1D by^{78,79}

$$p(u, t) = \frac{1}{\sqrt{2\Pi(\langle r^2(\Delta t) \rangle + \sigma^2)}} \exp\left(\frac{-u}{2(\langle r^2(\Delta t) \rangle + \sigma^2)}\right) \quad (2.24)$$

where σ corresponds to the positioning accuracy (see Equation 2.19). In the data analysis σ is set as a fixed parameter in the fitting procedure with a value of e.g. $\sigma = 5$ nm corresponding to the typical positioning accuracy of the data.

The cumulative probability in 1D is

$$P(U, \Delta t) = \int_0^U p(u, \Delta t) du = \int_0^U \frac{1}{\sqrt{2\Pi(\langle r^2(\Delta t) \rangle + \sigma^2)}} \exp\left(\frac{-u}{2(\langle r^2(\Delta t) \rangle + \sigma^2)}\right) du \quad (2.25)$$

$$P(U, \Delta t) = erf\left(\sqrt{\frac{U}{2(\langle r^2(\Delta t) \rangle + \sigma^2)}}\right) \quad (2.26)$$

where erf is the error function, $P(U, t)$ gives the probability that u does not exceed a value U .

For each value of Δt , the cumulative probability distribution $P(U, \Delta t)$ is constructed from a trajectory by counting the number of squared displacements with values $\leq U$ normalized by the total number of data points. $P(U, t)$ is plotted in Figure 3.27a for an exemplary trajectory in a semi-log scale against the squared step length U for the time lag $\Delta t = 1$ s.

A second term can be added to this function if the system contains heterogeneities like adsorption sites where the single molecules remain immobile for a few frames

$$P(U, \Delta t) = (1 - \alpha) \cdot erf\left(\sqrt{\frac{U}{2(\langle r^2(\Delta t) \rangle + \sigma^2)}}\right) + \alpha \cdot erf\left[\sqrt{\frac{U}{2\sigma^2}}\right] \quad (2.27)$$

where α is the weight of the population of adsorbed states in a trajectory.

Chapter 3

Translational, orientational and spectral dynamics of single dye molecules in highly oriented mesoporous materials

3.1 Introduction to mesoporous materials

Micro- and mesoporous materials have attracted worldwide attention as one of the key materials in nano-technology because of the possibility to control their physical and chemical properties. According to the international union of pure and applied chemistry (IUPAC) classification, materials containing pores with diameters not exceeding 2 nm are named microporous materials, and materials containing pores with diameters between 2 nm and 50 nm are named mesoporous materials.⁸⁰ The parameters that can be controlled include pore diameter, pore interconnectivity, as well as the polarity or chemical affinity of the inner surface.^{29,30,81}

Furthermore, by incorporating guest molecules into porous solids, one can form so-called host-guest systems that provide an interesting platform for novel technological applications.^{30,82} Among the promising porous host materials are crystalline structures, like microporous AlPO₄-5 crystals from the family of zeolites,⁸³⁻⁸⁵ and mesoporous templated silica materials such as M41S.²⁹ AlPO₄-5 forms large crystals (μm -sized) containing homogeneous and one-dimensional pores with a diameter of 0.73 nm. AlPO₄-5 crystals allow one to accommodate guest species, for example Xe, and even tightly fitting small dye molecules. Hence, they have attracted much attention particularly in fields where

molecular recognition is needed, such as catalysis, separations and chemical sensing. The high regularity of such a structure makes it also interesting for applications in which the stability of the host-guest system is a desirable property. Examples are artificial antennas,⁸⁶ ordered materials,⁸⁷ non-linear optical materials, micrometer-sized dye lasers,^{88,89} waveguides,⁹⁰ and photochromic switches.⁹¹ Moreover, it is often desirable to accommodate larger species into an ordered porous host, such as biomolecules, large dye molecules or catalytically active complexes. Sol-gel glasses which may accommodate such species are limited by a high intrinsic disorder.^{92,93} In contrast, mesoporous materials prepared through cooperative assembly of surfactant and inorganic species provide pore diameters of sizes larger than approximately 2 nm up to 20 nm, while retaining an ordered channel system.⁹⁴ Their high specific surface area, their large specific pore volume, and narrow pore size distribution make mesoporous materials ideal hosts for the incorporation of molecular guests. The many different available host-guest systems are used in a wide scope of applications like heterogeneous catalysis,^{33,95} chromatography,³² dye-sensitized photovoltaic cells,³⁷ selective sequestration of contaminants,⁹⁶ and chemical sensing of molecules that are too large for fitting within crystalline zeolite molecular sieves, which have smaller (0.2 to 1.5 nm) micropores.³⁵

The starting point of intensive research in the area of mesoporous materials was the disclosure of the M41S family of silicate/aluminosilicate mesoporous molecular sieves by scientists from the Mobil company.^{92,97} Cationic surfactants possessing alkyl chains from 8 to 22 carbons were used as templates during the hydrothermal synthesis. Among different phases, a hexagonal phase was discovered and named MCM-41 (mobil catalytic materials N°41). This material possesses arrays of parallel channels with diameters ranging from 1.5 to 10 nm depending on the template used, the addition of auxiliary organic species, and the synthesis parameters, e.g. synthesis time, synthesis temperature, or postsynthetic treatments. The template can eventually be removed by calcination at about 450 °C, or milder solvent extraction. At present, periodic mesoporous materials can be readily synthesized in a wide range of pH, at temperatures ranging from ambient to approximately 150°C, and using a variety of surfactants and polymers as structure directing agents, thus leading to different mesophase structures and morphologies.^{29,30}

The ordered mesoporosity is given by the specific mechanism of formation that employs the interaction of liquid-crystal templating and the cooperative self-assembly of inorganic and organic (micellar) species. The model that is now accepted to describe the formation of these materials is the cooperative formation mechanism of inorganic-organic interfaces.^{94,98,99} In this mechanism the multidentate charge density matching between soluble inorganic species and surfactant molecules determines the initial interaction between them. Within this charge density matching constraint, hydrophobic parts of the surfactant molecules reorganize (form micelles) by minimizing the van der Waals in-

teraction and inorganic/organic charge energies to form final hybrid organic/inorganic mesophase structures

Many of the applications of mesoporous materials, however, are hindered by the fact that many mesoporous solids have been produced only as powder with small domain sizes ($< 1\mu\text{m}$) that have no orientational alignment of the pores over a macroscopic lengthscale. Progress in orienting these materials has been made by growing thin films of mesoporous silicates at surfaces via the evaporation-induced self-assembly (EISA) method.¹⁰⁰ Ordered mesoporous films are characterized by the same properties typical for the powdered mesoporous materials, such as mesophase structure, pore diameter, surface area and stability. The inspiration for creating such architectures comes from the fact that many of the envisioned industrial applications of the mesoporous materials, such as separation membranes, chemical sensors, surfaces for heterogeneous catalysis, optoelectronic devices, or low dielectric constant layers, could benefit from growing thin films of mesoporous silicates at surfaces or interfaces.

One important parameter that influences the structure and order of the mesoporous films prepared by EISA is the relative humidity (RH) of the surrounding atmosphere during the deposition process.^{101–105} Humidity-controlled meso-structuration in the cetylhexyltrimethylammoniumbromide (CTAB) templated mesoporous silica films showed that the water content is a critical parameter, as poorly ordered, two-dimensional hexagonal, or three-dimensional cubic structures can be obtained, depending on the relative humidity.¹⁰¹ Another critical factor that can change the final mesophase structure of the mesoporous films is the post-synthetic treatment. As-deposited films show not complete condensation of the silica framework, therefore processes that increase cross-linking of the silica, such as basic- or acid-catalyzed silica condensation or thermal treatment, can stabilize the final mesophase structure.^{100,106}

Crucial for the improvement in the design and the possibility to control the so-called smart-materials based on porous materials is a thorough understanding of the dynamics of the guest molecules within the host matrix, as well as the host-guest interactions. Standard characterization methods, such as NMR, IR, UV/Vis spectroscopy, electron microscopy and X-ray diffraction have been employed successfully to characterize host-guest materials.^{40,41,107} However, the behavior of the molecules on the nanometer-scale is both spatially and temporally heterogeneous. A complete characterization of the host-guest material is not possible with these ensemble methods because information about such heterogeneities is lost in the inherent averaging process.

SMS techniques are the methods of choice to directly observe details of the molecular behavior because they work on a molecule-by-molecule basis.^{67,108} The translational motion of individual fluorophores can be detected and characterized either via fluo-

rescence correlation spectroscopy (FCS),^{109,110} or directly by following the molecule's trajectory.^{21,111–113} Orientational dynamics, on the other hand, can be studied by modulating the excitation polarization^{6,8,114} or by analyzing the emission polarization.^{8,9} Furthermore, spectral dynamics of single molecules reflect the energetic interactions of the fluorophore with its direct environment and can be detected at cryogenic temperatures^{115–117} as well as at room temperature.^{55,118}

Single molecule spectroscopy (SMS) is a modern and powerful tool that can elucidate the interactions between an individual molecule and its immediate environment. The experimental data reveal the behavior of each molecule directly, and thus, ensemble averaging is suppressed in SMS measurements.^{67,108,119,120} The observed spatial and temporal heterogeneities yield a thorough description of the molecule's dynamical behavior as well as of the environmental influence. SMS methods have been successfully used to characterize the dynamics of individual fluorophores, such as spectral dynamics,^{25,118,121} translational motion,¹²² and orientational dynamics.^{8,62,123–126} In the case of molecules incorporated into porous solids, the molecules act as reporters and convey information from the material's inner structure via their interactions. Host-guest materials based on porous solids have been investigated using SMS, revealing for example the influence of the pore structure upon the orientation,^{62,114} fluorescence intensity, energy transfer behavior¹²⁷ and diffusion^{16,128} of the molecules situated therein.

Moreover, by simultaneously applying different SMS techniques one can investigate different properties, like the position, orientation and emission spectrum of an individual molecule in the host matrix. While the measurement of an individual property (e.g. spectrum, orientation, position, etc.) already provides valuable details about the host-guest material, a deeper understanding for the underlying molecular mechanism can be gathered by correlating different properties. For example a long standing question in SMS studies regards the mechanisms behind the commonly observed fluctuations of emission spectra.⁵⁵ This problem can be addressed by inferring if and how a molecule's spectrum is affected by its orientation in the material. To date, there have been efforts to correlate the molecule's orientation with its emission spectrum¹²⁹ as well as its orientation with its position.^{4,7,62,130}

This chapter focuses on the investigation of the dynamics of single TDI dye molecules in various silica templated mesoporous silica materials. The first section (3.2) presents the investigation of diffusion and orientation of single TDI molecules in different mesophases of Brij-56-templated mesoporous films. The dye molecules act as beacons while they diffuse through the different structural phases of the host: the structure of the trajectories, the diffusivities and the orientation of single molecules are distinctive for molecules travelling in the lamellar and the hexagonal mesophase. This is followed by the investigation

of the dynamics of TDI molecules in the unidimensional pores of a hexagonal CTAB-templated mesoporous film (section 3.3). By measuring and correlating the molecules position, orientation and emission spectrum it will be demonstrated that SMS allows valuable molecular insight into host-guest dynamics within mesoporous systems, thus helping to understand host-guest properties. The last section of this chapter (section 3.4) presents experimental data that show that CTAB-templated mesoporous films can undergo rearrangement of its structure on timescale of days after synthesis. For the first time, large and highly structured domains (up to 100 μm in size) were obtained where the parallel pores are extremely linear. An investigation of the growth of these domains is presented, followed by their characterization via SMS.

3.2 Diffusion and orientation of single TDI molecules in different mesophases of Brij-56-templated mesoporous films

In this section, it will be shown how single TDI dye molecules can be used as nanoscale probes to map out the structure of Brij-56-templated mesoporous thin films. The diffusion and orientation of the single TDI molecules are investigated in three different topologies: an hexagonal mesophase, a lamellar mesophase, and a mixture of these two phases.

3.2.1 Sample systems

Mesostructured silicas were prepared in the form of thin films *via* cooperative self-assembly of surfactant molecules Brij-56, (Figure 3.1a) with polymerizable silicate species (see experimental section 3.5). Strongly fluorescent terrylenediimide molecules¹³¹ (TDI, Figure 3.1a), acting as molecular beacons, were added at very low concentrations to the synthesis solutions of the mesoporous films. They were thus incorporated into the pores during the evaporation-induced self-assembly of the material in the spin-coating process. This process results in thin silica films with a thickness of about 200 nm. An interesting aspect of these materials is that by varying the molar ratio between the surfactant and the silica oligomers of the precursor solution, materials with different mesoporous topologies can be prepared. In order to obtain data with statistical significance, some 35 film samples were prepared and over 50 single molecule tracking movies were analyzed. Here data are presented from three samples. Two of these consist of a single, pure mesophase (hexagonal and lamellar, see below), synthesized with either a low or a high surfactant/silica molar ratio, respectively. A third one was synthesized with an intermediate mixture, such that the two mesophases coexist in the sample. The X-ray diffraction (XRD) patterns of the samples with the pure phases (blue and green in Figure 3.1c) show one peak at a different position for the two different structures. In combination with transmission electron microscopy (TEM) cross-section images of these pure phases (Figure 3.1d), the green XRD pattern (right peak) can be assigned to a hexagonal phase and the blue XRD (left peak) to a lamellar phase. The diffraction pattern of the third sample (black) with two coexisting topologies shows two peaks located at the same positions as the individual peaks in the pure phases. The right panel in Figure 3.1d shows a cross-section TEM of this sample, where the lamellar phase is visible on top of the hexagonal channel system. Note that it is difficult to judge the true size of the crystalline phases and domains of homogeneous ordering of the pores, because they are larger

than the TEM cross-sections. Furthermore, the TEM images give no information about the real connectivity of the pores for molecules diffusing in them. The peak positions in the XRD permit the calculation of the mean pore-to-pore distance in the two phases. For the lamellar phase this distance is 6.1 (± 0.1) nm and for the hexagonal phase 6.3 (± 0.1) nm. Based on the broadness of the peaks it is clear that only average values can be calculated and that a distribution of pore-to-pore distances and pore sizes can be present in the samples. Typical wall thicknesses in these systems amount to about 1 - 2 nm, thus a pore diameter of 4 - 5 nm is filled with template and provides the space for molecular movement.

In the following it is demonstrated that these topologies in fact strongly influence the diffusion of the molecules inside the pores. The fluorescence of the single molecules in as-synthesized films was collected in an epifluorescence microscope and detected with a highly sensitive CCD camera in a widefield imaging setup. No further sample preparation was needed. Since the films were much thinner than the focal depth of the microscope objective used ($> 1 \mu\text{m}$), images contain data from molecules at all heights inside and on the surface of the sample. Series of 1000 images were acquired with a temporal resolution of down to 100 ms per frame. In each movie frame single molecules show up as bright spots on a dark background. Their positions were obtained by fitting theoretical diffraction patterns to the spots with a positioning accuracy of down to 10 nm. Single molecule trajectories were then built up by tracking spots from frame to frame. Here measurements in the pure phases are first presented, which is followed by a detailed discussion of the observations in the third sample that consists of a mixture of these two phases.

3.2.2 Diffusionnal behavior of single TDI molecules in pure hexagonal and lamellar phases

In Figure 3.2 the measurements in the pure hexagonal phase on the left are set in contrast to those in the lamellar phase on the right. In the widefield images of the hexagonal phase only Gaussian-shaped diffraction patterns are observed (Figure 3.2a), whereas the single molecules in the lamellar phase appear as doughnuts (Figure 3.2b). Such doughnut diffraction patterns have previously been assigned to single molecules with their transition dipoles (here the long molecular axis of TDI) aligned along the optical axis of the microscope. In the present case this means that molecules in the lamellar phase are oriented perpendicular to the glass substrate and thus normal to the silica planes of the lamellar phase. The exposure times for the movies in the two different phases differ by a factor 16, as the molecules in the hexagonal phase diffuse much faster

3.2. DIFFUSION AND ORIENTATION OF SINGLE TDI MOLECULES IN
44 DIFFERENT MESOPHASES OF BRIJ-56-TEMPLATED MESOPOROUS FILMS

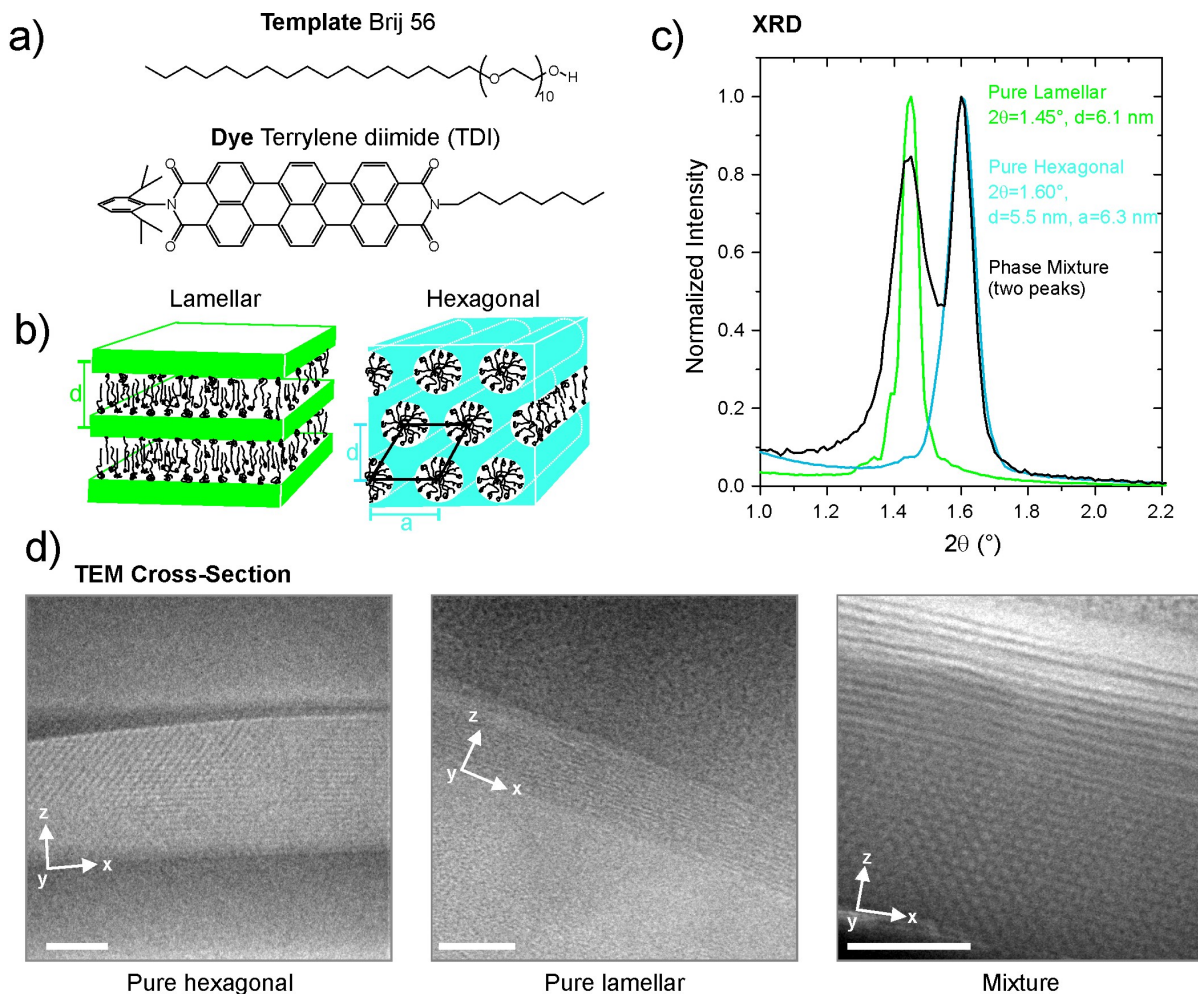


Figure 3.1: Sample systems. (a) Structure-directing agent poly(oxyethylene)cetyler-copolymer (Brij-56) and fluorescent terrylenediimide derivative (TDI), which are incorporated into the mesopores. (b) The small-angle X-ray diffraction patterns show the different peak positions for the lamellar (green) and the hexagonal (blue) phases. The two peaks in the diffractogram of the third sample (black) reveal the presence of the two phases present in the same film. The lamellar phase has a d-spacing of 6.1 nm. The hexagonal phase has a d-spacing of 5.5 nm (unit cell dimension $a = 6.3\text{nm}$). (c) Schematic diagrams of the lamellar and hexagonal pore topologies with the respective arrangement of the template inside the pores. (d) The cross-section TEM on the left clearly shows the openings of hexagonally arranged pores and the middle one shows the stacking of the lamellae. For the phase mixture (right), it shows the different mesophases stacked on top of each other. A different stacking order can be observed in other areas of this sample. In all of the images, the glass substrate is visible at the bottom and the silica-air interface is visible at the top, the arrows point along the optical axis of the wide-field microscope (z-direction) in the observation plane (x-y direction, y is pointing into the drawing plane). The scale bars represent 50 nm.

than in the lamellar phase. The strong differences in the diffusion behavior in the two phases are illustrated in more detail in Figure 3.2c-f and below in Figure 3.4. Molecules in the hexagonal phase travel in a highly non-random manner over distances of several microns (blue tracks in Figure 3.2c) during the acquisition time of the movie (500 s).

In contrast, the doughnut patterns in the lamellar phase show regular diffusion on a much slower timescale, and cover areas smaller than $1 \mu\text{m}$ during the same time interval (63 frames with 8 s exposure, green tracks in Figure 3.2d). A detailed picture of an individual trajectory in the hexagonal phase is shown in Figure 3.2e. The molecule travels first along the C-shaped structure on the right (1) and after 65 s enters side-arm 2. Then, 100 s later, it passes into the linear structure at the bottom (3). After another 144 s it enters region 4 and moves around there for 69 s before coming back to region 3. At the end it passes into region 5, where it moves back and forth for 109 s until the end of the film. Note that the molecule apparently probes the domain boundaries in this process, by repeatedly ‘bouncing’ back from dead ends of the channel regions. This is one of the many striking examples which show how a single molecule explores the structure of the host. Such non-random diffusion, which was repeatedly seen in the hexagonal phase, directly maps the alignment of the channels and the domain structure, since: (i) TEM and XRD data show that the pores are horizontal in the focal plane; (ii) the widths of regions 1 - 5 exceed both the tracking error (small boxes around track points) and the pore spacing, implying that part of the time the molecule is in different but aligned pores; (iii) surface features seen in AFM images (data not shown) do not resemble in any way the structures seen by particle tracking (this excludes the movement of the molecules on distinct surface structures). Therefore it can be concluded that the tracks do indeed map out domains in the heart of the material. In addition, the observation of the molecular motion shows the accessibility of the channels and connectivity of the domains in an unprecedented way. To our knowledge there is no other method that can provide this kind of structural and dynamical information.

In contrast to the highly structured motion of the molecules in the tubular surfactant micelles of the hexagonal phase, Figure 3.2f depicts an example of a molecule in the lamellar phase. It diffuses randomly in two dimensions, as would be expected for molecules trapped in the surfactant layer between the silica planes.

In addition to the translational diffusion, polarization dependent confocal microscopy can provide information about the orientational dynamics of the TDI molecules inside the surfactant-filled pore systems. The orientational dynamics of the TDI molecules were measured in the lamellar as well as in the hexagonal pure phases. The widefield measurements have indicated that the TDI molecules in the lamellar phase are oriented perpendicular to the substrate, showing up as doughnut patterns. Hence, a mesoporous film of pure lamellar phase was observed from the side to obtain a better excitation of the fluorophores. Details of the setup can be seen in Figure 3.3a.

The TDI molecules were embedded in the mesoporous film at ensemble concentration to provide a sufficient fluorescence signal in this geometry, and the excitation polarization

3.2. DIFFUSION AND ORIENTATION OF SINGLE TDI MOLECULES IN 46 DIFFERENT MESOPHASES OF BRIJ-56-TEMPLATED MESOPOROUS FILMS

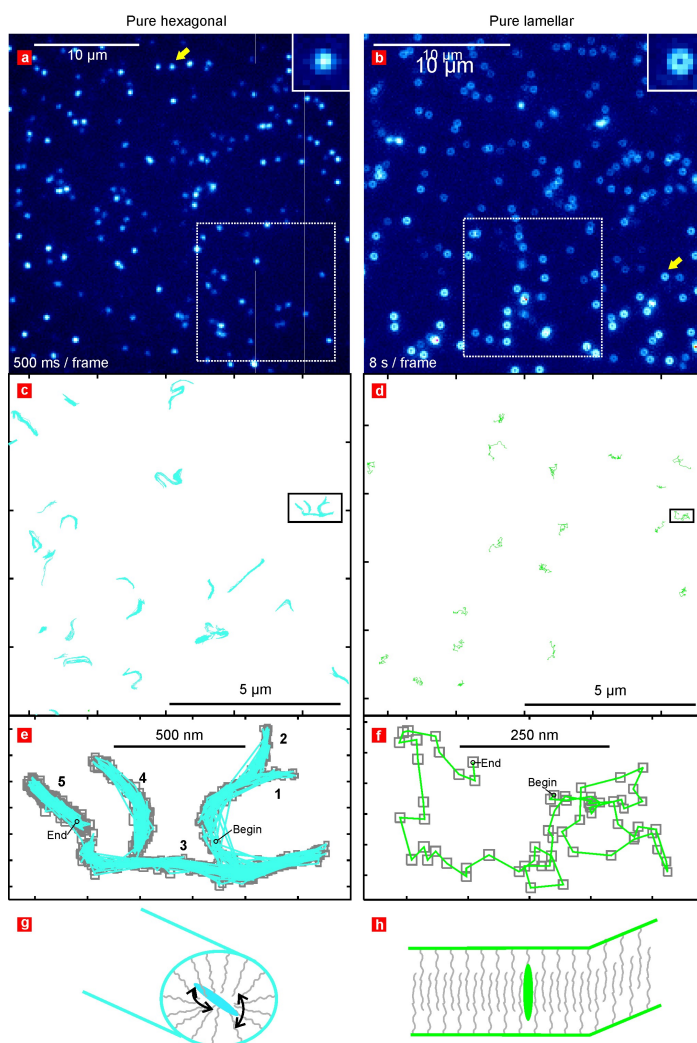


Figure 3.2: Single molecules images and trajectories of the pure hexagonal and lamellar phases of the mesoporous hosts obtained by wide-field imaging. The temporal resolution for the film of the hexagonal phase was 500 ms per frame and for the lamellar phase 8 s per frame. The scale increases from the top to the bottom as we zoom into the pictures, so that more and more details of the structure are resolved. The rectangular boxes indicate the enlarged regions. (a,b) The single molecules images in the hexagonal phase show only Gaussian-shaped diffraction patterns (a), whereas in the lamellar phase only doughnut-shaped patterns (b) are observed. The doughnuts are attributed to molecules oriented perpendicular to the substrate. Magnified images of the molecules indicated by the arrows are shown in the top right corners. (c,d) Trajectories of the diffusion obtained by SPT in the regions indicated by the white squares in a,b. Molecules showing structured diffusion in the hexagonal phase are plotted in blue (c); molecules with doughnut-shaped patterns in the lamellar phase are shown in green (d). (e,f) Sample trajectories in the hexagonal (e) and the lamellar (f) phases (highlighted in the rectangular boxes in c,d). The trajectory of the fast-diffusing molecule in the hexagonal phase shows a pronounced structure that reflects the structure of the hexagonal channels, whereas the trajectory of a doughnut-shaped pattern in the pure lamellar phase shows random-walk behavior. The grey boxes correspond to one standard deviation of the fit to the diffraction spot. (g,h) Schematic view of the arrangement of the guest molecules inside the hexagonal (g) and lamellar (h) topologies of mesoporous silica. (Detailed measurements of the molecular orientation can be found below).

was rotated continuously. Figure 3.3b shows a fluorescence image of the mesoporous film which appears as a thin striped vertical line. This reveals that the dye molecules are not randomly oriented within the lamellar phase, but all aligned in the same direction. To determine the average direction of the alignment, the confocal volume was placed some micrometers inside the mesoporous film and a fluorescence intensity trace was recorded (Figure 3.3c). The red line shows the modulation of the transmission intensity of the excitation light which is detected behind a fixed polarizer and acts as a reference for the determination of the angles (the angle of a horizontal line in Figure 3.3b is set to 0°). A cosine-square modulation of the fluorescence intensity (black line) is observed. The extracted angle is $2^\circ \pm 3^\circ$, which is the mean angle of the distribution of the orientations of the transition dipole moments of the dye molecules. This corresponds exactly to the direction perpendicular to the mesoporous film and thus perpendicular to the silica planes of the lamellar phase.

The orientation behavior of TDI molecules in the hexagonal phase was investigated with the mesoporous film placed in the focal plane of the microscope. In the widefield movies the molecules appear as Gaussian spots, and therefore do not keep a constant orientation along the z-axis of the microscope. The measurements with confocal setup were also done at ultra low concentration to gain information about the orientation dynamics of the individual emitters which are otherwise lost in ensemble averaging. First, a fluorescence image is recorded to visualize the single molecule emission patterns (not shown here). Second, the confocal volume was placed directly on the position of the molecule and the excitation polarization was rotated continuously similarly to the measurements above. Figure 3.3d shows a typical polarization fluorescence intensity trace for a single TDI molecule in the hexagonal phase. The blinking event between 0.5 s and 0.8 s, and the photobleaching step at 3.1 s are typical signatures for a single molecule. In contrast to the graph in Figure 3.3c, no periodic modulation of the fluorescence intensity (black line) is observed according to the rotation of the polarization in the excitation beam (~ 500 ms). Moreover, strong fluctuations of the fluorescence intensity can be observed. These are most probably due to the diffusion of the molecule in and out of the focus of the confocal spot. All 26 investigated molecules exhibit a similar orientational behavior. Thus the molecules do not keep a preferential orientation, but constantly reorient during their diffusion in the hexagonal template filled pores of the hexagonal phase.

These strong differences of orientational behavior of TDI in the lamellar and in the hexagonal phases are interpreted in terms of interactions between the hydrophobic dye molecules and the amphiphilic template molecules. The very ordered state of the molecules in the lamellar phase can be explained by strong interactions of the dye molecule with the template molecules (see Figure 3.2h). In contrast, the continuous reorientations in the hexagonal phase indicate much weaker interactions with the tem-

3.2. DIFFUSION AND ORIENTATION OF SINGLE TDI MOLECULES IN 48 DIFFERENT MESOPHASES OF BRIJ-56-TEMPLATED MESOPOROUS FILMS

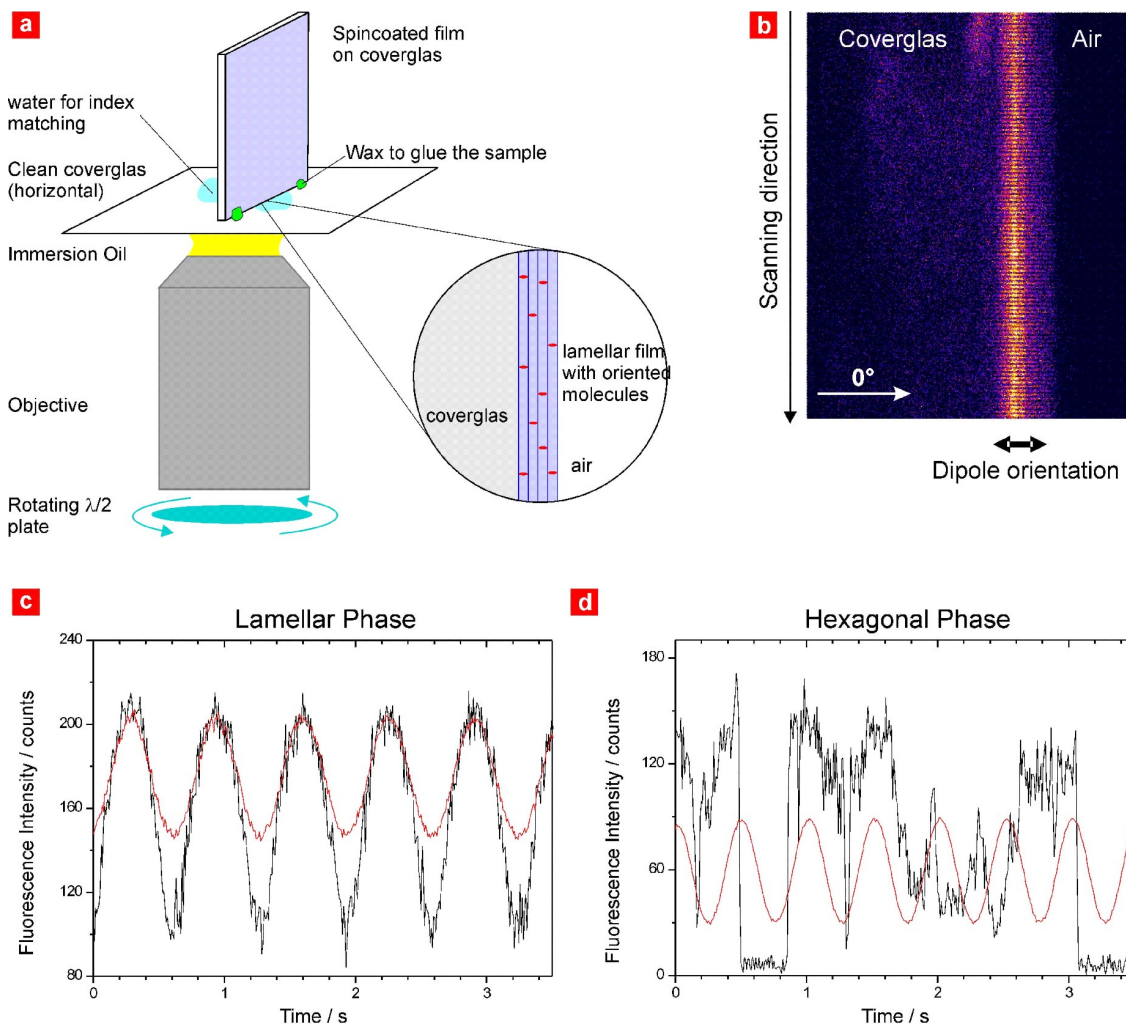


Figure 3.3: Measurements of the orientation of the molecules in the two phases. (a) Sketch of the alignment of the lamellar film perpendicular to the focal plane. (b) Confocal image of the fluorescence in the lamellar phase aligned like in a. The image was scanned line by line with rotation of the $\lambda/2$ plate. (c) Fluorescence intensity trace in the lamellar phase (black), transmission reference curve in red. (d). Fluorescence intensity trace of a single molecule in the hexagonal phase and transmission reference. The fluorescence signal is not modulated according to the transmission reference, thus the molecule is rotating constantly.

plate than in the lamellar phase, as sketched in Figure 3.2g. These differences in the interaction strength may also explain the much faster diffusion in the hexagonal phase compared to the lamellar phase. Furthermore, the higher surfactant/silica ratio used for the synthesis of the lamellar phase may result in a higher concentration of template and thus a higher viscosity in this phase.

3.2.3 Diffusion of single TDI molecules in the phase mixture - Phase switching

Similar observations as described above for the two pure phases are made in the third sample, consisting of a mixture of the two phases. 3.4a shows the first image from a movie, collected with a time resolution of 500 ms per frame in a $28.4 \mu\text{m} \times 25.4 \mu\text{m}$ area of this sample. Here, Gaussian-shaped and doughnut patterns coexist within the same region. The inset depicts magnified images of the two molecules indicated by the arrows. As the doughnuts are barely visible on this short timescale, an average over 8 s, i.e. 16 frames of 500 ms each, is presented here in order to make it comparable to the exposure time of Figure 3.2b, which shows the pure lamellar phase. Single particle tracking from this movie results in the 117 trajectories in Figure 3.4b. Overall, one can distinguish four populations of molecules based on their different diffraction patterns and diffusive behavior in this movie. The first type comprises molecules with Gaussian-shaped spots, which are diffusing along distinct structures over a large range of one to five microns (109 blue tracks in Figure 3.4b). The second type has characteristic doughnut-shaped diffraction patterns, see Figure 3.4a and inset. Since their patterns are barely visible at 500 ms exposure, no tracking of such doughnuts was done in this movie. On a timescale of minutes to hours, however, these molecules show unstructured diffusion in two dimensions. Another, much smaller population consists of molecules that diffuse much faster, without showing any particular structure in their trajectories. Five examples are shown in red. An additional important observation is that multiple changes between these three types of mobility were observed for many of the molecules. Finally, very few immobile molecules are observed (to within the positioning accuracy).

In accordance with the observations in the pure phases from Figure 3.2 the structured trajectories of population 1 can be assigned to molecules in regions with hexagonal arrangement of pores, and the molecules with doughnut-shaped patterns of population 2 that are diffusing very slowly and randomly, to other regions with lamellar structure, present simultaneously within this sample.

The transport behavior of the two remaining populations is not correlated with the pore topologies in the sample. In fact, the fast molecules of population 3 (red), with unstructured trajectories, could be removed by washing the surface of the sample with water, clearly indicating that the molecules were on the surface of the film. The immobile molecules of the small population 4 may be either captured in very small cavities inside the material or strongly adsorbed on the surface of the pore walls.

The different types of diffusing molecules are observed within the same area of the sample, implying overlaid hexagonal and lamellar phases as seen in the cross-section

3.2. DIFFUSION AND ORIENTATION OF SINGLE TDI MOLECULES IN 50 DIFFERENT MESOPHASES OF BRIJ-56-TEMPLATED MESOPOROUS FILMS

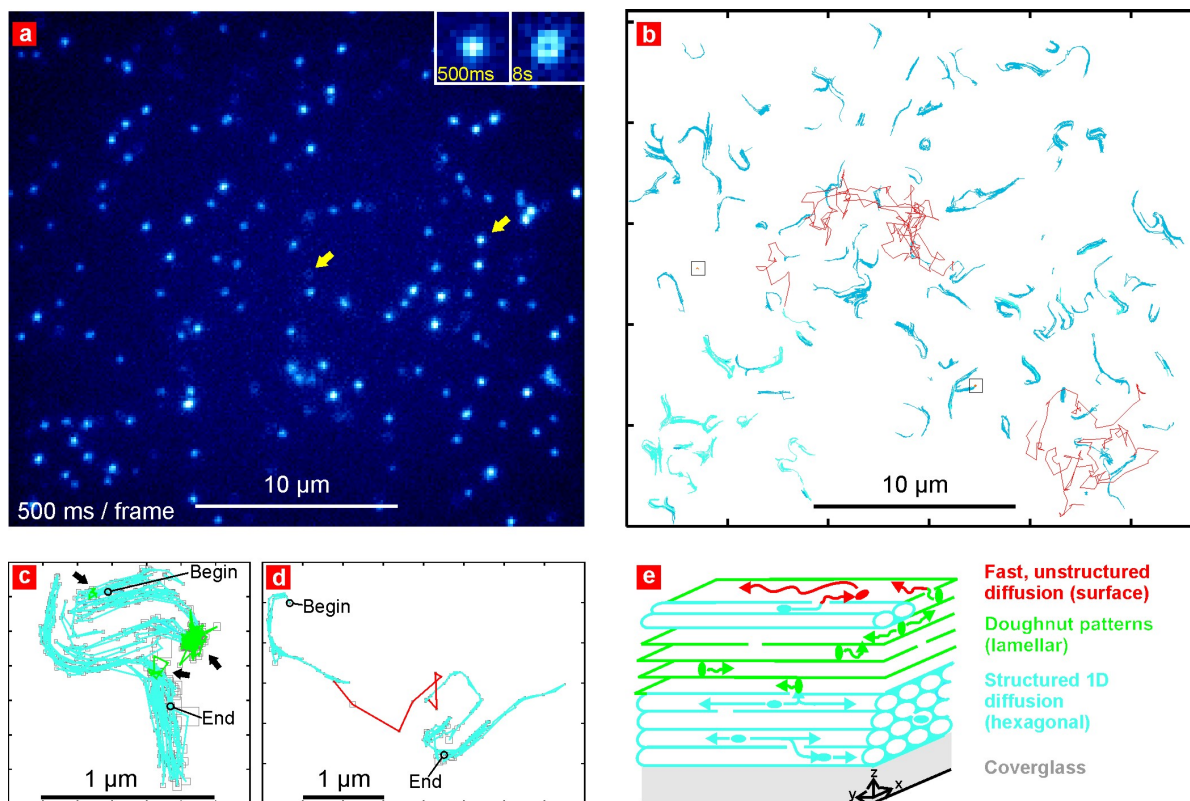


Figure 3.4: Diffusion of single molecules in the phase mixture. Temporal resolution: 500 ms per frame. (a) A single molecules image of the phase mixture contains both Gaussian- and doughnut-shaped diffraction patterns. Magnified images of the molecules indicated by the arrows are shown in the upper right corner. The doughnut-shaped pattern was averaged over 16 images, so it is presented with the same temporal resolution as in Figure 3.2b. (b) Map of all of the trajectories in the wide-field movies obtained by SPT. Structured trajectories are shown in blue, fast unstructured diffusion in red and immobile molecules in orange highlighted in square boxes. (c) An individual molecule undergoing several changes between the hexagonal (blue parts) and the lamellar (green parts, indicated by the arrows). (d) A molecule showing structured motion in the beginning for 42.5 s (blue), reaches the surface (red) and comes back into the hexagonal phase after 2.5 s. (e) Schematic diagram of the diverse diffusion modes observed in the wide-field movies of the phase mixture. Molecules diffusing randomly in the lamellar phase are oriented perpendicular to the surface (doughnuts in the wide-field measurements). Structured diffusion over long distances takes place in the hexagonal phase. Molecules on the surface show fast, unstructured diffusion. Transitions between the different diffusion modes are explained by connections between the pore topologies.

TEM in Figure 3.1d. The diffusion behavior in this phase mixture fits remarkably well with that in the pure phases described above. Interestingly, some molecules can be seen migrating between the phases. This observation demonstrates clearly that the two phases are actually interconnected. A specific example is shown in Figure 3.4c. The molecule first appears with a Gaussian diffraction pattern and diffuses for 5 s (10 frames) until it produces a doughnut pattern for a short period of 3.5 s. For the following 105 s it diffuses in a highly structured manner (Gaussian spot). Then the spot suddenly returns

to doughnut shape again for 197 s. During this time it hardly moves, due to the much lower diffusion coefficient in the lamellar phase (Figure 3.5). Structured diffusion with a Gaussian spot resumes in frame 622 and lasts for 66 s. After spending another 5.5 s as a doughnut pattern, i.e. in the lamellar phase, the molecule finally diffuses back and forth inside a system of parallel channels until the end of the movie. Again, as in the pure hexagonal phase, the shape of the trajectory explored by the Gaussian pattern clearly reflects the underlying pore structure of the hexagonal phase. This molecule changed three times from a Gaussian spot to a doughnut and back with different residence times in each phase. Such switching phenomena clearly show that the two phases are actually connected, probably *via* structural defects at the phase boundaries. Interestingly, other cases can be observed where the molecule switches several times from a Gaussian to a doughnut pattern at exactly the same position, showing that molecules sometimes pass repeatedly through the same defect region between phases.

Besides migrating between phases, some molecules actually exit the film, thus showing up at the top surface. Figure 3.4d shows an example from which this is deduced.

Here the molecule diffuses first in the hexagonal phase for 42 s, than exits on to the surface, where it moves very fast and randomly, and comes back into the hexagonal phase after 2.5 s, about 1 μm away from where it appeared at the surface. A similar example that was measured with a higher temporal resolution, showing a longer period of random diffusion on the surface is presented in Figure 3.3a. A detailed trace of a doughnut in the phase mixture is also provided in Figure 3.3b.

Based upon the above discussion, one can correlate the different diffusion behavior with the structural information in Figure 3.1 and the observations in the pure phases in Figure 3.2. A schematic general picture of the different phases present in the film and the migration within as well as between the phases is shown in Figure 3.4e.

3.2.4 Mean squared displacement analysis

The different diffusive behavior can also be visualized by plotting the mean-square displacements (MSD) $\langle r^2 \rangle$ of the individual molecules as a function of time t (Figure 3.5). Assuming regular Brownian motion according to the Einstein-Smoluchowski relation,⁷⁴ $\langle r^2 \rangle = 2 dDt$, with $d = 1, 2$, or 3 according to one-, two- or three-dimensional diffusion, respectively, the diffusion coefficient can be extracted from the vertical intercepts of double logarithmic plots of $\langle r^2 \rangle$ *vs* t . Figure 3.5 shows that (i) the molecules in the different populations in fact have distinct mobilities (bundles of roughly straight lines with a slope close to unity) and (ii) a certain spread exists for the diffusion coefficients (vertical inter-

3.2. DIFFUSION AND ORIENTATION OF SINGLE TDI MOLECULES IN
52 DIFFERENT MESOPHASES OF BRIJ-56-TEMPLATED MESOPOROUS FILMS

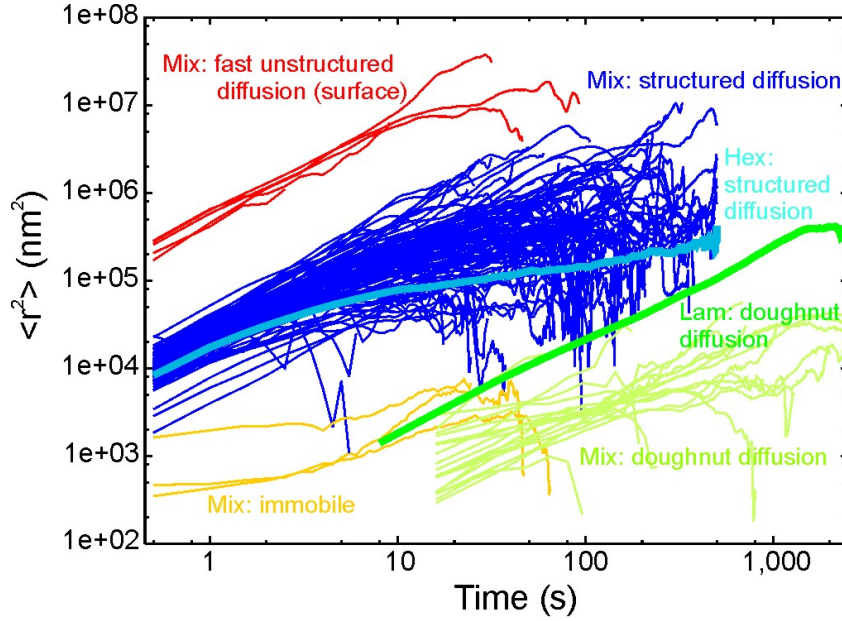


Figure 3.5: Mean-square displacement as a function of time. The individual molecules in the different mesoporous samples and also within the same sample can be separated according to their different diffusion coefficients. For the sake of clarity, individual tracks are plotted only for the phase mixture, the thick lines represent the average values for the pure hexagonal (pale blue) and pure lamellar (dark green) phases. Molecules with structured tracks in the phase mixture, population 1, are plotted dark blue, the diffusion of the doughnuts, population 2 in the phase mixture, in light green and fast and unstructured diffusion of population 3 in the phase mixture in red. The horizontal orange curves correspond to immobile molecules (population 4 in the phase mixture).

cepts within a bundle). This spread might be explained by the width of the peaks in the XRD patterns, indicating a certain distribution of pore sizes present in the individual phases. The diffusion coefficients differ by approximately two orders of magnitude both between populations 1 (hexagonal channels) and 2 (lamellar) and between populations 1 and 3 (surface). Furthermore, the dark blue lines for the molecules of population 1 can be overlaid with the thick light blue line, which corresponds to the average value for the molecules in the pure hexagonal phase ($D = 5.0 \times 10^{-3} \mu \text{ m}^2 \text{ s}^{-1}$, fitted with $d = 1$). An interesting observation for the hexagonal phase is that the linear plots for short lags bend towards a horizontal asymptote for large time intervals. This is characteristic for diffusion in confined regions, which in this case are the domains explored by the molecules. The statistical information given here agrees well with the direct observation of dead ends in the individual trajectories of molecules in the pure hexagonal phase (Figure 3.2e). The domain size, extracted from the horizontal asymptote, ranges from several hundred nanometers up to one micrometer. For the dark blue lines the asymptotes are reached at higher values of $\langle r^2 \rangle$, indicating larger domains. This is in agreement with the direct observation of the trajectories in the mixture compared to the pure hexagonal phase in Figure 3.4 and Figure 3.2c, respectively. The plots for the doughnut-shaped patterns in

the phase mixture are in about the same range as the molecules in the lamellar phase, indicated by the thick dark green line ($D = 5.3 \times 10^{-5} \mu\text{m}^2\text{s}^{-1}$, with $d = 2$). For the sake of clarity only the mean values are plotted for the pure phases. The diffusivities given above thus confirm the previous assignment of the populations to the different phases. Possible explanations for the small differences of the diffusion coefficients of the doughnuts in the phase mixture and the pure lamellar phase include a slightly different amount of template in a given volume element, or a different degree of compression normal to the film surface, respectively. Especially for samples with a phase mixture the distribution of template into the two phases can slightly differ from that in the pure phases.

3.2.5 Conclusion

It has been shown in this section how tracking of single molecules by fluorescence microscopy techniques can be used to trace out the pore system of a mesoporous thin film. Whereas TEM is restricted to small areas and very thin layers, wide-field microscopy can be used to investigate diffusion over an area of $30 \mu\text{m} \times 30 \mu\text{m}$ or more. Structured trajectories are seen, following the pores in the material for as much as 5 - 10 μm . On the basis of the structure of the trajectories, the diffusivities and the orientation of the molecules, it is possible to distinguish dyes travelling on the external surface from those travelling inside the pore system, dyes that diffuse along horizontal channels of the hexagonal phase, and those that move much more slowly in lamellar galleries of the mesoporous material. It is even possible to observe the same single molecule migrating between one type of surrounding, for example the hexagonal channel system, and another such as the lamellar phase. In addition, the structural heterogeneity of the channels is reflected by the complex modes of motion observed for single molecules within the hexagonal phase.

3.3 Translational, orientational and spectral dynamics of single TDI molecules in CTAB-templated mesoporous films

We have seen that the investigation of the translational and orientational behavior of single molecules in a mesoporous film reveal details of the host structure, its domains and the accessibility as well as the connectivity of the channel system. However, while the measurement of an individual property (e.g. spectrum, orientation, position, etc.) already provides valuable details about the host-guest material, a deeper understanding for the underlying molecular mechanism can be gathered by correlating different properties. This section reports on single molecules investigations of the dynamics of TDI dye molecules within the unidimensional pores of a M41S CTAB-templated mesoporous silica material. By measuring and correlating the molecules position, orientation and emission spectrum it is demonstrated that single molecule spectroscopy (SMS) allows deep insight into host-guest interactions and dynamics within mesoporous systems on a molecular level, thus helping to understand host-guest properties.

3.3.1 The M41S CTAB-templated mesoporous system

Thin films, containing bundles of hexagonally arranged pores with 3-4 nm pore diameter, were prepared by spin-coating using the cationic surfactant CTAB as template (see experimental section 3.5). Figure 3.6a and b show two TEM images of such samples. The films consist of small domains (typically 20 - 100 nm in size) with different alignments of the pores.^{132, 133} TDI molecules (about 2.5 nm in length), were incorporated as guests in these films at ultra low concentrations. As will be seen in the following, CTAB-templated mesoporous materials are well suited for investigating the single molecule traffic as well as the dynamics of the host-guest interactions in the nanometer-sized channels. Since residual water remaining within the pores might influence the dynamics, the sample were placed at constant relative humidity of $\sim 40\%$ during all the measurements presented in this section.

3.3.2 Simultaneous measurement of orientational and translational dynamics

Figure 3.7a shows a polarization modulated confocal image of single TDI molecules diffusing in the pores of such a film. The individual molecules appear with the characteristic

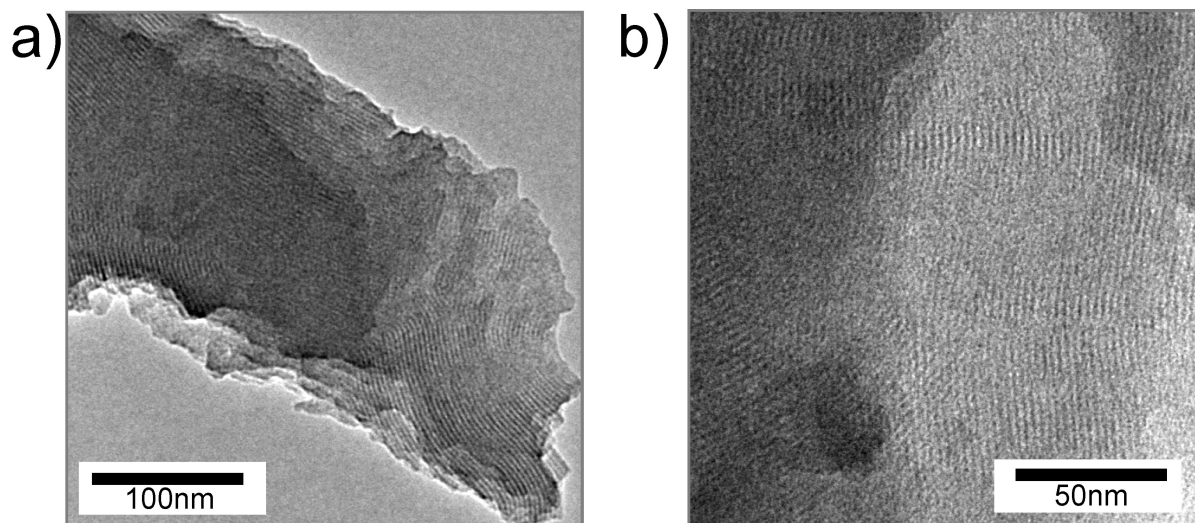


Figure 3.6: Exemplary TEM images of a as-synthesized CTAB-templated mesoporous film. Small domains of parallel and curved pores can be observed of about 100 - 200 nm in size.

fluorescence-intensity profile. Molecules A, B and C, for example, exhibit stripped pattern along the scan line because of the rotation of the excitation polarization. Figure 3.7b and c display the trajectories of two single TDI molecules extracted from a movie of 75 frames (~ 150 min) together with the angle of the molecules's transition moment. An immediate observation is that the movement of the single guest molecules is very slow in this system compared to the study presented in section 3.2 with Brij-56 as template for the mesoporous hexagonal phase. The diffusion of the molecule corresponding to 3.7b remains confined within a region of about 100 - 200 nm. However, the trajectory of the dipole moment shows pronounced orientational dynamics interrupted by periods of time where the orientation remains constant (for example in the time interval between 26 and 44 min). The points without orientation in the graph are positions where the molecule reorients faster than the time required to determine its orientation (~ 0.8 s). Two other examples of such reorienting single molecules can be seen in Figure 3.7a (molecules D and E; they can be readily identified because their fluorescence profile is not stripped). A close inspection of the points of the trajectory displayed in Figure 3.7b in the time intervals during which the angle of the dipole moment remains constant reveals that the molecule is immobilized during these periods of time (within the positioning accuracy which is in this case ~ 70 nm). This observation suggests the presence of specific sites in the mesoporous film where the molecule can be adsorbed for a certain period of time. This phenomenon of adsorption can be clearly visualized with the trajectory for another single TDI molecule displayed in Figure 3.7c. The molecule remains immobile (within the positioning accuracy) with a constant angle of the dipole moment of $95 \pm 3^\circ$ during more than 2 h, being most probably trapped in an adsorption site within the material.

Then it suddenly desorbs from the adsorption site and undergoes strong lateral as well as orientational diffusion until the end of the trajectory where it photobleaches.

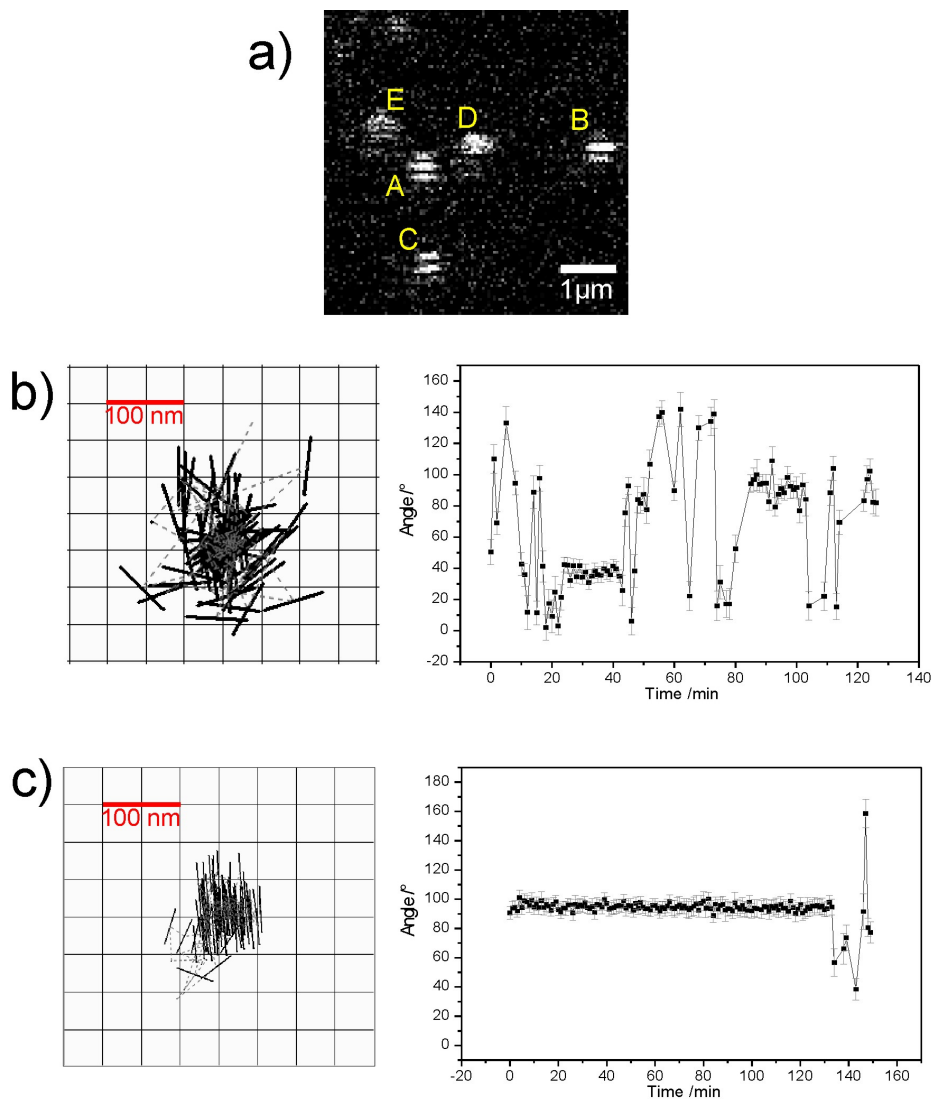


Figure 3.7: (a) Polarization modulated confocal fluorescence image of single TDI molecules diffusing in the pores of a CTAB-templated mesoporous thin film. The molecules appear with a characteristic fluorescence-intensity profile (stripped patterns of molecules A, B and C) due to the polarization modulation during the scan. Molecules D and E show a more complex fluorescence-intensity profile due to their reorientation during their scanning time (about 0.8 s). (b) Exemplary trajectory (left panel) of a single TDI molecule. The two dimensional orientation of the dipole moment is indicated by black thick lines. The right panel displays the extracted angular time trajectory of the molecule. This molecule diffuses in a confined region and shows occasionally a constant orientation of its transition dipole moment for several frames. (c) Trajectory and angular time trajectory for another molecule. The TDI molecule remains immobilized at an adsorption site for about 2 hours until it escapes at the end of the trajectory.

Another typical behavior in these at first sight unstructured domains is illustrated for another molecule in Figure 3.8. It reveals regions, marked A and B, of about 100 - 200 nm in size, in which the molecule remains confined, and between which the molecule moves rapidly. The trajectory of the molecule in its movement between the confinement regions does not show a particular structure. Moreover, in many positions it is not possible to determine an orientation for the molecule as it changes its orientation faster than the measurement time (~ 0.8 s). This translational and orientational behavior may occur if the confinement regions are connected to comparatively large defect sites or hollow domain boundaries. Such defects are known to occur in M41S films. Furthermore, the behavior of the mobile molecule within the confinement regions A and B is characterized primarily by the detected orientational dynamics (see Figure 3.8 b). Similarly to the two previous examples, the molecule in these regions, is not constantly rotating, but is instead found to keep well-defined orientations for extended periods of time ranging from seconds to tens of minutes. Moreover, the orientations in the two regions A and B (0 - 29 min and 42 - 90 min respectively) are not randomly distributed (see zoom-ins in Figure 3.8a). This is an indication that a structural feature prevents the molecule from moving freely. One such structural feature is the existence of domains with preferential pore-orientation. The molecule may move with a certain angle within such a domain but switches between a few accessible domains with different angles. These domains, however, are smaller than the spatial resolution of the experiment.

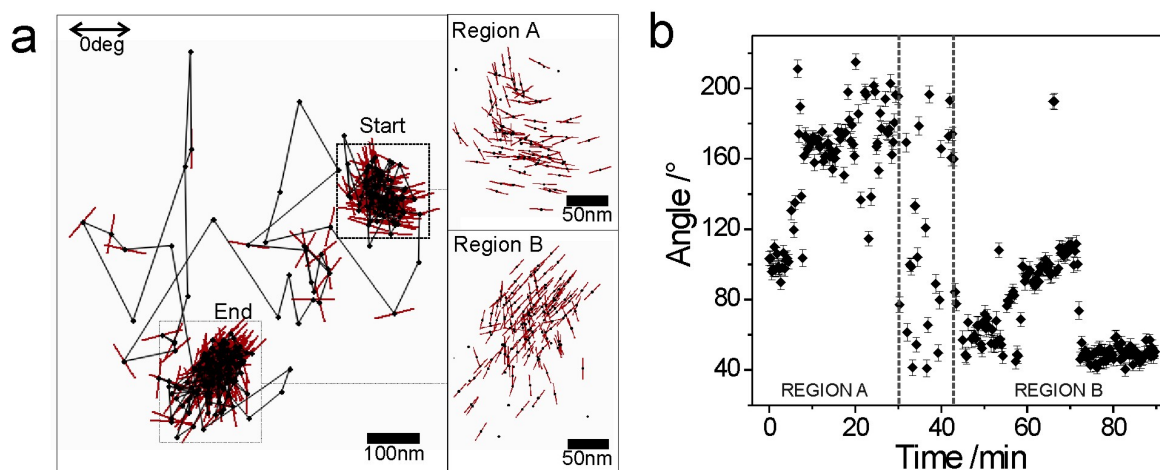


Figure 3.8: Intra and inter-domain diffusion of a single TDI molecule in a M41S film. (a) Trajectory of a molecule which starts and ends in confined regions. The orientation of the molecule determined by the data analysis is shown by red lines. The points of the trajectory without orientation are positions where the molecule reorients faster than the time required to determine its orientation (~ 0.8 s). The insets are zoom-ins which show the confined diffusion in regions A and B. (b) Angular time trajectory of the molecule displaying periods of stable orientations as well as periods of frequent re-orientations.

3.3.3 Simultaneous measurement of orientational and spectral dynamics

The interactions between the fluorescent probe and its immediate environment in the confinement regions can be described in more detail by investigating simultaneously the molecule's orientation and emission spectrum. The emission spectrum is an extremely sensitive measure since small changes in the host-guest interactions result in a detectable change in the spectrum.^{55,134}

In this section the simultaneous measurement of orientational and spectral dynamics of single dye molecules incorporated into the channels of two types of host-guest material are presented. Oxazine-1 dye molecules incorporated into the channels of microporous $\text{AlPO}_4\text{-5}$ crystals do not have the freedom to re-orient and show limited spectral dynamics. This system represents a static material in which the molecules are entrapped and immobilized in a solid matrix and stands as an example for a static host-guest material, which is desirable for various solid-state optical applications.^{82,127} The second host-guest system correspond to the TDI / CTAB-templated mesoporous film which was investigated in the previous section. As mentioned above, an individual molecule can diffuse within confined regions (such as regions A and B described in Figure 3.8) for tens of minutes. By placing the confocal detection volume directly on the molecule's position it is possible to temporally zoom-in into the trajectories. Here, changes in orientation are used as an indicator for molecular movement. In parallel, the observed spectral dynamics give information about the interactions between the dye molecule and its direct environment. This type of system stands as an example for materials in which dynamics play a fundamental role, as is desirable for sensor and catalysis applications.^{135,136} Here, one can observe orientational dynamics that are accompanied by spectral dynamics.

The two systems that have been studied are depicted in Figure 3.9. In the first system oxazine-1 molecules are encapsulated into the unidimensional channels of $\text{AlPO}_4\text{-5}$ crystals (a zeotype structure). In this case the width of the molecules (~ 0.8 nm) and the diameter of the pores (0.73 nm) are comparable (Figure 3.9a). The molecules fit tightly into the channel structure, and the molecules are not expected to re-orient, or to show any mobility at all, in accordance with previous studies.¹¹⁴ Absorption and emission spectra for a highly loaded crystal ($\sim 10^{-8}$ mol/g) are shown in Figure 3.9b.

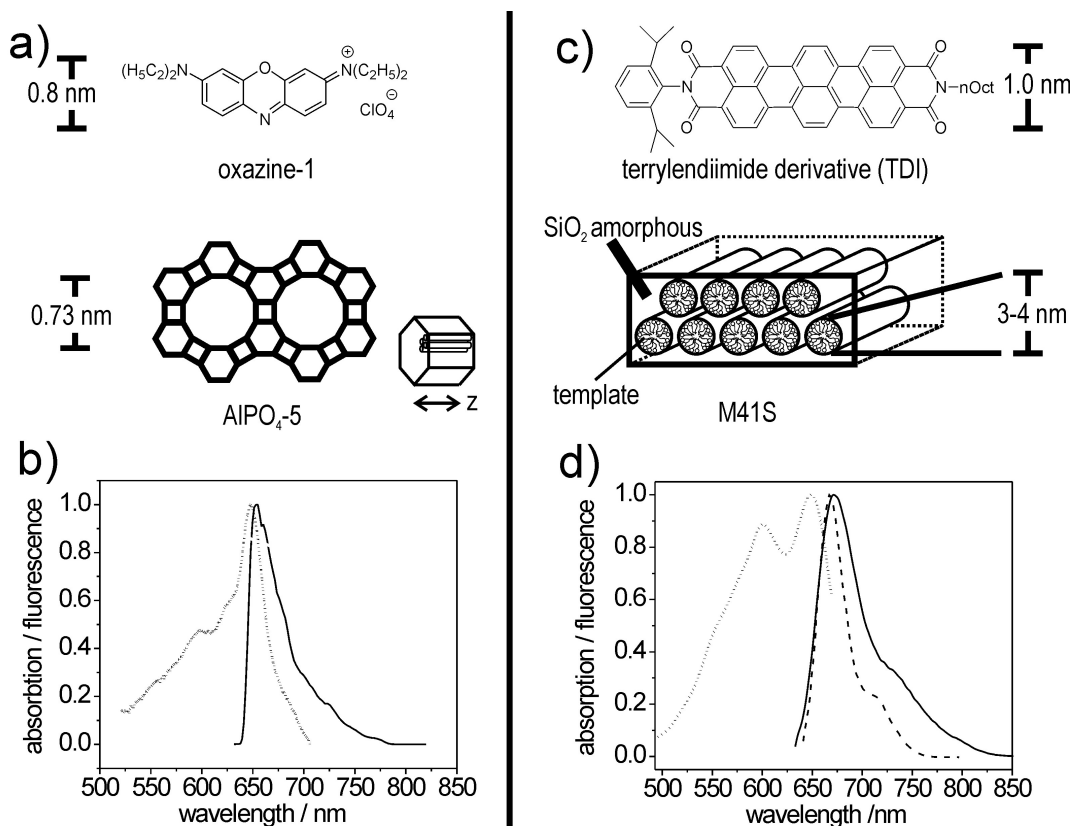


Figure 3.9: Chemical structures, sizes of guests and hosts, and spectra of the investigated samples. (a) Oxazine-1 (width 0.8 nm) and the unidimensional channels of AlPO₄-5 (diameter 0.73 nm) viewed from front. The small scheme on the lower right shows the crystal habitus and the direction of the pores. (b) Absorption (dotted line) and emission (solid line) spectra of oxazine-1 in high loading (10^{-8} mol g⁻¹) in AlPO₄-5 crystals. (c) Terrylenediimide derivative (TDI, 1.0 nm in width) and the hexagonally ordered channels (diameter 3-4 nm) of the template filled M41S structure. (d) Absorption (dotted line) and emission (solid line) spectra of TDI in ethanol, and emission spectrum of TDI in high concentration (10^{-5} mmol/L) in a M41S film (dashed line).

In the second system the sizes of host and guest to allow for more orientational dynamics. Absorption and emission spectra for higher concentration ($\sim 10^{-8}$ mol/L) are shown in Figure 3.9d. TDI molecules are extremely photostable, a single molecule can be studied for several minutes, sometimes hours (compared to only a few seconds of observation time for a typical oxazine molecule). Thus TDI molecules are ideally suited as reporters for different environments within the nanoporous network.

3.3.3.1 Oxazine-1 / AlPO₄-5 system.

A typical fluorescence microscopy cross-section through an AlPO₄-5 crystal containing oxazine-1 molecules is shown in Figure 3.10a. The approximate boundary of the crystal

in this image is obtained from transmission images. The individual molecules are visible as diffraction limited fluorescence spots. The confocal volume can be placed on one of the corresponding positions to acquire data from an immobilized single molecule. During this acquisition the excitation polarisation is rotated continuously. Excerpts from the data-sets for a single oxazine-1 molecule in $\text{AlPO}_4\text{-5}$, that is, the polarization dependent intensity trace and the sequence of spectra, are shown in Figure 3.10b and c.

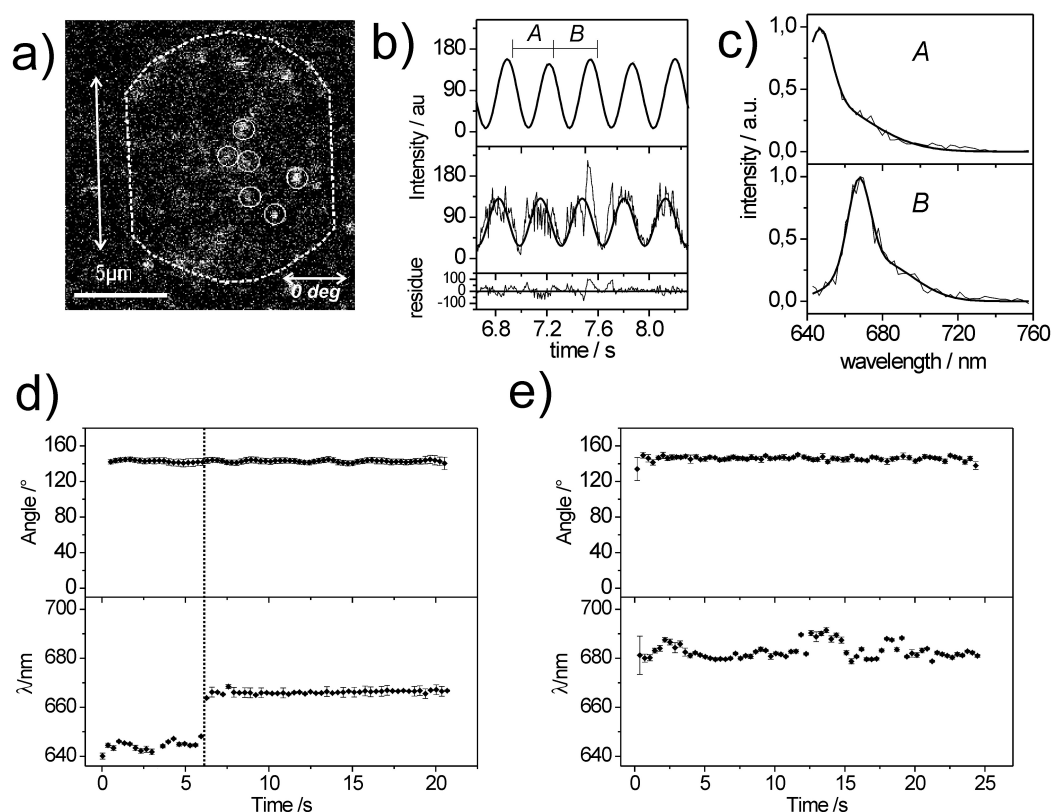


Figure 3.10: The simultaneous measurement of orientation and spectra of single oxazine-1 molecules in $\text{AlPO}_4\text{-5}$ in loadings of 10^{-10} mol/g. (a) Confocal cross-section through an $\text{AlPO}_4\text{-5}$ crystal showing single molecules as diffraction limited fluorescence spots. The outline of the crystal shape (dotted line) and the pore orientation (arrow) are inferred from transmission images. (b) Polarization dependent intensity trace for transmitted excitation light (upper graph) and single molecule fluorescence (middle graph). The solid curve is the fit of equation 2.14 to the data. The lower graph shows the residuals of the fit. (c) Two consecutive spectra (with fits) corresponding to the time segments A and B (indicated in 3b showing a pronounced spectral jump of 26 nm). (d) Complete angular and spectral trajectories corresponding to the graphs in 3b and 3c. Error bars in 3d and 3e denote the standard deviation of the fit. (e) Angular and spectral trajectories for another oxazine-1 molecule showing the most common case encountered in this system.

The curves in Figure 3.10b show the typical cosine-square modulation for the transmitted light (top graph), and a single oxazine-1 molecule (middle graph). The data can be fitted with equations 2.13 and 2.14 respectively. The orientation of the molecule remains

constant with a value of $143^\circ \pm 2^\circ$. The angular distribution of all molecules is broad and roughly aligned with the main axis of the crystal.¹¹⁴ Altogether 60 molecules in 5 different crystals were measured and all molecules remained with a fixed orientation during the measurement. This confirms the expectation that the tight fit of oxazine-1 molecules in $\text{AlPO}_4\text{-5}$ results in immobile molecules that do not have any freedom to move or to rotate.

Simultaneously with the polarization data, fluorescence spectra were recorded and spectral dynamics were observed. With these data one can differentiate between fast spectral fluctuations and rare spectral jumps. In the first case, the spectral position of the emission maximum fluctuates continuously around a mean value. The amplitude of these fluctuations varies and is typically in a range of 2 to 8 nm. In contrast, *spectral jumps* occur abruptly as isolated events and the jump is typically larger in magnitude than the *spectral fluctuations*. An example showing such a pronounced *spectral jump* is shown in Figure 3.10c. The two spectra were taken consecutively and correspond to the time segments A and B indicated in the intensity trace in Figure 3.10b. The spectra before the jump resemble spectrum A, and the ones after the spectral jump event resemble B (data not shown). An intermediate and broadened spectrum is not observed on going from spectrum A to spectrum B. This is a clear indication that the jump itself takes place on a time-scale well below the temporal resolution (~ 300 ms)

The data analysis of the modulated intensity trace and sequence of spectra gives $\Phi(t)$, the angular trajectory, and $\lambda_m(t)$, the spectral trajectory. The graphs in Figure 3.10d and e show the corresponding data for the molecule displaying the spectral jump mentioned above, and for another, more representative oxazine-1 molecule in an $\text{AlPO}_4\text{-5}$ crystal. In the first case one observes that the emission maximum makes a jump of 26 nm to larger wavelengths at approx. 7.5 s in Figure 3.10d. However, before and after the jump the orientation remains constant. Upon closer inspection of the polarization dependent data shown in Figure 3.10b it is possible to note a burst in the intensity trace at the time when the spectral jump occurred. This jump might indicate a short lived change in the environment. Spectral jumps of this magnitude have been observed rarely in this system; 3 out of 60 molecules showed a single spectral jump. On a cumulative time-scale, this corresponds to about one jump per 3 minutes of observation time. The second set of data (Figure 3.10e) is more representative for the oxazine-1 / $\text{AlPO}_4\text{-5}$ systems. The orientation of the molecule also remains constant ($149^\circ \pm 5^\circ$) while the spectra fluctuate rapidly around a mean value of 685 nm in a range of 2 to 8 nm.

The encountered spectral dynamics are a consequence of the changes of the underlying electronic energy levels. It has been suggested that they can have *intrinsic* or *extrinsic* origins. Different interconvertible structural conformations of a chromophore producing

spectral shifts are an example for intrinsic factors.¹²¹ On the other hand, the interactions between the electronic states of the chromophore with its immediate environment can lead to spectral fluctuations of extrinsic origin. This is the case if the immediate vicinity of the molecule is subject to dynamical changes or if the molecule moves to different environments in the host. Possible causes for the fluctuations in the molecule's direct vicinity include the motion of small charged molecules in neighbouring channels or conformational changes in the host structure near the site at which the fluorescent molecule is located.

The absence of detectable orientational dynamics confirms that in this system oxazine-1 is tightly confined in the pores of AlPO₄-5. On the other hand, spectral dynamics are clearly visible and confined to a range of typically 3 - 5 nm. In a few isolated cases pronounced spectral jumps (up to 26 nm) have been observed. These fluctuations reflect dynamical changes in the environment around the molecule since the molecule is not moving to different sites in the crystal. Possible causes for such small and rapid fluctuations can be fluctuations in the AlPO₄-5 structure¹³⁷ or interactions with co-adsorbed species (ions, water, template) which are comparatively free to diffuse in the pores of the material.¹⁰⁷ The large spectral jumps must result from more pronounced and rarely occurring events. Possible reasons for these events could be the direct interaction with a co-adsorbed species in the same channel or (counter-) ions changing between comparatively stable adsorption sites in neighboring pores interacting via the Stark-effect. Whereas in this section the behavior of individual dye molecules in a static material was observed, we turn in the next section to a dye-pore system in which the dye molecules have more space to undergo orientational dynamics.

3.3.3.2 TDI / M41S system

The orientational and spectral dynamics in the TDI / M41S system are expected to be more complex than in the oxazine-1 / AlPO₄-5 system because of the larger mobility of the molecules in this matrix. The TDI molecules are smaller (~2.5 nm in length, ~1.0 nm in diameter) than the M41S pore diameter (3-4 nm). However, it is important to recall here that the structured channels in the otherwise amorphous SiO₂ body are left uncalcined, that is, the pores in which TDI molecules are situated are filled with the micellar template CTAB used for the synthesis. Translational diffusion occurs in this medium and allows the molecules to explore different environments. During this movement the molecule is free to change its orientation. Translational diffusion, however, is slow enough to ensure that a molecule remains within the detection volume of the confocal microscope for several minutes.

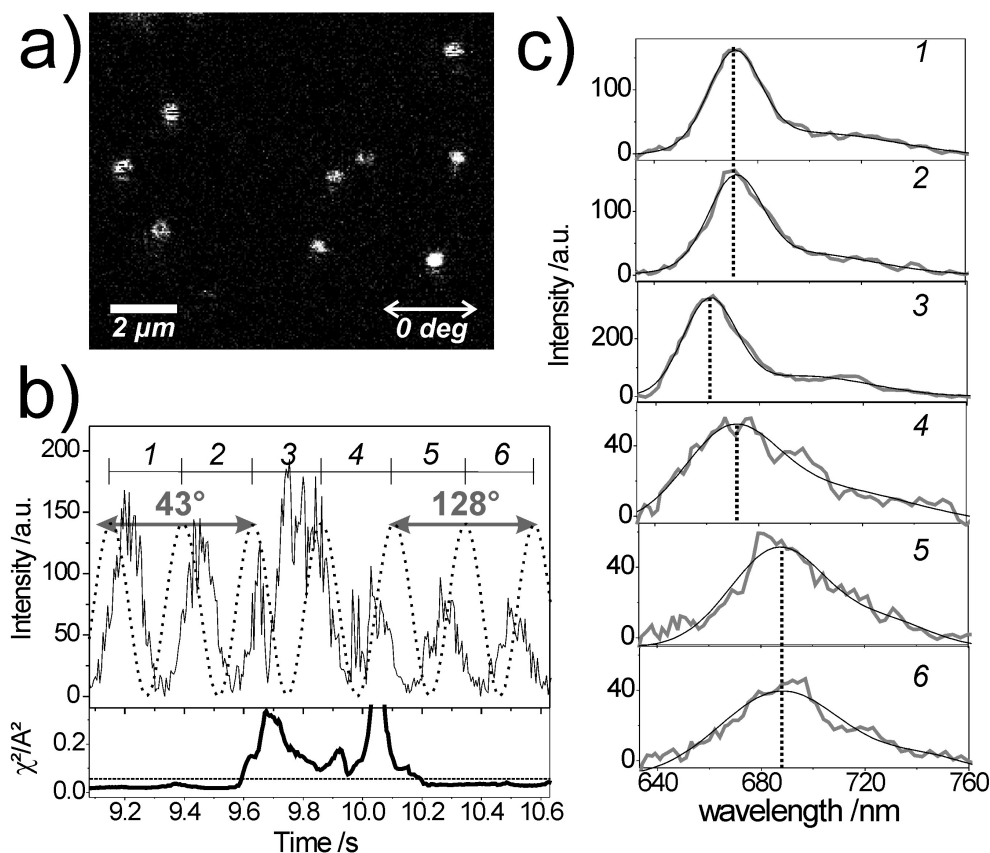


Figure 3.11: Images and data sets for single TDI molecules in an M41S film. (a) Fluorescence image showing diffraction limited fluorescence spots of individual TDI molecules in a M41S film. (b) Polarization dependent fluorescence intensity trace (black) and transmitted excitation light (grey) curves showing orientational dynamic of an individual TDI molecule. The lower graph shows the normalized χ^2 which is used as a criterion (threshold given by dotted line) to assign an orientation to a time segment. For details see text. (c) Sequence of spectra corresponding to the segments indicated in (b). The dashed line indicates center position of the fit to the spectrum.

A typical data set consisting of images, orientational and spectral data of TDI in M41S is shown in Figure 4. The data were obtained in the same manner as described for the oxazine/ $\text{AlPO}_4\text{-5}$ system. For clarity, the discussion is divided into three parts. The different types of orientational dynamics encountered in this system will first be presented, and in the second part these data will be correlated with the spectral dynamics. In the last part a global statistical description using all observed dynamics is given for 72 investigated molecules.

3.3.3.3 Orientational Dynamics

TDI in M41S shows pronounced orientational dynamics. A typical example is depicted in Figure 3.11b. In this excerpt from a longer intensity trace, the molecule starts with a well defined orientation (of $43^\circ \pm 2^\circ$) and remains oriented for about 0.6 seconds. Then, in the time interval between 9.6 s and 10.1 s, it is not possible to determine a stable orientation. This is a clear indication that in this period the molecule is undergoing orientational dynamics that are below the temporal resolution of 300 ms. Then at 10.1 s, the molecule finds a new stable orientation, at a different angle ($128 \pm 3^\circ$). It is interesting to note that the intensities before and after the re-orientation period are not equal. This is most likely caused by different (out-of-plane) orientations of the molecule with respect to the optical axis of the experiment. Other possibilities for a change in fluorescence signal are the lateral diffusion out of or into the center of the confocal volume, or the fact that the molecules may explore different environments which may affect the fluorescence intensity.¹³⁸

This type of orientational dynamics, that is, a molecule starting with one well-defined orientation, undergoing some form of movement in the porous matrix and ending at a new stable orientation, is the most commonly observed case in the TDI / M41S system. This can be interpreted as a molecule moving between different adsorption sites in the material. The nature of these adsorption sites is currently not very well understood, possible interactions include direct contact with silica walls, electrostatic interactions with the cationic template as well as interactions at defect sites. The binding to the adsorption site is revealed by the molecule's fixed orientation for a certain period of time. The duration of this period relates to the strength with which the molecule interacts with the site. Therefore, in the following discussion the adsorption duration will be used as a measure for the interaction strength.

To describe the orientational behavior in more detail we now turn to another single molecules example depicted in Figure 3.12. The polarization dependent intensity trace is shown in the upper panel of Figure 3.12a. The middle graph shows the extracted angular trajectory $\Phi(t)$. Only those data points are displayed for which a well-defined orientation can be determined, i.e. the orientation is constant during at least one period of the polarisation modulation. The omitted points correspond to segments during which the molecule underwent rapid reorientations, so that no stable orientations could be determined. The two hatched segments correspond to so-called blinking events, where the molecule rests in a dark-state.

The time-scales on which the orientational dynamics occur range from below the temporal resolution used, 300 ms, to tens of seconds. A few exemplary time-segments illustrates

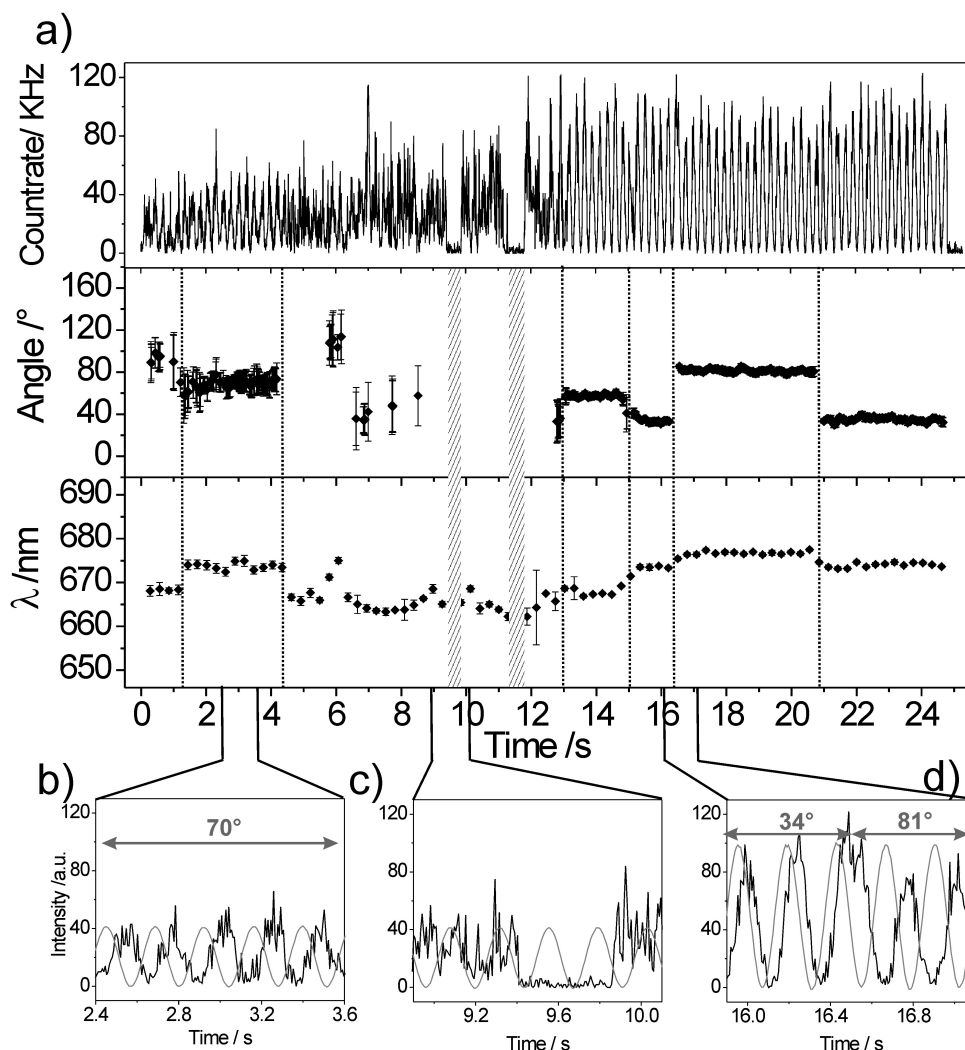


Figure 3.12: Orientational behavior of TDI in a M41S film. (a) The upper panel shows the polarization dependent fluorescence trace. The middle and lower panels give the angular and spectral trajectory after data analysis. (b)-(d) Excerpts from the curve in (a). The continuous thin line corresponds to the excitation polarization. (b) A stable orientation of $\sim 70^\circ$ over a period of seconds. (c) Segment where no preferred orientation could be assigned and blinking event occurred. (d) Time window with distinct jump from 34° to 81° .

this in Figures 3.12b-d which are taken from the complete trace of Figure 3.12a. The segment in Figure 3.12b shows that orientations may remain stable on a time scale of seconds. This indicates that strong adsorption sites in the material are accessible to the moving molecule.

The graph in Figure 3.12c is an excerpt from the period between 4.2 and 13 seconds and shows a different characteristic behavior. Here, the molecule undergoes rapid orientational dynamics for a period of seconds. This indicates the presence of regions in which the interactions between the molecule and the matrix are weaker. In this region, the

molecule is continuously tumbling between different environments.

In Figure 3.12d an abrupt re-orientation is shown, in contrast to the more commonly observed phenomenon, where a period of high dynamics is found in between two adsorption events, described above. In this example, the movement itself is much faster than resolution limit of the setup. The molecule starts with an orientation of $34^\circ \pm 2^\circ$ and jumps to $81^\circ \pm 2^\circ$. Later in the trajectory (at about 21 s), as can be seen in the middle graph of Figure 3.12a, the molecule switches back abruptly to the same angle of 34° . This particular case shows a molecule switching abruptly back and forth between preferential orientations. This switching is likely caused by sites where two stable positions, i.e. two minima in the effective potential, are present. This is a clear example for a situation where additional information about the molecule e.g. its emission spectrum could help to distinguish between two plausible explanations.

The individual molecules explore various environments in which the time-scale of the orientational dynamics varies dramatically. In one extreme case a molecule may stay at a specific well-defined orientation, at a strong adsorption site for many seconds - indicated by a constant orientation angle. On the other hand a molecule can be found to undergo fast orientational dynamics that last for a period of several seconds, if it is within a region in which the host-guest interactions are comparatively weak and the molecule is able to sample different areas. Altogether these behaviors reflect the heterogeneous structure of the environment that is explored by the molecule.

In the next section the spectral data are included in order to address the question how the travel to different adsorption sites can affect the spectral properties of the fluorescent molecules.

3.3.3.4 Combined spectral and orientational dynamics

In order to gain a more detailed understanding about the nature of the observed adsorption sites the fluorescence spectra of the individual dye molecules were simultaneously recorded. Taken by themselves, the spectral dynamics in the TDI / M41S system are similar to those observed in the oxazine-1 / AlPO₄-5 system, that is, one observes fast changes of the emission spectra on a 2-30 nm scale. Likewise, it is possible to differentiate between *spectral fluctuations* (occurring continuously and fast) and *spectral jumps* (isolated events, larger in magnitude and less frequent). Such large spectral jumps, spanning a range of 27 nm are shown in Figure 3.11c. These spectra correspond to the numbered segments of the fluorescence intensity trace shown in Figure 3.11b. The emission maximum of the spectrum remains nearly constant (at around 685 nm) in the first two spectra. During that time the polarization analysis yields a stable angle of 43° .

The emission maximum changes in the next two periods (spectra 3 and 4) until a new stable position is found in spectrum 5 and in the subsequent segments with an emission maximum at 688 nm. Here, the molecule is found at a fixed orientation of 128° .

Upon closer inspection of the periods during which the spectral jumps occur, one can observe that spectrum 3 is narrower than spectrum 4. This indicates that the interaction with the environment leading to spectrum 3 does not cause large fluctuations. At the same time, the polarization signal of the molecule does not allow to find a stable orientation. This may be so if the molecule stayed at a preferential orientation for a time just below the temporal resolution. Therefore, the orientation in segment 3 was determined using only half a modulation period and an angle of 105° was obtained, however with a large error of 20° . Altogether, this information suggests that the molecule first switches rapidly between adsorption sites on going from segment 2 to 3 and then undergoes even faster spectral and orientational dynamics in segment 4.

The correlation between orientational and spectral dynamics is shown on a larger time-scale in the lower panel of Figure 3.12a for another single molecules. For clarity, the complete spectrum is not displayed but the spectral position of the emission maximum is shown, $\lambda_m(t)$. First, one can note the presence of periods during which the maximum of the emission spectrum remains at a constant value, thus yielding a plateau in the time-trace. Each plateau in the spectral trajectory can be assigned to a plateau in the orientational trajectory, in the same time-range. Spectral and orientational jumps can be seen in the whole time trajectory. These jumps are usually neither correlated in size nor in direction. However, sometimes reversible jumps are observed. An example is seen in the three last plateaus that correspond to two distinguishable spectral positions (674 nm, 677 nm) and can be assigned to the two angular positions (34° , 81°), as discussed above. This further strengthens the argument that in these last periods (from 14.8 s to 24.5 s) the studied molecule switches back and forth between two well-defined adsorption sites.

The many details obtained by the method used reveal some more characteristic effects that are worth mentioning. To illustrate these, it is shown two more trajectories in Figure 3.13a and b. Due to the high photostability of TDI it is possible to observe the behavior of a single molecule on a time scale of minutes. The behavior is extremely heterogeneous. In the first part of the trajectory in Figure 3.13a (until 85 s) the plateaus extend over a long period of time. Here, the molecule is situated in a region where the interactions with the material are strong. Then, in the time segment between 85 and 150 s the molecule undergoes a long period of orientational and spectral dynamics. Here, the molecule has moved into an environment where the interactions are weaker. This allows the molecule to explore a more extensive set of adsorption sites. In the last part of the trajectory, i.e. after 150 s in the trace, the interactions become stronger again.

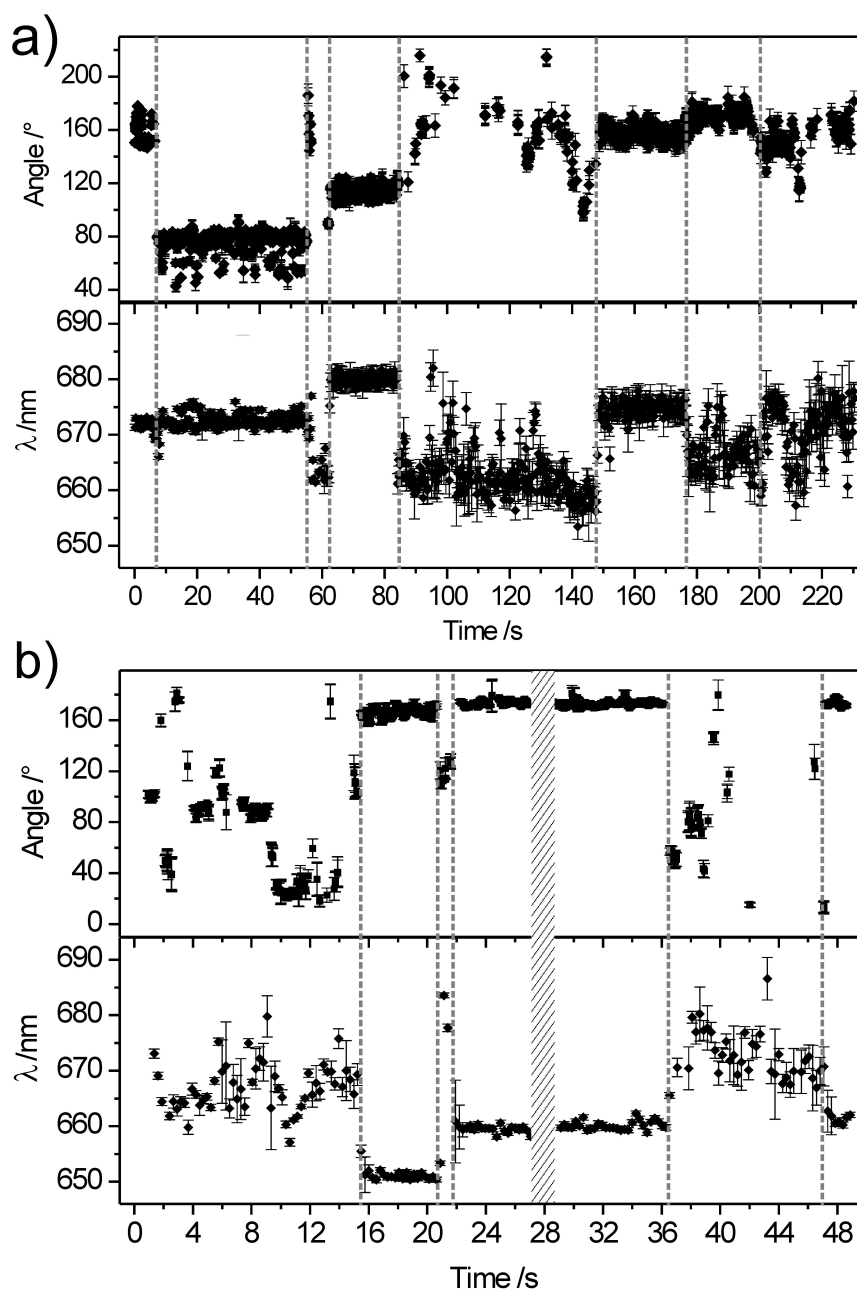


Figure 3.13: Angular and spectral trajectories for two TDI molecules in M41S. The trajectories in (a) and in (b) show special cases of orientational and spectral dynamics discussed in the text. The error bars denote the standard deviation of the fits.

A special case can be seen at about 8 s in the trajectory (indicated by an arrow in the Figure). The molecule undergoes a large orientational jump from the stable orientation at 150° to a stable orientation at 82°. The corresponding spectra, however, are peaked at identical wavelengths. While the orientational jumps manifest that the molecule

changes its position, the similarity of the spectra suggests that the molecule finds two environments which are similar in terms of host-guest interaction.

The second trajectory displayed in Figure 3.13b, shows the data from a different molecule which displays similar spectral and orientational dynamics during large parts of the trajectory. Moreover, a rare case is also observed where the molecule visits a particular adsorption site twice, interrupted by a long time interval between the events. The adsorption site yields the molecule at a stable orientation ($175^\circ \pm 2^\circ$) between 22 and 36 s. This period is followed by a long interval of strong orientational and spectral dynamics from 36 s to 47 s. After this period both the angle and the emission maximum return to the original values. In this case, the molecule is either returning to the same adsorption site or - by coincidence - finds another adsorption site with the same angle and with a very similar environment.

In conclusion, the juxtaposition of orientational and spectral behaviors, gives a more complete picture of the system investigated. The observed strong correlation between spectral and orientational jumps shows that the spectral fluctuations are a direct consequence of the host-guest interactions.^{125,139} Therefore, it is possible to use an individual molecule as a reporter for its immediate nanoenvironment. Furthermore, from these data one can conclude that the interaction between the molecule and an adsorption site in the material is quite specific. That is, a distinct host-guest interaction produces its own characteristic spectrum. The spectral fluctuations are comparatively small when a molecule is fixed at an adsorption site. Moreover, molecules are exploring different adsorption sites as indicated by simultaneous occurrence of orientational and spectral jumps. The part of the trajectory during which a molecule moves is characterized by rapid re-orientations that cannot be assigned to a specific angle, as well as by strong fluctuations in the spectral trajectory. The magnitude of the fluctuations during this period is significantly larger than the magnitude of the fluctuations when the molecule is found to have a constant orientation. A likely cause for these large fluctuations is the rapid succession of different environments explored by the molecule during its motion. Thus, a single molecules can explore nanometer scale heterogeneities in its surroundings. The recorded data, the orientation and emission spectrum, are clear footprints of these heterogeneities.

3.3.3.5 Statistical analysis of all traces

While the high sensitivity of SMS reveals many details of host-guest interactions – in fact, every single trace is unique - it is also useful to compare the behavior of all molecules by computing histograms and correlations. The following questions will be addressed:

(a) What is the typical time a molecule spends at a specific orientation? (b) What is the typical time a molecule is found with a specific spectrum? (c) Can the distribution of spectral and orientational jumps be characterized? (d) Do all spectral jumps occur simultaneously with orientational jumps?

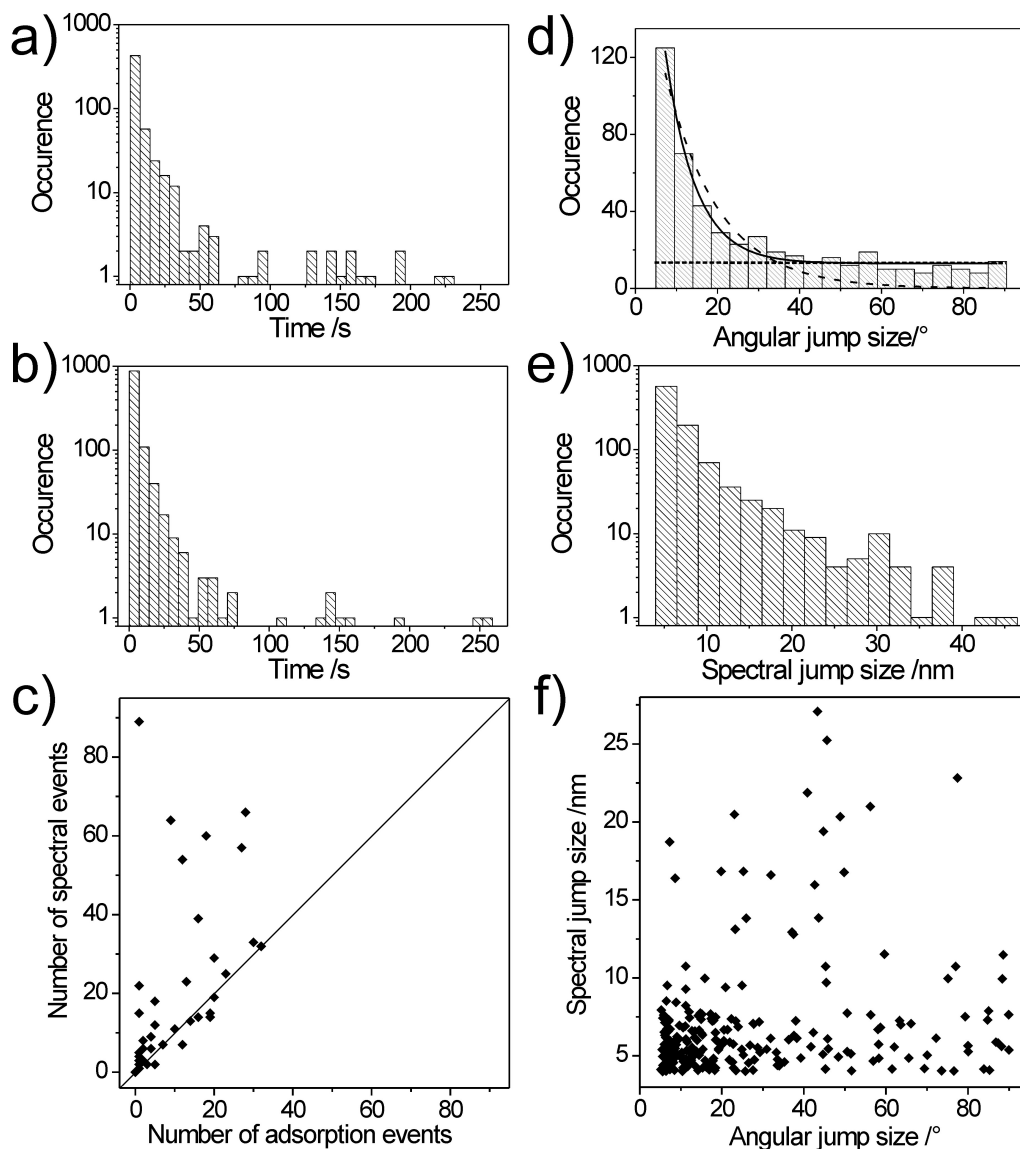


Figure 3.14: Global correlation between adsorption and spectral residence times of TDI molecules in M41S. (a) Histogram showing the distribution of adsorption (angular) times. (b) Histogram of spectral residence times. (c) Cross correlation between number of spectral and adsorption events per molecule. (d) Histogram showing the distribution of angular jump sizes. A single exponential fit to the data (dashed line) does not agree with the observed distribution. A single exponential fit (solid line) in combination with an offset (dotted line) describes the data much better (see text for details). (e) Histogram of the spectral jump size. (f) Cross correlation between magnitudes of concomitant angular and spectral jumps.

Histograms of orientational and spectral residence times (the lengths of the plateaus in the graphs) have been computed from 72 trajectories. The result is displayed in Figure 7a. The typical time a molecule spends at a specific orientation is computed from the angular trajectory using a threshold criterion for the variation in the angle from data point to data point. The time a molecule spends at one orientation ends with an orientational jump exceeding a threshold value of 5° (this value is about two times the typical experimental error). The distribution of residence times is shown in Figure 3.14a. It does not follow a mono-exponential model; this indicates that there are different effects leading to the distribution. These effects include the kinetics of adsorption and desorption of a dye molecule to specific sites of the matrix, influence of template dynamics and of other species present in the porous network. In order to obtain a characteristic time the median of the distribution is determined, which for this system is 2.3 s.

Similarly, the distribution of spectral residence times are obtained by applying a threshold value of 4 nm (twice the typical experimental error). Likewise, the distribution (Figure 3.14b) does not follow a mono-exponential model. The median, used to describe a characteristic time between jumps is 2.2 s. Usually, diffusion of molecules occurs on much faster time-scales. Therefore in this system albeit diffusion is possible it is greatly hindered by strong adsorption sites and the presence of the template.

To verify quantitatively to what extent angular and spectral jumps are correlated the number of angular jumps is plotted *versus* the number of spectral jumps per molecule in Figure 7c. If the orientational and spectral jumps were absolutely correlated all data points would be located on the $y = x$ diagonal. The graph shows, however, that while spectral jumps correlate with orientational jumps, they also occur in the absence of orientational jumps; in this case the data points are above the diagonal. The converse case, of orientational jumps occurring without a concomitant spectral jump is not significant; they are either coincidental or due to analysis errors, e.g. an undetected spectral jump below the threshold criterion. In all trajectories together 1108 spectral jumps and 570 angular jumps were detected. For 86% of the angular jumps a spectral jump occurred simultaneously.

The distribution of the angular jump sizes is shown in Figure 3.14c. In order to understand the jump size distribution it is important to recall the structural organization of the M41S material. This system is characterized by hexagonally arranged unidimensional pores which form ordered domains of typically 100 - 200 nm in size. The domains are interconnected and randomly oriented with respect to each other. Furthermore it is known that the structure also shows regions with curved and interrupted pores.

A complete rotation of the TDI molecules, which are about 2.5 nm long, in the 3 - 4 nm sized pore is most probably hindered by the presence of the CTAB template. Therefore the distribution of angular jump sizes for a molecule in a pore is likely to be narrow. In contrast to this, the angular jumps are expected to be equally distributed for molecules moving between domains or in defects, since the relative orientation of neighboring domains are random and defect sites provide enough space for the molecule to freely rotate. The observed distribution shows the presence of at least two sub-populations of jump sizes. The first sub-population corresponds to jumps below 30° , which are overrepresented. In this sub-population only small angular jumps are allowed. This presumably reflects the influence of the geometric constraints in the pore on the orientational motion of the molecules. The second sub-population is superimposed as an offset on the whole distribution (see line in Figure 3.14d). In this sub-population the size of angular jumps are equally distributed. Most probably these jumps occur in regions between domains or at defect sites which are larger than the molecules dimensions.

Figure 3.14e displays the distribution of spectral jump sizes. Likewise, this distribution does not follow a mono-exponential decay (note the logarithmic scale), indicating the presence of strong heterogeneities such as local changes, structural deformation or impurities. The median is 7 nm, and gives the characteristic amplitude of the spectral jumps. Furthermore, the question whether there is a correlation between magnitudes of spectral and orientational jumps is investigated. The sizes of concomitant spectral *versus* angular jumps is displayed in Figure 3.14f. No significant correlation is observed. The emission spectrum of the single molecules is determined by the chemical nature of the local environment which is spatially heterogeneous. Therefore a molecule moving within the mesoporous structure experiences different environments leading to different spectral jumps.

3.3.3.6 Comparison between oxazine-1/ $\text{AlPO}_4\text{-5}$ and TDI/M41S systems

The two host-guest systems, oxazine-1 in $\text{AlPO}_4\text{-5}$ and TDI in M41S show different types of spectral / orientational behaviors as expected from a comparison of guest and pore sizes. In the oxazine-1 / $\text{AlPO}_4\text{-5}$ system, where the individual molecules are fixed, spectral fluctuations of small amplitude (3-5 nm) are observed and, rarely, pronounced spectral jumps of 10 nm and above. In $\text{AlPO}_4\text{-5}$ all molecules showed a distinct and stable orientation along the channel axis in accordance what was reported in a previous study. The spectral dynamics thus arise from extrinsic effects, which can be divided into rare distinct events (e.g. charge dislocation between strong adsorption sites in the vicinity of the molecule) and frequently occurring events (fluctuations of the host structure, diffusion of co-adsorbed species) which lead to spectral diffusion. The molecule in this

medium acts as a reporter on a particular location.

In contrast the TDI / M41S system provides more freedom for the mobility of the guests. The dynamic behavior is therefore more complex. First, in this host-guest system the molecules are found to switch between fixed orientations (adsorbed states) and undefined orientations (tumbling movement of the molecules) on different time-scales, as the molecules move between adsorption sites in the material. Second, the emission spectra show fluctuations similar in magnitude to the ones found in the oxazine-1 / AlPO₄-5 system. However, the frequency of the occurring jumps is (i) higher (3 spectral jumps >10 nm per minute for TDI compared to 0.3 per minute for oxazine-1) and (ii) 86% of the observed orientational jumps occur simultaneously with a spectral jump. The spectral behavior in this sample is a superposition of (at least) two effects, namely uncorrelated spectral fluctuations (which were also observed in oxazine-1 / AlPO₄-5) and spectral fluctuations arising from different environments explored by the mobile molecule. The molecule acts as an active reporter, exploring different environments.

3.3.4 Conclusion

The simultaneous examination of spectral and orientational behavior of a single guest molecule in a host material provides valuable information for the characterization of the structural and chemical heterogeneities in the host. Moreover, the relative size of the guest molecule with respect to the pores of the host affects the observed dynamics. Oxazine-1 molecules tightly fit in the pores of the microporous AlPO₄-5. The resulting host-guest material represents a static material, i.e. rigid in nature, where the incorporated molecules are entrapped at a specific site in the host structure. In the second system studied the relevant sizes of the TDI molecules and the pores of the mesoporous M41S films allow for a slow mobility of the guest in the host pores. First, it is observed that the typical motion of TDI molecules in the pores of M41S is not continuous, but interrupted by stops at adsorption sites. Additionally, in the TDI / M41S system the observed spectral dynamics are found to be correlated with the orientational dynamics and thus arise directly from the different environments and adsorption sites that become explored by a mobile molecule.

3.4 Preparation and single molecule investigation of highly structured domains in CTAB-templated mesoporous films

The data and analysis presented in the previous section revealed in CTAB-templated mesoporous films the presence of regions, of about 100 - 200 nm in size, in which the diffusion of single TDI guest molecules is confined, and between which they can move rapidly. The translational and orientational behavior of the TDI molecules in these (at first sight) unstructured domains can be understood if one keeps in mind the structural organization of the mesoporous films. As mentioned above, TEM of such films (Figure 3.6a and b) show ordered domains of hexagonally arranged unidimensional pores which are randomly oriented. However, the pores are not perfectly linear but can be more or less curved in these domains, and the size of these latter does not exceed some hundreds nanometers. The synthesis and characterization of mesoporous host materials with an increasing degree of order of the channel system have been extensively reported recently.¹⁴⁰⁻¹⁴³ The control of the mesochannel orientation at macroscopic scale is highly desirable, and is an essential issue for practical applications of these materials. This section is divided in two parts. The first part shows how perfect alignment of the channels over a length scale up to 100 μm can be obtained with a post-synthesis treatment. The second part of this section presents a single molecule study of the translational and orientational dynamics of TDI guest molecules within these highly structured domains.

3.4.1 Growth of the highly structured domains

3.4.1.1 Introduction

An important finding of this study is that CTAB-templated mesoporous films with small domain sizes, such as those investigated above, can be treated after synthesis to lead to more structured materials with macroscopic-sized domains of nearly perfectly linear channel systems. A critical parameter of the post-synthetic treatment of the mesoporous films is the relative humidity (RH). It is known that water plays a key role during and after the synthesis of the mesoporous films.¹⁰¹⁻¹⁰⁵ First, water is essential in the fabrication of these films to ensure the hydrolysis of the silica precursor. Moreover, the structure of the silica matrix with template filled pores is fully rigid in nature, and resembles partially a liquid crystal. This flexibility allows rearrangement of the silica structure even after the synthesis of the film and the evaporation of the solvent. RH plays an important role in this phenomenon because water molecules can be found at the

surface of the micelles as well as in the silica network itself. The influence of water on the porous structure of CTAB-templated systems has been investigated in details by Grosso et al.^{101,102,144} and Gibaud et al.^{103–105} An interesting result of these studies is that raising the RH can yield phase transformations after synthesis of the film, which clearly shows that strong rearrangements of the mesoporous material can occur. However, the timescales on which these experiments were conducted didn't exceed some hours after the synthesis of the mesoporous films. Indeed, after this period of time the mesoporous films were considered to have reached thermodynamical equilibrium because no significant changes could be observed on longer timescales with the methods of analysis used in other studies.

Mesoporous materials are commonly characterized by X-Ray diffraction (XRD) and transmission electron microscopy (TEM).^{40,41} However, these standard techniques have severe limitations. From XRD patterns the average pore-to-pore distances in the host-system can be calculated, but no information about the alignment of the pores on the substrate and on the arrangement of domains of parallel pores can be obtained. In contrast TEM gives a very detailed image of the pore structure, but the areas of the sample which can be imaged are limited to a few hundreds of nanometers in size, and more importantly TEM imaging requires a special, mostly invasive preparation, like scratching, grinding and ion milling.

The possibility to identify easily these large domains by the fluorescence signal emitted from guest dye molecules such as TDI incorporated into the channels, and to measure areas of the mesoporous films on length scales up to hundreds of micrometers makes fluorescence microscopy an ideal tool to investigate the formation and the growth of large highly structured domains of linear channels within a mesoporous film.

3.4.1.2 Fabrication of large highly structured domains

TDI dye molecules were incorporated in the pores of CTAB-templated mesoporous films (Synthesis procedure described in section 3.5). However, here the fluorophore is used at ensemble concentration ($c = 10^{-6}$ mol/L) in order to render visible the totality of the domains investigated. Additionally, a lambda half plate is constantly and slowly rotated during the scan of the laser beam in order to measure the orientation of the dipole moment of the dye molecules.

Figure 3.15a shows a patchwork of nine fluorescence images recorded from a region of about 500 μm in total size of a CTAB-templated mesoporous film, and taken directly after spin-coating of the film (time 0). An homogenous fluorescence signal is visible over the whole fluorescence image. In particular, no modulation of the fluorescence intensity

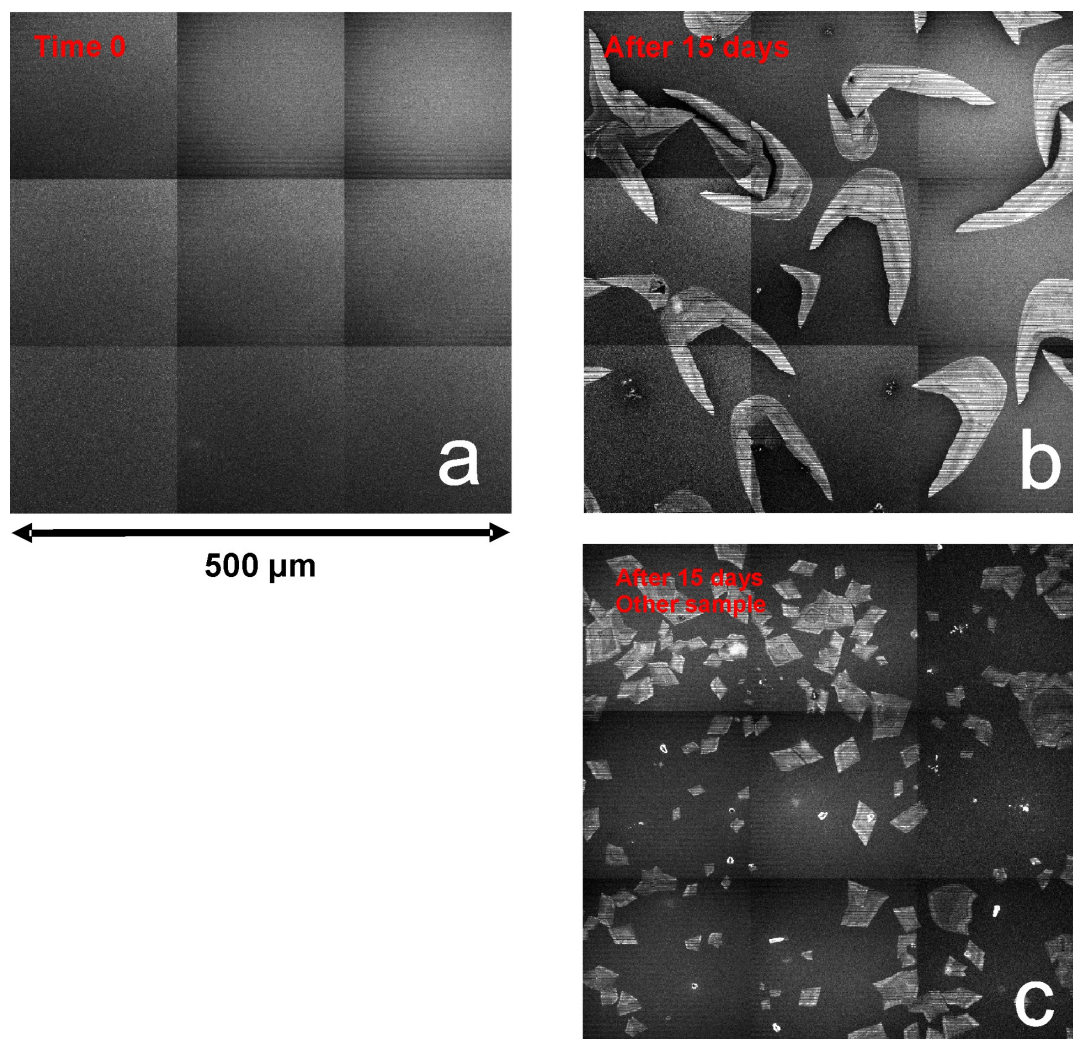


Figure 3.15: Slow formation of highly structured domains after spin-coating of the CTAB-templated mesoporous films. (a) Patchwork of nine confocal fluorescence images of a mesoporous film loaded with TDI at ensemble concentration observed directly after spin-coating. Only a fluorescence background signal is visible. (b) Same sample after 15 days of storage at a constant RH of about 50 %. Bright, highly structured domains have been formed. (c) Another sample after 15 days of storage at a constant RH of 50 %. The form of the bright domain is different.

can be detected during the revolution of the polarization of the laser. This indicates that the TDI molecules are distributed equally over the sample without preferential orientation of their dipole moments. This is consistent with the TEM micrographs shown in Figure 3.6a and b. Indeed, the small size (10 - 100 nm) of these regions and the curvature of the channels explain that no preferential orientation of the TDI dye molecules is expected on the lengthscale of the optical resolution of a confocal microscope, which is about 300 nm.

Figure 3.15b shows a patchwork of nine fluorescence images of the same sample 15 days after synthesis. During this period, the sample was stored at a constant RH of about

50%. In addition to the homogeneous fluorescence background, regions up to 100 μm in size exhibit a much brighter fluorescence signal. The formation of such regions is observed in all the ten investigated samples stored at the same RH. However, it is observed that the shape and the size of these regions can vary. Figure 3.15c corresponds to another sample synthesized and stored at the same experimental conditions. Here, the domains exhibit a more rectangular shape, and are slightly smaller in size (tens of micrometers).

Figure 3.16a shows a zoom in such a region. Stripped horizontal lines, with the same periodicity in time as the polarization modulation of the laser beam, can be seen over all the three distinct regions. The fact that the fluorescence signal is modulated and demonstrates that TDI dye molecules have a preferential orientation in each of these regions. Indeed, an homogeneous signal would result from randomly oriented fluorophores which emit light in all directions. Moreover, the diffusional and orientational behavior of the TDI dye molecules in the channels of these regions will be investigated in section 3.3.2. As will be shown, the molecules show linear movement, with their transition dipole moment aligned along their trajectories, reflecting well-ordered structural areas of the host. Hence, it can be concluded that these regions of bright, oriented dye molecules correspond to highly structured domains of parallel channels in which the fluorophores are remarkably aligned along the direction of the pores. Moreover, the fact that all the dipole moments of the TDI molecules lie in these domains perfectly perpendicular to the optical axis of the setup offers an ideal configuration for an optimal excitation of the fluorophores. This can explain the much brighter signal observed for TDI molecules encapsulated in such domains compared to the rest of the mesoporous film.

An additional important information that can be obtained from the analysis of these polarization-modulated patterns is the absolute direction of the channel system in the structured domains. The insert shown in Figure 3.16a is a zoom in the region highlighted in red. The junction between two domains can be clearly seen in the middle part of the image (indicated by an arrow). Two domains have grown until they have reached each other. A phase shift in the stripes of the polarized fluorescence light can be clearly seen at the junction of the two domains, revealing two distinct directions of the channel system. The analysis method of such polarization-modulated fluorescence images is explained in detail in Section 2.1.3.4. Fits of the fluorescence patterns were computed at arbitrary and equally distributed positions in the domains. The orientation of the molecules and thus of the pores at these positions are overlayed to the fluorescence image as yellow bars in Figure 3.16b. The angle between the pore directions at the junction of these two distinct domains is about 50° . A very interesting observation is that the channels are not perfectly parallel over a lengthscale of tens of micrometers inside a domain, but can have a certain curvature. This can be observed for each of the three domains shown in 3.16b. The pores are slightly curved like in the domain situated in the left upper part

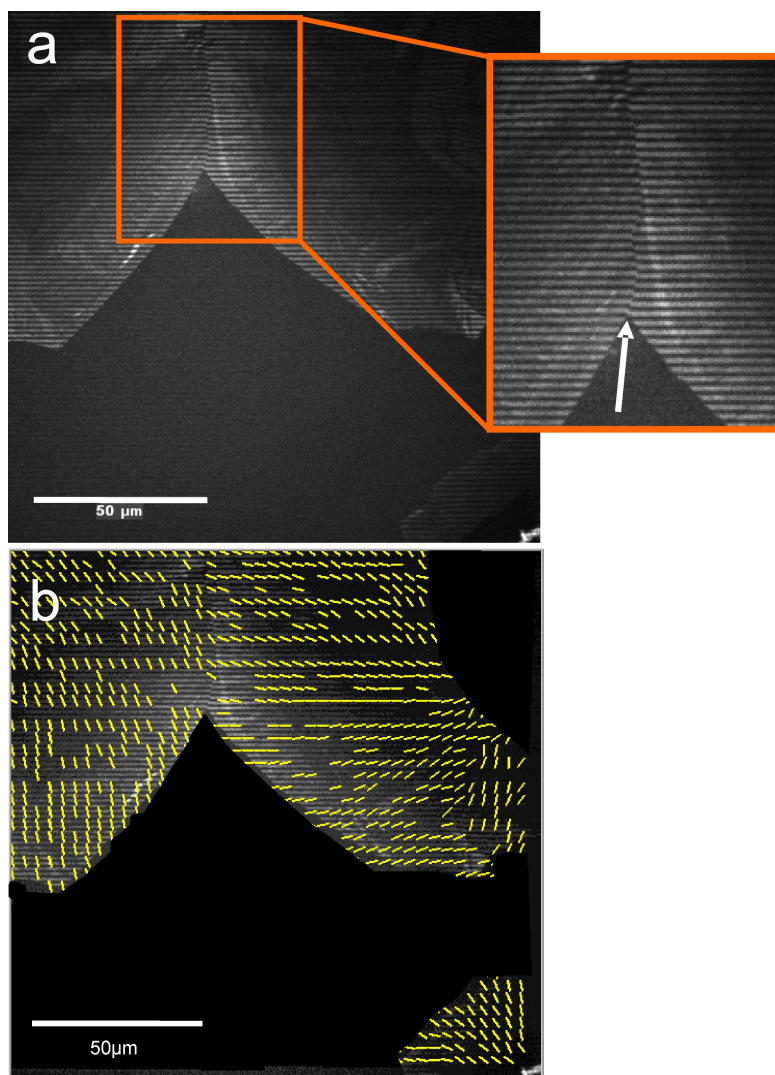


Figure 3.16: Polarization modulated confocal fluorescence images of three highly structured domains. (a) The stripes in the domains indicate that the TDI molecules are oriented in the same direction in each of the domains. The inset shows a zoom into the region marked with the red rectangle. A phase shift at the boundary of the two domains shows clearly that the orientation of the fluorophores in each domain is different. (b) The same fluorescence image with orientations of the dipole moment of the TDI molecules overlaid as yellow bars at different arbitrary positions (see section 2.1.3.4 for details about the analysis of the data) . The orientations shows that the pores are not perfectly parallel within a domain, but slightly curved over a lengthscale of tens of micrometers.

of the image, or the direction of the channels can show a roughly circular symmetry, growing in all directions as can be seen for the two remaining domains of the image.

3.4.1.3 Influence of the relative humidity

We have seen that these highly structured domains are not present in the samples directly after the synthesis of the films, but are formed on timescale of days after rearrangement of the mesoporous network, which leads to higher ordering of the system with pores oriented over a macroscopic lengthscale. The formation and the growth of these domains is a very slow process and is strongly dependent of the RH in the atmosphere surrounding the sample during its storage. The influence of the RH was investigated by recording at different time points confocal images of six samples synthesized at the same time point, and under the same experimental conditions. The samples were stored directly after synthesis at different RH: 0%, 30%, 40%, 50%, 60% and 80%.

Figure 3.17 shows patchworks of confocal images for these six samples after 15 days of storage. The first sample (0% RH) was placed in a desiccator in presence of silicagel to ensure the absence of water in the atmosphere surrounding the sample. Only fluorescence background is visible for this sample (Figure 3.17a). In contrast, the fluorescence images of the sample stored at 30% RH (Figure 3.17b) show the presence of many small domains (about $1 \mu\text{m}$ in size). Oriented domains can also be observed for the two samples at 40% RH and 50% RH (Figure 3.17c and d respectively). However, they are much larger in size (up to $100 \mu\text{m}$) than for the sample stored at 30% RH.

Surprisingly, no domains can be observed for the two last samples stored at 60% RH and 80% RH. Instead, small crystal-like particles are visible (Figure 3.17e and f). However, their shape is very irregular and their fluorescence signal shows no modulation under rotation of the polarization of the laser beam. It is known that CTAB-templated films degrade in presence of water. The presence of the small particles indicates that the mesoporous films are unstable above a RH of 60%. To confirm the destructive effect of high RH on the samples, Atomic Force Microscopy (AFM) measurements were performed of the surface of the mesoporous films. A region of $40 \mu\text{m} \times 40 \mu\text{m}$ of the surface of a film stored during 15 days at 40% RH after synthesis was imaged (Figure 3.18a).

An immediate observation is that the surface of the film is not uniform as would be expected from the last layer of pores on the top of the film. In fact, many holes (identified in the AFM image by dark signals) can be seen at the surface of the sample. Figure 3.18b shows a cross-section along the red line displayed in the AFM image. The graph exhibits steps of 3 - 4 nm in height. This value corresponds roughly to the layer-to-layer distance that was calculated from the XRD patterns (Figure 3.20c). It can be concluded that the layers at the top of the film are not perfect. Hence, in this image at least the two first different layers of pores can be distinguished.

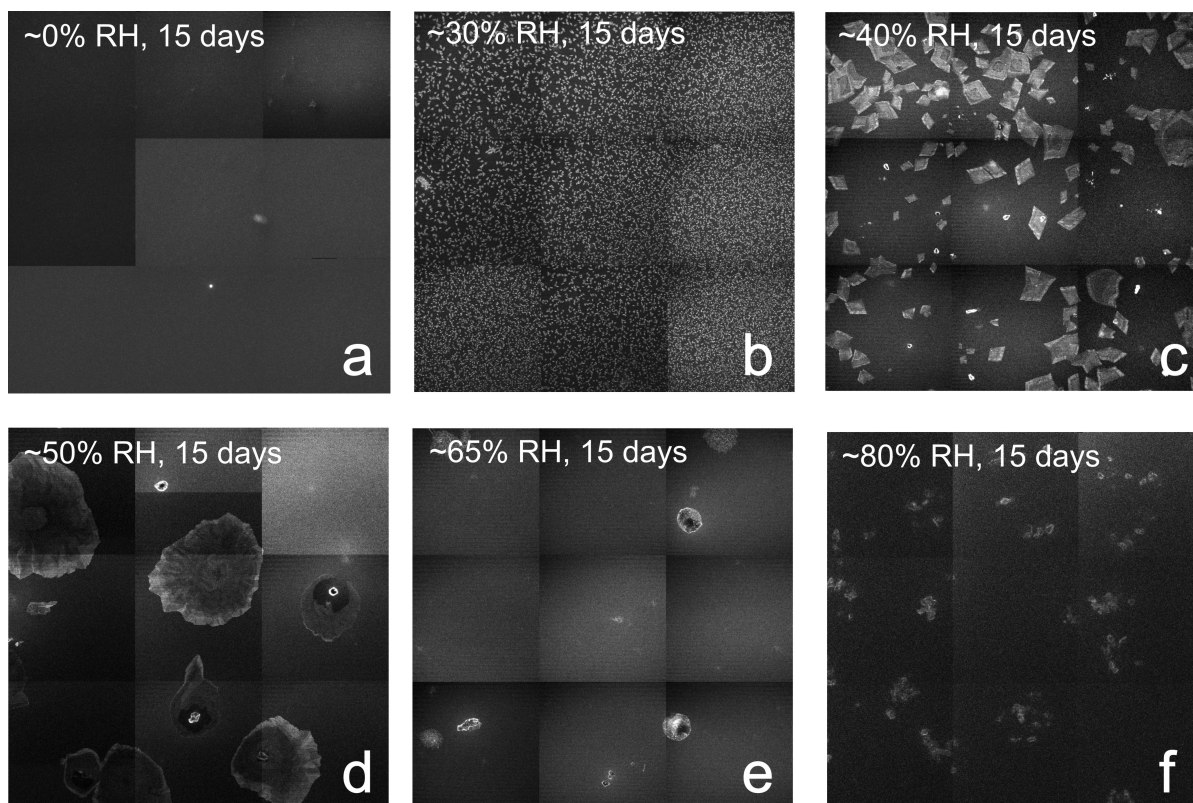


Figure 3.17: Influence of the relative humidity (RH) on the growth of the domains. Patchwork of nine confocal fluorescence images of a mesoporous film loaded with TDI at ensemble concentration observed directly after 15 days of storage at a constant RH of about (a) 0%, (b) 30%, (c) 40%, (d) 50%, (e) 65%, and (f) 80%. The optimal range for the growth of large, highly structured domains is 40 - 50%. At very high RH the films degrade.

Figure 3.18c shows an AFM image of the same sample after 1 h of storage at 80% RH. This image is dramatically different from the previous one. The cross section displayed in Figure 3.18d shows that some plateaus separated by about 4 nm are still visible. However, their surface is much rougher than in Figure 3.18b, and shows some granularity. This demonstrates that water has an invasive action on the CTAB-templated mesoporous films. Considering that the sample was stored only one hour at 80% RH, it is very probable that the two samples stored at 60% and 80% RH described previously were degraded by water.

To conclude, it has been shown that the RH of the atmosphere in which the mesoporous films are placed during storage plays a critical role in the formation of the highly structured domains. No domains were formed if water was suppressed from the surrounding atmosphere, and the optimal range for the growth of large domain is around 40% - 50% RH. Below this value, the domains do not appear or are relatively small (in the order of micrometer). Above this value the mesoporous film degrades under the presence of excessive water.

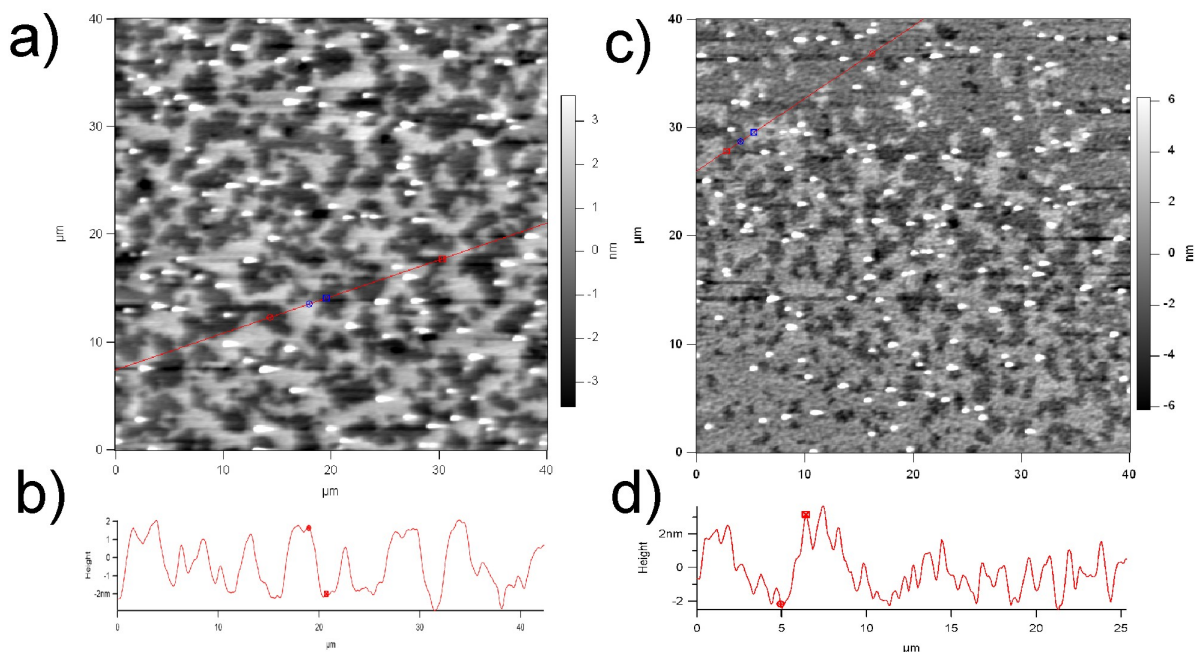


Figure 3.18: AFM images of the surface of a film before and after storage at high RH. (a) AFM image directly after spin-coating of a film. (b) Cross-section along the red line shown in (a). Plateaus can be observed separated by about 3 - 4 nm, corresponding the 2 - 3 last layers of pores. (c) The same sample after 1 h of storage at 80 % RH. (d) Cross-section along the red line shown in (c). The plateaus are nearly not visible anymore, indicating degradation of the film.

3.4.1.4 Time-dependent measurements of the growth of the structured domains

The phenomenon of formation of highly structured domains days after the synthesis of the mesoporous films opens new questions: what is the starting point of the growth of the domains? What are the kinetics involved? Is the reaction of formation of these domains over after a certain period of time, or can the domains grow as long as the experimental conditions are maintained constant?

To address these questions the same area of a TDI-loaded mesoporous film was imaged by confocal microscopy during a period of 15 days after the synthesis. The sample was kept at a constant RH of about 45% during the observation time, and times series of fluorescence images were recorded. The time interval between two frames is 45 min, and the polarization of the laser was kept linear here. Figure 3.19a shows a fluorescence image of the mesoporous film recorded 5 days after spin-coating. The formation of the structured domains has still not started at this point in time, which is the starting point of the measurements (time 0). The fluorescent images of this area taken during the next 21 hours (data not shown) are identical to Figure 3.19a i.e. no highly structured domains are observed. However, after 21 h of observation time, a first fluorescent spot appears

(Figure 3.19b), indicating the abrupt starting point of the formation of structured domains. Figure 3.19c shows the image of the same region at $t = 22.5$ h. One can observe that the domain corresponding to the fluorescent spot of Figures 3.19b has dramatically grown, and that two additional domains appeared. It is very interesting here to note that the formation of each of the three domains start almost exactly at the same time (within 1 h 30 min).

The growth of these domains can be followed in the next frames. Figures 3.19d and e show the same domains at $t = 24$ h and 54 h, respectively. An immediate observation is that the size of domains clearly increases with time. This growth can be quantified by plotting the area of a domain as a function of time. The area of the domains was measured using a threshold for the fluorescence intensity in the confocal images. Figure 3.19e shows such a threshold image corresponding to $t = 24$ h. The domains appear here as white pixels whereas the background is black. The area of the domain to the left is plotted versus time in Figure 3.19f. As mentioned above, the domain does not exist in the first 21 h of measurement time. It appears at $t = 21$ h, and its total area increases until it reaches a maximum at about $t = 40$ h. After this time the silica matrix has probably lost much of its flexibility, so that the rearrangement of the structure is not possible any longer.

The fact that the domains appear suddenly more than 5 days after synthesis of the mesoporous film is surprising, and suggests that a factor external to the system (for example a nimble movement of the setup) initiated their formation. This phenomenon is an aging process which is equivalent to crystal growth where the apparition of micro-crystals initiates the whole process of crystalline growth. Six other samples investigated under the same experimental conditions showed a similar behavior i.e. sudden appearance of highly structured domains some days after the synthesis. However, the time lag before apparition of the domains can vary between 3 and 9 days depending on the sample.

The need for a certain time lag before formation of the domains may indicate that the silica matrix has to achieve enough condensation before reorganizing into a more stable structure. In a too early stage after synthesis, the system is probably still too flexible, and would probably not gain in stability by rearranging its pore structure. On a longer timescale (tens of days up to months), however, nearly no modification of the domain areas is observed (data not shown). An explanation is that the silica structure is fully condensed after such a long time, so that the whole system becomes too rigid to allow reorganization of its matrix. Hence, the phenomenon of formation of highly structured domains seems to be very sensitive to the condensation process of the silica: there is an optimal degree of the silica condensation where the mesoporous film gains in stability by reorganizing its structure.

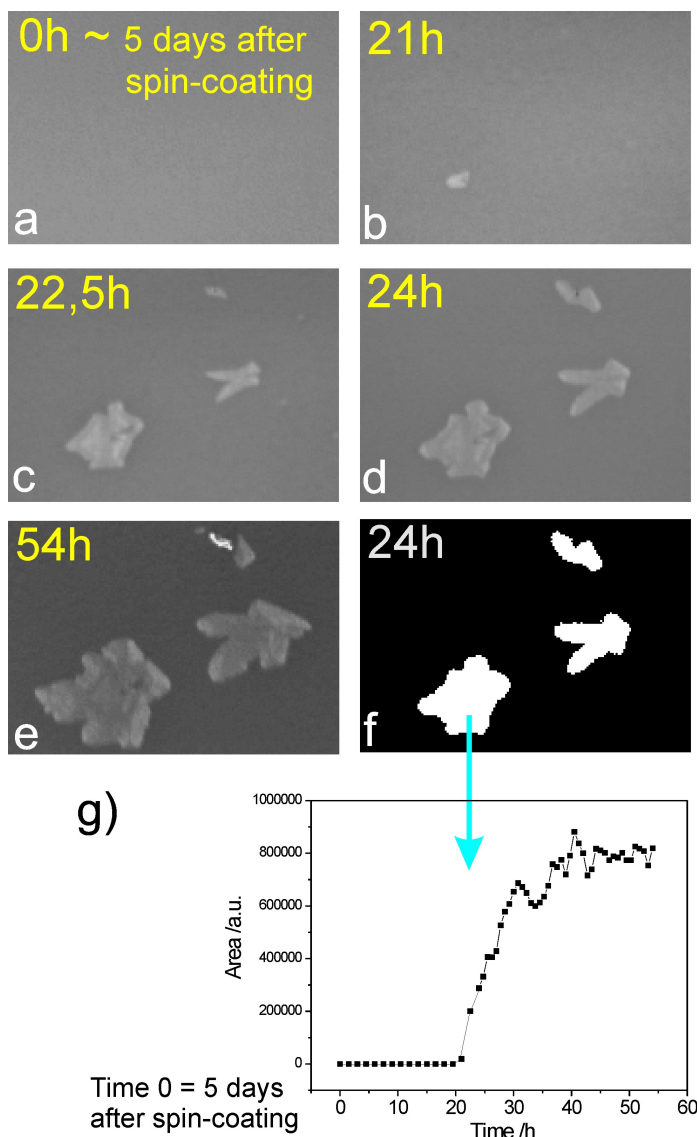


Figure 3.19: Real time measurements of the growth of highly structured domains in a CTAB-templated mesoporous film loaded with TDI at ensemble concentration. (a) Confocal fluorescence image of the film 5 days after spin-coating which is the time zero for these measurements. Only a fluorescence background is detected. (b) The same region of the mesoporous film observed after 21 h. A first domain appears. (c) After 22.5 h. Two other domains are visible. (d) and (e) The same domains after 24 h and 54 h respectively. (f) Threshold image of the image shown in (d) used for the analysis of the area of the domains. (g) Plot of the total area of the domain to the left versus time. The formation of the domains starts suddenly after 21 h of observation time, and a maximum of the area of the domains is reached about 20 h later.

3.4.1.5 Conclusion

It has been shown that the mesoporous structure of CTAB-templated thin films can rearrange on a timescale of days after synthesis into large, highly structured domains of

extremely linear channels. The formation and the growth of these domains is strongly dependent on the RH, with an optimal range of 40 - 50% of RH for the formation of large domains (up to 100 μm in size). The growth starts suddenly after a storage period of 3 - 9 days, and the area of the domains reaches their maximum several hours later.

Further investigations with complementary methods such as X-ray scattering or TEM are currently in progress in order to characterize and to understand the phenomenon of the formation and growth of these highly structured domains in depth.

3.4.2 Translational and orientational dynamics of single TDI molecules diffusing in the highly structured domains

Section 3.2 showed how single molecules can be used as nanoscale probes to map out the structure of different topologies of Brij-56-templated mesoporous thin films. Furthermore, the simultaneous observation of the orientational and spectral dynamics of the dye molecules within a mesoporous network with CTAB as template provided direct information about the influence of the local environment on the guest molecule.

This section presents the detailed analysis of the diffusional and orientational behavior of single TDI dye molecules diffusing in the CTAB-filled linear pores (2 - 3 nm in diameter) of the highly structured domains described above. As already mentioned, the films contain linear channels which are highly ordered in domains of up to 100 μm in size. To date such a high degree of order over long distances has not been reported before, and can be easily mapped out with single molecule techniques.

The diffusion of the guest molecules can be switched on and off by the surrounding atmosphere of the host-guest system. Whereas the TDI molecules are nearly immobile in air atmosphere, they start moving as soon as chloroform vapor is added to the system. The channels dictate the direction of the diffusion as well as the orientation of the single TDI molecules, i.e. while diffusing along the porous system the molecules keep a constant orientation along the channels. The trajectories were measured with such a high spatial accuracy that the diffusion in individual channels can be resolved. The trajectories reveal the presence of defects within the mesoporous film such as dead ends or small connections between the channels. Moreover, the diffusion of the single TDI molecules is not a normal 1D random walk due to the presence of heterogeneities.

Terrylenediimide (TDI) dye molecules were incorporated into the pores of a M41S mesoporous thin film templated with CTAB at very low concentration (10^{-10} mol/L) to ensure that the molecules can be observed individually. Figure 3.20a shows the structures of TDI and the template molecule cetyltrimethylammoniumbromide (CTAB). The transition dipole moment of the TDI molecule is aligned on its long axis. Figure 3.20b shows a scheme of the templated M41S hexagonal system.

Transmission electron micrograph (TEM) images of the mesoporous M41S film with TDI molecules incorporated into the pores show highly ordered linear mesopores over a complete observable area of about $1.5 \mu\text{m} \times 1.5 \mu\text{m}$. An exemplary magnified region of about $100 \text{ nm} \times 100 \text{ nm}$ is shown in Figure 3.20b. A typical X-ray diffractogram is displayed as an inset. The peak, in combination with the TEM image, manifests the presence of a hexagonal mesophase. From the position of the peak ($2\theta = 2.4^\circ$) it is

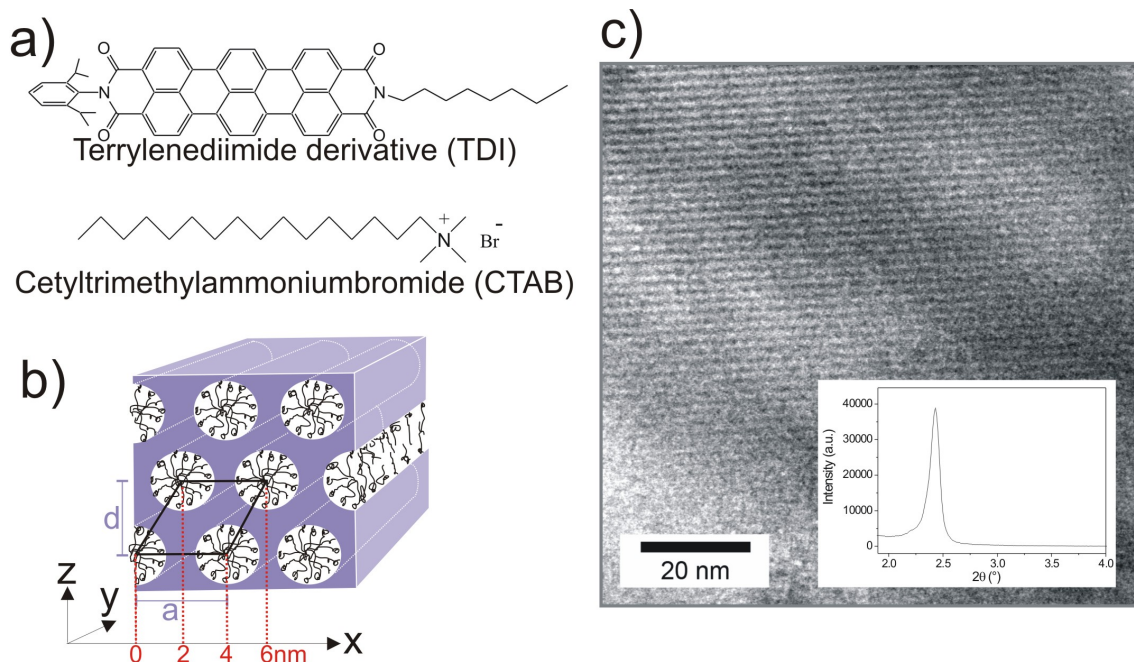


Figure 3.20: Sample system. (a) Fluorescent terylenediimide derivative (TDI) and structure-directing agent cetyltrimethylammoniumbromide (CTAB). The direction of the transition dipole moment of TDI is aligned on the long axis of the molecule. (b) Schematic diagram of the hexagonal mesoporous system with the arrangement of the CTAB template inside the pores. The pore-to-pore distance $a = 4.2 \pm 0.2$ nm and the layer-to-layer distance $d = 3.7 \pm 0.2$ nm are shown as well as the distances to the neighboring pores for a two dimensional projection on the x, y plane. (c) TEM image of the mesoporous film showing a region of parallel pores. The inset displays the small-angle X-ray pattern which exhibits a strong peak corresponding to the hexagonal phase.

possible to calculate the average pore-to-pore distance $a = 4.2 \pm 0.2$ nm and a layer-to-layer distance of $d = 3.7 \pm 0.2$ nm (both indicated in Figure 3.20b). Typical wall thicknesses in these systems amount to about 1 - 2 nm, thus the pore diameter is about 2 - 3 nm. Note here that these values slightly vary with time due to the shrinking of the mesoporous film as a result of the silica condensation. Hence, all the measurements including X-ray diffractometry were performed at the same time point (15 days after synthesis). Altogether, these data show that the mesoporous films obtained are very well structured in a hexagonal phase with pores parallel over a range up to $1.5 \mu\text{m}$. However, from these data it is not possible to obtain information about the structure on a longer lengthscale, or on the dynamics of guest molecules inside the porous network. Single molecule methods were used to overcome these limitations.

Polarization modulated confocal microscopy was performed to monitor simultaneously the diffusional and orientational behavior of the TDI molecules. The movement of a single TDI dye molecule in the pores of a highly structured domain is shown in Figure 3.21. Figure 3.21a shows three confocal images where single, mobile TDI dye molecules ap-

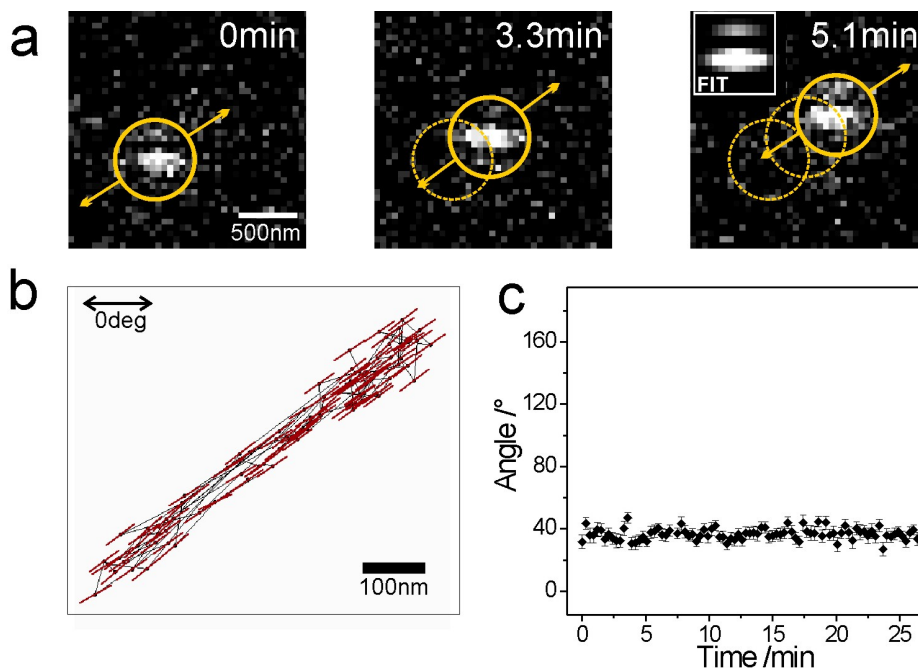


Figure 3.21: Diffusion of a single TDI molecule in a M41S film. (a) Sequence of fluorescence images. The fluorescence signal of the single molecules shows a striped pattern along the scan line due to the rotation of the excitation polarization. The inset at $t = 5.1$ min shows a fit according to the analysis procedure (see experimental section). (b) Extracted trajectory for this molecule. The two dimensional orientation of the dipole moment is indicated by red lines. (c) Extracted angular time trajectory of the molecule. The error bars show the standard deviation of the fit.

pear with a characteristic fluorescence-intensity profile (stripped patterns) due to the polarization modulation during the scan. From these patterns both the position of the molecule, and the orientation of its transition dipole moment (shown as yellow bars) are computed (see Section 2.1.3.4). Figure 3.21b displays the trajectory of a single TDI molecule extracted from a movie of 89 frames (~ 27 minutes) together with the angle of the molecule's transition dipole moment. The molecule is found to move back and forth and the movement is extremely linear, with the overall distance covering $\sim 1 \mu\text{m}$ and the width transverse to the main movement direction limited mainly by position accuracy to about 80 nm. Furthermore, the orientation of the molecule is aligned with its trajectory. The stability of the molecule's orientation is expressed in the angular trajectory (angle *versus* time) displayed in Figure 3.21c. The orientation angle fluctuates only slightly ($\pm 7^\circ$) around a mean value of 39° , and coincides with the tilt angle of the entire trajectory in Figure 3.21b. This behavior reflects the structural features of the underlying material i.e. unidimensional, straight, cylindrical pores. Our spatial resolution does not allow us to unambiguously identify whether the molecules move always within a single channel. It may sometimes switch to neighboring channels of identical orientations, due

to rare defects in the channel walls. However, clearly the structure of the pores directs the molecule's trajectory as well as its orientation.

This behavior is observed frequently across large areas of the film, which form particularly well-ordered domains. A typical example of such an area is shown in Figure 3.22. The domain in which the molecules undergo linear movement with constant dipole orientation (such as the example shown in Figure 3.21) is extremely large with dimensions of about $20\mu\text{m} \times 20\mu\text{m}$ (in this case). Similar domains with sizes of more than $100\mu\text{m}$ can be observed. In the area shown in Figure 3.22, 90% of the molecules share the orientation ($\pm 10^\circ$) dictated by the underlying pore structure. Among these molecules more than 70% move in the direction of the pores during the observation time ($\sim 4\text{ h } 20\text{ min}$). In summary, such domains provide a highly ordered matrix which controls the traffic of the incorporated molecules.

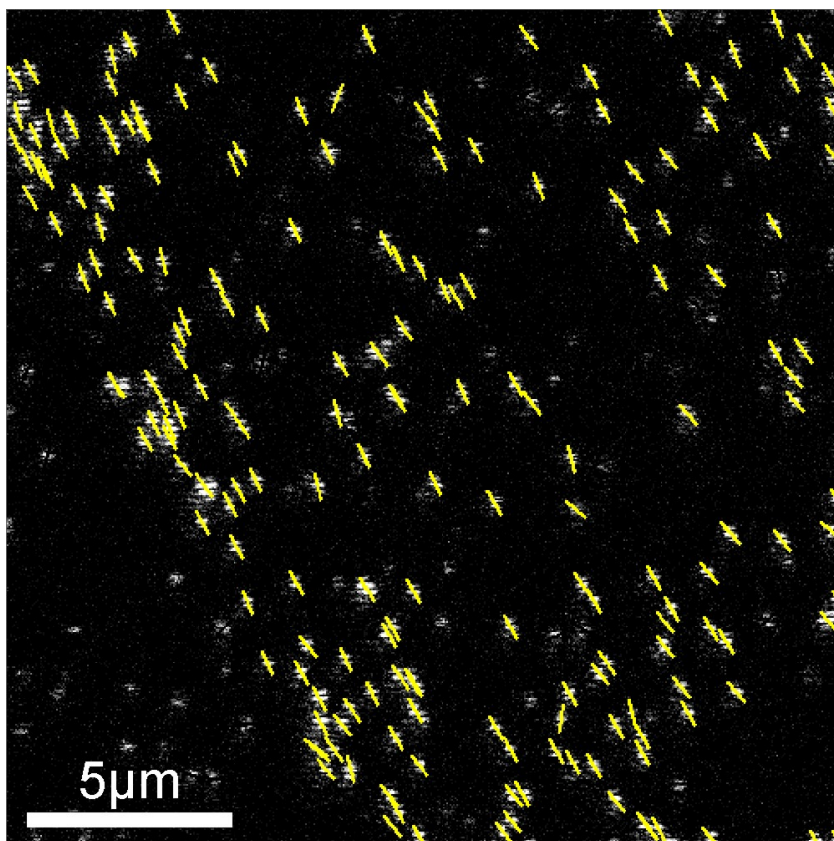


Figure 3.22: Single molecules embedded in mesoporous films highlight the existence of domains. The image shows the fluorescence signal of a single-frame taken from a movie. The orientations of the dipole moment of the molecules as determined by the data analysis are depicted by yellow bars which are overlaid over the fluorescence signal. For clarity only orientations that remained stable (with s.d. $< 10^\circ$) over the observation time (247 frames, 4 20 min) are depicted.

However, external parameters such as the RH of the atmosphere surrounding the film influences strongly the diffusional behavior of the TDI molecules, as will be explained

bellow. During the measurements of the data presented in Figure 3.22 the RH was fixed to 60% and the guest molecules exhibit a certain mobility. Figure 3.23a shows a polarization modulated fluorescence image of oriented single TDI molecules encapsulated in another domain, and measured at a RH of about 40 %.

A time-sequence of consecutive images was recorded for the region shown in Figure 2a with 30 s per frame over a total time of about 90 min. The movie shows that all the 95 observed molecules remain immobile with the same parallel orientation. None of the other ten areas investigated exhibited diffusion of the fluorophores under these conditions. For all these measurements the sample was placed in air atmosphere at 40% relative humidity (R.H.). It is known that the R.H. influences the diffusion behavior of guest molecules inside the pores.¹⁴⁵ As shown above at higher R.H. the molecules can diffuse very slowly in air atmosphere. However, at very high RH (above 70%), the CTAB-templated films are unstable and degrade within a few hours.

Therefore, different conditions which would give high mobility without destroying the films during the observation time were looked for. Indeed, in saturated chloroform atmosphere the films could be studied for several hours and the molecules were highly mobile. The three fluorescence images in Figure 3.23b are taken from a movie (223 frames, 30 s per frame) after an observation time of 0, 2, and 4 min respectively. The trajectory of the single TDI molecule marked with a circle in the images is displayed in the Figure 3.23c, together with an indicator bar for its orientation. In contrast to the above measurements in air atmosphere, diffusion of the dye molecules is observed. Moreover, as soon as chloroform is exchanged with air no more movement of the dye molecules is observed (data not shown here). This demonstrates that the diffusion of the TDI guest molecules in the porous film can be switched ON and OFF reversibly by changing the surrounding atmosphere.

The animation of this trajectory shows that the molecule is moving linearly back and forth over a distance of about 2 μm , but remains remarkably aligned with the direction of the diffusion which is assigned to the direction of the pores. Figure 3.23d shows the time evolution of the angle of the transition dipole moment of this molecule. The angle is constant, fluctuating slightly around a mean value of $2^\circ \pm 3^\circ$. This remarkable alignment of the fluorophores with the pores results from the tight fit of the TDI molecules (approx. 1.1 nm in diameter and 2.5 nm in length) within the nanometer sized channels (2 - 3 nm in diameter), preventing the TDI molecules from free rotation. Let us recall that the pores are still filled with the template used during the synthesis and thus the hydrophobic dye searches the inner part of the templated filled pores. This reduces even more the effective volume which is available for the TDI molecule. In summary, the orientation of the single TDI molecules and their trajectories map directly the direction of the channels

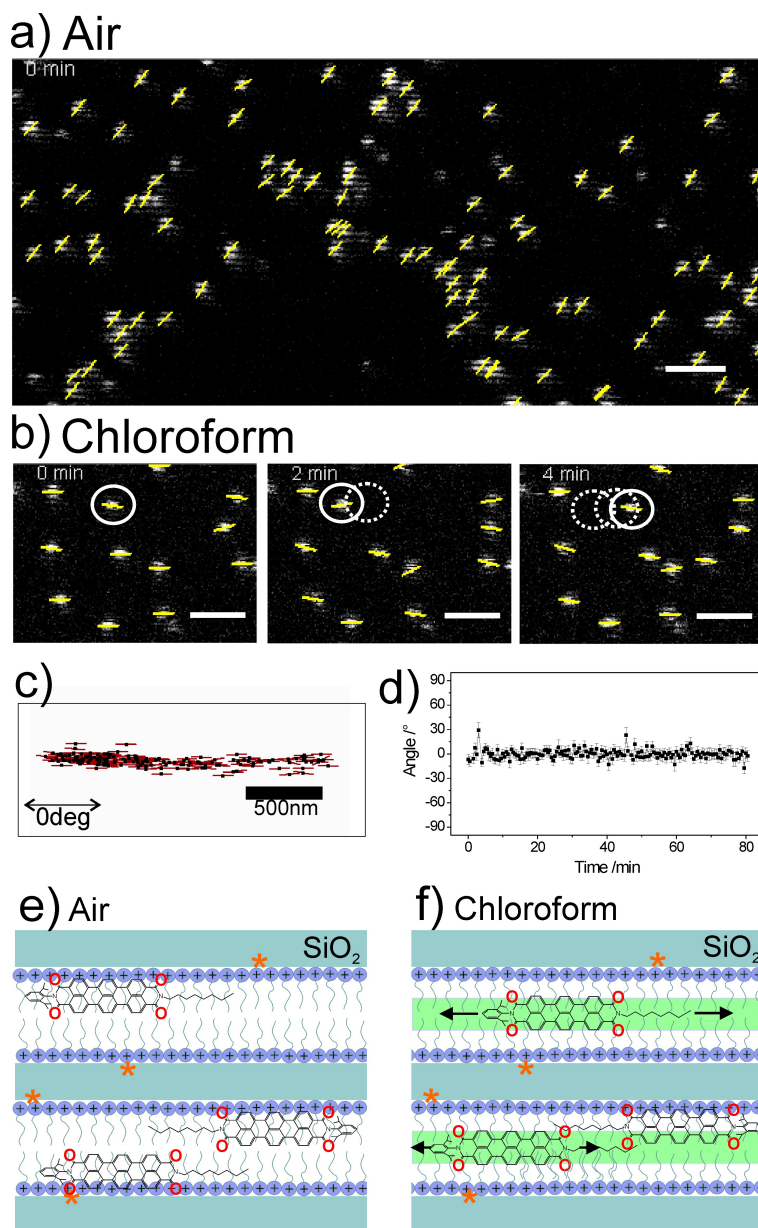


Figure 3.23: Parallel orientation and diffusion of single TDI molecules in highly structured domains. (a) Single TDI molecules embedded in parallel pores in air atmosphere. The fluorescent image shows oriented single TDI molecules (stripped patterns) and is extracted from a time-series. All visible molecules are immobile during the observation time (90 min). The determined orientation of the transition dipole moment of the molecules are depicted by yellow bars overlaid on top of the fluorescence signal. Scale bar: 2 μm . (b) Sequence of fluorescence images showing linear diffusion of single TDI molecules in chloroform atmosphere extracted from a time-series. Scale bar: 2 μm . (c) Trajectory extracted from the molecule marked with a white circle in (b). (d) The calculated angular time trajectory of the same molecule. (e) Schematic of TDI molecules immobilized in the mesoporous material in air atmosphere. The stars indicate the presence of active silanol groups. (f) TDI molecules in the mesoporous material in the presence of chloroform. The TDI molecules are solvated (green stripes) and diffuse along the channels, and their walk is occasionally interrupted by adsorption events.

and the domains of parallel channels.

These data show clearly that: i) The TDI molecules are immobile in air atmosphere whereas they are free to diffuse in chloroform atmosphere. ii) The diffusion is linear along the pores. iii) The transition dipole moment does not change its orientation along the trajectories. In other words the chloroform can be used to switch on reversibly the motion of the molecules on highly structured trajectories i.e. linear motion with constant orientation of the transition dipole moment. The immobility of the TDI molecules in air atmosphere is most likely caused by the interactions between TDI and template molecules. The dye molecule has four oxygen atoms pointing to the side (Figure 3.23e) whose lone pair electrons can interact with the positively charged heads of the CTAB molecules. In addition interactions are also possible with active silanol groups or other defects in the walls of the channels.^{?,146,147} In contrast, when chloroform, a good solvent for TDI, is added to the system it is likely that the small solvent molecules form a lubricant-like phase inside the pores (Fig. 2f). As a result, the TDI molecules can be solvated and diffuse along the pores. Hence, the solvent exchange allows for an easy control of the diffusional behavior of the guest molecules.

Knowing that the orientation of the molecules doesn't change during their movement through the linear pores, an alternative experimental technique can be used, namely wide-field microscopy which is advantageous since much higher temporal resolution and positioning accuracy can be achieved. Series of 1000 images were acquired with a temporal resolution of 1 s per frame. Figure 3.24a is the overlay of an entire image series from TDI molecules embedded in a highly structured domain of the M41S mesoporous film, and placed in air atmosphere at 40% R.H. The single TDI dye molecules appear here as diffraction limited spots. Their positions were obtained by fitting 2D-Gaussian to the intensity profiles and the resulting trajectories are plotted in red in Figure 3.24a, as an overlay to the sum of the 1000 fluorescence images. All molecules are immobile within the experimental accuracy. This is consistent with the results obtained with the confocal setup in air atmosphere. Figure 3.24a (left inset) shows an exemplary trajectory of a TDI molecule which is found to remain immobile during the complete observation time of the movie (about 16 min). The right inset shows the histogram of a cross-section along the y-axis. This distribution can be fitted with a Gaussian function with the standard deviation $\sigma = 5$ nm.

Figure 3.24b shows trajectories of molecules measured in chloroform atmosphere. As expected, the molecules diffuse along a particular direction dictated by the orientation of the pores on an overall distance of 500 - 1000 nm. In order to analyze such a uni-dimensional trajectory it is useful to project its coordinates onto the long axis x of the trajectory and its perpendicular axis y, and to analyze the new x and y coordinates

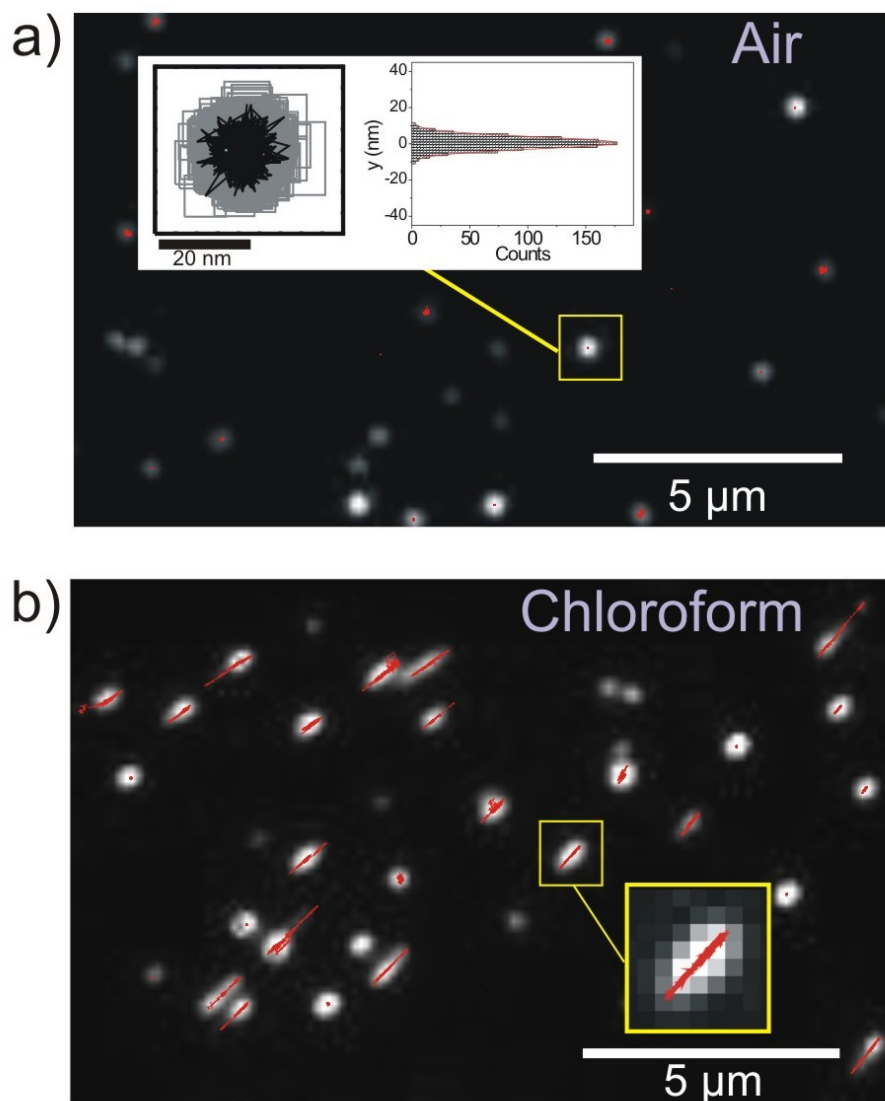


Figure 3.24: Switching of the diffusion in air and chloroform atmosphere. (a) Overlay of 1000 widefield fluorescence images acquired with 1 s per frame showing individual TDI molecules embedded in the mesoporous film and immobile in air atmosphere. The single molecule trajectories are overlaid in red in the fluorescence images. The left panel of the inset displays the trace of a single, immobile TDI molecule as indicated by the yellow square. The right panel shows the histogram of the y cross-section of the trace. The standard deviation of the distribution is $\sigma = 5$ nm. (b) Overlay of 1000 fluorescent images acquired with 1 s per frame together with single molecule trajectories (red) revealing the linear motion of TDI molecules. The linear traces map out the porous landscape of the highly structured domain. The inset is a zoom into such a trace.

separately. Figure 3.25a (left panel) shows an example of a linear trajectory taken from Figure 3.24b, and Figure 3.25b shows the time evolution of the $x(t)$ and $y(t)$ components. The $x(t)$ curve shows pronounced diffusion over a range of about 600 nm. Interestingly, this molecule seems to bounce back several times at the positions $x = 0$ and $x = 600$ nm and remains confined between these two extremities. This phenomenon can be attributed

to “dead ends” within the porous system due to defects closing the pores at specific locations. In contrast, there are very little dynamics in the direction perpendicular to the trajectory. The histogram of the $y(t)$ values shown in Figure 3.25b can be fitted by a Gaussian function. Although the amplitude of the fluorescence signal obtained by the fit is about 20% higher than for the immobile molecule mentioned above indicating an even higher positioning accuracy, the standard deviation $\sigma = 7$ nm not is slightly higher (compared with $\sigma = 5$ nm for the immobile molecule). This suggests that the diffusion of this TDI molecule does not occur in a single channel, but in a few parallel ones. Thus, connectivity between the channels has to be assumed, which can be explained by the presence of small defects within the silica walls of the pores through which the dye molecule occasionally escapes to a neighboring channel. Let us note here that the whole section of the mesoporous film (~ 120 nm of thickness as measured by ellipsometry) is in the focus of the laser spot (>1 μm in size along the optical axis). Thus, all jumps between neighboring channels in the xy plane as well as in the z direction can occur and should show abrupt jumps of about 2, 4 or 6 nm (see the projections of the pore centers onto the x axis in Figure 3.20c. However, as these values are in the same order or smaller than the positioning accuracy, it is not possible to determine the exact number of pores in which the molecule moves.

To understand better the observed dynamics of the TDI molecules and particularly the pore geometry simulations were performed by Michael Bude and Irmgard Frank in our group using a 3D random walk model of a particle diffusing in parallel channels (for details see experimental section). The model of the geometry of the pores in which the molecule can diffuse was adapted in order to match the shape of the experimental trajectory, and is displayed to its right in Figure 3.25a. Moreover, a certain permeability of the pore walls due to the presence of defects in the silica walls was taken into account i.e. each time the particle hits a pore wall in the simulation there is a probability for it to jump to the next pore. Two simulated trajectories are displayed to the right in Figure 3.25a with a permeability of 10% and 0.1%, respectively. Such a constant permeability represents the simplest approximation and does not take into account heterogeneities neither within the silica structure nor in the template. At first sight both the simulated trajectories resemble the data. However, a closer comparison between simulation and experiment can be drawn by looking at the x and y time trajectories displayed in Figure 3.25d and e for the simulations with 10% and 0.1% of permeability respectively. The $x(t)$ graphs of the two simulated curves show similar confined diffusion with 1D back and forth movement of the particle. This is different for the $y(t)$ graph. Whereas the $y(t)$ graph of the simulation with high permeability (10%) shows fluctuations around a mean value, the $y(t)$ graph with lower permeability (0.1%) exhibits a stronger tendency to plateaus, which is in better accordance with the experimental data. Therefore it can be concluded that

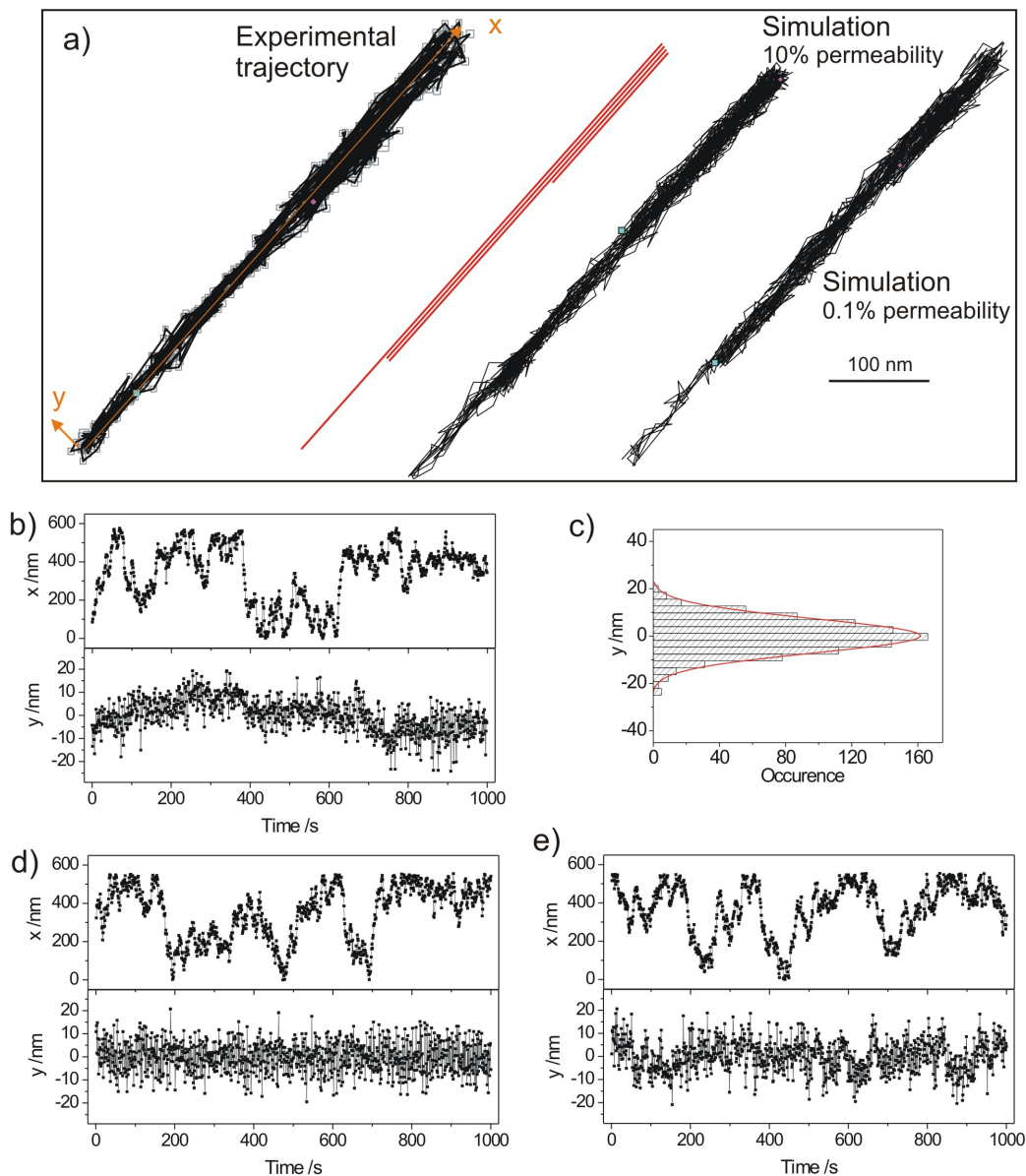


Figure 3.25: Diffusion analysis of an individual trajectory. (a) From the left to the right: experimental trajectory, model of the geometry of the pores, and simulated trajectories with 10% and 0.1% permeability between neighboring pores respectively. (b) Projected coordinates onto the long axis of the experimental trajectory (x , upper panel), and onto the transversal axis (y , lower panel) *versus* time. (c) Histogram of the y transversal coordinates together with a Gaussian fit. The standard deviation is $\sigma = 7$ nm. (d) and (e) Projected x and y coordinates for the simulated trajectories with 10% and 0.1% permeability respectively.

the lower permeability is the more realistic description of the observed diffusion. These results suggest that it is possible to simulate the experimental trajectory on the basis of a simple model, and that the defect density along the pores has to be relatively low to lead to rare transitions between pores. Note, however, that the experimental trajectories

are not detailed enough to discriminate clearly between a constant permeability along the full length of the pores, and jumps at discrete defect sites.

In order to observe more accurately jumps between neighboring pores measurements were performed using a three fold higher laser power (0.50 kW cm^{-2} at the entrance of the objective). The obtained trajectories are shorter in time due to faster photobleaching, but higher temporal resolutions (500 ms/frame) as well as higher spatial resolutions ($\sigma = 2 - 3 \text{ nm}$ for the brightest molecule) could be achieved. Figure 3.26a shows the $x(t)$ and $y(t)$ graphs obtained from the tracking of a single TDI molecule diffusing in only a few neighboring channels (trajectory shown in Figure 3.26b, top). By inspection of the $y(t)$ graph this trajectory can be divided into two distinct parts which are the time intervals before and after 103 s. Figure 3.26b (bottom) displays the histograms of $y(t)$ before (green full bars), and after (black dashed bars) 103 s. These distributions are clearly distinct, and can be fitted by two Gaussian curves with a maximum at 0.6 and 6.1 nm, and with $\sigma = 2.9$ and $\sigma = 2.3 \text{ nm}$ respectively. These dynamics are interpreted as a molecule switching between at least two pores separated by 5-6 nm.

The $x(t)$ graph in Figure 3.26a shows a back and forth movement of the molecule which remains clearly confined between $x = 0$ and $x = 40 \text{ nm}$ during the first 150 s of the trajectory. At this time, the molecule finds its way out of this confined region and is able to diffuse further.

The experimental trajectories described above reveal certain connectivity between fairly close channels. In some cases the molecule can even explore much more distant pores. This is illustrated by the trajectory shown in Figure 3.26c. Here the single molecule diffuses in clearly separated parallel channels. The animation of this trajectory shows that the molecule spends the first 340 s in the upper right part of the trajectory where it undergoes strong longitudinal and transversal diffusion. Then, it suddenly finds its way out of this region (within below 1s, the temporal resolution) and moves more rapidly to the lower left part of the trace where it remains during the next 100 s. Finally the fluorophore diffuses up again following another distinct parallel channel until it photobleaches. The histogram displayed below Figure 5c shows the distribution of the $y(t)$ values in the time intervals in which the molecule diffuses in the middle part of the trajectory. Two Gaussian distributions can clearly be distinguished, with their maximum separated by 22 nm. This value corresponds to about 6 channels. The standard deviations of the single peaks are each $\sim 5 \text{ nm}$, which corresponds to the positioning accuracy for this particular molecule. This analysis confirms that the molecule does not diffuse in a single channel but in parallel pores which are interconnected by small defects in the structure.

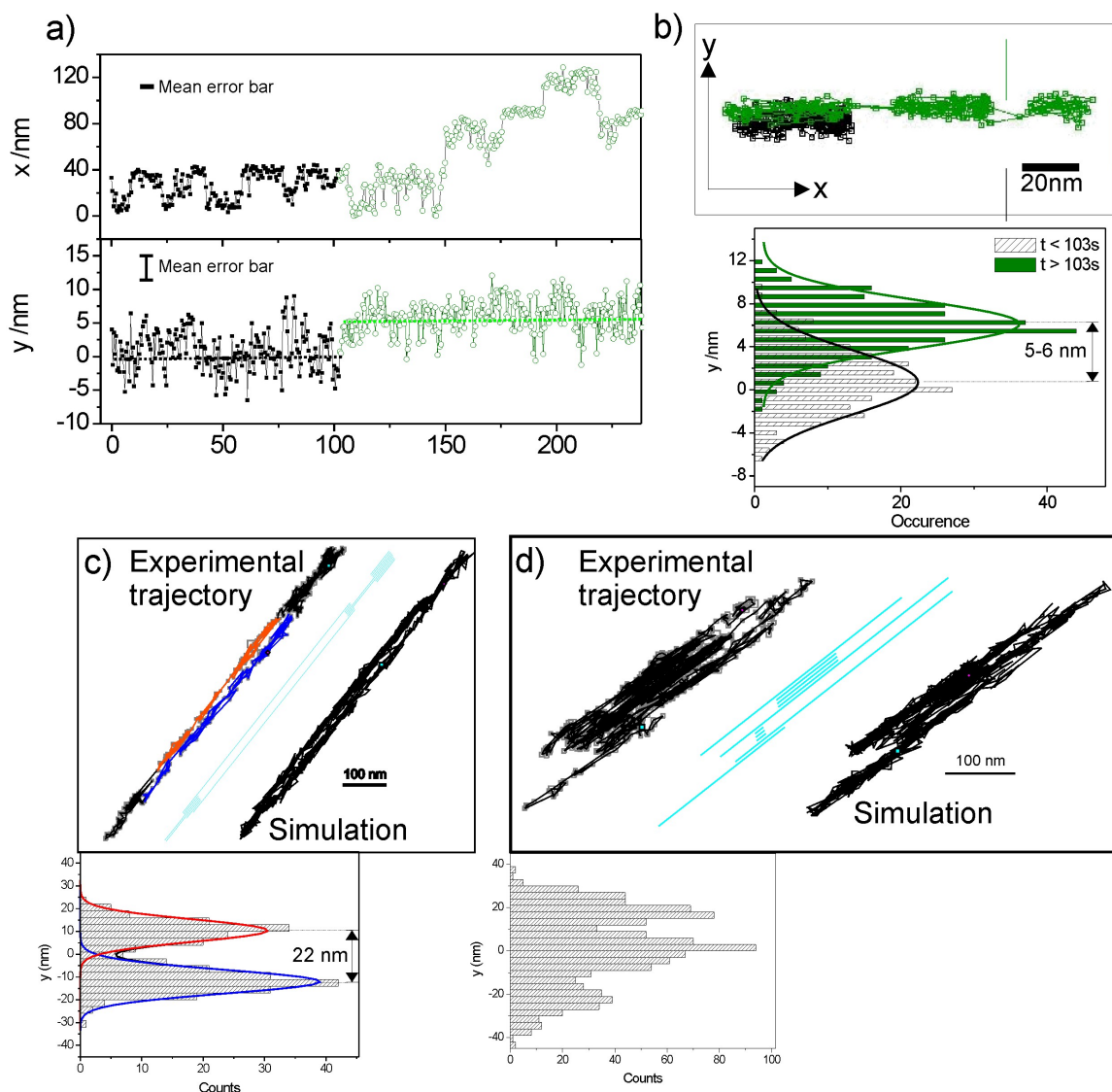


Figure 3.26: Diffusion through defects in the silica pore walls. (a) Projected x and y coordinates for a single TDI molecule diffusing at least in two distinct neighboring pores. While in the first 103 s the molecule diffuses back and forth in one pore (black squares) it then switches to another pore, where it resumes its lateral diffusion (green circles). (b) Trajectory of the molecule (top), and histograms of the y lateral coordinate for the time intervals before (black striped bars) and after (green full bars) the time $t = 103$ s together with their Gaussian fits (bottom). The two maxima are separated by 5 - 6 nm. (c) Trajectory showing the diffusion in parallel pores. From the left to the right: experimental trajectory, the model of the pores used for the simulation, and the simulated trajectory. The lower panel shows the histogram of the lateral y coordinates in the middle part of the trajectory (red and blue points in the experimental trajectory). (d) Diffusion in a region rich in defect sites. The lower panel shows a diagram of the linear diffusion in the long unidimensional channels. Transition between neighboring channels can occur though small defects within the silica structure.

Moreover, it is observed that the density of such nano-defects can vary within the same highly structured domain. Figure 3.26d is an example of a trajectory where a strong

lateral diffusion occurs with overall amplitude of about 70 nm in the lateral direction. The corresponding histogram of the y coordinates (below Figure 3.26d) shows a broad distribution where several peaks can be observed. Here the dye molecule frequently jumps from one pore to another revealing the presence of a region rich in defect sites.

Similarly to the trajectory described in Figure 3.25, the two trajectories discussed above could be simulated. The right parts of Figure 3.26c and d show the channel structures used for the simulations as well as the simulated trajectories. This shows that even in a more complex distribution of defects the simulations can describe well the data.

Up to this point it has been shown that the study of the diffusion of single TDI guest molecules gives structural information about the host material because it allows mapping out the structure of the porous network in great details. Moreover, it reveals the presence of defects like dead ends or small openings within the porous system.

Additional insight can be gained about the interactions between the guest molecule and the host matrix. For instance, by inspecting the $x(t)$ and $y(t)$ time trajectories one can notice the presence of time intervals during which the molecule seems to remain immobile. In Figure 3.25a, for example, both $x(t)$ and $y(t)$ remain constant between $t = 176$ s and $t = 194$ s, suggesting that the molecule is immobilized (within the positioning accuracy). This means that the molecule is occasionally trapped at some sites along its trajectory. This “stop and go” movement is interpreted as the influence of adsorption sites. We have seen in the discussion of Figure 3.23e,f that interactions with the cationic heads of the template molecules or with defect sites are two likely causes for the observed adsorption in air atmosphere, leading to an immobilisation of the TDI molecules. In presence of chloroform these interactions also have an influence on the diffusion of the guest molecules, which can be resolved with the higher time resolution of the wide-field experiments. However, the strength of these interactions is reduced by the lubricant-like behavior of chloroform and therefore the TDI molecules are only occasionally immobile. Such an adsorption could occur if the TDI molecules escape from the shell of chloroform and interact directly with the charged head groups of CTAB. Similar diffusional behavior has been reported previously for other adsorbates diffusing at silica surfaces both at the ensemble as well as at the single molecule level. For example, cationic dioctadecyl-tetramethylindocarbocyanine perchlorate (DiI) dye molecules^{20,148} as well as nucleotides¹⁴⁹ were monitored at a chromatographic interface of chemically modified fused silica. Higgins et al have investigated the diffusion of Nile Red dye molecules in CTAB-templated as well as in calcined mesoporous films.⁷ In this study it was concluded that the lateral transport the molecules is described by fast lateral diffusion interrupted by rare, reversible, adsorption to defect sites. It was postulated that strong adsorption occur at active silanols via hydrogen bonding to the quinonal oxygen of Nile Red. In our

experiments a third physical explanation for the immobilisation of the guest molecule may be the presence of pores with a smaller diameter. Indeed, the X-rays micrograph (Figure 3.20, inset) shows the presence of a peak at $2\theta = 2.4^\circ$, which is relatively broad. One explanation of the broadening of the peak is that the pore diameters are not perfectly uniform, but exhibit a broad distribution. Since the interior diameter of the pores is only slightly larger than the diameter of the TDI molecules a small reduction of the diameter could already have a drastic effect on the diffusion of the molecules, thus leading to an adsorption site.

To investigate quantitatively the diffusion of TDI in the mesoporous film and to evaluate the influence of the adsorption sites on the diffusion in presence of chloroform a statistical analysis has been performed of the linear trajectories of about 80 single TDI molecules. A first intuitive and straightforward model for the diffusion in such linear pores is a 1D random diffusion along the x-axis. The analysis of this diffusion was based on the cumulative probability distributions of the squared displacements. Compared with the standard method of the mean-square displacement (MSD), the use of the cumulative probability distributions greatly increases the information of mobility studies, allowing us to resolve more complex behavior, including the effect of local heterogeneities within the sample. Figure 3.27a shows the probability distribution of the squared displacements where the probability of every step is plotted against the squared step for a time lags of 1 s. In the case of a one dimensional random walk this distribution should be described by an Error Function (Equation 2.25 in experimental section).

The red dashed line is the fit of Equation 2.25 to the data ($\chi^2 = 7.4 \cdot 10^{-4}$). It is obvious that a 1D random walk model is too rough for a model to describe the observed diffusion. The gray dotted line shows the fit using a linear combination of a 1D random walk and a second term which takes into account the presence of adsorbed states (Equation 2.27, for details see experimental section). This model describes the data better and the chi-squared of this fit ($\chi^2 = 9.1 \cdot 10^{-5}$) is 8 fold reduced compared to the fit using Equation 2.25, which justifies the use of additional terms. The determined fit parameters are the mean squared displacement = $1470 \text{ nm}^2/\text{s}$, and the weight of the population of adsorbed states $\alpha = 13\%$. In other words during its whole walk and for a time lag of $t=1\text{s}$ the TDI molecule is in average 13 % of the time immobilized at adsorption sites, and diffuses the rest of the time with a 1D random walk. The percentage in time of adsorption clearly depends on the time resolution of the measurements (1 s per frame in this case), and decreases with higher time lags. All the other trajectories could be well described by this model, confirming the presence of adsorption sites distributed over all the mesoporous film. The same procedure was applied for time steps of 2 s, 3s , until 100 s. The resulting MSDs (corresponding to 10% of the total acquisition time of the trajectory) are plotted *versus* time for 80 molecules in Figure 3.27b. Most of these plots are not perfectly linear

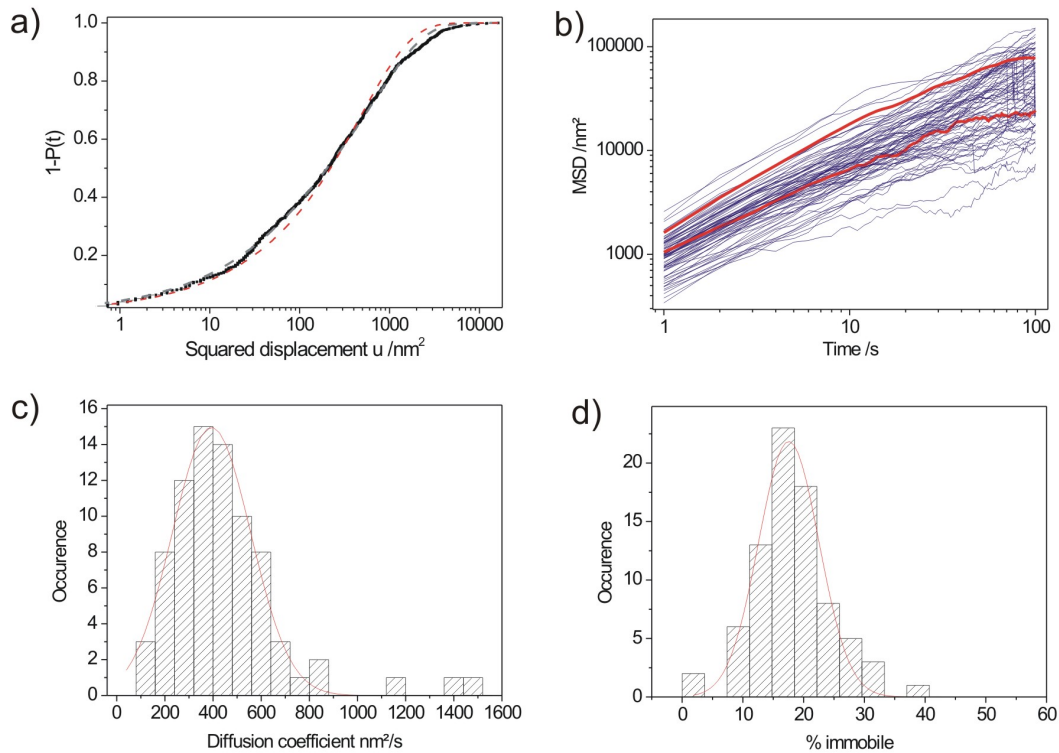


Figure 3.27: Statistical analysis of the diffusion. (a) The cumulative probability distribution $P(u,1 s)$ for a time lag $t_{lag} = 1 s$ for the trajectory shown in Figure 3.25. The separation of the 1D diffusion and the adsorbed states is obtained by a statistical evaluation of squared step lengths (see text for details). (b) Mean squared displacement of the linear diffusion as a function of time. The upper red thick line corresponds to the trajectory displayed in Figure 4. The lower red thick line is an example of confined diffusion due to the presence of “dead ends” closing the pores at specific locations. (c) Histogram of the diffusion coefficients D extracted from the MSD plots. The distribution can be fitted with a Gaussian function with a mean diffusion coefficient of $390 nm^2/s$. (d) Histogram of the percentage of adsorbed states in a trajectory for a time lag of $t_{lag} = 1 s$. The red line is the Gaussian fit with a mean adsorption time per trajectory of 18%.

as it would be expected for a normal random walk, but are slightly curved for high time values. This indicates the presence of a confined diffusion, which is consistent the presence of “dead ends” in the structure already mentioned previously. However, the MSD graphs are approximately linear for the first 10 points and it is possible to extract a diffusion coefficient using the relationship between MSD and time for a random walk in one dimension:⁷⁴

$$MSD = \langle r(t) \rangle = 2 \cdot D \cdot t \quad (3.1)$$

where D is the diffusion coefficient.

The distribution of the diffusion coefficients for the 80 trajectories is shown in Figure 3.27c. It resembles a Gaussian curve with a mean diffusion coefficient of $390 \text{ nm}^2/\text{s}$. Figure 6d displays the histogram of the percentage of adsorption time per trajectory for a time lag of 1 s. The distribution is also a Gaussian with a maximum at 18% of time, which means that a molecule spends in average 18% of its walk immobilized at an adsorption site.

3.4.3 Conclusion

The diffusion of TDI molecules in highly structured domains of the CTAB-templated mesoporous film was investigated with the positioning accuracy down to a single-channel, and the information obtained are of two types:

- structural information about the silica structure: highly linear channels on micrometer lengthscale, presence of rare defects in the structure such as "dead ends" where the pores are closed or small connections between the pores.
- information about dynamics of guest species: presence of two kinds of populations of diffusional behavior, the overall diffusion process being a 1D random walk interrupted occasionally by time intervals where the molecule is trapped at adsorption sites.

The ability to orient mesostructured materials on a macroscopic lengthscale opens the possibility to exploit the organization of mesoporous solids for applications in which ordered, anisotropic, monolithic structure is required. Promising applications include separations, catalysis, chemical sensors and host-guest chemistry. The methodology presented here is a valuable tool to characterize large structured areas of such mesoporous films. In particular, a lot of information can be gained about defects within the structure, which is of paramount importance to improve the synthesis procedure for an utilization such as highly structured molecular membranes for molecular sieving.

3.5 Experimental section

Diffusion and orientation of single TDI molecules in different mesophases of Brij-56-templated mesoporous films

Synthesis of the Brij-56-templated mesoporous films: The deposition mixtures were prepared applying a two step procedure: First, 2.08 g (0.01 mol) tetraethylorthosilicate (TEOS, Aldrich) was mixed with 3 g 0.2 M HCl, 1.8 g H₂O and 7.9 g ethanol and heated at 60 °C for 1 h to accomplish acid-catalyzed hydrolysis-condensation of the silica precursor. This solution was mixed with a second solution containing 566 mg, 906 mg or 2716 mg Brij-56 and 7.8 g, 12.5 g and 37.5 g ethanol, respectively. The samples were prepared by spin-coating the precursor solutions on glass slides (Marienfeld, size: 20 × 20 mm, thickness: 170 μm). The glass surface was previously cleaned by ultrasonification in 0.5% Hellmanex II solution (Hellma) at 50 °C, followed by five minutes rinsing with de-ionized water. Samples were analysed as synthesized. The film thickness was determined by Ellipsometry (Woollam ESM-300 Ellipsometer).

X-Ray Diffraction: X-Ray diffraction patterns were obtained in a Bragg-Brentano geometry using an XDS 2000 diffractometer (Scintag).

TEM: TEM images were obtained with a Jeol 2010 transmission electron microscope operated at 200 kV; cross-sections were prepared by dimple grinding followed by argon ion polishing, with a dimple grinder and a precision ion polishing system (Gatan).

Methods for orientation measurements in the pure lamellar phase of a Brij-56-templated mesoporous film: The mesoporous films were investigated with a modified inverted confocal laser scan microscope (ZEISS LSM 410). An oil immersion objective with a high numerical aperture (ZEISS 63× 1.4 oil) and a 633 nm He-Ne laser were used for the excitation of the TDI dye molecules. The fluorescence light was separated from the laser light using a combination of filters consisting of a dichroic mirror (Q640LP AHF Analysentechnik) and a combination of two fluorescence filters (633 nm Notch Kaiser; HQ720/150 AHF Analysentechnik). The fluorescence is detected outside the microscope with a single photon counting avalanche photodiode (EG&G SPCM-AQ 141). For the measurements of the pure lamellar phase, the bottom of the substrate was embedded in water to obtain a better matching of the refractive indices. To measure the orientation a rotating, broad band $\lambda/2$ plate, which is placed just before the objective, is used to modulate the polarization plane of the excitation light. The fluorescence intensity of the dyes is recorded in dependence to the polarization angle of the excitation light. The polarization modulation is monitored by recording the transmitted excitation light intensity behind the sample and after a polarization filter. Both signals are described by a

cosine-squared function with the same frequency, which results from the rotation of the $\lambda/2$ plate. The phase difference between the fluorescence and reference signals is equal to the angle of the transition dipole moment of the molecule relative to the orientation of the polarizer whose direction is defined as 0° (see Figure 3.3). The phases are obtained by fitting the measured data with a cosine-squared function. This method is explained in detail elsewhere.¹¹⁴ Experiments have been carried out with a pure lamellar phase film aligned perpendicular to the focal plane containing TDI molecules at high concentration ($c \sim 10^{-5}$ mol/L in the synthesis solution) and with a hexagonal phase film in the focal plane containing TDI molecules at ultralow concentration ($C \sim 10^{-11}$ mol/L) in order to observe single molecules.

Translational, orientational and spectral dynamics of single TDI molecules in a CTAB-templated mesoporous film

Synthesis of oxazine-1 / AlPO₄-5 system: Oxazine-1 loaded AlPO₄-5 crystals were prepared by the microwave-assisted hydrothermal synthesis as described previously.^{85,114} The crystal structure of the samples was determined by X-ray diffraction (Philips PW-1050 X Change, Cu-Ka1, Bragg-Brentano geometry, secondary monochromator), and its morphology was visualized by scanning electron microscopy (ISI-100B, 15 kV - data not shown). The crystal structure and the morphology of the AlPO₄-5 are not affected by the inclusion of the dye molecules. The AlPO₄-5 crystals appear as micrometer sized hexagonal barrels with bulges on both ends (size $\sim 8 \times 5 \mu\text{m}$). The crystals with low loading contain dye-concentrations of $\sim 10^{-10}$ mol/g. The one-dimensional pores are perpendicular to the hexagonal sections of the crystals, that is, parallel to the long axis of the barrel.

Synthesis of TDI / M41S system: The hexagonal M41S silica films were synthesized onto glass coverslips via evaporation-induced self-assembly (EISA).¹⁰⁰ Samples were prepared by spin-coating onto glass microscopy cover-slips. In order to avoid unspecific fluorescence from impurities, the glass substrate was cleaned before the synthesis procedure using a 1% Hellmanex solution (Hellma) in an ultrasonic bath (2 min at 60 °C) and subsequent rinsing with deionized and UV irradiated water. 10 mmol (2.08 g) of tetraethoxysilane in 534 mmol (7.9 g) ethanol were prehydrolyzed at 60 °C for one hour under acidic catalysis (using 3 g of 0.2 molar hydrochloric acid and 1.8 g of water). 1.75 mmol (638 mg) of cetylhexyltrimethylammoniumbromide (CTAB), the structure directing agent, in 1068 mmol (15.8 g) ethanol were added. Furthermore, TDI was added to the solution at ultra low concentration (10^{-10} mol/L). This precursor solution was then spin-coated onto a cover-slip. The fast evaporation of the volatile solvent induces the micellization of the template and self-organization of the silica-species simultaneously

with the condensation of the silica. This procedure results in structured silica films with a thickness of about 120 nm (determined by ellipsometry). The films are left uncalcined, that is, the template in the pores of the M41S films acts as a solvent.

Preparation and single molecule investigation of highly structured domains in CTAB-templated mesoporous films

Formation of the highly structured domains: The as-synthesized CTAB-templated mesoporous films with small domains sizes, can be treated after synthesis to lead to more structured materials with macroscopically-sized domains of almost perfectly linear channels. The observed changes are caused by a very slow reorganization of the silica matrix. A critical parameter for this process is the relative humidity (R.H.) of the atmosphere in which the samples are placed. In this study the mesoporous films were stored directly after spin-coating for about 2 weeks in air atmosphere with a R.H. of 50%. This procedure leads to the formation of large domains (up to 100 μm in size) of linear and parallel pores. All data described in this work were measured in such domains.

X-Rays diffractometry (XRD): The structure of the pores in the film was determined using a Scintag XDS 2000 powder diffractometer in a $\theta/2\theta$ Bragg-Brentano scattering geometry. The mesostructured films exhibit 2D-hexagonal order, that is, the amorphous silica surrounding the CTAB-micelles forms hexagonally packed cylindrical pores with 3-4 nm pore diameter parallel to the substrate (see Figure 3.20b).

Transmission Electron Micrographs (TEM): The TEM images of the mesoporous films were obtained with a JEOL 2011 transmission electron microscope operating at 200 kV. For sample preparation the mesostructured film was scratched off the substrate using a razor blade; the resulting powder of mesoporous material was transferred onto an electron microscopy copper grid. Two typical examples of TEM images are shown in Figure 3.6. The pores are organized in 100-500 nm sized crystal-like domains. In the plane of the substrate these domains are randomly rotated against each other.⁴¹

Atomic force microscopy (AFM) measurements: The surface images were taken with a commercial AFM (Asylum Research MFP3D) in tapping mode. The Olympus AC160 SiN Cantilever was driven 5 % below its resonance frequency with a target amplitude of 1.2 V. In the measurements a Setpoint of 0.85 V was used to scan each surface with a resolution of 512×512 pixels and a scanning rate of 2 Hz per line.

Simulations: The experimental trajectories were modeled using three-dimensional random-walk simulations. A random walk with a step length of 0.5 nm was used, and every 16000th step was monitored in the trajectory. The intervals were chosen in order to yield

an effective step length of 32 nm, in accordance with the data. Due to the nature of the undirected, statistical motion with many steps back and forth such a high number of random walk steps is necessary to obtain the experimentally observed effective step length. A Gaussian blur with a standard deviation of $\sigma = 5$ nm was added to every point of the trajectories. The pore geometries with a single layer of linear parallel pores of different length were chosen as to yield best agreement with the experimental trajectories. Transitions between neighboring pores were allowed along the full pore length with a constant probability (permeability) P if a random walk step would transfer the particle from one pore to another. Values between 10% and 0.1% were chosen for the permeability P .

Chapter 4

New photostable water-soluble terrylenediimide derivatives for applications in single molecule studies and membrane labelling

4.1 Introduction: novel fluorophores for biological labelling

The use of labels or membrane staining agents has greatly helped the study of complex biological processes. In living cells, for example, the exact localizations of marked molecules can be monitored using fluorescence microscopy, revealing the dynamics of biological molecules such as proteins, DNA or lipids. Labels which are environmentally sensitive can be used as molecular reporters since information on what is happening in their surroundings can be derived from their fluorescence signals. Furthermore SMS has become a common method to study the dynamical behavior of biomolecules e.g. it is now possible to measure dynamic processes in biopolymers such as protein folding, or to monitor the mobility of single motor proteins.^{112, 150-155}

Organic dyes are amongst the earliest types of fluorescent labels used in biology. During the last few years, the interest in new water-soluble fluorescent organic dyes has strongly increased.¹⁵⁶⁻¹⁶⁰ Many commercially available fluorescent dyes, such as rhodamine, cyanine, oxazine etc., are water-soluble and fulfil additional requirements of a powerful fluorophore: high extinction coefficient, high fluorescence quantum yield, and chemical stability. However, their photostability is limited, and photobleaching typically occurs

after 10^4 to 10^6 photocycles. Photobleaching is a major disadvantage since it severely restricts the monitoring time, thus limiting the amount of information collected during the experiment.

Furthermore, fluorescent dyes are often used in "live cell imaging" experiments where single proteins, viruses, drugs or other single bio-particles are labelled in order to follow the pathway and/or the interactions of these particles inside the living cell.^{46,161–163} However, while individual fluorescent molecules can be detected with high signal-to-noise ratio in solutions, in solid matrixes or on surfaces, the cellular environment contains a broad set of fluorescent compounds which produce a non-negligible background of autofluorescence. Hence, dyes that absorb and fluoresce above 600 nm are highly desirable since autofluorescence background of living cells is negligible in this spectral region. Up to date, very few, if any, water-soluble fluorophores present both a high photostability and a fluorescence emission above 600 nm.

Rylene derivatives are known for their exceptional photophysical and photochemical stability as well as for their high fluorescence quantum yield, which is close to unity in organic solvents.^{14,164} Unfortunately, they are not water-soluble. Water solubility can be achieved by introducing hydrophilic substituents onto the hydrophobic skeleton of these molecules. In many cases, fluorescence is strongly diminished because the additional flexibility of the side groups enhances the non-radiative decay channels. Furthermore, aggregation due to the hydrophobic core of such chromophores can lead to fluorescence quenching. Sulfonation decreases the aggregation tendency, presumably due to steric effects and to increased polarity induced by the sulfonic acid group. A perylenediimide chromophore containing four charged sulfonyl groups (structure shown in Figure 4.1b) has recently been synthesized¹⁶⁵ and its photophysical properties characterized.¹⁵⁹ It is water-soluble, highly fluorescent, and very photostable. However, the perylene dyes absorption region lies below 600 nm, whereas terrylene dyes absorb far above this wavelength. In addition, our experience shows that terrylene is even more photostable than perylene. Therefore water-soluble terrylene derivatives should be even more ideal fluorophores for single molecule and live-cell imaging experiments.

Following this rationale, the group of Prof. Müllen (MPI, Mainz) has recently synthesized a new water-soluble terrylenediimide derivative: the terrylenediimide dye 1,6,9,14-Tetra(4-sulfonylphenoxy)-N,N'-(2,6-diisopropylphenyl)-terrylene-3,4:11,12-tetracarboxydiimide, (further referred to WS-TDI) which structure is shown in Figure 4.7a. This molecule shows a nicely balanced effect between the hydrophilic sulfonic groups and hydrophobic core. The sulfonic groups are responsible for the water solubility; however, due to the large pi-electron system of the rigid hydrophobic core, many of the molecules are still stacked, forming aggregates. The ambivalent nature of this molecule offers ad-

ditional interesting properties since the terylene core presents a strong affinity to e.g. lipid membranes. This property makes WS-TDI an exceptional label for artificial as well as biological membranes. The results of these investigations are presented in Section 4.2.

Two additional dyes that derive from WS-TDI have further been synthesized in Müllen's group: WS-TDI dodecyl (Figure 4.7b) and WS-TDI pyridoxy (Figure 4.7c). Those derivatives were expected to exhibit not only similar photophysical performances to those of the original WS-TDI, but also additional biologically valuable properties rendering them more powerful for biological studies. The addition of a dodecyl group to WS-TDI was expected to allow a better incorporation in lipid bilayer membranes of living cells. Strong changes in photophysical properties were expected for WS-TDI pyridoxy which is bearing positively charged side groups *versus* negatively charged side groups compared in WS-TDI. These two WS-derivatives have been characterized, as reported in Section 4.3, focussing on their capacity to stain membranes of living cells (lipid bilayer).

Finally, proof is given that these new WS-TDI derivatives are valuable biological markers for monitoring endosome maturation (Section 4.4). The three dyes' pathway in the endocytic system allows a better understanding of the dye-uptake process in living cells. Details to the biological system used in those assays are further described in Section 4.4.

4.2 WS-TDI as a powerful dye for applications in single molecule studies and membrane labelling

The aim of this Section is the investigation of the photophysical properties and aggregation behavior of WS-TDI in purely aqueous media and in the presence of surfactants. The absorption and the fluorescence behavior strongly depends on the extent of aggregation and, thus, on the solvent used. A single molecule study of the photostability is also conducted to compare WS-TDI to other dyes and to establish its outstanding properties. In addition, the ability to label proteins with this dye is demonstrated using Fluorescence Correlation Spectroscopy (FCS) measurements. Furthermore, the possibility of labelling artificial and natural membranes is investigated showing, for example, the exceptional imaging properties of this dye for lipid membrane compartments in living cells.

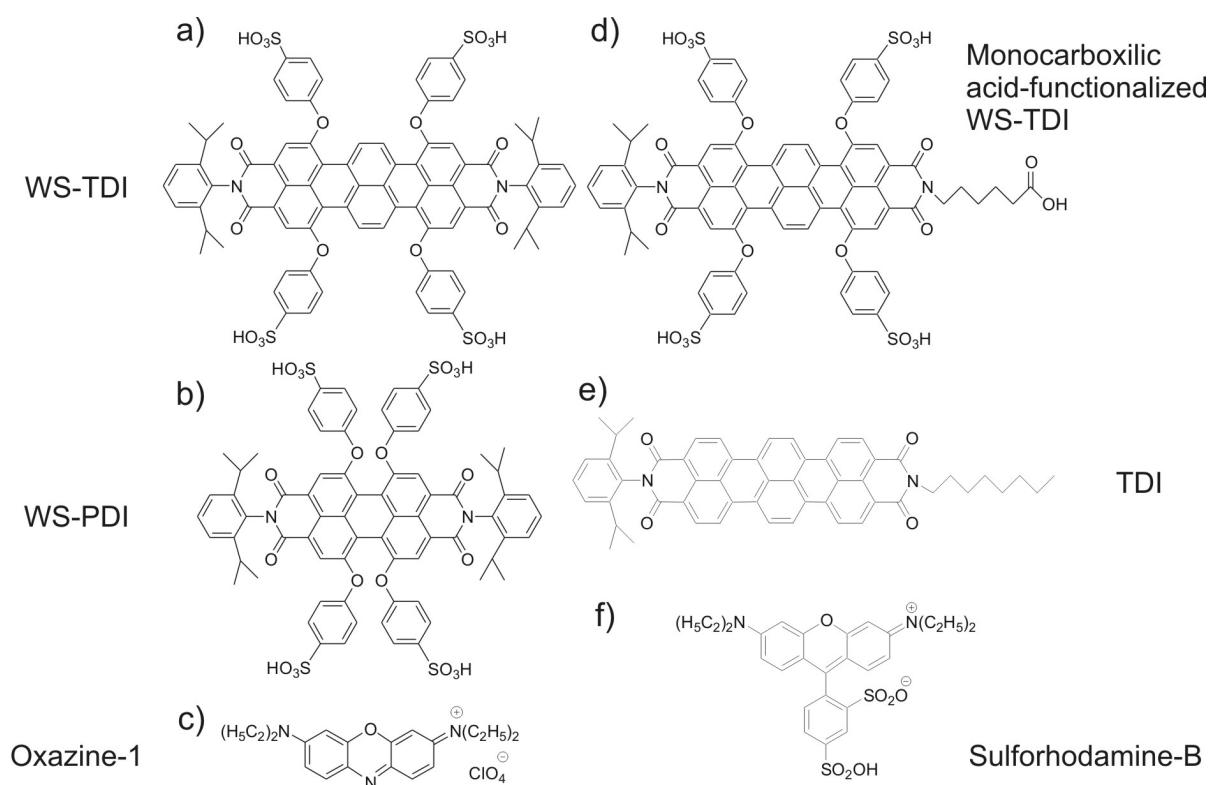


Figure 4.1: Structure of (a) WS-TDI (1,6,9,14-Tetra(4-sulfonylphenoxy)-N,N'-(2,6-diisopropylphenyl)-terrylene-3,4:11,12-tetracarboxydiimide), (b) WS-PDI, a water soluble perylenediimide derivative, (c) oxazine-1, (d) monocarboxylic acid-functionalized terrylenediimide (1,6,9,14-Tetra(4-sulfonylphenoxy)-N-(2,6-Diisopropylphenyl)-N'-(5-carboxypentyl)-terrylene-3,4:11,12-tetracarboxydiimide), (e) terrylenediimide derivative, and (f) sulforhodamine-B.

4.2.1 Absorption and emission spectra

The spectral and luminescence properties of WS-TDI depend substantially on the environment. This is due to the favorability of forming aggregates in polar media, such as water, while it remains monomeric in other solvents such as dimethylsulfoxide (DMSO). The absorption and emission spectra of WS-TDI dissolved in DMSO with a concentration of $c = 10^{-5}$ mol/L are shown in Figure 4.2a (solid lines). Two distinct absorption bands can be assigned to two different electronic transitions in the monomeric molecule, the S_0 - S_1 from 550 to 720 nm and the S_0 - S_2 from 390 to 460 nm.¹⁶⁶

The S_0 - S_1 presents a maximum at 677 nm with a molar extinction coefficient of $36800 \text{ M}^{-1}\text{cm}^{-1}$. The Stokes shift of fluorescence emission is 43 nm, while the quantum yield of fluorescence is $\varphi_f = 0.08$ in DMSO. In addition, time-resolved measurements have been performed to investigate the photophysical parameters of this dye. The fluorescence decay of a 10^{-5} mol/L WS-TDI solution in DMSO was monoexponential with a lifetime of $\tau = 0.88$ ns. From the quantum yield $\varphi_f = k_f / (k_f + k_{nr})$, where k_f is the fluorescence rate constant and k_{nr} is the nonradiative rate constant, and the lifetime $\tau = 1 / (k_f + k_{nr})$, we obtain $k_f = 8.9 \times 10^7 \text{ s}^{-1}$, and $k_{nr} = 1.0 \times 10^9 \text{ s}^{-1}$. Hence, $k_{nr} \gg k_f$.

In contrast to the data in DMSO, the absorption spectrum of WS-TDI in water (dotted line, Figure 4.2b) consists of a main band at a shorter wavelength of 637 nm and of a weak band at 690 nm. Nearly no fluorescence emission signal is observed in the region of the fluorescence spectrum (dotted line, Figure 4.2d, excitation 645 nm). Self-association of dyes in solution is a frequently encountered phenomenon in dye chemistry owing to strong inter-molecular forces.^{167,168} WS-TDI is a relatively rigid molecule with a large planar π -electron system with hydrophobic nature and has a strong tendency to aggregate in polar solvents like water. Previous studies have already characterized aggregates of π - π stacked perylene diimide dyes in solution,¹⁶⁹ which have a slightly smaller π -electron system than WS-TDI.

In general, aggregates in solution exhibit distinct changes in absorption and fluorescence properties compared to monomeric species. Molecular excitonic theory describes two main species of dye aggregates distinguished as H- and J-aggregates (see Figure 4.2c). H-aggregates are formed by parallel stacking whereas J-aggregates occur in a head-to-tail arrangement.^{170,171} In H-aggregates the absorption maximum is blue shifted with respect to the isolated chromophore and the fluorescence is normally quenched. However, J-aggregates usually show fluorescence and both the absorption and emission maxima are red-shifted.¹⁷² Comparing these statements with the observations of this study, one concludes that WS-TDI forms H-aggregates in water.

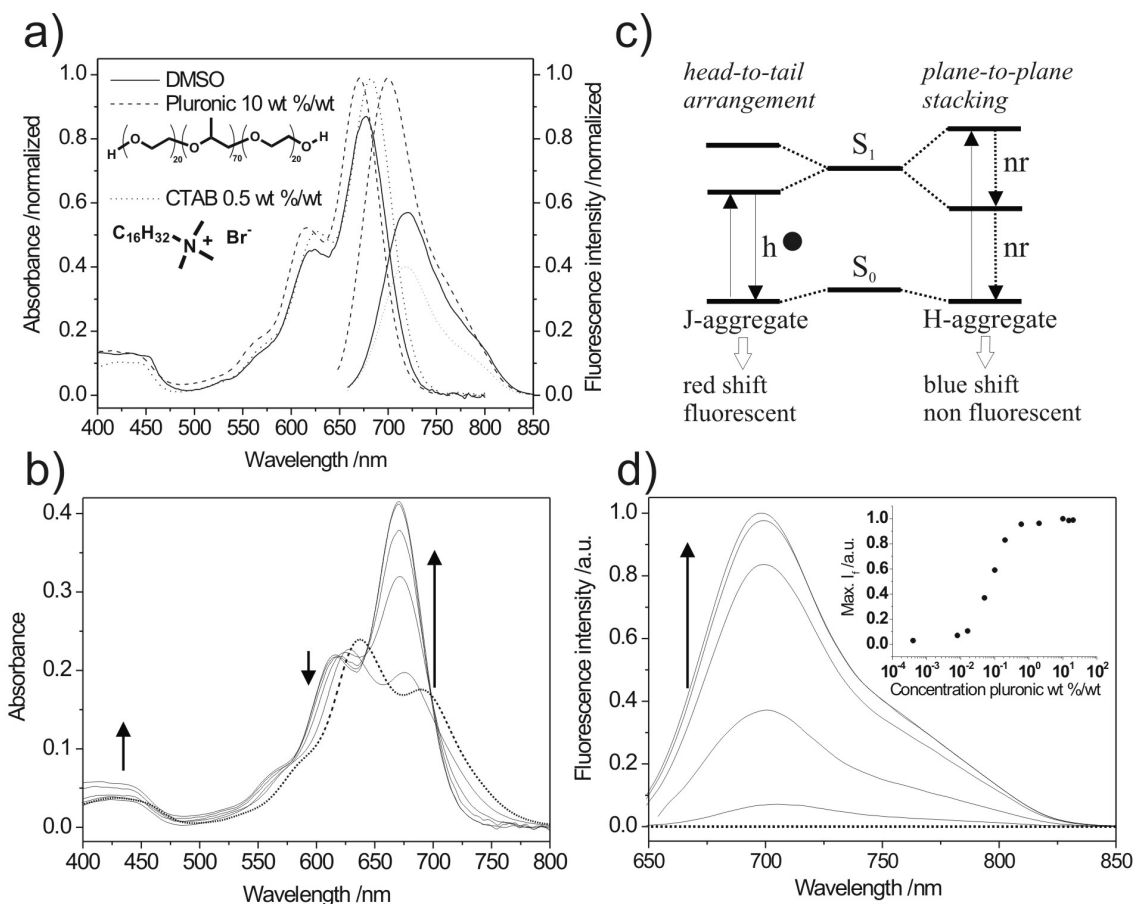


Figure 4.2: (a) Absorption spectra of 10^{-5} mol/L WS-TDI solutions in DMSO (continuous line), in water in presence of 10% wt/wt Pluronic P123 (dashed line), in water in presence of 0.5% wt/wt CTAB (dotted line), and their corresponding fluorescence spectra ($\lambda_{ex} = 655, 643,$ and 653 nm respectively). The spectra are normalized to the absorption and fluorescence maxima of WS-TDI in water taken in the presence of 10% wt/wt Pluronic P123. Schematic structures of Pluronic P123 and CTAB are shown in the inset. (b) Effect of Pluronic P123 concentration on the absorption spectrum of WS-TDI in water ($c = 10^{-5}$ mol/L). The broken line represents the absorption spectrum of WS-TDI in water without addition of surfactant. The solid lines represent a titration with Pluronic P123. Arrows indicate the direction of change with increasing Pluronic concentration (0.008, 0.05, 0.2, 2 and 20% wt/wt respectively). (c) Schematic diagram of H- and J- aggregates and their influence on the energy levels and fluorescence behavior of WS-TDI. (d) Normalized fluorescence emission spectra ($\lambda_{ex} = 640 - 650$ nm) corresponding to the absorption spectra in panel b. Inset shows the plot of the maximum of fluorescence intensity *versus* Pluronic P123 concentration.

Light scattering measurements show the presence of particles of a size of 449 ± 53 nm at a WS-TDI concentration of 10^{-5} mol/L in water, whereas no signal from light scattering is detected in DMSO at the same WS-TDI concentration. Moreover, the size of the aggregates in water decreases with diminishing dye concentration (472 ± 117 nm at 10^{-4} mol/L and 114 ± 24 nm at 10^{-6} mol/L). This is a typical observation of dye aggregation in water solution, whereas in DMSO, no light scattering signal was detected,

suggesting that no aggregation takes place.

Further measurements were conducted in the presence of the nonionic block copolymer surfactant poly(ethyleneoxide)-poly(propylene oxide)-poly(ethyleneoxide) (Pluronic P123, BASF), at different surfactant concentrations for a 10^{-5} mol/L WS-TDI concentration in water. The absorption and fluorescence spectra are shown in Figures 2b and 2d. The concentration of Pluronic P123 was increased from 0.0004 to 20% wt/wt. A pronounced reduction in the intensity of the band absorbing near 630 nm in favor of the band at longer wavelength (670 nm) is observed with increasing concentration of Pluronic P123. Moreover, a small fluorescence signal appears already with the lowest concentration of Pluronic P123. The fluorescence intensity increases dramatically with higher surfactant concentrations. The inset in Figure 2d shows the fluorescence intensity as a function of Pluronic P123 concentration. The fluorescence intensity is near zero with the WS-TDI in water and increases drastically for surfactant concentrations above 0.04 wt/wt. This concentration corresponds to the critical micelle concentration (CMC) of Pluronic P123¹⁷³ i.e. the starting point of the formation of micelles. The fluorescence intensity saturates for surfactant concentration above about 2%.

Furthermore, the measurements of the size of the particles by light scattering in a solution of WS-TDI in presence of 2% and 10% Pluronic show the presence of particles with a diameter of 9 ± 3 nm and 18 ± 3 nm respectively, which is the diameter of the hydrophobic micelles themselves formed by Pluronic at these concentrations.¹⁷⁴ No light scattering signal is detectable anymore at a particle diameter around 449 nm, which was observed for pure water solutions of WS-TDI at the same concentration. In addition, a similar shape of the absorption spectra of WS-TDI in DMSO and in water in presence of Pluronic above CMC is observed, as illustrated in Figure 4.2. These results suggest that WS-TDI molecules are incorporated into micelles and that most of the molecules are present in a monomeric form associated with the hydrophobic micelles. The extinction coefficient of this monomeric absorption band (670 nm) in presence of 10% wt/wt of Pluronic is estimated to be $42\,000\text{ M}^{-1}\text{ cm}^{-1}$. The corresponding quantum yield of fluorescence φ_f is equal to 0.17.

The absorption and emission spectra of a WS-TDI solution ($c = 10^{-5}$ mol/L) in presence of the cationic surfactant cetyltrimethylammonium bromide (CTAB) at a concentration 10% wt/wt, much above the CMC of $\sim 0.03\%$ wt/wt, are compared to the spectra of the dye in DMSO and in water in presence of 10% of Pluronic (Figure 4.2). Addition of CTAB leads to shifts in the absorption and emission maxima to 682 and 718 nm, respectively. This is accompanied by a decrease in the fluorescence quantum yield of WS-TDI ($\varphi_f=0.05$) compared to the hydrophobic Pluronic environment. However, the absorption spectrum is very similar to those in DMSO and in water in the presence of

10% wt/wt Pluronic. In particular, the ratios of the intensities of the two adsorption bands around 675 nm and 630 nm are the same in all three cases. No signal was obtained by light scattering measurements. It is expected that micelles of CTAB are smaller than those formed by Pluronic due to the shorter hydrophobic chains of CTAB¹⁷⁵ and may be below the detection limit of the setup. More important, the peak of particle sizes around 449 nm found in pure water vanishes, indicating that WS-TDI is present only in the monomeric form, solubilized in micelles of CTAB. All spectral and photophysical data of this Section are summarized in Table 4.1.

Table 4.1: Photophysical parameters for WS-TDI in different solvents.

Solvent	λ_{abs}^{max} (nm)	λ_{em}^{max} (nm)	ϵ_{max} (/M/cm)	Φ_f	Particle size (nm)
DMSO	677	720	36800	0.08	/
Water	637	/	23900	/	449
Water 10% wt/wt Pluronic	670	700	42000	0.17	18
Water 0.5% wt/wt CTAB	682	718	41700	0.05	/

4.2.2 Single molecule studies

A common experimental approach in single molecule spectroscopy is to spatially resolve the fluorescence signals of immobilized single molecules. One way to immobilize and investigate single molecules is to dissolve highly diluted solutions in a polymer and spin coat a thin film of the polymer on a substrate. Under these conditions, the molecules are so widely separated that in average less than one molecule is in the confocal spot of the laser beam. Scanning the laser beam across the sample allows single molecules to be detected by their fluorescence (for details, see Section 2.1.3). Figure 4.3a shows a typical example of a $11 \times 12 \mu\text{m}^2$ confocal fluorescence image of individual WS-TDI molecules embedded in a PVA film. Each bright spot represents a single fluorescent molecule. The fluorescent intensities of individual molecules are observed by positioning the laser beam on such a spot and collecting the emitted fluorescence as a function of time. A typical fluorescence intensity trajectory is shown in Figure 4.3b. This trajectory shows blinking events at 33 s and 46 s, and one-step photobleaching at 65 s. The digital On-Off switching of the fluorescence intensity in the blinking and photobleaching behavior is a typical signature for a single molecule. From such a fluorescence intensity trajectory, the number of total emitted photons (TEP, gray area as integral over time in Figure

4.3a corrected by detection efficiency of the setup, see experimental section 4.6) and the survival time (ST, time to the irreversible photobleaching) can be extracted. The distributions of these two parameters characterize the fluorescence capability and the photostability of a fluorescent dye.

Fluorescence intensity trajectories of 79 single WS-TDI molecules were measured. The resulting probability distributions of TEP and ST for WS-TDI in PVA are plotted in Figure 4.3c and d (square points).

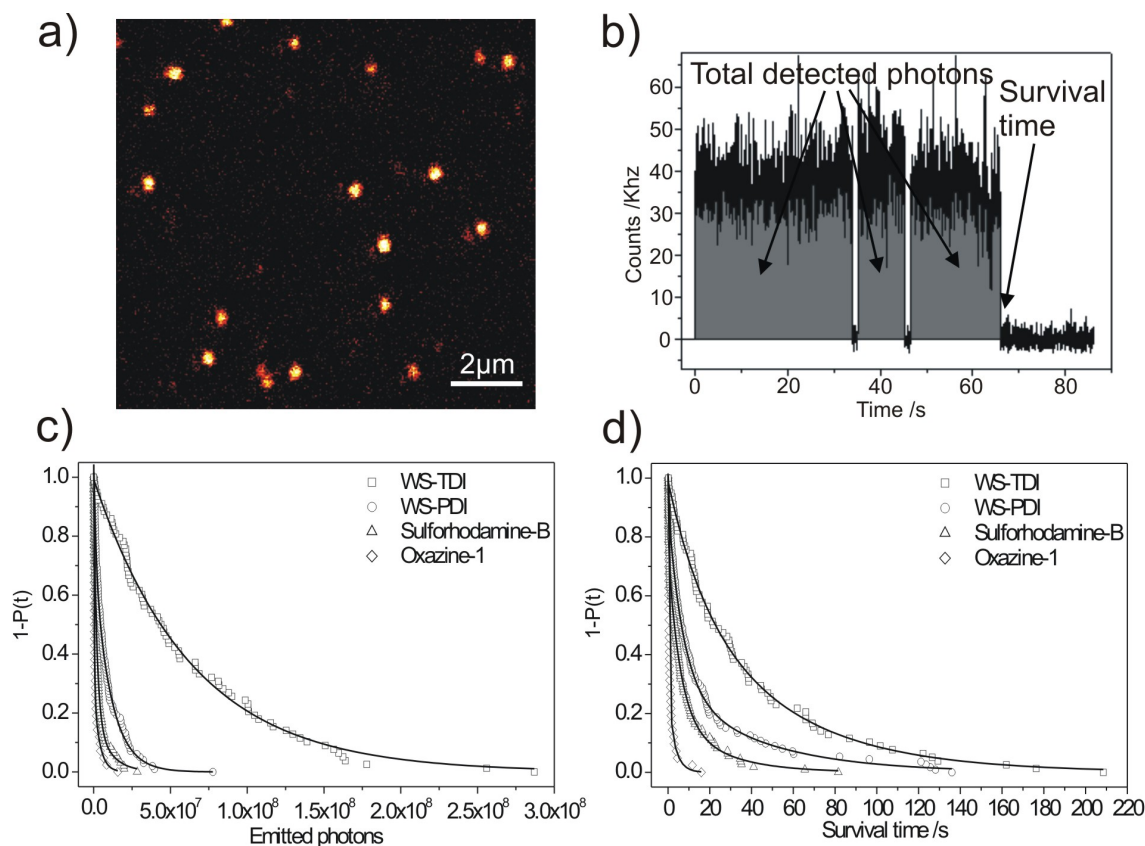


Figure 4.3: (a) Fluorescence image of single WS-TDI molecules embedded in PVA. (b) A typical fluorescence intensity trajectory. The molecule shows blinking behavior and undergoes irreversible photobleaching. (c) Accumulated probability distributions of the TEP for WS-TDI (squares), WS-PDI (circles), sulforhodamine-B (triangles), and oxazine-1 (diamonds). The curves cannot be fitted with a single component exponential decay. Instead, two-component decay was used and is shown as a solid line, rendering an average TEP. (d) The same evaluation for the ST with bi-exponential fits shown as solid lines.

These distributions are well describes by multi-exponential distributions and can be characterized by an average TEP and ST, as described in Section 2.1.2.2.

The experimental data were best fit with bi-exponential decays, exception of TDI, where a mono-exponential was sufficient to fit both the TEP and the ST. Similar bi-exponential

photobleaching kinetics have been reported for fluorescein in PVA and were tentatively attributed to the influence of dye-polymer interactions.¹⁷⁶ It should be noted that the photobleaching mechanisms and such multi-exponential decays are presently not fully understood on a molecular level.¹²

The average TEP for WS-TDI in PVA is calculated to be $63.7 \pm 0.7 \times 10^6$ and the average ST gives 40.3 ± 1.2 s. The fluorescence capability and photostability of WS-TDI was compared with three other dyes studied under the same experimental conditions. The probability distributions for 99 molecules of WS-PDI, 96 molecules of sulforhodamine-B and 43 molecules of oxazine-1, all dissolved in PVA, are shown in Figure 4.3c and d. The corresponding average TEP and ST are summarized in table 4.2. WS-TDI emits about 8, 18 and 53 times more photons before photobleaching, and lives 3, 5 and 37 times longer than WS-PDI, sulforhodamine-B and oxazine-1 respectively. Our results for WS-PDI are in good agreement with the data reported by Margineanu et al.¹⁵⁹ provided their detection efficiency is below 10% (The number, though reasonable, was unfortunately not given in their report).

Rhodamine and oxazine molecules are currently among the best performing water-soluble dyes. These results clearly show that WS-TDI emits many more photons over a longer period of time than the other dyes which were measured. The high number of emitted photons and the superior photostability combined with the absorption in the red spectral region (650nm, avoiding e.g. autofluorescence in live-cell imaging experiments) make this dye very promising for single molecule experiments.

Table 4.2: Average TEP and ST parameters of different dyes in spin-coated PVA and PMMA

Fluorophore	Matrix	λ_{em}	Total emitted photons ($\times 10^6$)	Survival time (s)
WS-TDI	PVA	633	63.7 ± 0.7	40.3 ± 1.2
WS-PDI	PVA	568	7.8 ± 0.4	14.7 ± 0.3
Sulforhodamine-B	PVA	568	3.6 ± 0.1	7.7 ± 2.1
Oxazine-1	PVA	633	1.2 ± 0.4	1.1 ± 0.3
WS-TDI	PMMA	633	109.9 ± 14.1	60.6 ± 3.7
WS-PDI	PMMA	568	11.1 ± 2.3	34.5 ± 2.1
TDI	PMMA	633	301.2 ± 18.5	98.0 ± 3.8

To make a direct comparison between WS-TDI and TDI (which can not be desolved in water or PVA), the photostability of both dyes in PMMA is investigated. TDI has the same terrylene chromophore as WS-TDI and is currently the most photostable and

best performing dye. Measurements on 71 WS-TDI molecules and 60 TDI molecules in PMMA yielded an average TEP of $110 \pm 14 \times 10^6$ and $301 \pm 19 \times 10^6$ and an average ST of 61 ± 4 s and 98 ± 4 s for WS-TDI and TDI respectively. The average TEP of WS-TDI is approximately 1/3 that of TDI and the decrease is attributed to the lower fluorescence quantum yield of the dye due to the influence of the flexible and charged sulfonyl groups attached to the chromophore. The difference in ST is decreased by 40%. In a sense, the lower TEP and ST is the price one has to pay to make TDI water-soluble.

PMMA has a stabilizing effect on WS-TDI, increasing the TEP by approximately 70% the ST by 50%. The reason for the improvement in these parameters may be related to the lower polarity of PMMA. PVA matrix has a dielectric constant $\epsilon = 5.0$ in comparison to a value $\epsilon = 3.2$ for PMMA. The results of these measurements are summarized in Table 4.2.

4.2.3 Protein labelling

The experiments described above show that WS-TDI is a promising dye for single molecule experiments due to its high photostability, red excitation spectrum, relatively high fluorescence quantum yield and solubility in water. To be an effective fluorophore for biological applications, it is essential that the fluorophore can be used for labelling proteins. Thus, the WS-TDI was modified and the new dye was used to stochastically label lysine residues on the surface of avidin. TDI monocarboxylic acid was mixed with avidin at a ratio of 10:1. The free dye was separated from labelled protein as discussed in the experimental section and the labelled protein investigated using FCS and single molecules fluorescence intensity measurements. These measurements were conducted by Barbara Müller.

The normalized autocorrelation curves for WS-TDI (circle points) and WS-TDI/avidin (square points) determined from FCS measurements in phosphate-buffered-saline buffer (PBS) are plotted in Figure 4.4a. The diffusion time is the average time a particle needs to diffuse across the confocal FCS volume. It is roughly the time at which the autocorrelation function has decayed to half of its initial amplitude. In Figure 4.4a, there is a clear shift to longer diffusion times for the WS-TDI-avidin complexes, indicating the mobility of WS-TDI is decreased by attachment to avidin and confirms that the protein has been successfully labelled. The exact values obtained from the fit of the curves with Equation 2.17 are $\tau_D = 0.56 \mu\text{s}$ for WS-TDI/avidin and $\tau_D = 0.19 \mu\text{s}$ for WS-TDI, corresponding to diffusion coefficients of $D = 48 \mu\text{m}^2/\text{s}$ and $D = 140 \mu\text{m}^2/\text{s}$ for WS-TDI/avidin and WS-TDI respectively. The three times lower diffusion coefficient of WS-TDI/avidin is expected due to the much larger hydrodynamic radius of WS-TDI/avidin.

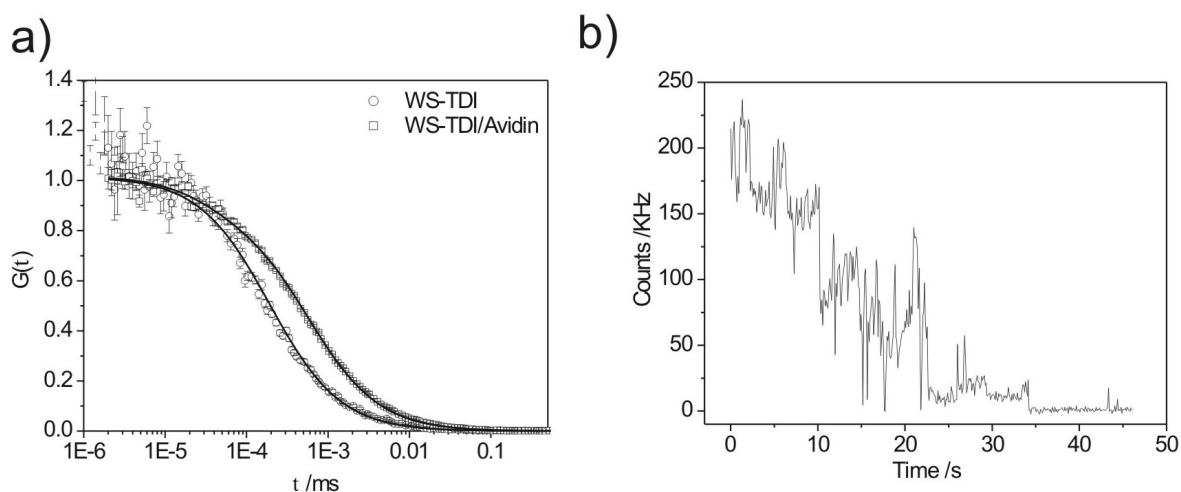


Figure 4.4: (a) Normalized autocorrelation curves of WS-TDI (circles) and of WS-TDI labelled avidin (squares) in phosphate-buffered-saline buffer (PBS). The shift of the curve of WS-TDI labelled avidin to the right compared to the free dye indicates a lower diffusion coefficient in PBS. (b) Example of a fluorescence intensity trajectory of a WS-TDI labelled avidin molecule. The step-wise decay reveals that several single WS-TDI molecules are bound to this protein.

Avidin has a molecular weight of 67 kDa compared to 1.524 kDa for WS-TDI.

Moreover, the amplitude of the autocorrelation curve is proportional to the inverse number of fluorescent molecules in the confocal volume and can thus yield the concentration of the fluorescent species. FCS measurements were performed on a 3.6×10^{-5} mol/L concentration of WS-TDI in PBS. The amplitude of the autocorrelation function shown normalized to 1 in Figure 4.4a is 0.18 corresponding to an average of 2 fluorescent molecules in the confocal volume. Thus, the concentration of fluorescent WS-TDI in the probe volume of approximately 1.3 fL is $c_m = 2.5 \pm 0.2 \times 10^{-9}$ mol/L. Therefore, one concludes that only about 1 molecule out of 14,400 is in monomeric fluorescent form in the solution. This confirms the qualitative result previously found that the vast majority of the molecules form non-fluorescing aggregates in water and only a small monomeric fraction shows fluorescence.

The fluorescence intensity trajectory of a WS-TDI/avidin complex dissolved in PVA is shown in Figure 4.4b. This shape of this trace is in sharp contrast to the single molecule trace shown in Figure 4.3b. A stepwise decay is observed rather than the digital on and off states previously observed. The behavior results from the combination of photoblinking and photobleaching of at least 5 WS-TDI molecules. As the sample is highly diluted, it is improbable that these molecules are in one confocal spot by chance. This can only be the case if they are bound to the same protein molecule, again verifying that the protein was successfully labelled.

4.2.4 WS-TDI as a membrane marker

4.2.4.0.1 Labelling of liposomes Measurements with Pluronic P123 or CTAB in water solutions show that the aggregation of WS-TDI can be strongly reduced above the CMC and strong fluorescence can be achieved. This leads to the idea that WS-TDI can be used for labelling membranes and compartments consisting of membranes like liposomes, endosomes, etc. WS-TDI is non fluorescent in water solution due to the strong formation of H-aggregates, whereas, in the presence of membranes, WS-TDI becomes monomeric and strongly fluorescent. In this way, membranes can be labelled by incorporation of the dye.

To test this hypothesis, the phospholipidic membrane of artificial liposomes with a diameter of 173 nm (measured by light scattering) was used as a straightforward test system. The fluorescent probe was dissolved in water and added to a suspension of pre-formed liposomes with gentle mixing. The ratio of lipid to fluorescent probe was greater than 300:1 to prevent changes in the liposome membrane structure. The suspension was left for 1 h to ensure complete incorporation of the probe into the lipid bilayer. After purification and dilution of the sample, diffusion of the labelled liposomes in Hepes buffer was monitored by wide-field fluorescence microscopy. Figure 4.5a shows a frame from an image sequence taken as a movie where each frame is recorded with an exposure time of 100 ms. Bright spots indicating the presence of single liposomes and in some cases small aggregates of liposomes can be seen diffusing freely in solution. Other particles can be seen moving with reduced intensity out of the focal plane of the setup. Fluorescence originates only from liposomes which have incorporated WS-TDI, since the possible remaining dye in water solution forms non-fluorescing aggregates. The emission spectrum obtained from the bright spots in Figure 4.5a is shown in Figure 4.5b, and presents a spectrum which is identical to the fluorescence spectrum of WS-TDI in presence of Pluronic P123 in Figure 4.2d. This clearly indicates the presence of WS-TDI attached to or incorporated in the membrane of the liposomes. Even after several months, the liposomes still contained WS-TDI and could be identified by their fluorescence. In summary, WS-TDI can thus be successfully used to label phospholipid membranes.

4.2.4.0.2 Observation of membrane containing compartments in living cells labelled with WS-TDI After having shown that WS-TDI can label artificial liposomes, the possibility of labelling membrane containing compartments with WS-TDI in living cells has been investigated. WS-TDI was compared with two other well known membrane labelling dyes: Alexa647/dextran and FM® 4-64 styryl dye.

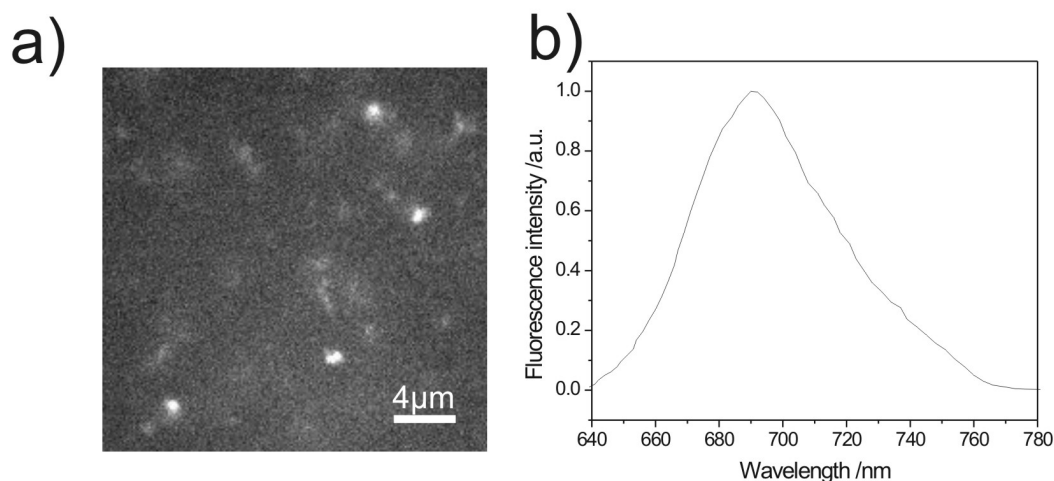


Figure 4.5: (a) Wide-field image extracted from a movie (100 ms per frame) of WS-TDI labelled liposomes freely diffusing in Hepes buffer. (b) Fluorescence spectrum acquired with the confocal set-up ($\lambda_{ex}=633$ nm) on a sample of the labelled liposomes 500 times more concentrated than visualized in panel (a).

Alexa647 is a widely used dye in biology, well known to yield photostable conjugates.¹⁵⁸ The linking of Alexa647 dye to the hydrophilic polysaccharide dextran creates a conjugate which is often used as a fluid phase marker.¹⁷⁷ This means that Alexa647 bound to dextran can be taken up by the cell in an endocytotic process, and thus is contained in endosomes, showing the pathways of these compartments in the living cell.

Using the water-soluble styryl dye, a different mechanism is applied for the imaging of membrane containing cell compartments. Here, the styryl dye is quasi non-fluorescent in water solution due to its high internal flexibility, but becomes fluorescent when it is incorporated into the membrane. In the membrane the dye loses most of its internal degrees of freedom, the non-radiative decay channels are blocked, and thus the dye starts to fluoresce. In contrast to the styryl dye, WS-TDI is non-fluorescent in water solution due to the strong formation of H-aggregates, but fluoresces strongly in membranes where it is monomeric.

In dye-uptake experiments, solutions of Alexa647/dextran, styryl dye and WS-TDI were added to living HeLa cells adherent on a cover-glass at 37 °C. The dye concentrations were in each case 4×10^{-6} mol/L (for details see experimental section 4.6). After an incubation period of 40 min, the solutions were washed in order to remove the excess of dye.

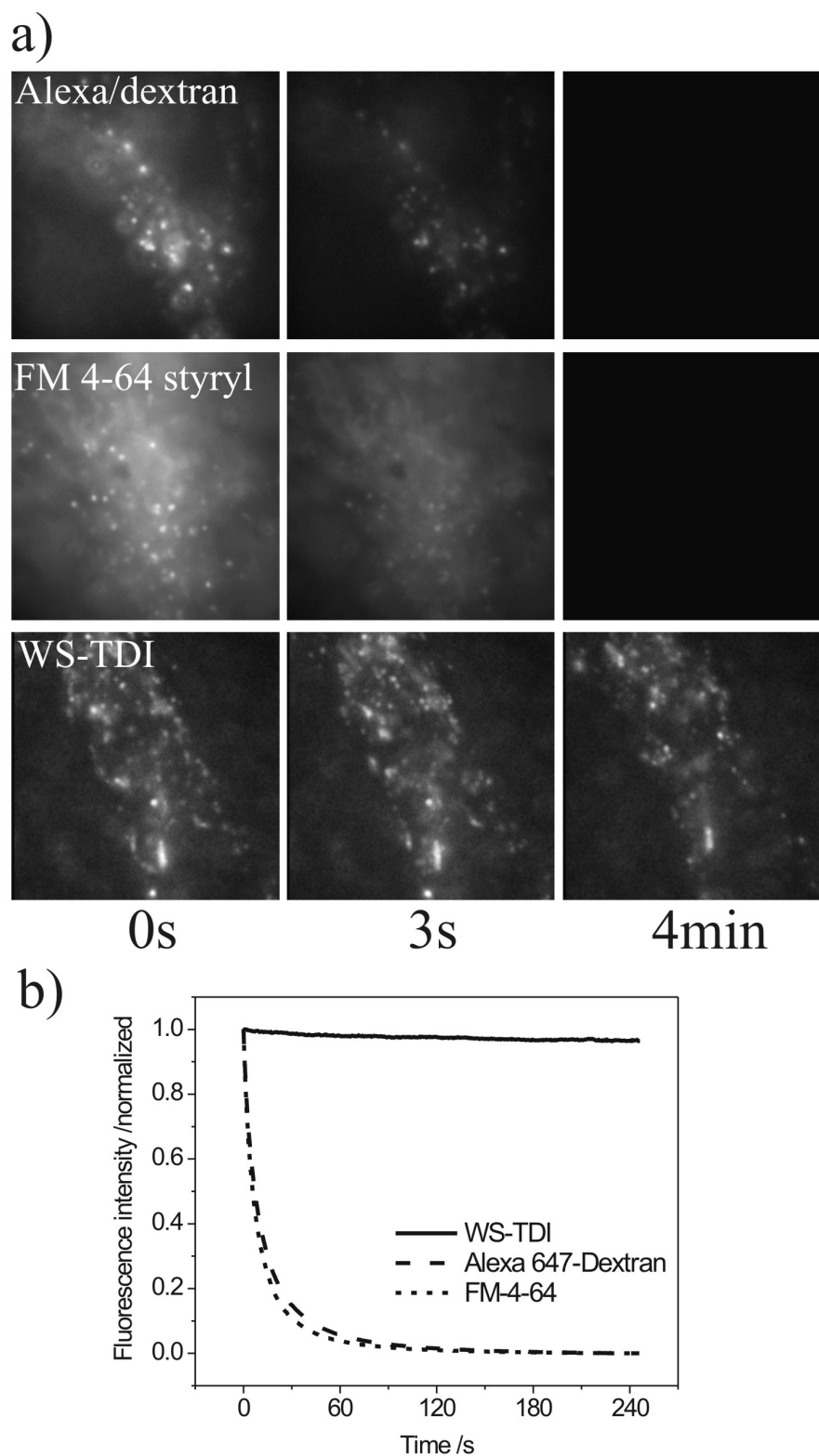


Figure 4.6: $23 \mu\text{m} \times 23 \mu\text{m}$ frames extracted from three sequences of images of HeLa cells adhered onto a cover glass in PBS and loaded with Alexa647/dextran (top), FM 4-64 Styryl dye (middle), and WS-TDI (bottom). The depicted images were acquired after 0 s (left), 3 s (middle) and 4 min (right) of illumination. (b) Plot of the normalized fluorescence intensity as a function of time for the three image sequences.

The three dyes could be easily detected by wide-field imaging. Movies have been recorded with an integration time of 500 ms per frame over a period of 4 min. Frames taken after 0 s, 3 s and 4 min of illumination time under identical conditions for all three dyes are shown in Figure 4.6a.

At the beginning of illumination, the images appear very similar. All three images clearly show many vesicles that were formed at the cell membrane, and the movies show their diffusion within the cell. No significant homogeneous fluorescence background in the cytoplasm was detected for any of the fluorophores, but the best contrast was obtained with WS-TDI. Already after 3 s, fading of intensity due to the photobleaching of Alexa647/dextran and the styryl dye can be clearly observed, and, after a period of about 40 s, nearly no signal of these dyes can be detected. In contrast, WS-TDI labelled cells still can be beautifully imaged even after 4 min. Additional measurements show that strong fluorescence intensity remains for WS-TDI even after more than 30 min of illumination of the cells, demonstrating again the remarkable photostability of this dye. In Figure 4.6b, the fading of the images is characterized. The total intensity of the sequence images are plotted *versus* time. The intensity curves for the three dyes clearly indicate the superior imaging quality of the WS-TDI dye due to its high photostability.

4.3 Two other WS-TDI derivatives: WS-TDI dodecyl and WS-TDI pyridoxy

4.3.1 New derivatives for a larger panel of applications

We have seen above that the combination of the hydrophilic terrylene core with four negatively charged sulfonyl side groups provide water-solubility to the WS-TDI molecule (Figure 4.7a) as well as a strong affinity to lipidic environments. Moreover, it was shown that membranes and membranes containing compartments of living cells can be labelled with WS-TDI and exhibit a bright signal. However, in some experiments it is also useful to label the cell membrane itself. It is in principle more difficult to mark the latter since its narrow thickness (typically in the order of 2-3 nm) limits the maximal uptake of fluorophore. The efficiency of the labelling of such membranes can be substantially improved by modifying the structure of WS-TDI in order to strengthen the interactions between the dye molecules and the lipid bilayer of the cell membranes. This was accomplished by adding to the WS-TDI a dodecyl alkyl tail (WS-TDI dodecyl). The structure is shown in Figure 4.7b. This new compound has higher hydrophobicity and, as a consequence, can better penetrate into the thin bilipid layer of the cell membrane.

Another parameter of WS-TDI that can be varied is the charge of the molecule. The molecule has four negative charges belonging to the sulfonyl groups. For some applications, it would be of great interest to develop a third water-soluble terrylene derivative with properties similar to those of WS-TDI i.e. water-solubility, high photostability and affinity for lipidic environment, but positively charged. This was achieved using pyridoxy cations as side groups during the synthesis leading to a four positively charged new WS-TDI derivative (WS-TDI pyridoxy, the structure is shown in Figure 4.7c). In this Section, the properties and the performances of these two new dyes are investigated and compared to the WS-TDI derivative previously investigated.

4.3.2 Photophysical parameters

4.3.2.1 Absorption and fluorescence spectra

The only structural difference between WS-TDI and WS-TDI dodecyl is the alkyl tail which confers higher hydrophobicity to the dye molecule. This should in principle have minor consequences on the photophysical properties of the dye since the apolar dodecyl chain has a weak influence on the terrylene core. The absorption and fluorescence

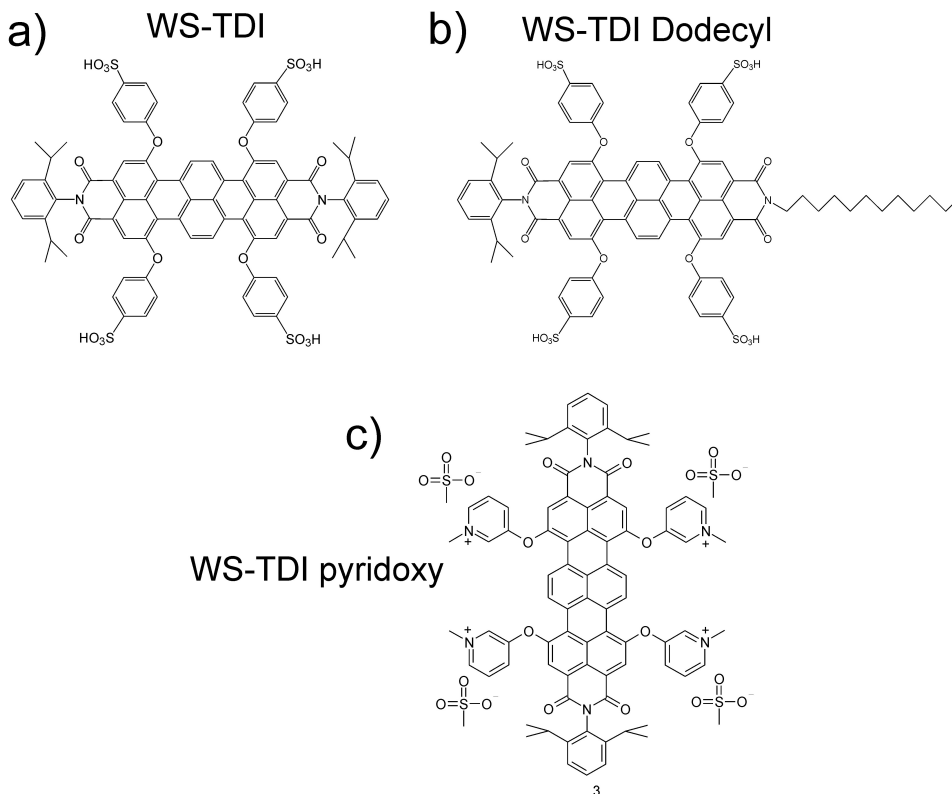


Figure 4.7: Structure of the three WS-TDI derivatives.

spectra of WS-TDI dodecyl in water are shown in figure 4.8a (black lines). As expected, both spectra resemble the corresponding spectra of WS-TDI (see Figure 4.2b and c). The absorbance spectrum shows a broad band with a maximum at about 634 nm which indicates the presence of aggregates, similarly to what was observed with WS-TDI (maximum at 637 nm for WS-TDI). No signal is detected in the corresponding fluorescence spectrum, which is consistent with the quenching phenomenon of the fluorescence when the dye molecules aggregate. Light scattering measurements were performed in an aqueous solution of WS-TDI dodecyl ($c \sim 10^{-5}$ mol/L), and revealed the presence of two populations of aggregate sizes: 58% of the particles have a mean size of 280 ± 47 nm, and 42% have a mean size of 950 ± 110 nm. The latter population contain much larger aggregates than in an aqueous solution of WS-TDI at the same concentration (449 ± 49 nm). The formation of this population with a size in the order of micrometer can be explained by the larger hydrophobic part of the WS-TDI dodecyl compared with WS-TDI. This leads to stronger inter-molecular interactions, and hence enhances the tendency of the molecules to aggregate.

The absorption and fluorescent spectra in presence of 10% wt/wt of Pluronic (blue lines) show a maximum at 666 nm for the absorption spectrum and a maximum of 693 nm for the fluorescent emission spectrum. These spectra are also very similar to

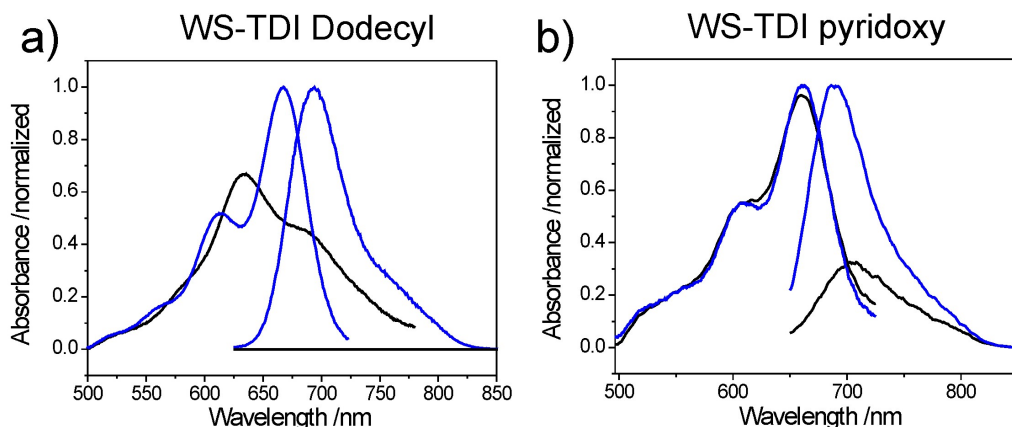


Figure 4.8: Absorbance and fluorescence emission spectra of the two new WS-TDI derivatives. (a) Absorbance and fluorescence emission spectra of WS-TDI dodecyl in water (black lines) and in presence of 10% wt/wt of Pluronic (blue lines). No fluorescence signal is observed in water, whereas the fluorescence is intense in presence of Pluronic. (b) The same for WS-TDI pyridoxy. The fluorophore fluoresces weakly in water.

those measured with WS-TDI in presence of Pluronic. Moreover, the quantum yield in water in presence of Pluronic for WS-TDI dodecyl and WS-TDI are very close (0.14 and 0.16 respectively). These results demonstrate that the disruption of non-fluorescent dye aggregates into micelles also occurs with WS-TDI dodecyl similarly to what was observed with WS-TDI. Moreover, the dodecyl chain has no significant influence on the quantum yield of the dye, as was expected.

The absorption and fluorescence spectra of WS-TDI pyridoxy contrast with those of WS-TDI and WS-TDI dodecyl (Figure 4.8). First, the absorbance spectra of WS-TDI pyridoxy in water (black line to the left) and in water in presence of 10% wt/wt of Pluronic (blue line to the left) are very similar, with a maximum of absorption at about 662 nm. Another significant difference compared to the two previously investigated dyes is that WS-TDI dodecyl fluoresces in pure water as well as in water containing micelles of Pluronic, with emission maxima at about 705 nm and 689 nm respectively. Finally, contrary to the two other WS-TDI derivatives no signal was detected in light scattering measurements of a solution of WS-TDI pyridoxy at the same concentration ($c \sim 10^{-5}$ mol/L). Altogether these observations suggest that WS-TDI pyridoxy molecules do not form aggregates in water. This can be explained by a stronger repulsion of the pyridoxy groups compared to the sulfonyl group of the two other terrylene derivatives, which leads to a better solubility of WS-TDI pyridoxy in water.

However, the intensity of the fluorescence emission in water is very weak ($\phi_f = 0.016$). This quenching of the fluorescence may rely on the influence of the very polar pyridoxy

groups. As WS-TDI pyridoxy does not form aggregates in solution, no dramatic increase of the quantum yield upon addition of Pluronic was expected here. Nevertheless, the quantum yield in water in presence of 10 % wt/wt Pluronic is about 2 fold increased ($\phi_f = 0.039$). This can be explained by a more suitable environment for the fluorophore in the hydrophobic inner part of the micelles, since it is known that the quantum yield of a fluorophore is very sensible to its environment. However, this value is below the values of the quantum yield of WS-TDI ($\phi_f = 0.16$) and WS-TDI dodecyl ($\phi_f = 0.14$). Such a low value can be explained by stronger interactions between the pyridoxy groups and the fluorescing terrylene core of the fluorophore than with the sulfonyl groups.

In summary the photophysical properties of WS-TDI and WS-TDI dodecyl are very similar, which shows that the dodecyl tail has a very weak influence of the chromophore. In contrast, pyridoxy groups of WS-TDI pyridoxy allow an increased solubility in water without formation of aggregates, although they quench significantly the fluorescence emission. Photophysical parameters are summarized in Table 4.3.

4.3.2.2 Photostability

The photostability of the three water-soluble terrylene derivatives was measured and compared with those of ATTO647N and Cy5, two fluorophores commonly used in biological studies, and known for their high photostability.

As previously the dye molecules were embedded at ultra-low concentration ($\sim 10^{-10}$ mol/L) in a thin Poly(vinylalcohol) (PVA) polymer film by spin-coating. Fluorescence intensity trajectories of individual molecules were measured. Two photostability parameters were extracted from the time-traces: the individual total emitted photons before photobleaching (TEP, integral over a time-trace), and the individual survival time (ST, total duration of the time-trace until photobleaching). The probability distributions of these two parameters were best fit with bi-exponential decays (similarly to those of WS-TDI), and average TEP and ST were extracted. The probability distributions are shown in Figure 4.9a (TEP) and b (ST) for the three water-soluble terrylene derivatives as well as those of Cy5 and ATTO647N in PVA. About 60 single molecules of each fluorophore were investigated under the same experimental conditions.

The average TEP for WS-TDI is calculated to be 58×10^6 , and the average ST is 42 s in PVA. Similar values were found for WS-TDI dodecyl with average TEP = 61×10^6 and average ST = 44 s. These values confirm that addition of the alkyl chain has no significant influence on the photostability of the dye. On the other hand, WS-TDI pyridoxy has an average TEP of 43×10^6 and an average ST of 36 s. WS-TDI pyridoxy emits then about 30% less photons than WS-TDI and WS-TDI dodecyl in PVA, and has

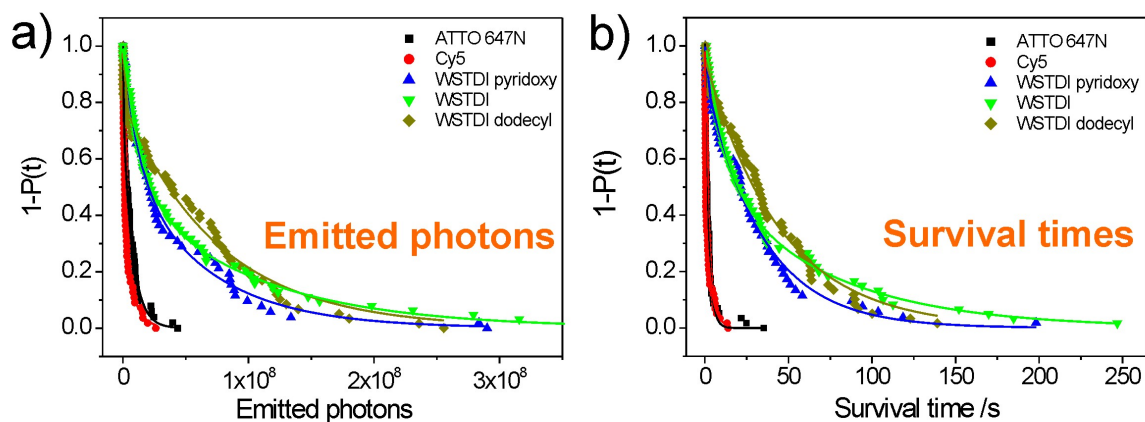


Figure 4.9: (a) Accumulated probability distributions of the TEP for WS-TDI (green triangles), WS-TDI dodecyl (yellow squares), WS-TDI pyridoxy (blue triangles), Cy5 (red circles), and ATTO 647N (black squares). Similarly to the study of WS-TDI the curves cannot be fitted with a single component exponential decay. Instead, two-component decays were used and are shown as solid lines, rendering average TEPs. (b) Similar evaluation for the ST with bi-exponential fits shown as solid lines.

Table 4.3: Photophysical parameters for the three water-soluble derivatives and other dyes

Fluorophore	$\lambda_{abs}^{max}, \lambda_{em}^{max}, \varphi_{f,H_2O}$	$\lambda_{abs}^{max}, \lambda_{em}^{max}, \varphi_{f,H_2O}$ 10% wt/wt Pluronic	Total emitted photons ($\times 10^6$)	Survival time (s)
WS-TDI	637 nm, -, 0	670 nm, 700 nm, 0.16	58 ± 5	42 ± 4
WS-TDI dodecyl	634 nm, -, 0	666 nm, 693 nm, 0.14	61 ± 3	44 ± 5
WS-TDI pyridoxy	660 nm, 705 nm, 0.016	661 nm, 688 nm, 0.039	43 ± 4	36 ± 2
ATTO 647N	-	-	5.3 ± 0.7	1.6 ± 0.2
Cy5	$\varphi_{ref} = 0.29$	-	3.4 ± 0.6	1.7 ± 0.2

an about 15% shorter lifetime before photobleaching. This lower TEP can be attributed to the strong influence of the positively charged pyridoxy groups on the terrylene core, which leads probably to the decrease of the quantum yield as well as of the photostability in PVA.

Nevertheless, all the three water-soluble terrylene derivatives emit over 8 times more photons before photobleaching, and live more than 21 times longer than ATTO647N or Cy5. These data show that all three water-soluble terrylene derivatives have a much

higher photostability than the two other investigated dyes. This makes these water-soluble derivatives very promising photostable dyes for ensemble as well as for single molecule experiments.

4.3.3 Fluorescence spectra in presence in cells

WS-TDI dodecyl is expected to penetrate more efficiently than WS-TDI into lipidic membranes because of the presence of its hydrophobic alkyl tail. The affinity of WS-TDI and WS-TDI dodecyl for membranes and membrane containing compartments of living cells was compared by fluorescence spectrometry in dye-uptake experiments.

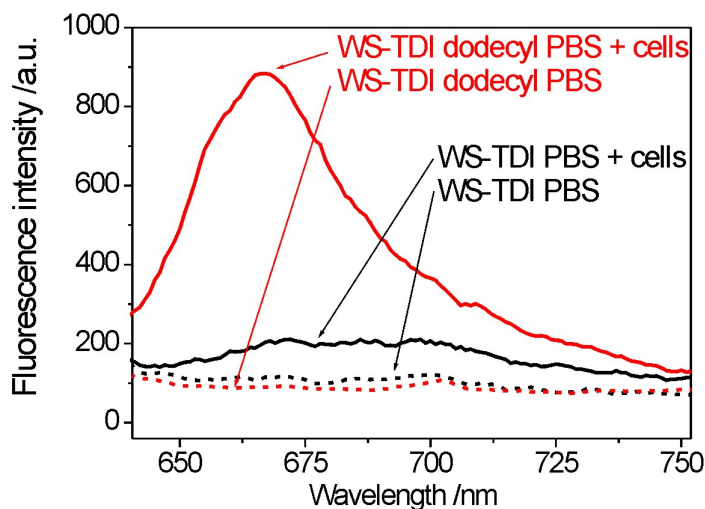


Figure 4.10: Fluorescence emission spectra of WS-TDI ($\sim 10^{-5}$ mol/L, black dotted line) and WS-TDI dodecyl ($\sim 10^{-5}$ mol/L, red dotted line) in PBS, and in PBS in presence of HeLa living cells ($\sim 10^{-5}$ mol/L, black and red full line respectively). Fluorescence emission in presence of living cells is observed for both dye, however with a much stronger intensity for WS-TDI dodecyl.

The fluorescence emission spectra of WS-TDI and WS-TDI dodecyl in a PBS solution at a concentration of 10^{-5} mol/L are displayed in Figure 4.10 (dotted black and red lines, respectively). In both cases no fluorescence signal is detected which was expected since the dye molecules are sequestered in non fluorescing aggregates in water. The black and red lines in Figure 4.10 show the fluorescence spectra of the same solutions of WS-TDI and WS-TDI dodecyl, one hour after addition of HeLa living cells. The appearance of a signal is observed in the fluorescence spectra of both dyes, with an maximal intensity at around 670 - 700 nm for WS-TDI, and around 670 nm for WS-TDI dodecyl. These observations can be explained by the disruption of the dye aggregates in membranes and membrane containing compartments of the living cells during the

dye-uptake process. This phenomenon is similar to the dissolution of the aggregates in the hydrophobic micelles of Pluronic, and leads to the formation of fluorescing WS-TDI and WS-TDI dodecyl monomers within the lipidic membranes of the cells. Another immediate observation is that the fluorescence intensity of WS-TDI dodecyl in presence of living cells is much more intense (about 4 times stronger) than for WS-TDI in presence of cells. This demonstrates that the dye-uptake process is clearly more efficient for WS-TDI dodecyl. Hence, the hydrophobic alkyl greatly helps the incorporation of the fluorophore in the lipidic membranes, as expected.

4.3.4 Membrane labelling in living cells

The high affinity of the three water-soluble terrylene dye molecules for lipidic environments can be used to image the membranes and membrane containing compartments of living cells. In dye-uptake experiments, solutions of WS-TDI, WS-TDI dodecyl, and WS-TDI pyridoxy were added at a concentration of 10^{-5} mol/L to living HeLa cells adherent onto cover glasses at 37 °C. After an incubation time of 1 h the three solutions were washed three times with an aqueous solution of PBS to remove the excess of dye.

The first part of this Section presents data acquired with a standard confocal microscope, and will be used to compare the imaging properties of the membranes and membrane containing compartments of living cells.

In a second part, a wide-field setup, which allows higher signal sensitivity and better temporal resolution, is used to image the endocytic traffic, and to evaluate the photobleaching of the three dyes within the living cells.

The three dyes could be easily detected with the standard detector (photo-multiplier) of a conventional confocal microscope. Figure 4.11a shows the fluorescence image of living HeLa cells stained with WS-TDI (left) juxtaposed with the corresponding transmission image (right). In each cell many vesicles appear as bright spots, and the cell membranes are slightly visible. Figure 4.11b shows the same images for WS-TDI dodecyl. Similarly to WS-TDI the endocytic system can be imaged. However, a remarkable difference here is that the cell membranes are much brighter. This stronger labelling efficiency of the cell membranes demonstrates again the higher affinity of WS-TDI dodecyl than WS-TDI for lipid bilayer membranes.

Figure 4.11c displays a fluorescence image of HeLa cells stained with WS-TDI pyridoxy. This is very similar to the fluorescence image of cells marked with WS-TDI shown in Figure 4.11a i.e. bright labelled endosomes can be seen whereas the cell membranes emit only a weak fluorescence signal.

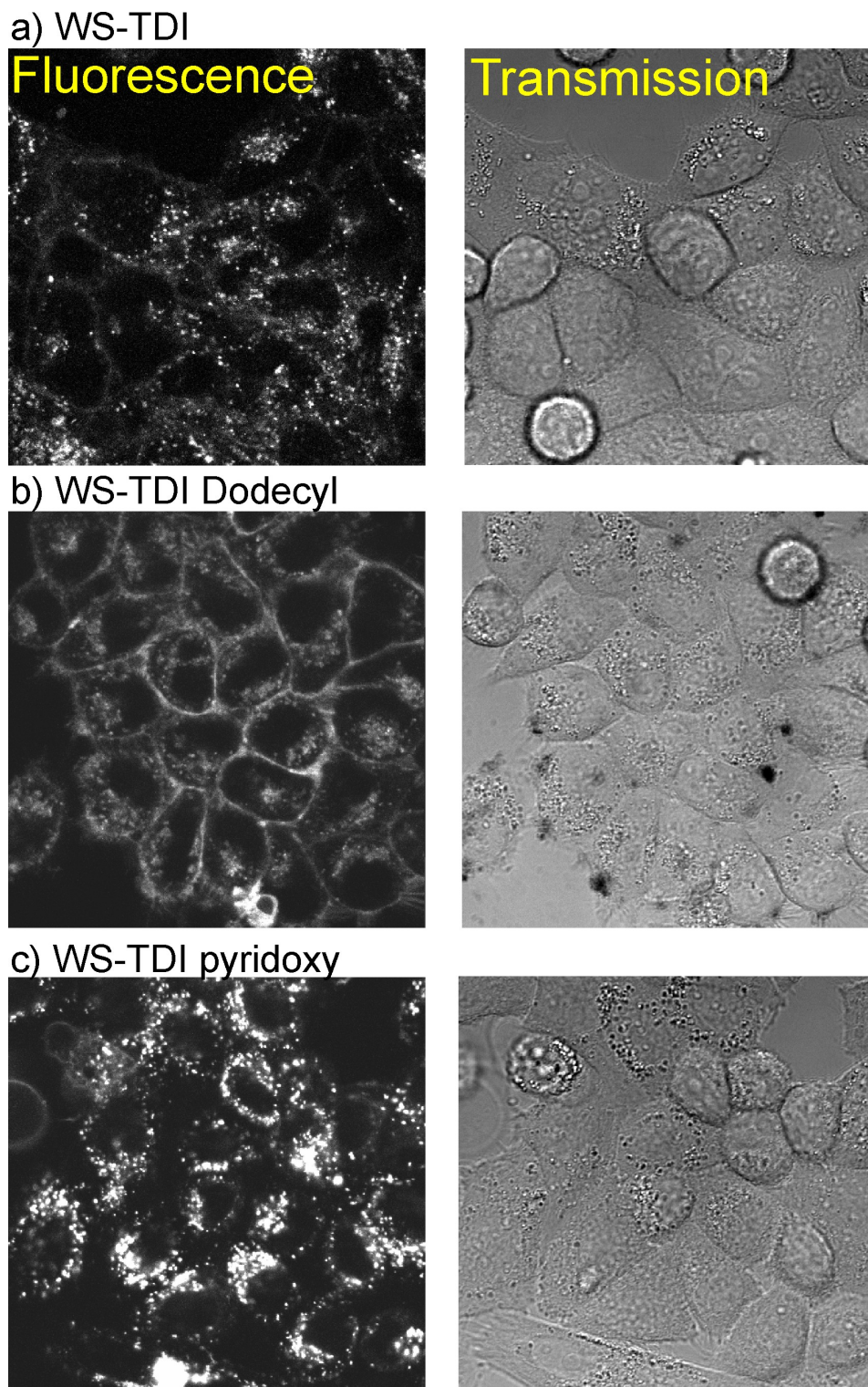


Figure 4.11: Confocal fluorescence images of living HeLa cells stained with WS-TDI, WS-TDI dodecyl, and WS-TDI pyridoxy (left) juxtaposed with the corresponding transmission image (right). The endocytic system is labelled with the three WS-TDI derivatives. The cell membranes particularly strongly labelled with WS-TDI dodecyl.

The pathway of the endosomes labelled with the new fluorophores can be monitored by wide-field microscopy. Figure 4.12a shows four fluorescence images extracted from movies (600 frames; 500 ms /frame, measured under the same experimental conditions) of HeLa cells stained with either WS-TDI, WS-TDI dodecyl, WS-TDI pyridoxy or Alexa647/dextran. This latter dye is a well known fluid phase marker. It was used here as a "reference" to evaluate the capability of the three new terylene derivatives to be used as fluid phase marker, and to compare their photostability when incorporated in membranes of living cells. The signal-to-noise ratio, which is an indicator for good data quality, is higher for WS-TDI and WS-TDI dodecyl compared to the two other dyes. The presence of non fluorescing aggregates in the plasma can explain the absence of background light for WS-TDI and WS-TDI dodecyl. As both WS-TDI pyridoxy and Alexa647/dextran fluoresce in water, a background may arise for these two fluorophores from the remaining dye molecules in the plasma of the living cells, or from molecules adsorbed onto the surface of the glass coverslip. This fluorescence background leads to the decrease of the signal-to-noise ratio.

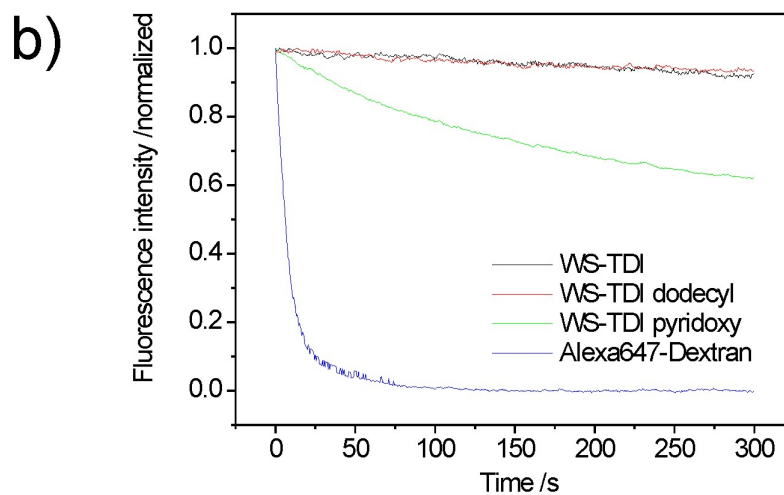
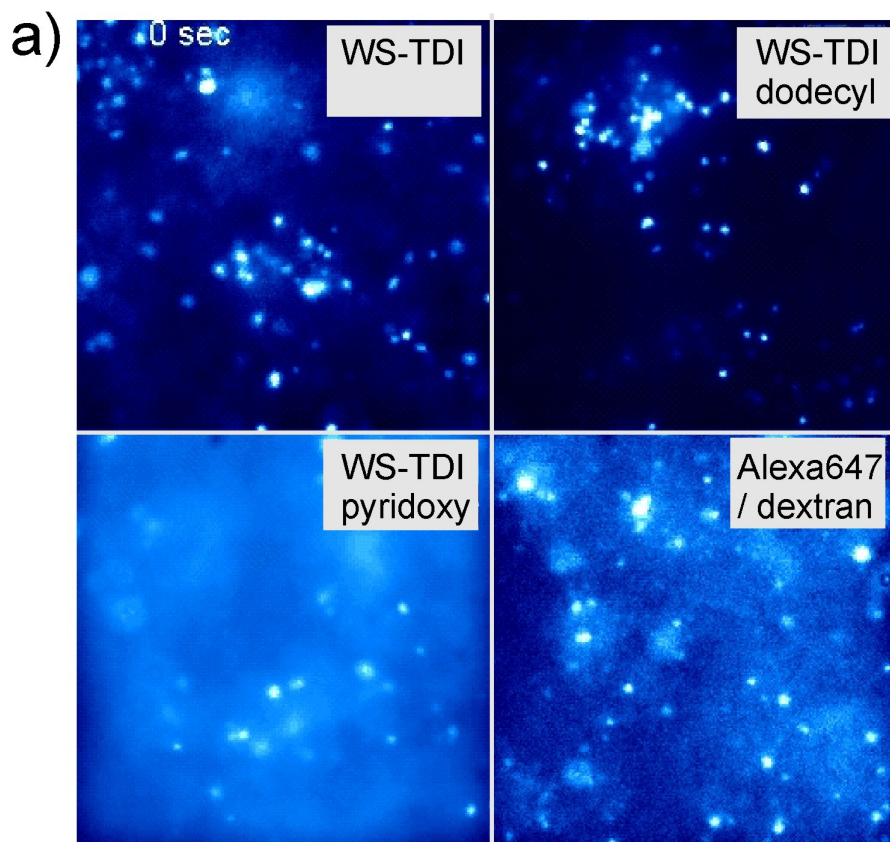


Figure 4.12: (a) $20\ \mu\text{m} \times 20\ \mu\text{m}$ frames extracted from four sequences of images of HeLa cells adhered onto a cover glass in PBS and stained with WS-TDI (upper left), WS-TDI dodecyl (upper right), WS-TDI pyridoxy (lower left), and Alexa647/dextran (lower right). The depicted images were acquired at the beginning of illumination. (b) Plot of the normalized fluorescence intensity as a function of time for the four image sequences.

In each of the four movies the movement of the endosomes can be nicely monitored. This demonstrates that the three water-soluble terrylene dye molecules act as fluid-phase markers like Alexa647/dextran i.e. the three new fluorophores can be used for marking the membrane containing compartments of living cells. However, the three water-soluble terrylene dyes show a superior photostability (visualized in Figure 4.12b). The total intensity decays of each frame is displayed *versus* time for the four investigated fluorophores. Whereas the fluorescence intensity of the Alexa647/dextran (blue line) decays rapidly to nearly zero within some seconds, the signal of WS-TDI (black line) and WS-TDI dodecyl (red line) remains nearly constant during the whole observation time, and the fluorescence intensity of WS-TDI pyridoxy (green line) fades of about 37%. To summarize, these data demonstrate that each of the three new water-soluble derivatives can be used as ideal fluid-phase markers. Furthermore, their very high photostability constitutes a major advantage compared with other dyes commonly used in biological studies like Alexa647/dextran.

4.4 Localization of the three WS-TDI derivatives in the early and late endocytic pathway of living cells

The three new water-soluble TDI derivatives are extremely photostable and can be used to image membranes and membrane containing compartments in living cells. An important question is the exact localization of the different dye molecules in the endocytic pathway. The endocytic system can be divided into two populations of endosomes according to their pH: the early endosomes that are involved in uptake of fluids from the outside of the cell membrane and whose pH is around 7, and the late endosomes that appear later in the endocytic pathway and are more acidic with a pH of about 5. In order to develop utilization of the new water-soluble terrylene derivatives for biological studies, it is of paramount importance to characterize the dye uptake process and the interactions involved between the markers and the components of the living cells like vesicles. To answer these questions, the dye uptake process in living cells was investigated for each of the new fluorophores. This study is based on co-localization experiments between the three red WS-TDI derivatives and green labelled Rab GTPases in the endocytic traffic of Human Hapatoma (HuH-7) living cells.

The Rab proteins are central players of the vesicular transport in cells, and are particularly important to ensure the specificity of transport.¹⁷⁸⁻¹⁸¹ The Rab proteins belong to the Ras superfamily of small GTPases. One of their main features is to exist as two conformations: a GDP-bound stage in which the protein is inactive and kept soluble in the cytosol, and a GTP-bound stage. The GTP-bound stage represents the active form of the protein and is tightly associated to the membrane of an organelle (cellular substructures) or to the membrane of transport vesicles through an hydrophobic lipid anchor. Once in the GTP-bound form, the Rab proteins binds to other proteins designed as Rab effectors, which will further facilitate vesicle formation and transport, membrane tethering and membrane fusion. Over 70 different Rab proteins have thus far been identified, and it is noteworthy that each of them displays a specific subcellular distribution, being associated to specific structures. The highly selective distribution of the Rab proteins among the membrane trafficking system in cells make them ideal endogenous markers/labels to define the identity and the route of vesicles. In this study, the Rab5 and Rab9 proteins have been chosen as markers since Rab5 specifically localized on early endosome while the Rab9 is found specifically on late endosome structures (see Figure 4.13).

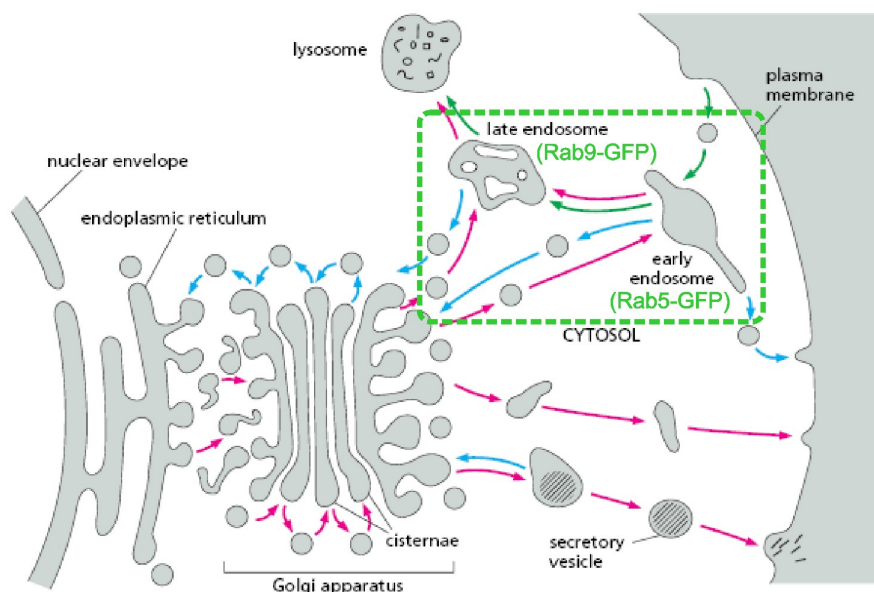


Figure 4.13: Endocytic pathways, adapted from Alberts et al.¹⁸² The early and late endosomes are highlighted with a green dotted rectangle.

In order to address the identity of the vesicles stained by the new dyes, co-localization assays were performed using HuH-7 cells that express either Rab5 fused to the Green Fluorescent Protein (GFP) or Rab9 fused to GFP (constructed in our group by Nadia Ruthardt). Each of those cell lines were marked with the three WS-TDI derivatives. The dye concentration was in each case 5×10^{-6} mol/L (see experimental section for details). GFP was excited with a 532 nm laser line whereas the WS-TDI derivatives were excited with a 633nm laser line. The fluorescence emission spectra of the WS-TDIs and GFP are well separated, which allows imaging the WS-TDI derivatives and the Rab GTPases simultaneously on two separated channels, allowing to address any co-localization between the endosomes labelled by the dye and Rab5 labelled early endosomes or Rab9 labelled late endosomes.

The HuH-7 cells marked with the WS-TDI derivatives were imaged with a confocal microscope using simultaneously two laser lines of 532 nm and 633 nm. The time evolution of the fluorophores in the endocytic pathway was observed for HuH-7/Rab5-GFP and HuH-7/Rab9-GFP at three different time points: (1) After 40 min of incubation time with the fluorophore, (2) 30 min after washing of the remaining dye and (3) 16 h 30 min after washing, which corresponds to a very long time in living cell experiments. Figure 4.14 shows overlays of the two channels where the red color corresponds to the fluorescent signal of the WS-TDI derivatives and the green color to the emission of the GFP Rab GTPases. Direct co-localization of the vesicle containing both Rab GTPases and a WS-TDI derivative will appear in yellow.

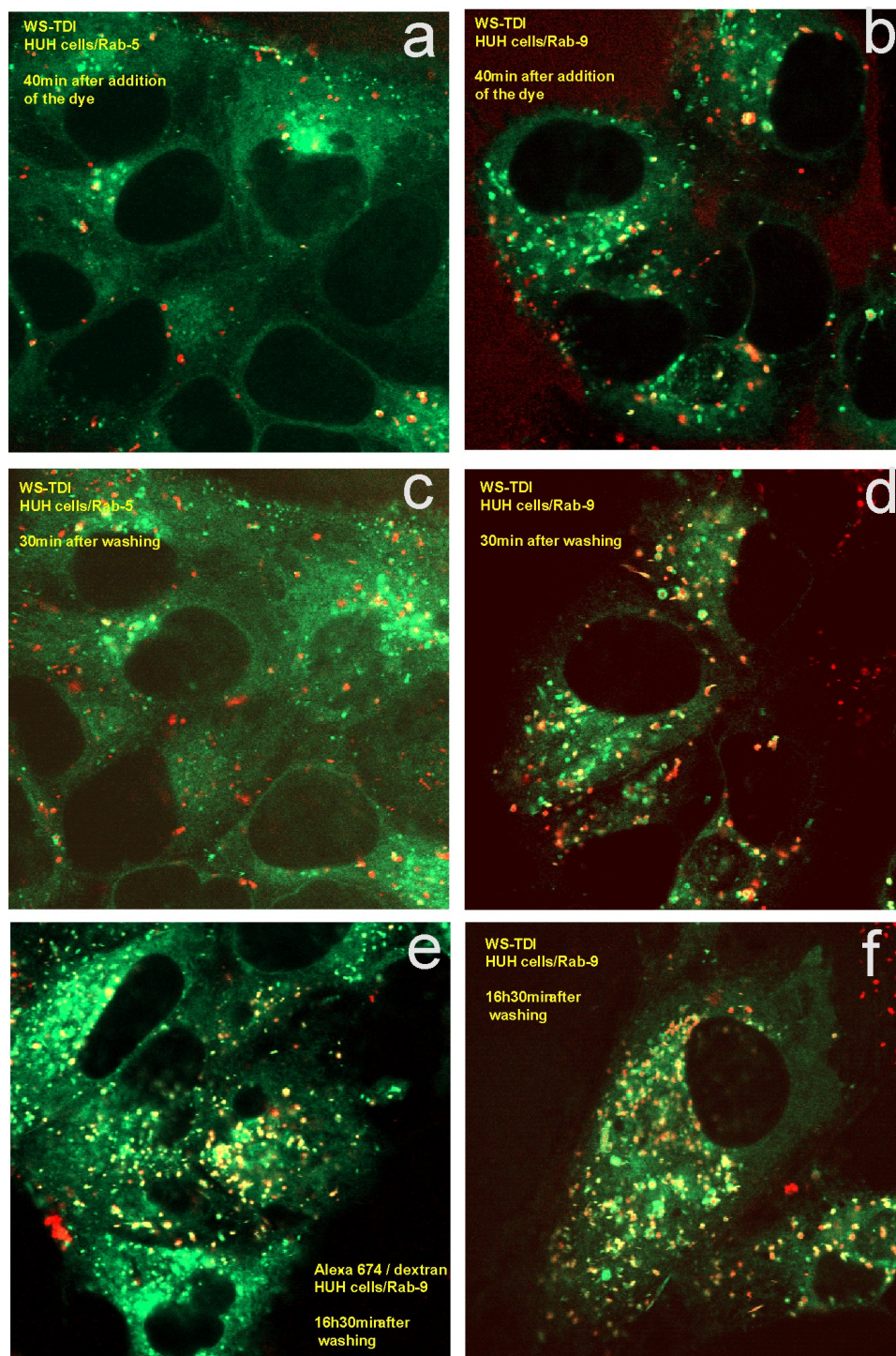


Figure 4.14: Fluorescence images of Human Hepatoma (HuH-7) living cells with Rab5 or Rab9 GTPases fused to the the Green Fluorescent Protein (GFP), and stained with WS-TDI or Alexa647 / dextran. A 532 nm laser was used for excitation of GFP-GTPases, which appear as green spots, and a 633 nm laser was used for excitation of WS-TDI (red spots). The endosomes containing both a Rab GTPase and WS-TDI appear as yellow dots. (a) and (b) HuH-7 cells/Rab5 and HuH-7 cells/Rab9 stained with WS-TDI, 40 min after addition of the dye. (c) and (d) HuH-7 cells/Rab5 and HuH-7 cells/Rab9 stained with WS-TDI, 30 min after removing of the excess of dye. (e) and (f) HuH-7 cells/Rab9 stained with Alexa647 / dextran and WS-TDI respectively, 5 h 30 min after washing of the excess of dye.

Figure 4.14a shows a fluorescence image of HuH-7/Rab5-GFP cells after 40 min incubation in a solution of WS-TDI. A first observation is that part of the vesicles appear in yellow, indicating that they contain both Rab5-GFP and WS-TDI. A close inspection of the remaining endosomes reveals that the green dots, i.e. Rab5-GFP containing endosomes, exhibit also a small fluorescent signal in the red detection channel. This means that they also contain WS-TDI, however at lower concentrations. The red dots do not show any signal in the green detection channel i.e. here WS-TDI is not encapsulated in Rab5 containing early endosomes, but in another type of endosomes. One can thus conclude that WS-TDI is able to stain early endosomes according to the overlay of red and green dots. However, there is a second population which doesn't co-localize with Rab5-GFP.

The identity of the second population of WS-TDI can be addressed investigating HuH-7 cells/Rab9-GFP stained with WS-TDI (at the same time point, see Figure 4.14b). Here some endosomes appear in yellow, which means that WS-TDI is contained in late endosomes (identified by Rab9-GFP). Moreover, endosomes containing Rab9-GFP but not WS-TDI can be observed (green dots), as well as endosomes containing WS-TDI without Rab9-GFP (red dots). This shows that after 40 min of incubation a part of the Rab9-GFP containing endosomes are already labelled with WS-TDI.

Moreover, the transition to the late endosomes is not completed after 40 min since some Rab9-GFP vesicles do not show the presence of WS-TDI i.e. they appear as green dots.

The dye uptake into endosomes can be investigated by washing out the cells with fresh medium in order to deplete dye molecules from the medium. Figure 4.14c and 4.14d show overlaid fluorescence images 30 min after washing out the dye of HuH-7/Rab5-GFP cells and HuH-7/Rab9-GFP cells respectively. Nearly no co-localization between the Rab5-GFP and WS-TDI containing endosomes can be observed in the image shown in Figure 4.14c. In contrast, Only yellow dots are visible in Figure 4.14d which i.e. WS-TDI is contained in the totality of the observable late endosomes. This demonstrates that WS-TDI is incorporated in the early endosomes which mature into late endosomes as long as the dye uptake process is possible, but that this process stops as soon as no dye is available anymore in the medium outside the cells. Moreover, after a certain time (already 30 min after washing), all the late endocytic system is labelled with WS-TDI.

The robustness of the labelling of the late endosomes with WS-TDI on longer timescale can be checked by monitoring the fluorescence of HuH-7/Rab9-GFP cells on a much longer timescale. Figure 4.14e which was recorded 16 h 30 min after washing. All the visible endosomes appear as bright yellow dots. This confirms that the late endosome system is still strongly labelled with WS-TDI even after longer time.

This ability of WS-TDI to label the late endocytic systems can be compared with those of a classical fluid phase tracer such as Alexa647/dextran. Figure 4.14e shows a fluorescence image of HuH-7/Rab9-GFP cells stained with Alexa647/dextran (which can be excited at 633 nm like WS-TDI) similarly to the previous experiment, and 16 h 30 after washing of the excess of fluorophore. This image is very similar to Figure 4.14f that is the totality of the late endosomes are labelled with Alexa647/dextran and appear as yellow spots. This confirms again that WS-TDI can be used like endosomal uptake markers since it follows the endocytic pathway.

Finally, all the measurements described above were performed with WS-TDI and WS-TDI dodecyl as well, with strictly identical results. To conclude, these data shed light on the pathway followed by the three water-soluble terrylene dyes after uptake in living cells. The fluorophores act as endosomal uptake markers: the dye molecules are first incorporated (within several minutes) in the early endosomes of the cells, then they are progressively transferred to the late endocytic system where the fluorescence signal is stably observed for several hours.

4.5 Conclusion

The photophysical properties of three new water-soluble terrylenediimide dyes have been investigated as well as their potential utilizations for applications in biological studies.

WS-TDI is water-soluble and forms H-type non fluorescent aggregates in water solution. The addition of surfactants, e.g. Pluronic P123 or CTAB, to an aqueous solution of WS-TDI leads to the formation of strongly fluorescent species that can be assigned as monomeric WS-TDI molecules incorporated in micelles.

A single molecule study showed a much higher photostability of WS-TDI in comparison with other well known water-soluble dyes such as oxazine-1, sulforhodamine B or a similar perylendiimide derivative. Furthermore, labelling of a single protein like avidin has been demonstrated and the properties of single WS-TDI labelled avidin molecules have been characterized by FCS and photostability measurements.

The uptake of WS-TDI in liposomes and in living HeLa cells demonstrates the outstanding capability of the WS-TDI to label artificial and natural lipid membrane containing compartments. To our knowledge there is no other dye which can image the trafficking of e.g. endosomes in living cells over such a long period with such a high brilliance.

WS-TDI dodecyl, which results from the addition of an alkyl tail onto WS-TDI, has similar properties as WS-TDI e.g. similar photophysical properties and the existence of aggregates which disrupt into the monomeric fluorescing form upon addition of a surfactant like Pluronic. However, the dye molecule is more hydrophobic than WS-TDI, and thus have more affinity for lipidic membranes of living cells.

WS-TDI pyridoxy, the positively charged form of WS-TDI, do not form aggregates and fluoresces weakly in water. This dye molecule has weaker quantum yield and photostability than the two other terrylene derivatives, which is probably due to the influence of the polar pyridoxy side groups on the terrylene fluorescing core.

Finally, the *in vivo* characterization established the WS-TDI derivatives as powerful potential tools for biological studies in membrane containing compartments traffic. Indeed, these dyes are well incorporated into early endosomes (colocalized with Rab5-GFP), and allow to further follow their maturation into late endosomes without affecting the cells over 16 hours.

4.6 Experimental section

UV-Visible Absorption and Fluorescence Spectroscopy: UV-visible measurements were performed with a Cary 50 Conc spectrophotometer (Varian), and fluorescence spectra measurements with a F900 luminescence spectrometer (Edinburgh Analytical Instruments). Particle sizes were measured by laser-light scattering using a Malvern Zetasizer 3000HS (Malvern Instruments, Worcestershire, UK). Quantum yields of fluorescence were measured by comparing the fluorescence intensity of the sample to that of optically dilute solutions of Cy5 in millipore water ($\varphi_f = 0.27$).¹⁸³ In the quantum yield experiments, changes in the absorption coefficient upon addition of Pluronic P123 or CTAB were compensated by shifting the excitation wavelength to keep the same total absorption of the sample. Excitation wavelengths varied between 640 - 655 nm.

Photostability measurements: To investigate the photostability on a single molecule level, the dyes were embedded in polymer matrixes. Two different polymers were used: polyvinyl-alcohol (PVA) and polymethyl-methacrylate (PMMA). Thin polymer films (100-200 nm) were prepared by spin-coating fluorophores in polymer solutions at a concentration of 10^{-9} mol/L (1 min at 1000 rpm, 2% wt/wt PVA in water; 1 min. at 3000 rpm, 2% wt/wt PMMA in chloroform). In addition to the photostability of WS-TDI, the photostability of four other dyes was investigated: water-soluble perylene diimide (WS-PDI) (Figure 4.1b), oxazine-1 (Figure 4.1c), terrylene diimide (TDI) derivative (Figure 4.1e) and sulforhodamine-B (Figure 4.1f). Sulforhodamine B and Oxazine-1 were purchased commercially (Lambdachrome). WS-PDI and Sulforhodamine-B have similar absorption spectra (data not shown) and were excited with a continuous wave (cw) krypton-ion laser (568 nm). The maximum of fluorescence emission was observed at around 610 nm. WS-TDI, TDI and Oxazine-1 were excited with a cw He-Ne laser (633 nm) and had the maximum of fluorescence emissions at approximately 700 nm. The confocal setup described in Section 2.1.3.3 was used to visualize fluorescence of the individual dye molecules. Using circular polarized excitation light, all in-plane molecular absorption dipoles were excited with the same probability. The excitation power at the entrance of the objective (ZEISS 40x 1.3 NA oil) was set to 18 μ W. The total detection efficiency of the experimental setup is estimated to be 2.5% and was used to calculate the total number of emitted photons.

Synthesis of Monocarboxylic Acid Functionalized WS-TDI: The monocarboxylic acid-functionalized terrylene diimide was synthesized by using *N*-(5-carboxypentyl)-naphthalenedicarboximide and a perylene dicarboximide in the one-pot synthesis (*t*-BuONa/DBN, diglyme) of terrylene diimide.⁵¹ Bromination of this terrylene diimide with elemental bromine in chloroform gives the corresponding tetrabrominated ter-

rylenediimide. The substitution under basic conditions of the four bromine atoms with phenol and subsequent sulfonation with concentrated sulfuric acid at room temperature afford the monocarboxylic acid-functionalized WS-TDI (1,6,9,14-Tetra(4-sulfonylphenoxy)-N-(2,6-Diisopropylphenyl)-N'-(5-carboxypentyl)-terrylene-3,4:11,12-tetracarboxidiimide). The structure is shown in Figure 4.1d.

Protein labelling: Terrylenediimide monocarboxylic acid was used to label the amine group of exposed lysine residues of avidin. The avidin protein was dissolved at a concentration of 10 mg/mL in PBS buffer (phosphate-buffered-saline). The monocarboxylic acid-functionalized terrylenediimide to be coupled was dissolved in the same buffer. The dye solution was added to the protein solution in a 10 molar-excess. An EDC (1-ethyl-3-[3-dimethylaminopropyl] carbodiimide Hydrochloride) solution was added to obtain a 20-fold molar-excess of EDC to the protein. The cross-linking reaction was performed in an Eppendorf tube. The tube was shaken on a test-tube-shaker for 4 h at 30 °C.

Micro bio-spin chromatography was used to purify the labelled avidin from unbound WS-TDI. A volume of 50 μ L of the reaction mixture was applied to a micro-spin column (Micro-spin G-50 column, Amersham) and centrifuged for 2 minutes at 3000 rpm. The procedure was repeated a second time to increase the purity of the labelled-protein sample.

Liposome labelling: The liposomes were a gift from Martin Hossann (Klinikum Grosshadern, Munich). Liposomes composed of DPPC (1,2-dipalmitoyl-*sn*-glycero-3-phosphocholine), DSPC (1,2-distearoyl-*sn*-glycero-3-phosphocholine), and DPPGOG (1,2-dipalmitoyl-*snglycero*- 3-phosphoglyceroglycerol) in a 5:2:3 molar ratio in N-[2-Hydroxyethyl] piperazine- N'-[2-ethanesulfonic acid] (HEPES) buffered glucose were prepared as described in the literature.¹⁸⁴

WS-TDI was incorporated into the membrane of the liposomes by incubation at room temperature for 1 h. The concentrations of WS-TDI and lipid in the liposome-probe were respectively 0.1 mmol/L and 32 mmol/L. WS-TDI-labelled vesicles were separated from non-inserted fluorophores by spin chromatography on saccharose solution (20% wt/wt) in HEPES buffer (14000 rpm for 90 min at 4 °C). Before performing single molecules wide-field microscopy measurements with the labelled liposomes, the purified sample was diluted 500 times in HEPES buffer.

Live-cell Measurements: HeLa cells (HeLa ACC57, DSMZ, Braunschweig, Germany) were grown in Dulbecco's modified Eagle's medium (DMEM) supplemented with 10% fetal calf serum at 37°C in 5% CO₂ humidified atmosphere. Cell culture, fetal calf serum and PBS buffer were purchased from Invitrogen GmbH (Karlsruhe, Germany). Dye-uptake experiments were conducted in HeLa cells at 37°C.

Solutions ($C = 4 \times 10^{-6}$ mol/L) of WS-TDI, Alexa 647/dextran and N-(3-triethylammoniumpropyl)-4-(6-(4-(diethylamino)phenyl)hexatrienyl)pyridinium dibromide (FM® 4-64 styryl dye, Molecular Probes) were added to the cells adherent on the surface of a cover-glass. After an incubation time of about 40 min, the solutions were washed out 4 times with PBS buffer to remove the excess dye. The fluorescence signal from labelled liposomes and HeLa cells was monitored by epifluorescence microscopy with the wide-field imaging setup described in Section 2.1.3.2. The dye was excited with a He-Ne laser (NEC) at 633 nm, or a Nd-YAG laser (Soliton) at 532 nm. The excitation powers were set to 1.7 mW at the entrance of the microscope. Movies were recorded with a resolution of 122 nm per pixel and an integration time of 100 ms per frame for the diffusion measurements of liposomes in Hepes buffer, and 500 ms per frame for the measurements with HeLa cells.

Chapter 5

Summary

5.1 Single molecule traffic in mesoporous materials

Mesoporous host materials form one of the key materials in nanotechnology, because their nanometer sized channels provide room for guest species at the molecular level. In this thesis single dye molecules are incorporated within the channels of various mesoporous films, and their translational, orientational as well as spectral dynamics within the host matrix are investigated via Single molecule spectroscopy (SMS). This method reveals structural and dynamic features, which are otherwise obscured by ensemble averaging in conventional spectroscopic techniques. Moreover, it provides valuable insight into host-guest dynamics within the porous matrix, thus helping to understand host-guest properties.

Diffusion and orientation of single TDI molecules in different mesophases of Brij-56-templated mesoporous films

It is shown how single terrylendiimide (TDI) molecules can be used as nanoscale probes to map out the structure of different topologies of Brij-56-templated mesoporous thin films. Three different populations of diffusing species can be distinguished: (1) Molecules showing very structured pathways reflecting the ordered structure of the hexagonal phase of the porous host system on a long range of several micrometers. (2) Donought shaped diffraction patterns corresponding to molecules diffusing randomly within the lamellar phase and orientated perpendicular to the substrate. (3) Dye molecules travelling randomly on the external surface of the mesoporous film. Furthermore, occasional transitions between one type of surrounding, for example the hexagonal mesophase, and another such as the lamellar phase can be observed for the same individual dye molecule.

Translational, orientational and spectral dynamics of single TDI molecules in a CTAB-templated mesoporous film

This study shows how by measuring and correlating translational and orientational dynamics as well as orientational and spectral dynamics of single molecules one is able to determine the nano-scaled heterogeneities of the mesoporous host. First, the translational and orientational movement of single TDI dye molecules incorporated as guests in the pores of an CTAB-templated mesoporous film are observed simultaneously. The motion of the TDI molecules is characterized by jumps between regions where the molecule's dynamics are relatively confined. Secondly, the orientational and spectral behavior of single molecules in nanostructured materials was examined simultaneously. Two types of host-guest systems have been investigated: oxazine-1 dye molecules were fixed rigidly in the channels of microporous AlPO₄₋₅ crystals, and TDI dye molecules moving in the mesoporous network of the CTAB-templated mesoporous film. In the first system both spectral fluctuations (< 5 nm), and rare spectral jumps (> 10 nm) of the emission maximum are observed. However, the orientation of the emission dipole of the dye-molecules remained constant. In contrast, the second system shows orientational dynamics as well as substantially more spectral dynamics. In this system the molecules are found to move between different regions in the host. The typical motion of the TDI molecules in the pores of M41S is not continuous, but characterized by jumps between adsorption sites. Moreover, the spectral and orientational dynamics are correlated and arise directly from the different environments that are being explored by the mobile molecule.

Preparation and single molecule investigation of highly structured domains in CTAB-templated mesoporous films

It is shown for the first time how the mesoporous structure of CTAB-templated mesoporous thin films can rearrange on a timescale of days after synthesis into large, highly structured domains of extremely linear channels. The formation and the growth of these domains is strongly dependent on the RH, with an optimal range of 40 - 50% of RH for the formation of large domains (up to 100 μm in size). In order to investigate these highly structured domains single TDI molecules are incorporated as guests into their long, linear channels. In air atmosphere, the guest molecules show no movement but perfect orientation along the pore direction. The diffusion of the TDI molecules can be induced by placing the mesoporous film in a saturated atmosphere of chloroform. In single molecule measurements with very high positioning accuracy, down to 2 - 3 nm, the movement of molecules could be observed even between neighboring channels. This reveals directly the presence of defects like dead ends closing the pores or small openings in the silica walls between neighboring channels, where molecules can change from one channel to the next. A statistical analysis demonstrates that the diffusion of TDI

in the mesoporous film cannot be described with a 1D-random diffusion but is more complicated due to the presence of adsorption sites in which the TDI molecules can be occasionally trapped.

5.2 Photostable water-soluble terrylenediimide derivatives for applications in single molecule studies and membrane labelling

WS-TDI as a powerful dye for applications in single molecule studies and membrane labelling

A new water-soluble terrylenediimide-based dye (WS-TDI) has been synthesized and its photophysical properties are characterized. WS-TDI forms non-fluorescing H-aggregates in water which show absorption bands being blue shifted with respect to those of the fluorescing monomeric form. The ratio of monomeric WS-TDI to aggregated WS-TDI was determined to be 1 in 14,400, suggesting the presence of a large amount of soluble, non-fluorescent aggregates in water. The presence of a surfactant such as Pluronic P123 or CTAB leads to the disruption of the aggregates due to the formation of monomers in micelles. This is accompanied by a strong increase in fluorescence. A single molecule study of WS-TDI in polymeric films of PVA and PMMA reveals excellent photostability with respect to photobleaching, far above the photostability of other common water soluble dyes, such as oxazine-1, sulforhodamine-B and a water-soluble perylenediimide derivative. Furthermore, labelling of a single protein like avidin is demonstrated and the properties of single WS-TDI labelled avidin molecules are characterized by FCS and photostability measurements. The high tendency of WS-TDI to form non-fluorescent aggregates in water in connection with its high affinity to lipophilic environments is used for the fluorescence labelling of lipid membranes and membrane containing compartments such as artificial liposomes or endosomes in living HeLa cells. The superior fluorescence imaging quality of WS-TDI in such applications is demonstrated in comparison to other well known membrane staining dyes such as Alexa647 conjugated with dextran and FM 4-64 lipophilic styryl dye.

Two other WS-TDI derivatives: WS-TDI dodecyl and WS-TDI pyridoxy

Two further WS-TDI derivatives are investigated: WS-TDI dodecyl, which results from the addition of a dodecyl tail onto WS-TDI, and WS-TDI pyridoxy, which have four positively charged pyridoxy groups as side groups. Similarly to WS-TDI, WS-TDI dodecyl have high photostability and form in aqueous solution aggregates which disrupt upon addition of a surfactant like Pluronic P123. Moreover, the dye can also be used to mark the endocytic system of living cells like HeLa cells. However, due to its higher hydrophobicity, WS-TDI dodecyl penetrates more efficiently in cell membranes. This is shown with fluorescence spectra measurements of WS-TDI-dodecyl and WS-TDI in PBS

solutions containing HuH-7 living cells. The intensity of the fluorescence spectrum of WS-TDI-dodecyl is about fourfold higher than for WS-TDI at the same concentration. Moreover, confocal images of HeLa cells marked with the two fluorophores show that the cell membranes are much brighter for WS-TDI dodecyl. In contrast, WS-TDI pyridoxy molecules do not form aggregates in solution and its fluorescence is not totally quenched in water. However, its quantum yield in presence of Pluronic P123 and its photostability are lower than for WS-TDI and WS-TDI-dodecyl. Nevertheless, it can be used to label the endocytic system of living cells, similarly to the two other WS-TDI derivatives. Hence, the tuning of the properties of WS-TDI obtained by addition of the dodecyl alkyl tail, or by use of positively charged side groups offers a real panel of photostable dyes for diverse and targeted biological studies.

Localization of the three WS-TDI derivatives in the early and late endocytic pathway of living cells

This study addresses the question of the exact localization of the different dye molecules in the endocytic pathway of living cells. The dye uptake process in HuH-7 living cells is investigated for each of the new fluorophores. The method used is based on colocalization experiments between the three red WS-TDI derivatives and green labelled Rab GTPases in the endocytic traffic of HuH-7 living cells. It is demonstrated that the dyes are first incorporated into early endosomes (colocalized with Rab5-GFP), and allow to further follow their maturation into late endosomes (colocalized with Rab9-GFP) without affecting the cells over 16 hours. This *in vivo* characterization establishes the WS-TDI derivatives as powerful potential tools for biological studies in membrane containing compartments traffic of living cells.

Chapter 6

Appendix

6.1 Orientation of TDI molecules encapsulated in ordered mesoporous channels in anodic alumina membrane hosts

Many of promising applications of mesoporous materials such as catalyst supports and nanoreactors will benefit from arrangements of preferentially aligned, ordered mesoporous guest materials. The evaporation-induced self-assembly (EISA) method has been established as an efficient process for the preparation of thin films with small oriented domains. It has been shown in Section 3.4.1 that the degree of ordering of these films can be dramatically increased with the formation post-synthesis of large, mono-oriented domains up to 100 μm in size.

However, the obtained films display hexagonally ordered channels that are aligned parallel to the surface of the substrate.⁴¹ Recently, the synthesis of mesoporous materials within the regular, larger channels of anodic alumina membranes (AAMs) has been explored, with the aim of attaining greater control over the morphology of the mesoporous system. In particular, using the ionic surfactant CTAB the Bein's group (Munich) obtained hexagonally structured mesopores that are oriented along the AAM channels.¹⁸⁵

The method used here for the self-assembly of the ordered silica/surfactant nanocomposites in the channels of the anodic alumina membranes is depicted in Figure 6.1. The AAMs used in this study showed almost hexagonal packing of vertical pores, with diameters in the range of 120 - 200 nm, through the entire thickness of the membrane. The synthetic mixtures containing the silica precursor and CTAB as structure-directing agents were introduced into the pores of the AAM by soaking the membranes at room

temperature in a flat pool of liquid. As a result of evaporation of the solvent, which progressively increases the concentration of the surfactant and other nonvolatile components of the synthetic mixtures, the self-assembly process is driven towards the formation of micelles and the condensation of silica, followed by a disorder-to-order transition to provide the final, extended mesophase structure.

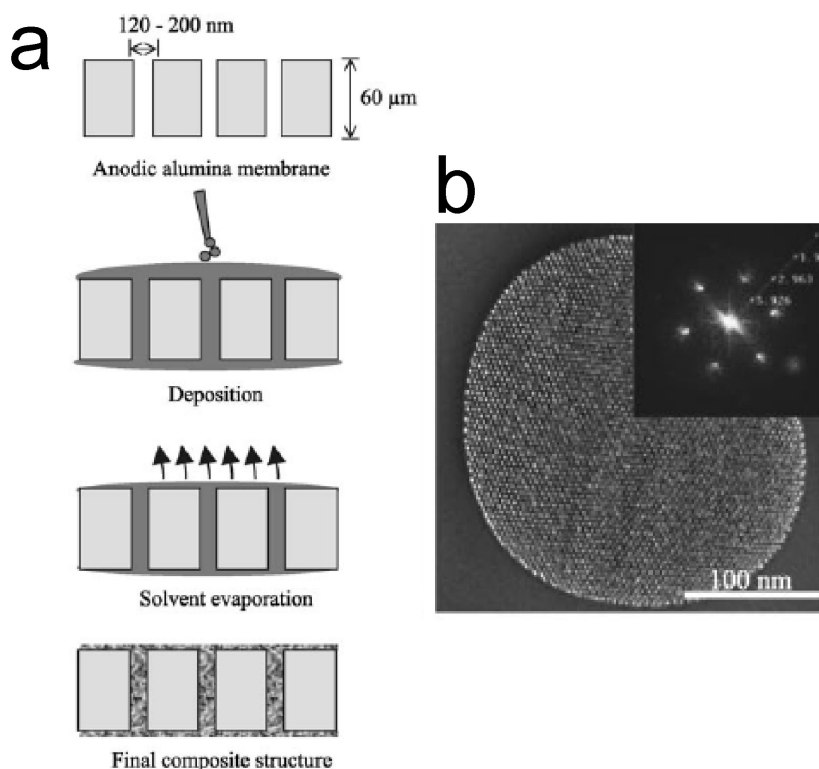


Figure 6.1: Ordered nanoporous alumina membranes. (a) Schematic representation of the synthetic route to obtain mesostructured silica-surfactant nanocomposites in the anodic alumina membranes (AAMs). (b) Plan-view TEM images of AAMs. (Adapted from Platschek et al.¹⁸⁵)

These highly structured mesophases can be directly observed in the representative plan-view TEM images shown in Figure 6.1b. The behavior of guest species incorporated in the mesopores can be studied by fluorescence spectroscopy.

TDI molecules were incorporated during synthesis into the CTAB-templated mesopores similarly to the experiments in thin film, which allows a direct comparison. As the AAMs are non transparent solids, it is not possible to image them by fluorescence microscopy as it. The preparation of the samples for investigation consists in snapping in its middle a dye loaded AAM, and printing this cut onto a microscope coverslip covered by a gluing non fluorescent polymer (provided by BASF). This procedure leads to the sticking of bundles of mesopores contained originally into the pores of the AAM.

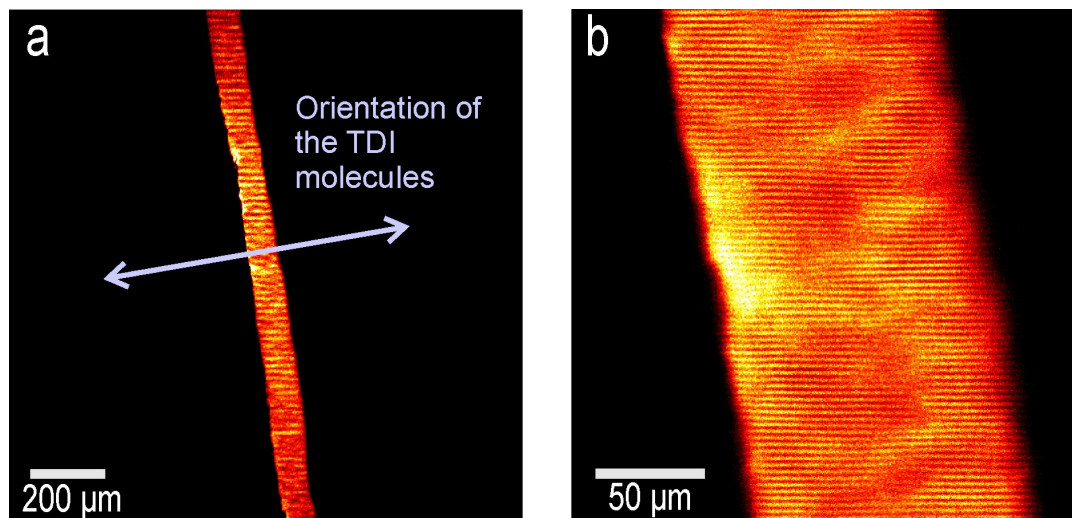


Figure 6.2: Polarization-modulated fluorescence images of TDI dye molecules encapsulated at ensemble concentration ($\sim 10^{-6}$ mol/L) in the very linear pores of an anodic alumina membrane (AAM). The transition dipole moments of the fluorophores have a preferential orientation, indicated by the white arrow.

Figure 6.2a shows a confocal image glue-covered coverslip marked with a AAM. The TDI dye molecules were dissolved at ensemble concentration (about 10^{-6} mol/L) in the synthesis solution. A strong fluorescent signal shows the linear shape of the marked region. The width of this band is about $200 \mu\text{m}$, which corresponds roughly to the thickness of the AAM used. Moreover, the polarization of the laser beam was continuously rotated during the confocal scan in order to detect and measure the orientation of the dye molecules. Figure 6.2b shows a zoom in of the fluorescing band. Stripped pattern are clearly visible along the whole band, demonstrating that the TDI molecule have a preferential orientation (see Section 2.1.3.4 for more details). The angle extracted from the fit of the stripped patterns is 10° , which corresponds exactly to the direction perpendicular the the fluorescing band. This direction is also the direction of the pores of the AAM, which are parallel to the silica mesopores as shown in Figure 6.1b. From these data it is possible to conclude that the direction of the parallel bundles of mesopores is conserved during the sticking of the AAM onto the coverslip, and, more importantly, that the TDI molecules are oriented along the direction of the mesopores.

6.2 List of abbreviations

AAM	Anodic alumina membranes
APD	Avalanche photodiode
Brij-56	Poly(oxyethylene)cetylother-copolymer
CMC	Critical micelle concentration
CTAB	Cetyltrimethylammoniumbromid
EISA	Evaporation-induced self-assembly
FCS	Fluorescence correlation spectroscopy
LSCM	Laser scanning confocal microscopy
MCM-41	Mobil catalytic materials N°41
PBS	Phosphate-buffered-saline
PDI	Perylenediimide
PMMA	Polymethyl-methacrylate
PVA	Polyvinyl-alcohol
PVA	Polyvinyl-alcohol
SMS	Single molecule spectroscopy
SPT	Single particle tracking
ST	Survival time
TDI	Terrylenediimide
TEP	Total emitted photons
WS-PDI	Water-soluble perylenediimide
WS-TDI	Water-soluble terrylenediimide

6.3 Published work and contributions to conferences and meetings

6.3.1 Publications

1. Jung, C.; Müller, B. K.; Lamb, D. C.; Nolde, F.; Müllen, K.; Bräuchle, C., A new photostable terryleneimide dye for applications in single molecule studies and membrane labelling. *Journal of the American Chemical Society* 2006, 128, (15), 5283-5291.
2. Jung, C.; Hellriegel, C.; Michaelis, J.; Bräuchle, C., single molecules traffic in mesoporous materials: Translational, orientational, and spectral dynamics. *Advanced Materials* 2007, 19, (7), 956-960.
3. Jung, C.; Hellriegel, C.; Platschek, B.; Wöhrle, D.; Bein, T.; Michaelis, J.; Bräuchle, C., Simultaneous measurement of orientational and spectral dynamics of single molecules in nanostructured host-guest materials. *Journal of the American Chemical Society* 2007, 129, (17), 5570-5579.
4. Jung, C.; Kirstein J., C.; Platschek, B.; Bein, T.; Bude M.; Frank I.; Michaelis, J.; Bräuchle, C., Diffusion of oriented single molecules with switchable mobility in networks of long unidimensional nanochannels. *Journal of the American Chemical Society* 2007, accepted.
5. Kirstein, J.; Platschek, B.; Jung, C.; Brown, R.; Bein, T.; Bräuchle, C., Exploration of nanostructured channel systems with single molecules probes. *Nature Materials* 2007, 6, (4), 303-310.
6. Wörmke, S.; Mackowski, S.; Brotosudarmo, T. H. P.; Jung, C.; Zumbusch, A.; Ehrl, M.; Scheer, H.; Hofmann, E.; Hiller, R. G.; Bräuchle, C., Monitoring fluorescence of individual chromophores in peridinin-chlorophyll-protein complex using single molecule spectroscopy. *Biochimica et Biophysica Acta (BBA) - Bioenergetics* 2007, 1767, (7), 956-964.
7. Mackowski, S.; Wörmke, S.; Brotosudarmo, T.; Jung, C.; Hiller, R.G.; Scheer, H.; Bräuchle, C., Energy Transfer in Reconstituted Peridinin-Chlorophyll-Protein Complex: Ensemble and Single Molecule Spectroscopy. *Biophysical Journal* 2007, 93, (9), 3249-3248.

6.3.2 Contributions to conferences and meetings

1. Postdoc and PhD Student Workshop on Single Molecule Detection in Living Cells, VolkswagenStiftung in Altleiningen 27.04 - 01.05.2003. *Poster presentation*
2. 4th International Symposium on Physics, Chemistry and Biology with Single Molecules, VolkswagenStiftung in Kloster Banz 22.02 - 25.02.2004. *Poster presentation*.
3. 16. Deutsche Zeolith-Tagung in Dresden 03.03 - 05.03.2004. *Poster presentation*.
4. SFB 486 Meeting. Workshop 2004 in Ringberg Castle, Tegernsee 28.03 - 31.03.2004. *Oral communication*.
5. Nanoscience: linking disciplines, CeNS Joint Workshop in Venice International university 27.09-1.10.2004. *Poster presentation*.
6. Bunsentagung 2005 in Frankfurt 05.05 - 07.05.2005. *Poster presentation*.
7. Diffusion Fundamentals I in Leipzig 22.09 - 24.09.2005. *Poster presentation*.
8. 18. Deutsche Zeolith-Tagung in Hannover 01.03 - 03.03.2006. *Poster presentation*.
9. Emerging Nanosystems - From Quantum Manipulation to Nanobiomachines, CeNS Workshop in Venice International university 25.09-29.09.2006. *Poster presentation*.
10. 19. Deutsche Zeolith-Tagung in Leipzig 07.03 - 09.03.2007. *Oral communication*.
11. Deutsch Physikalische Gesellschaft - Frühjahrstagung in Regensburg 26.03 - 30.03.2007. *Oral communication*.

Bibliography

- [1] W. E. Moerner and L. Kador. Optical detection and spectroscopy of single molecules in a solid. *Physical Review Letters*, 62(21):2535, 1989.
- [2] M. Orrit and J. Bernard. Single pentacene molecules detected by fluorescence excitation in a p-terphenyl crystal. *Physical Review Letters*, 65(21):2716, 1990.
- [3] Daniel Axelrod. *Chapter12: Fluorescence Polarization Microscopy (from Methods in Cell Biology)*, volume 30. Academic Press, 1989.
- [4] E Toprak, J Enderlein, S Syed, S. A McKinney, R. G Petschek, T Ha, Y. E Goldman, and P. R. Selvin. Defocused orientation and position imaging (dopi) of myosin v. *Proceedings of the National Academy of Sciences of the United States of America*, 103(17):6495–6499, 2006.
- [5] Andrew P. Bartko and Robert M. Dickson. Imaging three-dimensional single molecule orientations. *J. Phys. Chem. B*, 103:11237–11241, 1999.
- [6] Kenneth D. Weston and Lori S. Goldner. Orientation imaging and reorientation dynamics of single dye molecules. *J. Phys. Chem. B*, 105:3453–3462, 2001.
- [7] A. Schob, F. Cichos, J. Schuster, and C. von Borczyskowski. Reorientation and translation of individual dye molecules in a polymer matrix. *European Polymer Journal*, 40:1019–1026, 2004.
- [8] T. Ha, Th. Enderle, D. S. Chemla, P. R. Selvin, and S. Weiss. Single molecule dynamics studied by polarization modulation. *Phys. Rev. Lett.*, 77(19):3979–3982, 1996.
- [9] G. S. Harms, M. Sonnleitner, G. J. Schütz, H. J. Gruber, and Th. Schmidt. single molecules anisotropy imaging. *Biophys. J.*, 77(5):2864–2870, 1999.
- [10] Jr. W. Göhde, U. C. Fischer, H. Fuchs, J. Tittel, Th. Basché, Ch. Bräuchle, A. Herrmann, and K. Müllen. Fluorescence blinking and photobleaching of single ter-

- rylenediimide molecules studied with a confocal microscope. *J. Phys. Chem. A*, 102(46):9109–9116, 1998.
- [11] Jerker Widengren and Rudolf Rigler. Mechanisms of photobleaching investigated by fluorescence correlation spectroscopy. *Bioimaging*, 4:149–157, 1996.
- [12] R Zondervan, F Kulzer, M. A Kol’chenko, and M. Orrit. Photobleaching of rhodamine 6g in poly(vinyl alcohol) at the ensemble and single molecules levels. *Journal of Physical Chemistry A*, 108(10):1657–1665, 2004.
- [13] James W. Gilliland, Kazushige Yokoyama, and Wai Tak Yip. Solvent effect on mobility and photostability of organic dyes embedded inside silica sol-gel thin films. *Chem. Mater.*, 17(26):6702–6712, 2005.
- [14] A Dubois, M Canva, A Brun, F Chaput, and J. P. Boilot. Photostability of dye molecules trapped in solid matrices. *Applied Optics*, 35(18):3193–3199, 1996.
- [15] Tsuyoshi Kawai, Sunao Yoshihara, Yasuhide Iwata, Tuyoshi Fukaminato, and Masahiro Irie. Anisotropic translational diffusion of single fluorescent perylene molecules in a nematic liquid crystal. *ChemPhysChem*, 5(10):1606–1609, 2004.
- [16] C. Seebacher, C. Hellriegel, F.-W. Deeg, C. Bräuchle, S. Altmaier, P. Behrens, and K. Müllen. Observation of translational diffusion of single terrylenediimide molecules in a mesostructured molecular sieve. *J. Phys. Chem. B*, 106:5591–5595, 2002.
- [17] Marija Vrljic, Stefanie Y. Nishimura, Sophie Brasselet, W. E. Moerner, and Harden M. McConnell. Translational diffusion of individual class ii mhc membrane proteins in cells. *Biophys. J.*, 83(5):2681–2692, 2002.
- [18] Skylar A. Martin Brown, Yi Fu, Ginagunta Saroja, Maryanne M. Collinson, and Daniel A. Higgins. single molecules studies of diffusion by oligomer-bound dyes in organically modified sol-gel-derived silicate films. *Anal. Chem.*, 77(2):486–494, 2005.
- [19] J. Schuster, F. Cichos, and Ch. von Borczyskowski. Anisotropic diffusion of single molecules in thin liquid films. *The European Physical Journal E - Soft Matter*, 12(S1):75–80, 2003.
- [20] Mary J. Wirth, Derrick J. Swinton, and Melody D. Ludes. Adsorption and diffusion of single molecules at chromatographic interfaces. *J. Phys. Chem. B*, 107:6258–6268, 2003.
- [21] T. Schmidt, G.J. Schütz, W. Baumgartner, H.J. Gruber, and H. Schindler. Imaging of single molecule diffusion. *Proc. Natl. Acad. Sci.*, 93:2926–2929, 1996.

- [22] Daniel A. Higgins and Maryanne M. Collinson. Gaining insight into the nanoscale properties of sol-gel-derived silicate thin films by single molecules spectroscopy. *Langmuir*, 21(20):9023–9031, 2005.
- [23] D. A Higgins, M. M Collinson, G Saroja, and A. M. Bardo. single molecules spectroscopic studies of nanoscale heterogeneity in organically modified silicate thin films. *Chemistry of Materials*, 14(9):3734–3744, 2002.
- [24] Y. W. Hou, A. M. Bardo, C. Martinez, and D. A. Higgins. Characterization of molecular scale environments in polymer films by single molecule spectroscopy. *Journal of Physical Chemistry B*, 104(2):212–219, 2000.
- [25] W. E. Moerner. Low-temperature studies in solids. In *single molecules Optical Detection, Imaging and Spectroscopy*, pages 1–189. 1997.
- [26] F. Schindler, J. M. Lupton, J. Müller, J. Feldmann, and U. Scherf. How single conjugated polymer molecules respond to electric fields. *Nature Materials*, 5(2):141–146, 2006.
- [27] Renaud A. L. Vallée, Philippe Marsal, Els Braeken, Satoshi Habuchi, Frans C. De Schryver, Mark Van der Auweraer, David Beljonne, and Johan Hofkens. Single molecule spectroscopy as a probe for dye-polymer interactions. *J. Am. Chem. Soc.*, 127(34):12011–12020, 2005.
- [28] Karla S. McCain, David C. Hanley, and Joel M. Harris. single molecules fluorescence trajectories for investigating molecular transport in thin silica sol-gel films. *Analytical Chemistry*, 75(17):4351–4359, 2003.
- [29] G. A Ozin, A Kuperman, and A. Stein. Advanced zeolite materials science. *Angewandte Chemie-International Edition in English*, 28(3):359–376, 1989.
- [30] Mark E. Davis. Ordered porous materials for emerging applications. *Nature*, 417:813–821, 2002.
- [31] Avelino Corma. From microporous to mesoporous molecular sieve materials and their use in catalysis. *Chem. Rev.*, 97:2373–2419, 1997.
- [32] V Rebbin, R Schmidt, and M. Froba. Spherical particles of phenylene-bridged periodic mesoporous organosilica for high-performance liquid chromatography. *Angewandte Chemie-International Edition*, 45(31):5210–5214, 2006.
- [33] D. E De Vos, M Dams, B. F Sels, and P. A. Jacobs. Ordered mesoporous and microporous molecular sieves functionalized with transition metal complexes as catalysts for selective organic transformations. *Chemical Reviews*, 102(10):3615–3640, 2002.

- [34] Mary J. Wirth, R. W. Peter Fairbank, and Hafeez O. Fatunmbi. Mixed self-assembled monolayers in chemical separations. *Science*, 275:44–47, 1997.
- [35] H. S Peng, J Tang, L Yang, J. B Pang, H. S Ashbaugh, C. J Brinker, Z. Z Yang, and Y. F. Lu. Responsive periodic mesoporous polydiacetylene/silica nanocomposites. *Journal of the American Chemical Society*, 128(16):5304–5305, 2006.
- [36] G Wirnsberger and G. D. Stucky. Ordered mesostructured materials with optical functionality. *Chemphyschem*, 1(2):90, 2000.
- [37] M. Gratzel. Photoelectrochemical cells. *Nature*, 414(6861):338–344, 2001.
- [38] Cheng-Yu Lai, Brian G. Trewyn, Dusan M. Jeftinija, Ksenija Jeftinija, Shu Xu, Srdija Jeftinija, and Victor S.-Y. Lin. A mesoporous silica nanosphere-based carrier system with chemically removable cds nanoparticle caps for stimuli-responsive controlled release of neurotransmitters and drug molecules. *J. Am. Chem. Soc.*, 125(15):4451–4459, 2003.
- [39] Indrajit Roy, Tymish Y. Ohulchanskyy, Dhruva J. Bharali, Haridas E. Pudavar, Ruth A. Mistretta, Navjot Kaur, and Paras N. Prasad. Optical tracking of organically modified silica nanoparticles as dna carriers: A nonviral, nanomedicine approach for gene delivery. *PNAS*, 102(2):279–284, 2005.
- [40] E. M. Freer, L. E. Krupp, W. D. Hinsberg, P. M. Rice, J. L. Hedrick, J. N. Cha, R. D. Miller, and H. C. Kim. Oriented mesoporous organosilicate thin films. *Nano Letters*, 5(10):2014–2018, 2005.
- [41] M Klotz, P. A Albouy, A Ayril, C Menager, D Grosso, A Van der Lee, V Cabuil, F Babonneau, and C. Guizard. The true structure of hexagonal mesophase-templated silica films as revealed by x-ray scattering: Effects of thermal treatments and of nanoparticle seeding. *Chemistry of Materials*, 12(6):1721–1728, 2000.
- [42] N. K. Raman, M. T. Anderson, and C. J. Brinker. Template-based approaches to the preparation of amorphous, nanoporous silicas. *Chem. Mater.*, 8(8):1682–1701, 1996.
- [43] Michael J. Saxton and Ken Jacobson. Single-particle tracking: Applications to membrane dynamics. *Annu. Rev. Biophys. Biomol. Struct.*, 26:373–399, 1997.
- [44] Adam D. Douglass and Ronald D. Vale. single molecules microscopy reveals plasma membrane microdomains created by protein-protein networks that exclude or trap signaling molecules in t cells. *Cell*, 121(6):937–950, 2005.

- [45] Paul S. Pyenta, Petra Schwille, Watt W. Webb, David Holowka, and Barbara Baird. Lateral diffusion of membrane lipid-anchored probes before and after aggregation of cell surface ige-receptors. *J. Phys. Chem. A*, 107:8310–8318, 2003.
- [46] G. J Schütz, M Sonnleitner, P Hinterdorfer, and H. Schindler. Single molecule microscopy of biomembranes (review). *Molecular Membrane Biology*, 17(1):17–29, 2000.
- [47] Patricia R. Smith, Ian E. G. Morrison, Keith M. Wilson, Nelson Fernandez, and Richard J. Cherry. Anomalous diffusion of major histocompatibility complex class i molecules on hela cells determined by single particle tracking. *Biophysical Journal*, 76:3331–3344, 1999.
- [48] R. Seidel, J. van Noort, C. van der Scheer, J. G. P. Bloom, N. H. Dekker, C. F. Dutta, A. Blundell, T. Robinson, K. Firman, and C. Dekker. Real-time observation of dna translocation by the type i restriction modification enzyme ecor124i. *Nature Structural and Molecular Biology*, 11(9):838–843, 2004.
- [49] R. J. Davenport, G. J. L. Wuite, R. Landick, and C. Bustamante. single molecules study of transcriptional pausing and arrest by e-coli rna polymerase. *Science*, 287(5462):2497–2500, Mar 2000.
- [50] P. R. Bianco, L. R. Brewer, M. Corzett, R. Balhorn, Y. Yeh, S. C. Kowalczykowski, and R. J. Baskin. Processive translocation and dna unwinding by individual recbc enzyme molecules. *Nature*, 409(6818):374–378, Jan 2001.
- [51] F. Nolde, J. Qu, C. Kohl, N. G. Pschirer, E. Reuther, and K. Müllen. Synthesis and modification of terrylenediimides as high-performance fluorescent dyes. *Chem. Eur. J.*, 11(13):3959–3967, 2005.
- [52] W. E. Moerner. Examining nanoenvironments in solids on the scale of a single, isolated impurity molecule. *Science*, 265(5168):46–53, 1994.
- [53] L Fleury, A Zumbusch, M Orrit, R Brown, and J. Bernard. Spectral diffusion and individual 2-level systems probed by fluorescence of single terrylene molecules in a polyethylene matrix. *Journal of Luminescence*, 56(1-6):15–28, 1993.
- [54] C Blum, F Stracke, S Becker, K Müllen, and A. J. Meixner. Discrimination and interpretation of spectral phenomena by room-temperature single molecules spectroscopy. *Journal of Physical Chemistry A*, 105(29):6983–6990, 2001.
- [55] Frank Stracke, Christian Blum, Stefan Becker, Klaus Müllen, and Alfred J. Meixner. Two and multilevel spectral switching of single molecules in polystyrene at room temperature. *Chemical Physics*, 300(1-3):153–164, 2004.

- [56] C. Eggeling, J. Widengren, R. Rigler, and C. A. M. Seidel. Photobleaching of fluorescent dyes under conditions used for single molecules detection: Evidence of two-step photolysis. *Analytical Chemistry*, 70(13):2651–2659, 1998.
- [57] Andrzej Molski. Statistics of the bleaching number and the bleaching time in single molecules fluorescence spectroscopy. *J. Chem. Phys.*, 114(3):1142–1147, 2001.
- [58] Joseph R. Lakowicz. Principles of fluorescence spectroscopy. pages 129–130. Plenum Press: New York, second edition edition, 1999.
- [59] Murphy Douglas B. *Fundamentals of Light Microscopy and Electric Imaging*. John Wiley And Sons Ltd, New York, 2001.
- [60] Michael Lampton, Bruce Margon, and Stuart Bowyer. Parameter estimation in x-ray astronomy. *The Astrophysical Journal*, 208:177–190, 1976.
- [61] Norman Bobroff. Position measurement with a resolution and noise-limited instrument. *Rev. Sci. Instrum.*, 57(6):1152–1157, 1986.
- [62] Robert M. Dickson, D. J. Norris, Yih-Ling Tzeng, and W. E. Moerner. Three-dimensional imaging of single molecules solvated in pores of poly(acrylamide) gels. *Science*, 274(5289):966–968, 1996.
- [63] B. Sick, B. Hecht, and L. Novotny. Orientational imaging of single molecules by annular illumination. *Phys. Rev. Lett.*, 85(21):4482–4485, 2000.
- [64] F. Guttler, J. Sepiol, T. Plakhotnik, A. Mitterdorfer, A. Renn, and U. P. Wild. single molecules spectroscopy - fluorescence excitation-spectra with polarized-light. *Journal of Luminescence*, 56(1-6):29–38, 1993.
- [65] X. S. Xie and R. C. Dunn. Probing single molecules dynamics. *Science*, 265(5170):361–364, 1994.
- [66] Taekjip Ha, Ted A. Laurence, Daniel S. Chemla, and Shimon Weiss. Polarization spectroscopy of single fluorescent molecules. *J. Phys. Chem. B*, 103:9839–6850, 1999.
- [67] F Kulzer and M. Orrit. single molecules optics. *Annual Review of Physical Chemistry*, 55:585–611, 2004.
- [68] C. Seebacher. *Einzelmolekülspektroskopie von organischen Farbstoffmolekülen in porösen Festkörpern*. PhD thesis, LMU München, 2002.
- [69] C. Hellriegel. *Translational, orientational and spectral dynamics of individual molecules in nano-structured materials studied with single molecules spectroscopy*. PhD thesis, LMU München, 2005.

- [70] Elliott L Elson and D. Magde. Fluorescence correlation spectroscopy. i. conceptual basis and theory. biopolymers. 13:1-27. *Biopolymers*, 13:1–27, 1974.
- [71] Nancy L. Thompson. Fluorescence correlation spectroscopy. In J. R. Lakowicz, editor, *Topics in Fluorescence Spectroscopy, Volume 1: Techniques*, volume 1, pages 337–378. Plenum Press, New York, 1991.
- [72] Barbara K Mueller, Evgeny Zaychikov, Christoph Bräuchle, and Don C. Lamb. Pulsed interleaved excitation. *Biophysical Journal*, 89(5):3508–3522, 2005.
- [73] J Widengren and P. Schwille. Characterization of photoinduced isomerization and back-isomerization of the cyanine dye cy5 by fluorescence correlation spectroscopy. *Journal of Physical Chemistry A*, 104(27):6416–6428, 2000.
- [74] Howard C. Berg. *Random Walks in Biology*. Princeton University Press, 1983.
- [75] R. Simson, E. D. Sheets, and K. Jacobson. Detection of temporary lateral confinement of membrane-proteins using single-particle tracking analysis. *Biophysical Journal*, 69(3):989–993.
- [76] R.N. Ghosh and W.W. Webb. Automated detection and tracking of individual and clustered cell surface low density lipoprotein receptor molecules. *Biophysical Journal*, 66(5):1301–1318, 1994.
- [77] Ralf Bausinger, Katharina Von Gersdorff, Kevin Braeckmans, Manfred Ogris, Ernst Wagner, Christoph Bräuchle, and Andreas Zumbusch. The transport of nanosized gene carriers unraveled by live-cell imaging. *Angewandte Chemie International Edition*, 45(10):1568–1572, 2006.
- [78] G.J. Schütz, H. Schindler, and T. Schmidt. single molecules microscopy on model membranes reveals anomalous diffusion. *Biophysical Journal*, 73:1073–1080, 1997.
- [79] H. Qian and E.L. Elson M.P. Sheetz. Single particle tracking. analysis of diffusion and flow in two- dimensional systems. *Biophys. J.*, 60:910–921, 1991.
- [80] IUPAC. Manual of symbols and terminology, appendix 2, colloid and surface chemistry. *Pure Appl. Chem.*, 31:578, 1972.
- [81] Gernot Wirnsberger, Brian J. Scott, Bradley F. Chmelka, and Galen D. Stucky. Fast response photochromic mesostructures. *Adv. Mater.*, 12(19):1450–1454, 2000.
- [82] Simon U. Wark M. Laeri F., Schüth F. *Host-Guest-Systems Based on Nanoporous Crystals: Synthesis, Properties and Applications*. Eds. Wiley VCH, Weinheim, 2003.

- [83] S. L. Qiu, W. Q. Pang, H. Kessler, and J. L. Guth. Synthesis and structure of the [alpo-4]12 pr4nf molecular-sieve with afi structure. *Zeolites*, 9(5):440–444, 1989.
- [84] M. Ganschow, G. Schulz-Ekloff, M. Wark, W. Wendschuh, M. Josties, and D. Wöhrle. Microwave-assisted preparation of uniform pure and dye-loaded alpo4-5 crystals with different morphologies for use as microlaser systems. *Journal of Materials Chemistry*, 11(7):1823–1827, 2001.
- [85] S.T. Wilson. *Introduction to Zeolite and Science and Practice*. Amsterdam, 1991.
- [86] G. Calzaferri, S. Huber, H. Maas, and C. Minkowski. Host-guest antenna materials. *Angewandte Chemie-International Edition*, 42(32):3732–3758, 2003.
- [87] Guido Ihlein, Ferdi Schüth, Oliver Krauss, Uwe Vietze, and Franco Laeri. Alignment of a laser dye in the channels of the alpo4-5 molecular sieve. *Adv. Mater.*, 10(14):1117–1119, 1998.
- [88] U. Vietze, O. Krauss, F. Laeri, G. Ihlein, F. Schüth, B. Limburg, and M. Abraham. Zeolite-dye microlasers. *Physical Review Letters*, 81(21):4628–4631, 1998.
- [89] I. Braun, G. Ihlein, F. Laeri, J. U. Nöckel, G. Schulz-Ekloff, F. Schüth, U. Vietze, O. Weiss, and D. Wöhrle. Hexagonal microlasers based on organic dyes in nanoporous crystals. *Applied Physics B-Lasers and Optics*, 70(3):335–343, 2000.
- [90] Y. Sorek, R. Reisfeld, and R. Tenne. *Chemical Physics Letters*, 227:235, 1994.
- [91] K. Weh, M. Noack, K. Hoffmann, K. P. Schroder, and J. Caro. Change of gas permeation by photoinduced switching of zeolite-azobenzene membranes of type mfi and fau. *Microporous and Mesoporous Materials*, 54(1-2):15–26, 2002.
- [92] J.S. Beck, J.C. Vartuli, W.J. Roth, M.E. Leonowicz, C.T. Kresge, K.D. Schmitt, C.T.W. Chu, D.H. Olson, E.W. Sheppard, S.B. McCullen, J.B. Higgins, and J.L. Schlenker. A new family of mesoporous molecular sieves prepared with liquid crystal templates. *J. Am. Chem. Soc.*, 114:10834–10843, 1992.
- [93] D. Zhao, P. Yang, N. Melosh, J. Feng, B. F. Chmelka, and G. D. Stucky. Continuous mesoporous silica films with highly ordered large pore structures. *Advanced Materials*, 10(16):1380–+, 1998.
- [94] Jackie Y. Ying, Christian P. Mehnert, and Michael S. Wong. Synthese und anwendungen von mit supramolekularen templatzen hergestellten mesoporösen materialien. *Angew. Chem.*, 38:58–82, 1999.

- [95] W. M Van Rhijn, D. E De Vos, B. F Sels, W. D Bossaert, and P. A. Jacobs. Sulfonic acid functionalised ordered mesoporous materials as catalysts for condensation and esterification reactions. *Chemical Communications*, (3):317–318, 1998.
- [96] S. J. L. Billinge, E. J. McKimmy, M. Shatnawi, H. J. Kim, V. Petkov, D. Wermeille, and T. J. Pinnavaia. Mercury binding sites in thiol-functionalized mesostructured silica. *Journal of the American Chemical Society*, 127(23):8492–8498, 2005.
- [97] C.T. Kresge, M.E. Leonowicz, W.J. Roth, C.E. Vartuli, and J.S. Beck. Ordered mesoporous molecular sieves synthesized by a liquid-crystal template mechanism. *Nature*, 359:710–712, 1992.
- [98] A. Monnier, F. Schuth, Q. Huo, D. Kumar, D. Margolese, R. S. Maxwell, G. D. Stucky, M. Krishnamurty, P. Petroff, A. Firouzi, M. Janicke, and B. F. Chmelka. Cooperative formation of inorganic-organic interfaces in the synthesis of silicate mesostructures. *Science*, 261(5126):1299–1303, 1993.
- [99] Qisheng Huo, David I. Margolese, Ulrike Ciesla, Dirk G. Demuth, Pingyun Feng, Thurman E. Gier, Peter Sieger, Ali Firouzi, Bradley F. Chmelka, Ferdi Schüth, and Galen D. Stucky. Organization of organic molecules with inorganic molecular species into nanocomposite biphasic arrays. *Chem. Mater.*, 6(8):1176–1191, 1994.
- [100] C. Jeffrey Brinker, Yunfeng Lu, Alan Sellinger, and Hongyou Fan. Evaporation-induced self-assembly: Nanostructures made easy. *Adv. Mater.*, 11(7):579–585, 1999.
- [101] Florence Cagnol, David Grosso, Galo J.de A. A. Soler Illia, Eduardo L. Crepaldi, Florence Babonneau, Heinz Amenitsch, and Clément Sanchez. Humidity-controlled mesostructuration in ctab-templated silica thin film processing. the existence of a modulable steady state. *J. Mater. Chem.*, 13(1):61–66, 2003.
- [102] David Grosso, Florence Babonneau, Galo J. de A. A. Soler-Illia, Pierre-Antoine Albouy, and Heinz Amenitsch. Phase transformation during cubic mesostructured silica film formation. *Chem. Commun.*, 7:748–749, 2002.
- [103] S. Dourdain, A. Rezaire, A. Mehdi, B. M. Ocko, and A. Gibaud. Real time gisaxs study of micelle hydration in ctab templated silica thin films. *Physica B-Condensed Matter*, 357(1-2):180–184, 2005.
- [104] A. Gibaud, S. Dourdain, O. Gang, and B. M. Ocko. In situ grazing incidence small-angle x-ray scattering real-time monitoring of the role of humidity during the structural formation of templated silica thin films. *Physical Review B*, 70(16), 2004.

- [105] M. J. Henderson, A. Gibaud, J. F. Bardeau, and J. W. White. An x-ray reflectivity study of evaporation-induced self-assembled titania-based films. *Journal of Materials Chemistry*, 16(25):2478–2484, 2006.
- [106] Sophie Besson, Thierry Gacoin, Christian Ricolleau, Catherine Jacquiod, and Jean-Pierre Boilot. Phase diagram for mesoporous ctab silica films prepared under dynamic conditions. *J. Mater. Chem.*, 13:404–409, 2003.
- [107] Joerg Kaerger. Measurement of diffusion in zeolites – a never ending challenge? *Adsorption*, 9:29–35, 2003.
- [108] W. E. Moerner. A dozen years of single molecules spectroscopy in physics, chemistry, and biophysics. *J. Phys. Chem. B*, 106:910–927, 2002.
- [109] E Haustein and P. Schuille. Ultrasensitive investigations of biological systems by fluorescence correlation spectroscopy. *Methods*, 29(2):153–166, 2003.
- [110] R Rigler, U Mets, J Widengren, and P. Kask. Fluorescence correlation spectroscopy with high count rate and low-background - analysis of translational diffusion. *European Biophysics Journal with Biophysics Letters*, 22(3):169–175, 1993.
- [111] C Hellriegel, J Kirstein, and C. Bräuchle. Tracking of single molecules as a powerful method to characterise diffusivity of organic species in mesoporous materials. *New Journal of Physics*, 7(23):1–14, 2005.
- [112] Ahmet Yildiz, Joseph N. Forkey, Sean A. McKinney, Taekjip Ha, Yale E. Goldman, and Paul R. Selvin. Myosin v walks hand-over-hand: Single fluorophore imaging with 1.5-nm localization. *Science*, 300(5628):2061–2065, 2003.
- [113] J Schuster, F Cichos, and C. von Borczyskowski. Diffusion measurements by single molecules spot-size analysis. *J. Phys. Chem. A*, 106(22):5403–5406, 2002.
- [114] Christian Hellriegel, Christian Seebacher, Christoph Bräuchle, and Dieter Ganschow, Matthias Woehrle. Orientational behavior of single molecules in molecular sieves: A study of oxazine dyes in alpo4-5 crystals. *J. Phys. Chem. B*, 107(23):5445–5452, 2003.
- [115] W. P. Ambrose and W. E. Moerner. Fluorescence spectroscopy and spectral diffusion of single impurity molecules in a crystal. *Nature*, 349(6306):225–227, 1991.
- [116] A Zumbusch, L Fleury, R Brown, J Bernard, and M. Orrit. Probing individual 2-level systems in a polymer by correlation of single molecular fluorescence. *Physical Review Letters*, 70(23):3584–3587, 1993.

- [117] A Kiraz, M Ehrl, C Bräuchle, and A. Zumbusch. Low temperature single molecule spectroscopy using vibronic excitation and dispersed fluorescence detection. *Journal of Chemical Physics*, 118(24):10821–10824, 2003.
- [118] Yunfeng Lu, Rahul Ganguli, Celeste A. Drewien, Mark T. Anderson, C. Jeffrey Brinker, Weilang Gong, Yongxing Guo, Hermes Soyez, Bruce Dunn, Michael H. Huang, and Jeffrey I. Zink. Continuous formation of supported cubic and hexagonal mesoporous films by sol-gel dip-coating. *Nature*, 389:364–368, 1997.
- [119] Eli Barkai, YounJoon Jung, and Robert Silbey. Theory of single molecules spectroscopy: Beyond the ensemble average. *Annual Review of Physical Chemistry*, 55:457–507, 2004.
- [120] Maarten B. J. Roeffaers, Bert F. Sels, Hiroshi Uji i, Frans C. De Schryver, Pierre A. Jacobs, Dirk E. De Vos, and Johan Hofkens. Spatially resolved observation of crystal-face-dependent catalysis by single turnover counting. *Nature*, 439:572–575, 2006.
- [121] A. J Meixner and M. A. Weber. Single molecule spectral dynamics at room temperature. *Journal of Luminescence*, 86(3-4):181–187, 2000.
- [122] T. Schmidt, G. J. Schütz, W. Baumgartner, H. J. Gruber, and H. Schindler. Characterization of photophysics and mobility of single molecules in a fluid lipid-membrane. *Journal of Physical Chemistry*, 99(49):17662–17668, 1995.
- [123] J Hofkens, W Verheijen, R Shukla, W Dehaen, and F. C. De Schryver. Detection of a single dendrimer macromolecule with a fluorescent dihydropyrroloporrole-dione (dpp) core embedded in a thin polystyrene polymer film. *Macromolecules*, 31(14):4493–4497, 1998.
- [124] Andrew P. Bartko, Kewei Xu, and Robert M. Dickson. Three-dimensional single molecule rotational diffusion in glassy state polymer films. *Physical Review Letters*, 89(2):026101–1–4, 2002.
- [125] C. R Viteri, J. W Gilliland, and W. T. Yip. Probing the dynamic guest-host interactions in sol-gel films using single molecule spectroscopy. *Journal of the American Chemical Society*, 125(7):1980–1987, 2003.
- [126] Hiroshi Uji-i, Sergey M Melnikov, Ania Deres, Giacomo Bergamini, Frans De Schryver, Andreas Herrmann, Klaus Müllen, Jorg Enderlein, and Johan Hofkens. Visualizing spatial and temporal heterogeneity of single molecule rotational diffusion in a glassy polymer by defocused wide-field imaging. *Polymer*, 47(7):2511–2518, 2006.

- [127] S Megelski, A Lieb, M Pauchard, A Drechsler, S Glaus, C Debus, A. J Meixner, and G. Calzaferri. Orientation of fluorescent dyes in the nano channels of zeolite 1. *Journal of Physical Chemistry B*, 105(1):25–35, 2001.
- [128] Y Fu, F. M Ye, W. G Sanders, M. M Collinson, and D. A. Higgins. Single molecule spectroscopy studies of diffusion in mesoporous silica thin films. *Journal of Physical Chemistry B*, 110(18):9164–9170, 2006.
- [129] Laurent Cognet, Gregory S. Harms, Gerhard A. Blab, Piet H. M. Lommerse, and Thomas Schmidt. Simultaneous dual-color and dual-polarization imaging of single molecules. *Applied Physics Letters*, 77(24):4052–4054, 2000.
- [130] E. J. G Peterman, H Sosa, L. S. B Goldstein, and W. E. Moerner. Polarized fluorescence microscopy of individual and many kinesin motors bound to axonemal microtubules. *Biophysical Journal*, 81(5):2851–2863, 2001.
- [131] F. O. Holtrup, G. R. J. Müller, H. Quante, S. Defeyter, F. C. DeSchryver, and K. Müllen. Terrylenimides: New nir fluorescent dyes. *Chemistry-a European Journal*, 3(2):219–225, 1997.
- [132] R. Bandyopadhyaya, E. Nativ-Roth, R. Yerushalmi-Rozen, and O. Regev. Transferable thin films of mesoporous silica. *Chemistry of Materials*, 15(19):3619–3624, 2003.
- [133] M Matheron, A Bourgeois, A Brunet-Bruneau, P. A Albouy, J Biteau, T Gacoin, and J. P. Boilot. Highly ordered ctab-templated organosilicate films. *Journal of Materials Chemistry*, 15(44):4741–4745, 2005.
- [134] L. Fleury, A. Zumbusch, M. Orrit, R. Brown, and J. Bernard. Spectral diffusion and individual two-level systems probed by fluorescence of single terylene molecules in a polyethylene matrix. *Journal of Luminescence*, 56(1):15–28, 1993.
- [135] Z Konya, V. F Puentes, I Kiricsi, J Zhu, P Alivisatos, and G. A. Somorjai. Novel two-step synthesis of controlled size and shape platinum nanoparticles encapsulated in mesoporous silica. *Catalysis Letters*, 81(3-4):137–140, 2002.
- [136] Z Konya, V. F Puentes, I Kiricsi, J Zhu, J. W Ager, M. K Ko, H Frei, P Alivisatos, and G. A. Somorjai. Synthetic insertion of gold nanoparticles into mesoporous silica. *Chemistry of Materials*, 15(6):1242–1248, 2003.
- [137] P Bordat and R. Brown. Molecular mechanisms of photo-induced spectral diffusion of single terylene molecules in p terphenyl. *Journal of Chemical Physics*, 116(1):229–236, 2002.

- [138] Angela M. Bardo, Maryanne M. Collinson, and Daniel A. Higgins. Nanoscale properties and matrix-dopant interactions in dye-doped organically modified silica thin films. *Chem. Mater.*, 13(8):2713–2721, 2001.
- [139] S. M. Mahurin, Sheng Dai, and M. D. Barnes. Probing the diffusion of a dilute dye solution in mesoporous glass with fluorescence correlation spectroscopy. *J. Phys. Chem. B*, 107:13336–13340, 2003.
- [140] Y Yamauchi, M Sawada, A Sugiyama, T Osaka, Y Sakka, and K. Kuroda. Magnetically induced orientation of mesochannels in 2d-hexagonal mesoporous silica films. *Journal of Materials Chemistry*, 16(37):3693–3700, 2006.
- [141] V. R Koganti, D Dunphy, V Gowrishankar, M. D McGehee, X. F Li, J Wang, and S. E. Rankin. Generalized coating route to silica and titania films with orthogonally tilted cylindrical nanopore arrays. *Nano Letters*, 6(11):2567–2570, 2006.
- [142] Venkat R. Koganti and Stephen E. Rankin. Synthesis of surfactant-templated silica films with orthogonally aligned hexagonal mesophase. *J. Phys. Chem. B*, 109(8):3279–3283, 2005.
- [143] B Platschek, N Petkov, and T. Bein. Tuning the structure and orientation of hexagonally ordered mesoporous channels in anodic alumina membrane hosts: A 2d small-angle x-ray scattering study. *Angewandte Chemie-International Edition*, 45(7):1134–1138, 2006.
- [144] L. Pidol, D. Grosso, Gja Soler-Illia, E. L. Crepaldi, C. Sanchez, P. A. Albouy, H. Amenitsch, and P. Euzen. Hexagonally organised mesoporous aluminium-oxohydroxide thin films prepared by the template approach. in situ study of the structural formation. *Journal of Materials Chemistry*, 12(3):557–564, 2002.
- [145] Yanwen Hou and Daniel A. Higgins. Single molecule studies of dynamics in polymer thin films and at surfaces: Effect of ambient relative humidity. *J. Phys. Chem. B*, 106(40):10306–10315, 2002.
- [146] G. B. Cox. The influence of silica structure on reversed-phase retention. *Journal of Chromatography A*, 656(1-2):353–367, Dec 1993.
- [147] J. Nawrocki. The silanol group and its role in liquid chromatography. *Journal of Chromatography A*, 779(1-2):29–71, Aug 1997.
- [148] Mary J. Wirth and Derrick J. Swinton. single molecules probing of mixed-mode adsorption at a chromatographic interface. *Anal. Chem.*, 70(24):5264–5271, 1998.

- [149] Mary J. Wirth and Derrick J. Swinton. single molecules study of an adsorbed oligonucleotide undergoing both lateral diffusion and strong adsorption. *J. Phys. Chem. B*, 105:1472–1477, 2001.
- [150] X Michalet, A. N Kapanidis, T Laurence, F. Pinaud, S Doose, M Pflughoeft, and S. Weiss. The power and prospects of fluorescence microscopies and spectroscopies. *Annual Review of Biophysics and Biomolecular Structure*, 32:161–182, 2003.
- [151] S. Weiss. Measuring conformational dynamics of biomolecules by single molecule fluorescence spectroscopy. *Nature Structural Biology*, 7(9):724–729, 2000.
- [152] T. Ha. single molecules fluorescence resonance energy transfer. *Methods*, 25(1):78–86, 2001.
- [153] X Michalet and S. Weiss. single molecules spectroscopy and microscopy. *Comptes Rendus Physique*, 3(5):619–644, 2002.
- [154] E Haustein and P. Schwille. single molecules spectroscopic methods. *Current Opinion in Structural Biology*, 14(5):531–540, 2004.
- [155] E. J. G Peterman, H Sosa, and W. E. Moerner. single molecules fluorescence spectroscopy and microscopy of biomolecular motors. *Annual Review of Physical Chemistry*, 55:79–96, 2004.
- [156] Richard P. Haugland. *The Handbook: A Guide to Fluorescent Probes and labelling Technologies, Tenth Edition*. Invitrogen, Eugene, Oregon, 2005.
- [157] H Brismar, O Treppe, and B Ulfhake. Spectra and fluorescence lifetimes of lissamine rhodamine, tetramethylrhodamine isothiocyanate, texas red, and cyanine 3.18 fluorophores: influences of some environmental factors recorded with a confocal laser scanning microscope. *J. Histochem. Cytochem.*, 43(7):699–707, 1995.
- [158] N Panchuk-Voloshina, R. P Haugland, J. Bishop-Stewart, M. K Bhalgat, P. J Millard, F Mao, and W. Y. Leung. Alexa dyes, a series of new fluorescent dyes that yield exceptionally bright, photostable conjugates. *Journal of Histochemistry & Cytochemistry*, 47(9):1179–1188, 1999.
- [159] A Margineanu, J Hofkens, M Cotlet, S Habuchi, A Stefan, J. Q Qu, C Kohl, K Müllen, J Vercammen, Y Engelborghs, T Gensch, and F. C. De Schryver. Photophysics of a water-soluble rylene dye: Comparison with other fluorescent molecules for biological applications. *Journal of Physical Chemistry B*, 108(32):12242–12251, 2004.

- [160] A. N Kapanidis and S. Weiss. Fluorescent probes and bioconjugation chemistries for single molecules fluorescence analysis of biomolecules. *Journal of Chemical Physics*, 117(24):10953–10964, 2002.
- [161] Jennifer Lippincott-Schwartz, Erik Snapp, and Anne Kenworthy. Studying protein dynamics in living cells. *Nature Reviews*, 2:444–456, 2001.
- [162] Georg Seisenberger, Martin U. Ried, Thomas Endress, Hildegard Büning, Michael Hallek, and Christoph Bräuchle. Real-time single molecules imaging of the infection pathway of an adeno-associated virus. *Science*, 294:1929–1932, 2001.
- [163] Christoph Bräuchle, Georg Seisenberger, Thomas Endress, Martin U Ried, Hildegard Baening, and Michael Hallek. Single virus tracing: Visualization of the infection pathway of a virus into a living cell. *ChemPhysChem*, 3:299–303, 2002.
- [164] G Seybold and G. Wagenblast. New perylene and violanthrone dyestuffs for fluorescent collectors. *Dyes and Pigments*, 11:303–317, 1989.
- [165] Jianqiang Qu, Christopher Kohl, Mark Pottek, and Klaus Müllen. Ionic perylene-tetracarboxdiimides: Highly fluorescent and water-soluble dyes for biolabelling. *Angewandte Chemie*, 116(12):1554–1557, 2004.
- [166] R Gvishi, R Reisfeld, and Z. Burshtein. Spectroscopy and laser action of the red perylimide dye in various solvents. *Chemical Physics Letters*, 213(3-4):338–344, 1993.
- [167] S. B Brichkin, M. A Kurandina, T. M Nikolaeva, and V. F. Razumov. Effects of surfactants on the spectral properties of carbocyanine dyes in solutions. *High Energy Chemistry*, 38(6):373–380, 2004.
- [168] S Das, K. G Thomas, K. J Thomas, V Madhavan, D Liu, P. V Kamat, and M. V. George. Aggregation behavior of water soluble bis(benzothiazolylidene)squaraine derivatives in aqueous media. *Journal of Physical Chemistry*, 100(43):17310–17315, 1996.
- [169] F Wuerthner, C Thalacker, S Diele, and C. Tschierske. Fluorescent j-type aggregates and thermotropic columnar mesophases of perylene bisimide dyes. *Chemistry—a European Journal*, 7(10):2245–2253, 2001.
- [170] M Kasha, H.R Rawls, and M.A. El-Bayoumi. The exciton model on molecular spectroscopy. *Pure Applied Chemistry*, 11:371–392, 1965.
- [171] E. G McRae and M. Kasha. Enhancement of phosphorescence ability upon aggregation of dye molecules. *Journal of Chemical Physics*, 28(4):721–722, 1958.

- [172] James Franck and Edward Teller. Migration and photochemical action of excitation energy in crystals. *Journal of Chemical Physics*, 6:861–872, 1938.
- [173] P. Alexandridis, J. F. Holyworth, and Hatton T. A. Micellization of poly(ethylene oxide)-poly(propylene oxide)-poly(ethylene oxide) triblock copolymers in aqueous solutions: Thermodynamics of copolymer association. *Macromolecules*, 27:2414–2425, 1994.
- [174] N Hioka, R. K Chowdhary, N Chansarkar, D. Delmarre, E Sternberg, and D. Dolphin. Studies of a benzoporphyrin derivative with pluronics. *Canadian Journal of Chemistry-Revue Canadienne De Chimie*, 80(10):1321–1326, 2002.
- [175] M.J. Rosen. *Surfactants and interfacial phenomena*. New York, 2ed edition, 1989.
- [176] M. Talhavini and T.D.Z. Atvars. Dye-polymer interactions controlling the kinetics of fluorescein photobleaching reactions in poly(vinyl alcohol). *Journal of Photochemistry and Photobiology A: Chemistry*, 114(1):65–73, 1998.
- [177] I Ellinger, H Klapper, and R. Fuchs. Fluid-phase marker transport in rat liver: Free-flow electrophoresis separates distinct endosome subpopulations. *Electrophoresis*, 19(7):1154–1161, 1998.
- [178] B. L. Grosshans, D. Ortiz, and P. Novick. Rab3 and their effectors: Achieving specificity in membrane traffic. *Proceedings of the National Academy of Sciences of the United States of America*, 103(32):11821–11827, 2006.
- [179] K. Mohrmann and P. van der Sluijs. Regulation of membrane transport through the endocytic pathway by rabgtpases. *Molecular Membrane Biology*, 16(1):81–87, 1999.
- [180] M. R. G. Russell, D. P. Nickerson, and G. Odorizzi. Molecular mechanisms of late endosome morphology, identity and sorting. *Current Opinion in Cell Biology*, 18(4):422–428, 2006.
- [181] Karel W. A. Wirtz, Division North Atlantic Treaty Organization. Scientific Affairs, and Nato Study Institute on Molecular Mechanisms of Signalling and Targeting. Molecular mechanisms of signalling and membrane transport. NATO ASI series, vol. 101, Berlin ; New York, 1997.
- [182] Alberts B., A. Johnson, J. Lewis, Raff M., Roberts K, and P. Walter . *Chapter13: Intracellular Vesicular Traffic (From Molecular Biology of the Cell)*. Garland Science Textbooks, 4th edition, 2002.

-
- [183] R. B Mujumdar, L. A Ernst, S. R Mujumdar, C. J Lewis, and A. S. Waggoner. Cyanine dye labelling reagents - sulfoindocyanine succinimidyl esters. *Bioconjugate Chemistry*, 4(2):105–111, 1993.
- [184] L. H Lindner, M. E Eichhorn, H Eibl, N. Teichert, M Schmitt-Sody, R. D Issels, and M. Dellian. Novel temperature-sensitive liposomes with prolonged circulation time. *Clinical Cancer Research*, 10(6):2168–2178, 2004.
- [185] Barbara Platschek, Nikolay Petkov, and Thomas Bein. Tuning the structure and orientation of hexagonally ordered mesoporous channels in anodic alumina membrane hosts: A 2d small-angle x-ray scattering study. *Angew. Chem.*, 118(7):1152–1156, 2006.

Acknowledgments

Although this thesis bears the name of only one person, it would never have been possible to achieve all the work without the support and participation of many persons to whom I want to address all my gratitude.

First of all, I wish to thank my supervisor, Professor Christoph Bräuchle, for giving me the opportunity to discover such a fascinating interdisciplinary domain, his advices and the way he trusts me during all this project.

I thank Jens, Don, John and Prof. Bein whose expert knowledge was of great value. My thanks also to Moritz Ehrl for all the administrative procedures.

In addition, I am especially grateful to Johanna and Barbara who helped me so much during these years for many diverse things like correcting my German, giving me inspiration for new exciting experiments, or just talking about the last week-end.

Thanks to Iko, Stephan, Timo, Florian, Robert, Karla, Julia, Nadia, Monika, Barbara P., Andel, Ralf K., Erwin K., Stephan (the other), Joanna A., Hanna, Adam, Alexandra, Philipp, Ondrey, Ralf B., Gregor, Matthias, Sebastian, Serguey, Peter S., Peter S., Dorothee, Dina, Irmgard, Alper, Andreas Z., Thomas, Andrew, Gregor J., Elizabeth L., Christophe J. (oups!), for being great colleagues and for the nice atmosphere who made working in this group a pleasure. Special thanks to Stephan and Sebastian who involved me in their fascinating project, and to Hell who taught me a lot about our fantastic subject. Thanks to Wolfgang and to my trainees Barbara, Mark and Steffi.

Words of special gratitude are addressed to my family; especially my parents, my brother David and Emma, my grand-parents, Adrienne, Caroline and Ursula for their love and persistent support.

At last and further the most I owe to Sandrine and Nathalie. Without you and your unlimited patience, understanding, assistance and encouragement throughout these years, nothing of this would ever be possible. Thank you, thank you, thank you.

Perhaps you will read this in ten or twenty years, Maxime. Of course I didn't forget you. Thank you for being what you are; I am so proud of you!

Curriculum vitae

Name Christophe Jung
Geburtsdatum 18. Februar 1974
Geburtsort Haguenau, Frankreich
Familienstand verheiratet, ein Kind
Staatsangehörigkeit französisch

Abschluss **Baccalauréat C. (Abitur)**
Lycée d'Enseignement Général, Haguenau

Studium

1992 - 1994 **Classes préparatoires aux concours des Grandes Ecoles**
Lycée Kleber, Strassburg

1994 – 1995 **D.E.U.G. « Sciences de la matière » Physique-Chimie (Vordiplome)**
Université Louis Pasteur, Strassburg

1995 – 1996 **Licence-ès-sciences-physiques**
Université Louis Pasteur, Strassburg

1996 – 1997 **C.A.P.E.S. physique-chimie (Nationaler Wettbewerb zum Lehramt)**
I.U.F.M. (Institut de Formation des Maîtres), Strassburg

Berufstätigkeit

Lehrer für Physik und Chemie

1997 - 1998 Lycée Technique LETI, Haguenau
1998 – 1999 Lycée d'Enseignement Général Pierre Forest, Maubeuge
1999 – 2002 Collège Marcel Pagnol, Wittenheim

Weiteres Studium

2002 – 2003 **Maîtrise de Chimie Physique (Magister)**
Université Louis Pasteur, Strassburg

Seit 08.2003 Promotion im Arbeitskreis Prof. C. Bräuchle, LMU München